Scuola Internazionale Superiore di Studi Avanzati - Trieste

Doctoral Thesis

Galactic Dark Matter distribution and its implications for experimental searches

Candidate : Mihael Petač
Supervisor : Prof. Piero Ullio

September 2019

SISSA - Via Bonomea 265 - 34136 TRIESTE - ITALY

Contents

Abstract

Dark Matter presents one of the key missing pieces in our understanding of the Universe. On the one hand, there is a substantial amount of independent astronomical and cosmological observations, which provide convincing evidence for its existence through various gravitational signatures. On the other hand, any non-gravitational interactions of Dark Matter remain elusive, despite more than two decades of dedicated searches in various experiments. Several of them have contended successful detection, however, such claims remain disputed, since they are in tension with null results of other related experiments and often suffer from considerable modelling uncertainties.

One of the crucial unknowns entering the interpretation of direct and indirect Dark Matter searches is its distribution within galaxies. Together with rapid improvements in astronomical observations, this drives the need for accurate phase-space modelling of galactic Dark Matter distribution, which will be explored in detail throughout this thesis in various settings. First, a novel method for computing the phase-space distribution of relaxed Dark Matter component within axisymmetric systems will be presented. This method is of particular importance when addressing spiral galaxies and can have a significant impact on the interpretation of direct detection experiments, which crucially depends on the density and velocity distribution of Dark Matter in the solar neighbourhood. Therefore, the proposed phase-space distribution model will be applied to our Milky Way and carefully matched against recent measurements of the galactic kinematics. Furthermore, the corresponding impact on direct detection experiments and differences with respect to the traditional models, relying on Maxwellian velocity distribution and/or spherical symmetry, will be investigated. Regarding indirect detection, new results related to expected signals from dwarf satellite galaxies of the Milky Way will be presented, addressing the general case of velocity-dependent annihilation cross-section. Special attention will be given to a non-perturbative effect, commonly known as the Sommerfeld enhancement, which can lead to a significant boost of the annihilation signals. Similarly, as in the case of Milky Way, recent measurements of stellar kinematics within dwarf satellites will be used to bracket the astrophysical uncertainties entering the interpretation of corresponding indirect searches. Finally, a brand-new technique for detecting dark galactic subhalos will be proposed, which relies on the modern tools of machine learning and their ability to find subtle patterns in complex datasets. More precisely, the possibility of detecting tiny perturbations in stellar density and kinematics, induced by transpassing Dark Matter subhalos, will be addressed.

Acknowledgments

I would like to thank SISSA for providing me with the opportunity to pursue my research interests and introducing me to the world of cutting-edge research. Special thanks go to my supervisor, Prof. Piero Ullio, for his patience, guidance and granting me the freedom to explore my own interests. Big credit goes also to Mauro Valli for his assistance and sharing his valuable research experience with me. I would also like to give big thanks to the SISSA's Student Secretariat, who was always extremely helpful and fast in resolving administrative issues.

A big credit goes also my family and friends, who were always extremely supportive and encouraged me to nurture my curiosity. I am also very grateful to my office mates, Jiaxin and Alessandro, for their help and valuable insights regarding my work. Last but not least, I would like to thank to Gauri for all the positivity and happiness she shared with me.

1. Introduction

The 20th century will most certainly be remembered as the century of great discoveries. This is particularly true for the field of Physics, where fundamental insights allowed us to formulate theories that able to account for nearly all the phenomena encountered in the world around us. The advent of Quantum mechanics triggered a revolution in the way we think about the smallest constituents of the Universe and paved the way for formulation of the Standard Model of the elementary particles, which elegantly explains the origin of fundamental forces, apart from gravity, and predicts the behaviour of matter with staggering accuracy over a vast range of energies. In parallel, our understanding of gravity fundamentally changed through the theory of General Relativity, transcending the traditional concepts of space and time. Furthermore, it allowed us to pursue questions regarding the very beginnings of our Universe and study its evolution on cosmological scales.

Despite all the success, there are still many reasons to continue our pursuit of exploring the Laws of Nature. In modern Physics, there are several notable shortcomings, among which perhaps the most pressing one is the fact that Quantum Mechanics, as we know it, leads to inconsistencies when applied to curved spacetime, while the latter is a generic prediction of the General Relativity. Besides this, there are also observed phenomena, which can not be included in the framework of the standard theories, such as the existence of exotic forms of energy, namely the Dark Energy and Dark Matter (DM). This thesis will be devoted to the latter, with particular focus on the distribution of DM within galaxies, which represents one of the critical uncertainties entering the interpretation of various experimental efforts to detect its non-gravitational signatures that remain elusive up to this day. In chapter 1, I will begin with a short review regarding the phenomenon of DM and various experiments aimed at detecting its signatures. This will be followed by chapter 2, with a prelude regarding the phase-space distribution functions and Boltzmann transport equation, where several key concepts, used throughout the rest of the thesis, will be introduced. In chapter 3, I will discuss my work regarding the phase-space distribution modelling in axisymmetric systems and apply it to obtain the DM distribution within Milky Way from careful analysis of kinematic tracers. Furthermore, its implications for direct detection searches will be explored. In chapter 4 I will instead focus on the case of annihilating DM and prospects for its indirect detection through prompt emission of γ-rays in Milky Way's dwarf satellite galaxies. Again, DM phase-space distribution models will be carefully tuned to the observations of stellar kinematics within these objects and annihilation signals will be addressed in the general setting, where the leading order cross-section can carry non-trivial velocity dependence, paying particular atten-

tion to the possible enhancement of annihilation rates due to the Sommerfeld effect. Finally, in chapter 5 an exciting new technique for probing the small scale clustering properties of DM through perturbations in the galactic stellar field will be explored, which could provide interesting new information regarding the nature of this mysterious form of matter.

1.1 The missing mass

The nature of Dark Matter (DM) is one of the most pressing open questions in the modern understanding of elementary particles and cosmology. While there exists a considerable amount of insights into its properties, at least with respect to even more mysterious dark energy that dominates the energy budget of present Universe, we still lack a comprehensive understanding of its nature and how it relates to other well-known forms of matter. Its first mentions appeared more than a hundred years when leading astronomers of the time began to notice that visible matter is not sufficient to explain the motion of stars within Milky Way. One of the first quantitative studies was performed by Swiss astronomer Fritz Zwicky, who estimated the amount of DM needed to explain the dynamics within galaxy clusters [1, 2]. He postulated the existence of "dunkle Materie", which neither absorbs nor emits light and is much more abundant than the visible matter. His hypothesis was very provocative at the time and rightfully disputed, as it was later shown that his estimates for the abundance of DM were too large. However, further observational evidence in favour of the existence of DM kept accumulating in the following decades. First undisputed works demonstrating the need for DM component within galaxies are probably the ones of Vera Rubin et al. [3, 4] and Ken Freeman [5], who analysed rotation profiles and distribution of visible mass within nearby spiral galaxies and concluded that they must contain roughly ten times more DM then ordinary baryonic matter. Their findings stimulated the astronomic community and before long additional support in favour of the DM hypothesis was found through the phenomenon of gravitational lensing. Further, and up to now the most accurate, determination of DM abundance came in the 2000s by detailed analysis of the anisotropies in Cosmic Microwave Background (CMB) radiation [6, 7], which were in excellent agreement with the predictions of the standard cosmological model that contains large amounts of DM. The study of acoustic peaks in the CMB spectrum revealed that baryonic matter consists only about one-fifth of the total matter content of the Universe. In parallel with the findings in astronomy and cosmology, the standard model of elementary particles was developed and tested through extremely accurate accelerator experiments. It was soon clear that none of the presently known particles can constitute a significant fraction of the DM, pointing out a blind spot in otherwise extremely successful theory. This lead to a vast number of suggestions on how to extend the existing models to include the dark components of the Universe and numerous dedicated experimental searches have been performed. Unfortunately, no undisputed detection has been made so far. However, significant parts of parameter space in many existing models have been excluded. The robustness of such constraints and their interplay with the galactic DM distribution will be one of the main topics throughout this work.

In the following section, I will provide a short overview of the broad set

of observations that all call out for the existence of DM. This will be followed by a review of a few possible explanations of the phenomenon; however, the discussion will be unjustly brief, considering the vast amount of possible DM candidates found throughout the literature.

1.1.1 Observational evidence

All of the evidence in favour of DM comes from astronomical and cosmological observations of its gravitational effects. There existed hints that "bright matter" is not sufficient to explain the dynamics of astronomical objects, dating as far back as the end of 19th century, when Lord Kelvin draw this conclusion by estimating the velocity dispersion of stars in the Solar neighbourhood [8], however, quantitative measurements only began to pile up after the second half of the 20th century. I will begin the review with the initial works which were, similarly as Kelvin's approach, based on Newtonian dynamics of galaxies and galaxy clusters. This will be followed by probes based on gravitational lensing, which soon after the discovery of missing dynamical mass in galaxies provided further proof for its existence. Finally, I will present modern measurements related to the cosmological matter distribution, such as the CMB observations and vast galaxy surveys, which provide us with crucial information regarding the nature and abundance of DM.

Dynamics within galaxies and galaxy clusters

Most direct evidence for the existence of Dark Matter are probably the rotation curves of spiral galaxies. Using simple Newtonian physics one can show that the velocity of a circular orbit at radial distance R from the centre of the object is given by:

$$V_c(R) = \sqrt{\frac{GM(r=R)}{R}}\,, \tag{1.1}$$

where $M(r)$ is the total mass enclosed within given radius r, while G is the Newton's gravitational constant. Therefore, the rotational velocity profile of gas or stars in a spiral galaxy provides a good proxy for its radial mass distribution. In figure 1.1 rotation curves of galaxies are shown for several absolute magnitude bins, where observations of individual galaxies were rescaled according to their optical radius $R_{\rm opt}$ (defined as the distance from centre of galaxies to the isophote that encircles 83% of the total luminosity) and its corresponding circular velocity $V_c(R_{\rm opt})$, and then stacked upon each other. They reveal that the circular velocities of stars and gas can be attributed to the mass of luminous matter (dotted line) only in the central part of the disk, while at increasing radial distances additional mass (dashed line) is needed to produce the observed nearly constant $V_c(R > R_{\rm opt})$. From equation (1.1) it immediately follows that the enclosed mass must scale approximately as $M(r) \propto r$ to produce flat rotation curves, implying DM density profile $\rho(r) \propto r^{-2}$. This general picture has been confirmed by many independent studies, looking at velocity profiles of stars, as well as gas, in extensive catalogues of galaxies, always finding deficit of luminous matter with respect to the amount needed to account for the measured $V_c(R)$, see e.g. [3–5, 9–13].

Analogous arguments in favour of the existence of DM can be made for velocity dispersion supported systems, such as elliptical galaxies or galaxy clusters. Under the assumption that these systems are virialised, their total kinetic energy should be one half of the total potential energy, which implies:

$$\sigma^2 \sim \frac{GM}{R} \,, \tag{1.2}$$

where σ is the velocity dispersion of the observed tracers. Both, elliptical galaxies as well as galaxy clusters, show a systematic deficit of luminous matter for the large measured velocity dispersions of stars [14,15] and member galaxies [16,17], respectively.

Together, these observations established a strong case for the existence of additional matter component that does not interact with light and cools much less efficiently than ordinary matter (since it resides in halos that are much larger than the baryonic content), implying negligible interaction rates with standard model particles. As an alternative explanation, there were several attempts to modify the Newtonian dynamics on galactic scales. However, such models are becoming increasing disfavoured by modern observations, among which detailed studies of gravitationally lensed systems, discussed in the following, are particularly hard to reconcile with such modifications.

Gravitational lensing

The bending of light due to gravitational deformation of spacetime is a phenomenon that has been known for more than a century and played a crucial role in providing the first confirmation of the Einstein's theory of General Relativity. However, strongly lensed systems, where multiple images of the background object or characteristic light rings can be observed, have not been detected until 1979, when the first twin image of a quasar was discovered [18]. This provided a new probe for the investigation of DM since strongly lensed systems generally allow for accurate reconstruction of the matter distribution along the line of sight of the gravitational lens. Within the last decades, numerous strongly lensed systems were discovered, for which the lens mass is typically provided by galaxy clusters, while the background sources can vary from quasars, galaxies, or even other galaxy clusters. By independently constraining the baryonic content, the amount and distribution of DM in galaxy clusters can be determined [19], typically resulting in much better accuracy then, e.g., through arguments based only on the virial theorem. Furthermore, ever-increasing resolution of telescopes promises a unique way to probe the clustering of DM down to the smallest scales, which could provide clues towards its elusive particle physics properties, for example discussed in [20–22].

While strongly lensed systems are particularly interesting, since they allow highly accurate mass reconstruction, they are relatively rare. A much more common type of gravitational lensing is the weak lensing, where the trajectory of light is only slightly deformed due to spacetime curvature. However, by studying statistical properties of shear deformations in comprehensive galaxy surveys, the global distribution of matter can be inferred, and the observations again point towards a large discrepancy in the amount of luminous verses total gravitational mass [23, 24]. Furthermore, weak lensing was also used to reconstruct the mass distribution in the spectacular "Bullet Cluster" [25, 26], which

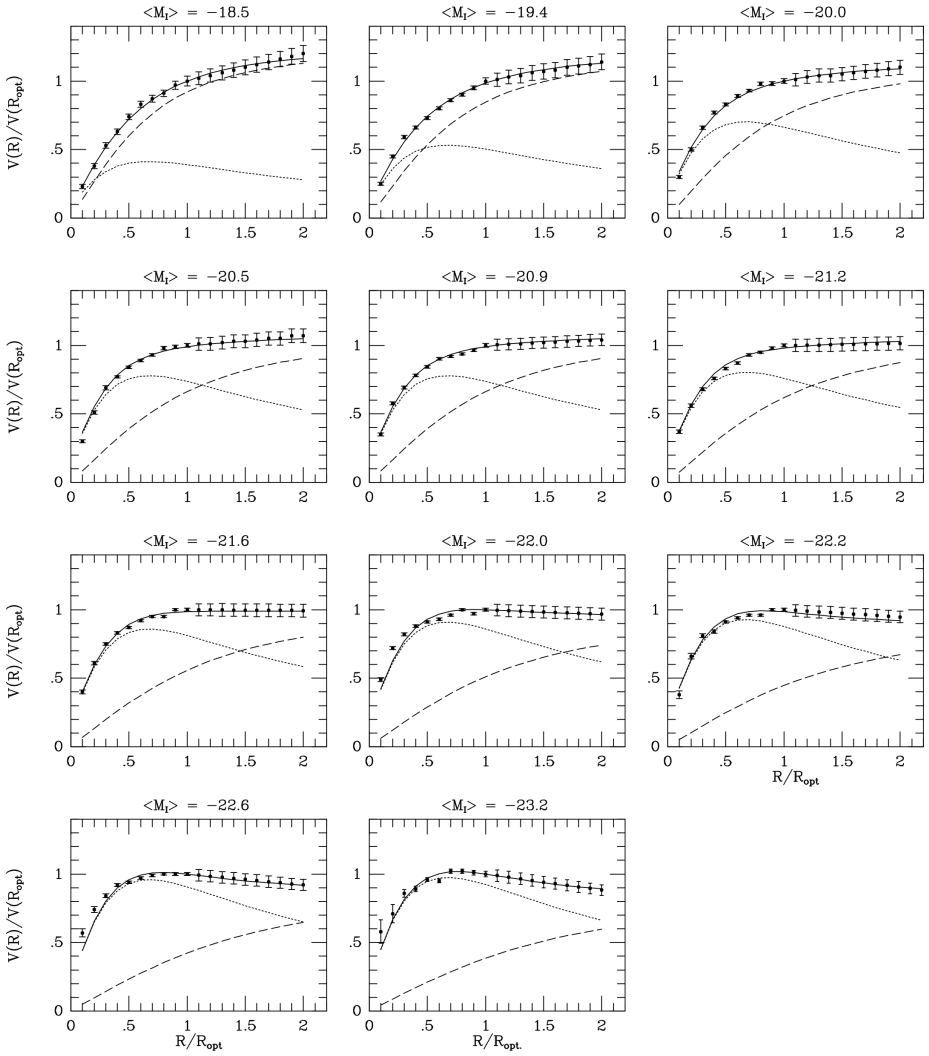

Figure 1.1: Compilation of rotation curves for galaxies with various absolute magnitudes [13]. The rotation curves of individual galaxies are rescaled according to their optical radii $R_{\rm opt}$ (defined as the distance from centre of galaxies to the isophote that encircles 83% of the total luminosity) and its corresponding circular velocity $V_c(R_{\rm opt})$ and then stacked, exhibiting surprisingly universal profiles. Dotted and dashed lines correspond to the inferred luminous and dark matter accordingly.

clearly shows the segregation of hot collisional gas and virtually collisionless DM in the encounter of two galaxy clusters, which is extremely hard to reconcile with non-particle explanations of DM phenomena, such as modified theories of gravity. Therefore, weak and strong lensing provides a convincing argument in favour of non-baryonic DM hypothesis, independent of claims based on the dynamics of galaxies and galaxy clusters.

Cosmic microwave background and structure formation

Arguably the most compelling evidence in favour of Dark Matter comes from the observation of Cosmic Microwave Background (CMB) radiation. It contains rich information regarding our Universe, from around the time when first atoms were formed down to the present time. Its discovery was accidental and unanticipated; however, since all the physical processes involved are relatively well understood, it soon became one of the most powerful cosmological probes. In a nutshell, the CMB radiation was produced when protons and electrons in cooling primordial plasma for the first time combined into atoms (a process commonly known by a misleading name of *re*combination). This pairing of charged particles into neutral atoms allowed the electromagnetic radiation to travel cosmological distances without scattering and can be efficiently detected even today. One of the amazing features of CMB is that it represents the most accurate measurement of black body spectrum up to now, implying thermal equilibrium and adiabatic evolution of the Universe throughout billions of years. However, there are small differences in the temperature of radiation, depending on the observed position on the sky, which can provide a surprisingly accurate determination of the cosmic abundance of DM. By statistically describing the perturbations in terms of spherical harmonics one obtains the angular power spectrum, shown in figure 1.2, that contains the characteristic acoustic peaks related to temperature fluctuations at the time of recombination [27]. Before the formation of atoms, the protons and electrons could not collapse to form large over-densities due to radiation pressure, but rather oscillated on scales determined by the sound speed of plasma and underlying gravitational potential wells. However, the CMB angular power spectrum shows that the density perturbations must have been growing even before the epoch of recombination, forming structure on scales that would have been washed out if the entire matter content of the Universe was coupled to the hot baryon-photon plasma. Therefore, the additional mass component must have been effectively pressureless, which is a behaviour typical of non-relativistic collisionless particles. From the amplitude and positions of the CMB acoustic peaks, one can accurately determine key cosmological parameters, among which is also the baryon-DM mass ratio. The most recent Planck satellite measurements show that the letter lies at $\Omega_{\rm b}/\Omega_{\rm DM} = 0.187 \pm 0.001$ [28]. The CMB determination of DM abundance is in good agreement with other observations and provides one of the pillars of the standard cosmological model. Furthermore, it establishes strong constraints on the DM interaction rate with primordial plasma, but also shows that it became non-relativistic long before the epoch of recombination. The observation of CMB also has profound implications for the subsequent formation of galaxies and galaxy clusters, which again requires a DM component.

With the discovery of CMB, it soon became clear that baryons alone could not have produced the galaxies we see today. It turns out that the structure

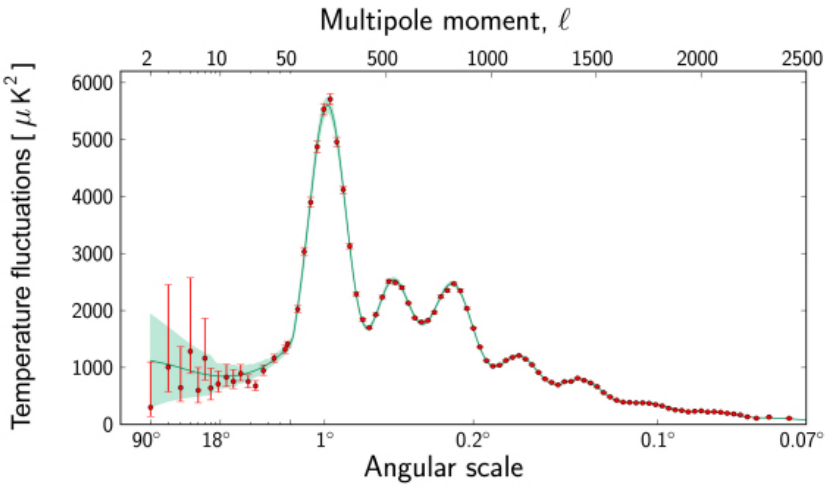

Figure 1.2: Angular power spectrum of temperature fluctuations as measured by the Planck satellite. The acoustic peaks that contain information regarding the matter content of the Universe at the time of recombination are measured with stunning accuracy. *Credit: ESA and the Planck Collaboration.*

formation requires additional cold, i.e. non-relativistic, DM component to produce the present extreme density contrasts from the primordial plasma within the age of our Universe. This has been formally shown through density perturbation theory, where the Einstein's equations are perturbatively solved in terms of density contrast, assuming nearly smooth initial conditions with small, scale-invariant, Gaussian perturbations, as implied by the CMB. When one includes DM, the solutions for matter power spectrum agree well with the observations over a huge range of scales, ranging from large scale structure (LSS) surveys, down to the scale of individual galaxies. In figure 1.3 the predicted matter power spectrum is shown along with a variety observational constraints. Furthermore, modern suits of numerical simulations are capable of replicating the galaxy formation from the initial perturbations and produce galaxies resembling the ones in present Universe with impressive accuracy [29, 30], confirming the need for cold DM in the formation of structures as we know them.

1.1.2 Dark Matter candidates

As presented in the previous section, there exist many independent observations that point towards the existence of DM. All of the evidence, however, relies on the gravitational effects, while other signatures, despite significant experimental efforts to detect them, remain elusive. This puts strong constraints on particle physics models that attempt to explain the existence of DM, but does not provide us with much insights regarding its actual nature. One of the few well-established DM properties is its *cosmological abundance*. Modern probes, such as CMB and LSS surveys, provide us with rather accurate measurements of its contribution to the energy budget of the Universe, which amounts to roughly 26% of the total present-day energy density. Furthermore, the baryon acoustic

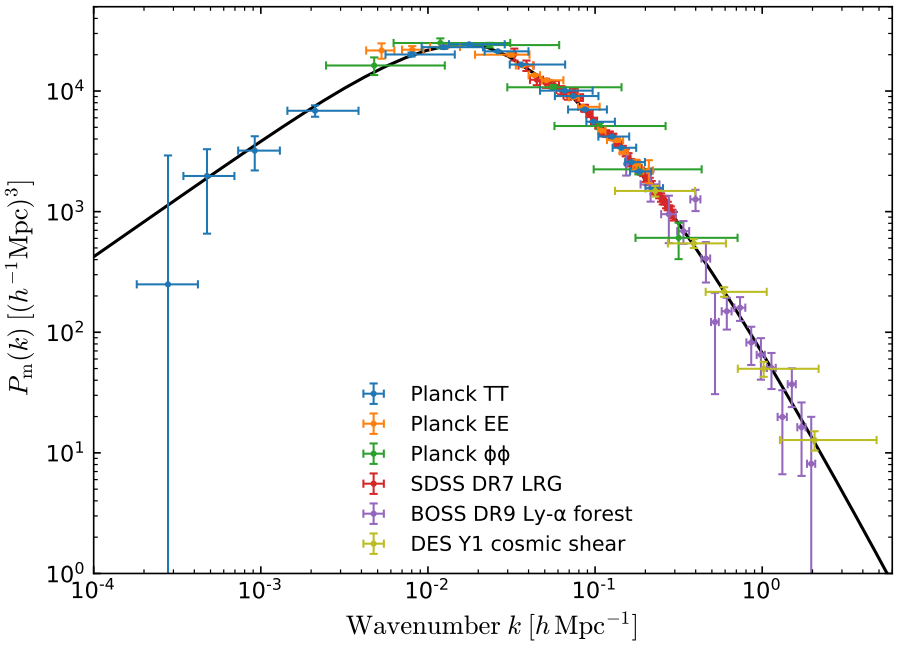

Figure 1.3: The amplitude of matter power spectrum as a function of scale with over-plotted observed values from different surveys. The image was taken from [28].

oscillations, as well as limits from Big Bang Nucleosynthesis, put strong constraints on its coupling to the primordial plasma. Together with the limits from collider experiments, these observations give us strong reasons to believe that DM has *no electric or colour charge*. While the SM neutrinos fulfil these criteria, they can constitute only a small fraction of the total DM abundance due to their tiny masses, making them relativistic even long after the Universe had entered the matter-dominated era. This is, however, in contradiction with the standard cosmological model, supported by CMB and LSS observations, where DM has to behave like *non-relativistic*, i.e. *pressureless*, matter to explain the observed growth of density perturbations. On the other hand, it remains unknown whether it consists of a single particle species or a larger collection of fields, like in case of the SM. Strong limits on DM coupling to the SM through new physics can be inferred and are primarily driven by results of collider experiments and (in)direct DM searches, which will be reviewed in the next section. Much less is known about interactions within the dark sector itself. However, several interesting upper limits on DM self-interaction rate exist from the aforementioned gravitational lensing observations of merging galaxies and small scale matter power spectrum. Finally, from the large cosmic abundance of DM, which must have been generated very early on in the history of Universe and survived until today, one can conclude DM particles must be *extremely long-lived or stable*, with lower bounds on its lifetime comparable to the age of the Universe. From the above properties one can conclude that DM can not be constituted from any of the known elementary particles [1] and an extension of the standard theory is needed.

Beyond these general properties, not much is known regarding DM, leaving great freedom in possible theoretical explanations. This reflects in the number of suggested schemes, raging from effective models to modifications or generalizations of fundamental theories. Given the vast amount of existing works, an exhaustive overview seems virtually impossible. Therefore, I will in the following present only a few simple, but fundamentally different, categories of DM particle candidates. A more complete review of viable DM models and existing constraints can be found, for example, in [32–35] and references therein.

Thermal relics

Perhaps the simplest explanation of DM can be realized in models that assume the existence of heavy particles that decoupled from the ordinary matter at some point in the very early Universe. In favour of this hypothesis, we know that the latter used to be much denser and hot in the past. Therefore, particles scattered more frequently and with higher energies. Under such conditions, the interaction rate of DM with SM fields could have been non-negligible, keeping the two components in thermal equilibrium, until their eventual decoupling due to the expansion of the Universe. Hence, DM candidates of this type are known as *thermal relics*. For a single species of DM particles, it is relatively easy to compute the cosmological abundance after the decoupling using the Boltzmann equation and will be discussed more thoroughly in section 2.2. Here I simply state the result for the evolution of number density, n_χ, of thermal relic particle χ with thermally averaged cross-section times relative velocity, $\langle \sigma_{\text{ann}} v \rangle$,

[1] Possible exceptions are exotic hadronic states, for example suggested in [31].

responsible for conversions between DM and SM states:

$$\frac{dn_\chi}{dt} + 3Hn_\chi = \langle\sigma_{\text{ann}}v\rangle \left((n_\chi^{\text{eq}})^2 - n_\chi^2\right) \ . \tag{1.3}$$

The terms on left hand side of the above equation are nothing but the change in number density of χ in a comoving volume, i.e. $d(n_\chi a^3)/dt$, with a being the scale factor and $H = \dot{a}/a$ the Hubbel expansion rate. The former has be equal to the yield of pair-creation/annihilation processes, described by the right hand side of the equation (1.3), where n_χ^{eq} stands for the equilibrium number density of χ. Under the assumption that χ becomes non-relativistic prior its decoupling, which is indeed the case for thermal relics with masses $m_\chi \gg$ GeV and weak scale $\langle\sigma_{\text{ann}}v\rangle$, its equilibrium abundance falls off exponentially, $n_\chi^{\text{eq}} \propto \exp(-m_\chi/T)$, leading to quickly diminishing annihilation rate $\Gamma = \langle\sigma_{\text{ann}}v\rangle n_\chi$. Therefore, when the Universe cools below the decoupling temperature T_{dec}, at which Hubbel expansion rate becomes comparable to the annihilation rate of χ, i.e. $H(T_{\text{dec}}) \sim \Gamma(T_{\text{dec}})$, the *freeze-out* occurs and χ's comoving number density remains nearly constant throughout the subsequent evolution. The resulting relic abundance mainly depends on the value of $\langle\sigma_{\text{ann}}v\rangle$, but also to a lesser degree on m_χ, as shown in figure 1.4. Interestingly enough, one obtains the correct amount of DM for $m_\chi \approx 100$ GeV and $\langle\sigma_{\text{ann}}v\rangle \approx 3 \cdot 10^{-26}$ cm^3/s^2, where the latter is of the order of typical weak force cross-sections. Such Weakly Interacting Massive Particles (WIMPs) are generically predicted in highly appealing theories of Supersymmetry [36–40], but also in Grand Unified Theories (GUTs) [41, 42] or models with additional compact dimensions [43, 44], where one or more of the many newly predicted particles could play the role of DM. However, one must note that the simple picture above can get significantly modified if DM is composed of several different particle species, leading to much richer phenomenology. Similarly, alternative production mechanisms are also possible, such as the so-called *freeze-in* mechanism, where DM is assumed to have extremely small $\langle\sigma_{\text{ann}}v\rangle$. In this case, the thermal equilibrium with SM particles is actually never reached, but never-theless the correct amount of DM particles can be produced in the early Universe through pair-creation processes. Most of the discussions in this thesis will tacitly assume WIMP-like DM, namely new heavy elementary particles that have small, but hopefully detectable, interactions with visible matter.

Sterile neutrinos

Neutrinos are one of the most enigmatic particles within the SM. Due to their neutrality under electromagnetic and strong force, they interact only weakly, which makes it difficult to study them experimentally. Non-the-less, several important observations regarding neutrinos have been made, among which the existence of their masses is perhaps the most striking one. In the SM only left-chiral states are assumed to exist, which prohibits them from obtaining masses through the Higgs mechanism, like the rest of SM fermions. Together with other motivations, such as the observed neutrino oscillation patterns and/or possible source of additional CP violation needed for explaining baryon asymmetry of the Universe, this lead to proposals assuming the existence of right-chiral (in context of DM often referred to as *sterile*) neutrinos [46–49]. Since the latter do not take part in weak interactions, they are truly neutral particles and can have

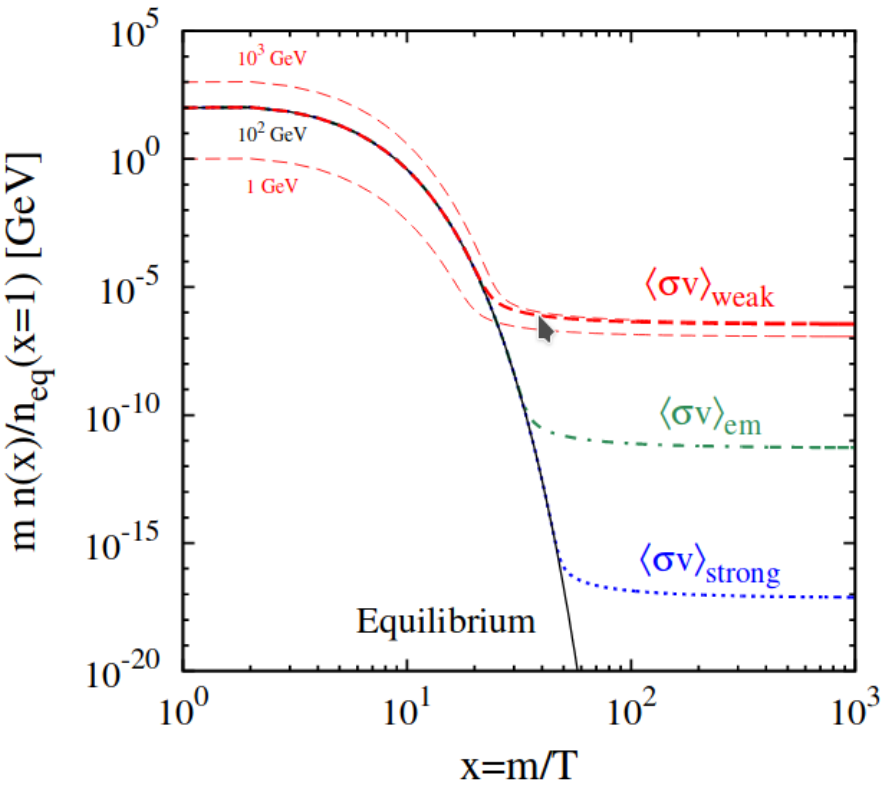

Figure 1.4: The abundance of thermal relic DM as a function of its mass to temperature ratio. Different colors show the evolution of number density for typical weak (red), electromagnetic (green) and strong (blue) force $\langle\sigma_{\rm ann}v\rangle$, assuming $m_\chi = 100$ GeV. For weak scale annihilations also the evolution of number density for $m_\chi = 1$ GeV and $m_\chi = 1$ TeV is show, demonstrating the mild dependence of the relic abundance on WIMP mass. The image was borrowed from [45].

several unique properties. Unlike the left-handed neutrinos, which are known to have tiny masses and can, therefore, constitute only a small fraction of DM, right-handed neutrinos could be Majorana particles with large explicit Majorana masses, making them viable DM candidates. Their possible large masses are further motivated by *see-saw* mechanism, that could explain the generation of small active neutrino masses, which are in the simplest realization inversely proportional to the ones of their right-chiral partners [50–53]. On the other hand, such truly neutral particles could only couple to other forms of matter through small mixing with left-handed neutrinos, which leads to stringent constraints on viable models by simply requiring that sterile neutrinos are produced with the correct relic abundance, but at the same time sufficiently long-lived to avoid the existing experimental constraints regarding their lifetime. An important difference that arises with respect to the WIMP-like DM candidates is that sterile neutrinos usually act as warm DM and exhibit suppression of matter power spectrum below certain scale, which depends on the sterile neutrino mass, as well as the details regarding their production in the early Universe. For an up-to-date review of viable sterile neutrino DM models see, e.g., [54–56]. While sterile neutrinos will not be further addressed in this thesis, they serve as an interesting alternative to the WIMP-like DM candidates, especially in the light of several recent claims of detection of X-ray signals associated with their decays [57–59], which however remain controversial due to possible astrophysical origin of the unexpected spectral line.

Scalar fields

Additional scalar degrees of freedom appear in many theories beyond the Standard Model of elementary particles. They often accommodate a wide range of parameter space, where they could act as DM. Again, these scalars must be non-relativistic and abundantly produced in very early Universe, but subsequently decouple (or always were decouples) from ordinary matter. Prototypical examples are axions [60], originally introduced to explain the smallness of CP violation in the strong sector, or axion-like particles [61], motivated by string theory. From the point of view of DM phenomenology, ultra-light scalar fields are particularly interesting [62,63], since they are expected to form macroscopic solitonic cores of the size of their de-Broglie wavelength:

$$\frac{\lambda}{2\pi} = \frac{\hbar}{m_s v} \approx 1.92\text{kpc} \left(\frac{10^{-22}\text{ eV}}{m_s}\right) \left(\frac{10\text{ km/s}}{v}\right) , \tag{1.4}$$

where m_s and v are the scalar field mass and velocity, while $\hbar$ is the reduced Planck's constant. This could help in explaining some observations that hint towards the suppression in the abundance of small scale structures and existence of cores in center of DM halos, contrasting the predictions obtained for heavy collisionless particles. Perhaps the most promising approach for detecting ultra-light DM is by testing the shape of small scale matter power spectrum, as for example done through observations of Lyman-α forest [64, 65], 21-cm astronomy [66], gravitational lensing [67, 68] or careful study of galactic kinematics [69]. On the other hand, existence of axions is currently being probed through possible coupling with electromagnetic field [70–72].

Primordial black holes

So far I've presented only particle candidates for Dark Matter. The main alternative explanation is perhaps the existence of primordial black holes [73,74]. On large scales they are expected to behave just like non-relativistic matter, however, they are fundamentally different in their nature. Since their production is generally linked to details regarding inflation, there exist large theoretical uncertainties, as well as relatively few empirical constraints. Increasingly strong limits on the abundance of primordial black holes can be inferred from the microlensing observations, as well as CMB and several other probes, which together seem to disfavour them from constituting all of the DM, see [75, 76] and references therein.

1.2 Dark Matter searches

The existence of DM is one of the most evident shortcomings of the Standard Model of elementary particles. While the latter is highly accurate in describing the behaviour of ordinary matter over a vast range of energies, it is only applicable to less than 20% of the total matter content in the present Universe. This motivated numerous dedicated experimental searches, which aim at providing new insights regarding the nature of DM component through various possible signatures. So far, no unambiguous detection has been achieved; however, there exist several controversial claims which drive the need for careful comparison among different experiments and improved theoretical modelling of the expected signals.

This section will be devoted to the three main complementary avenues of detecting DM, as schematically depicted in figure 1.5:: *i*) indirect detection through DM annihilation (or decay) products, *ii*) direct detection through scattering of DM with nuclei and *iii*) collider searches, which attempt to discover new physics by studying high energy collisions of SM particles. I will begin with a short review of collider searches, which, however, did not show any tangible hints in favour of the existence of new elementary particles, beyond the known SM states. This will be followed by a discussion of indirect searches, which rely on extremely high DM densities found in the centres of galaxies, leading to significant annihilation rates in many theoretical models that fall beyond the reach of colliders. In fact, various claims of excess radiation consistent with the expected DM signals have been made. They, however, remain inconclusiveness because of complicated modelling of background signals and significant uncertainties in the distribution of DM within galaxies. The latter turns out to be one of the critical uncertainties also in the direct DM searches, were the controlled laboratory environments, in which DM induced nuclear recoils are searched for, allow reaching extremely high sensitivities and, unlike indirect searches, suffer from much smaller background noise.

1.2.1 Collider experiments

Precise measurements and large energies achievable in modern colliders, such as the Large Hadron Collider (LHC), set them on the forefront of particle physics probes. This is equally true in the light DM searches since a wide range of

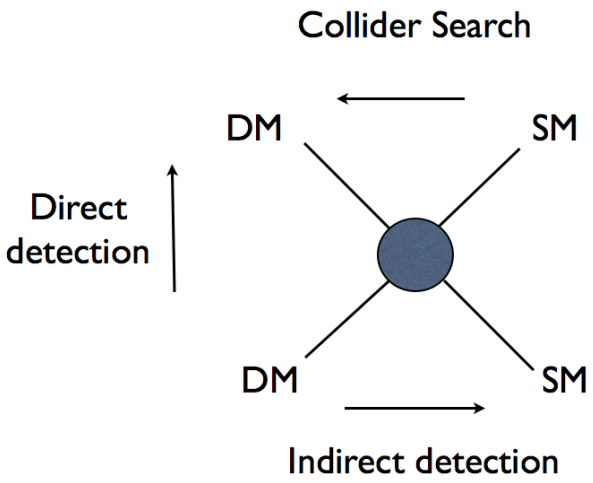

Figure 1.5: Schematic depiction of complementarity between the three main avenues for DM detection. DM and SM stand for Dark Matter and Standard Model particles respectively, while the grey circle contains new physics responsible for coupling between the two sectors.

models predicts signatures that should be detectable through an accurate reconstruction of high-energy collisions of SM particles. This can lead to either direct production of DM states or the discovery of new particles that are responsible for mediating the interactions between dark and visible sectors.

Collider constraints on DM particle are usually phrased in terms of effective theories or simplified models due to their universality. Significant efforts were also put in constraining concrete UV complete theories, such as various realizations of Supersymmetry. However, these generally introduce a large number of free parameters and, therefore, addressing simplified models is usually preferred. In the latter, the coupling between DM and quarks can be effectively described in terms of four parameters, namely the mass of DM, the mass of mediator particle responsible the interaction, and its couplings to SM field and DM. The main avenue for detecting DM in colliders is through the missing transverse energy (MET) and corresponding asymmetric particle emissions. MET generically indicates that scattering produced particles, which subsequently escaped the detector without triggering any of the sensors. Such behaviour is indeed expected for DM, as the existing limits strongly constrain its interaction rates with ordinary matter. In the production of secluded states, further detection signatures should appear in the form of a collimated spray of SM particles, which is usually referred to as mono-X, where X can be either a hadronic jet, Z/W/Higgs boson or a photon, and is crucial for reconstructing the details of such collisions. This is particularly important for distinguishing the new physics from incompletely reconstructed events or SM backgrounds, e.g. emissions of neutrinos that can also escape the detector without leaving a trace, but also learning about the nature of possible new processes. DM can manifest itself also in other collider signatures, such as the existence of processes that are forbidden within the Standard Model or displaced interaction vertices; however, such predictions are strongly model-dependent.

Unfortunately, no hints for new elementary particles have been discovered so far. Therefore, one can only construct conservative limits on many extensions of the SM that attempt to explain the phenomena of DM. Such constraints provide important complementary information to the direct detection searches; while the latter have better sensitivity at large DM masses, colliders can probe models with much more massive mediator particles between visible and dark sectors, which would result in negligible direct detection signals. Furthermore, they could also be used to independently test possible DM origins of indirect detection signals, provided that they fall within the energy range reachable in colliders. An example of exclusion plots obtained by LHC for simplified models with vector and axial-vector mediators are shown in figure 1.6.

1.2.2 Indirect detection

Strong constraints on DM properties can also be inferred from observations of regions where its density is particularly high, e.g. centres of galaxies or galaxy clusters. If DM particles decay, as it is the case for sterile neutrinos, or annihilate in pairs, which is generically true for WIMP-like candidates, emissions associated with these processes can provide one of the strongest, but indirect, non-gravitational signatures of DM. The signals can be searched in a broad range of channels, ranging from γ-rays, neutrinos to cosmic rays. Currently, the strongest limits on annihilation cross-section come from γ-ray observations of

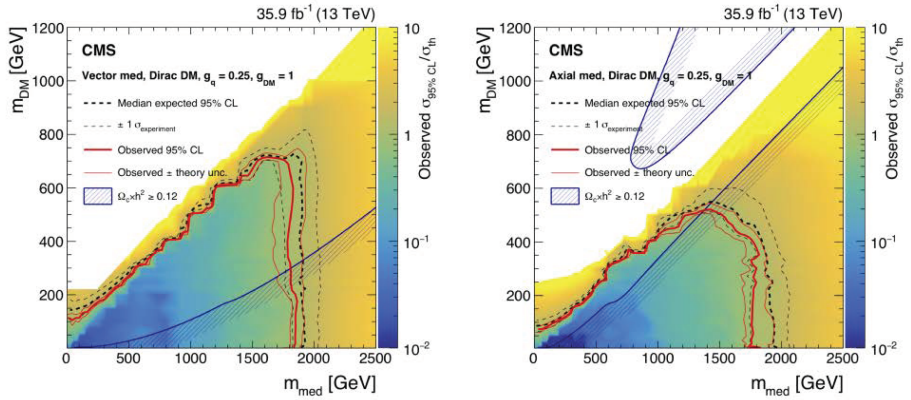

(**a**) CMS

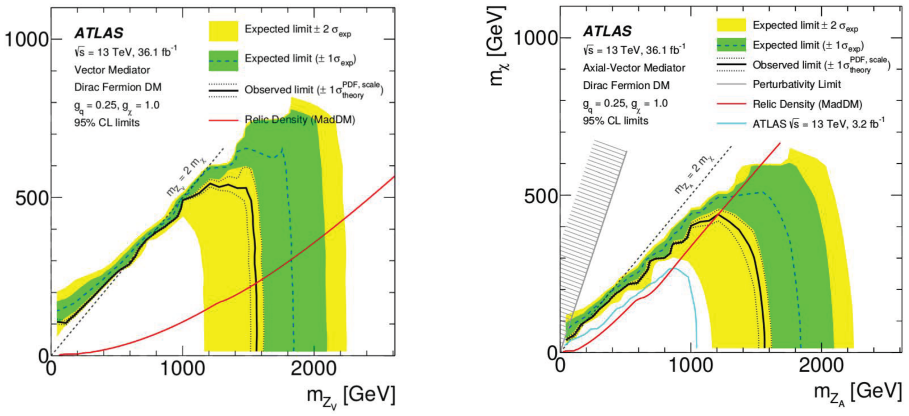

(**b**) ATLAS

Figure 1.6: An example of exclusion limits in the mediator vs. DM mass plane for LHC's CMS and ATLAS detectors. On the left/right hand side are the results for vector/axial mediator particle. The plots were taken from [77]

Milky Way's dwarf satellite galaxies (dSphs) and measurements of anti-matter fraction of cosmic rays, however, with the growing number of collected events also neutrino telescopes will become increasingly relevant in the near future. For a comprehensive review of indirect DM searches see, e.g., [78, 79].

The expected flux due to pair annihilation of DM into SM particles, in the following denoted as ψ, crucially depends on the underlying DM distribution. Given a galaxy with PSDF, $f(\vec{x}, \vec{v})$, for the DM component, the flux integrated over the angular acceptance $\Delta\Omega$ is given by:

$$\frac{d\Phi_\psi}{dE_\psi} = \frac{1}{8\pi} \frac{\langle \sigma_{\rm ann} v \rangle}{m_\chi^2} \frac{dN_\psi}{dE_\psi} \int_{\Delta\Omega} d\Omega \int_{\rm l.o.s.} d\ell \int d\vec{v}_1 f(\vec{x}, \vec{v}_1) \int d\vec{v}_2 \; f(\vec{x}, \vec{v}_2) \, S(|\vec{v}_{\rm rel}|) \,, \tag{1.5}$$

where the DM particle χ is assumed to be its own antiparticle (otherwise an extra factor of $1/2$ is needed), m_χ is its mass and dN_ψ/dE_ψ the energy spectrum of the produced ψ particles per annihilation. This formula is applicable to the general case, in which the pair annihilation cross-section times velocity, $(\sigma_{\rm ann} v)$, has a non-trivial dependence on the modulus of the relative velocity $v_{\rm rel} = |\vec{v}_1 - \vec{v}_2|$, with $\vec{v}_1$ and $\vec{v}_2$ being the velocities of two annihilating particles; $(\sigma_{\rm ann} v)$ is factorized into the velocity independent term $\langle \sigma_{\rm ann} v \rangle$ times a dimensionless factor fully comprising its dependence on relative velocity, $(\sigma_{\rm ann} v) = \langle \sigma_{\rm ann} v \rangle \cdot S(v_{\rm rel})$. By isolating the astrophysical contribution in equation (1.5), one can define:

$$\begin{aligned} J &\equiv \int_{\Delta\Omega} d\Omega \int_{\rm l.o.s.} d\ell \int d\vec{v}_1 f_{\rm DM}(\vec{x}, \vec{v}_1) \int d\vec{v}_2 \; f_{\rm DM}(\vec{x}, \vec{v}_2) \, S(v_{\rm rel}) \\ &\equiv \int_{\Delta\Omega} d\Omega \int_{\rm l.o.s.} d\ell \, \rho^2_{\rm DM}(\vec{x}) \; \langle S(v_{\rm rel}) \rangle (\vec{x}) \,, \end{aligned} \tag{1.6}$$

where this definition is in analogy to what is usually denoted in the literature as "J-factor", which is typically limited on the standard lore of s-wave annihilations, where $(\sigma_{\rm ann} v)$ is to a good approximation velocity independent and hence $\langle S(v_{\rm rel}) \rangle = 1$. In that case the expression can be significantly simplified by noting that, according to equation (2.2), the integrals of $f(\vec{x}, \vec{v}_i)$ over $d^3 v_i$ simply yield the corresponding DM density. However, the lack of tangible signals from the standard WIMP annihilations motivates us to consider more general scenarios that will be further explored in chapter 4. There are several cases in which a non-trivial $S(v_{\rm rel})$ arises; for example, models in which s-wave annihilations are forbidden or severely suppressed, and hence p-wave processes become relevant, leading to a $S(v_{\rm rel}) \propto v_{\rm rel}^2$ scaling. Alternatively, non-perturbative effects due to long range interactions introduce an additional velocity dependence proportional to inverse powers of $v_{\rm rel}$. Since DM particles in galactic halos typically have small velocities (i.e. are strongly non-relativistic), this leads to a large increase in the expected fluxes for indirect searches. Implications of this effect, commonly known as Sommerfeld enhancement, and its dependence on DM velocity distribution, will be carefully analyzed in section 4.3.1.

In the case of decaying DM, the picture is analogous, however, significantly simpler. Since decays are independent of DM velocity distribution, the differential decay flux into particles ψ is given by a line-of-sight integration over single DM density distribution:

$$\frac{d\Pi_\psi}{dE_\psi} = \frac{1}{4\pi} \frac{\Gamma}{m_\chi} \frac{dN_\psi}{dE_\psi} \int_{\Delta\Omega} d\Omega \int_{\rm l.o.s.} d\ell \; \rho(\vec{x}) \,, \tag{1.7}$$

where Γ is the process' decay width and dN_ψ/dE_ψ the decay spectrum. Analogously to the J-factors one can define the corresponding D-factors:

$$D \equiv \int_{\Delta\Omega} d\Omega \int_{\text{l.o.s.}} d\ell \; \rho(\vec{x}) \,. \tag{1.8}$$

Since one of the main goals of this thesis is to provide accurate phase-space models for galactic DM and study their impact on the DM searches, decaying DM is not of the prime interest and will not be further addressed. Non-the-less, it is an interesting possibility and there have been several exciting discoveries of X-ray spectral lines that could be due to decays of 7 keV sterile neutrino DM [57–59].

In the remaining part of this section, I will review the latest experimental results regarding DM annihilations into the three most promising observational channels: γ-rays, neutrinos and anti-matter fluxes.

γ-rays

Annihilation of DM with multi-GeV rest mass into SM states is generically expected to produce γ-ray emissions. The annihilation processes can lead to either photon-rich continuum, which is expected if DM annihilates into τ leptons, gauge bosons or any of the quarks, photon-poor continuum if primary annihilation products are muons and electrons, or spectral lines if DM can annihilate into two photons. Through observations of DM dominated objects, such as the dwarf spheroidal satellites (dSphs) of the Milky Way, photons are capable of providing the tightest, as well as highly robust, limits on DM annihilation rates. On the other hand, massive objects, such as our own Milky Way or nearby spiral galaxies, contain even higher DM densities, however, in these structures modelling of astrophysical backgrounds is very complicated, which makes it harder to identify possible emissions originating from DM annihilations.

As already mentioned, one of the strongest constraints on annihilation cross-section for thermal relics with masses in the GeV range come from γ-ray observations of dwarf galaxies through the Fermi-LAT satellite. The absence of signal allows to rule out the standard WIMP cross-section for $m_\chi \lesssim 100$ GeV [80–82] and provides one of the most robust constraints, as the main source of uncertainty is related solely to the DM distribution within the observed objects, while the γ-ray emissions due to astrophysical processes are negligible. On the other hand, an excess of γ-rays with respect to the background models was found in the centers of Milky Way [83, 84] and Andromeda galaxy [85], favoring DM annihilations in bottom quarks, i.e. $\chi\bar{\chi} \to b\bar{b}$ [86, 87]. However, as can be seen from figure 1.7, such an interpretation of the galactic centre excess is in strong tension with observations from dwarf galaxies, giving support to alternative explanations, such as the existence of an additional population of millisecond pulsars [88,89] or other astrophysical sources [84,90]. In either case, the presence of these tensions emphasizes the need for careful analysis on general grounds, where accurate distribution models for DM are used, and possible velocity dependences of the cross-section are taken into account. The constraints on DM annihilations in the TeV mass range are driven by the observations of imaging atmospheric Čerenkov telescopes, such as H.E.S.S [91] and VERITAS [92]. Currently, their bounds do not quite probe the benchmark weak-scale $\langle\sigma_{\text{ann}} v\rangle$ yet.

However, this is expected to improve with further data collection and upcoming CTA experiment, see, e.g., [93].

Neutrino portal

An alternative approach to searching for DM annihilation signatures through observations of γ-rays is to study the neutrino emissions. Similarly as for photons, copious amounts of neutrinos are expected to be produced in most of the annihilation channels, with the further advantage of the signals being unsuppressed in case of DM annihilations into muons or neutrinos themselves. Several unique neutrino telescopes have been constructed recently, among which the most important for DM searches are probably IceCube [94] and Antares [95], opening a new window to the multi-messenger astronomy. Both of the mentioned experiments are designed to detect Čerenkov radiation in huge bodies of water, as neutrinos interact only weakly and, therefore, very large detection targets are needed. For the same reason, the data acquisition process is rather slower, and one will still have to wait for a higher significance of their observations. As can be seen in figure 1.7 they provide few orders of magnitude weaker constraints on $\langle \sigma_{\rm ann} v \rangle$ then γ-ray observations, however, it should be kept noted that they are sensitive to channels in which the photon emissions can be highly suppressed.

Anti-matter

Strong constraint on DM annihilation and decay rates can also be set from the observations of cosmic rays. In particular, positron, anti-proton and anti-deuterium spectra are expected to be the key signatures, as their production in astrophysical processes is negligible, while annihilations or decays of DM are typically expected to produce matter and anti-matter in equal amounts. Therefore, accurate balloon-borne experiments and AMS-02 detector on board of the International Space Station, measuring primary cosmic rays fluxes, are capable of providing crucial information regarding the nature of DM. Similarly to the galactic centre γ-ray excess, there exist well-established excess of the galactic positrons as well as anti-protons [96]. Unfortunately, DM interpretation of the observed positron abundance turns out to be problematic, since it requires substantial DM annihilation cross-section, inconsistent with CMB observations. Additionally, the total electron-positron spectrum should also contain a characteristic feature if the entire excess was due to DM annihilations, but it does not seem to be present in the data. All this together perhaps points towards an astrophysical origin of the signal. On the other hand, the DM interpretation of anti-proton excess seems more likely. However, significant uncertainties in galactic diffusion of charged particles, anti-proton production rates and the possible existence of additional unaccounted astrophysical sources make it impossible to draw robust conclusions [97,98]. From the absence of γ-ray emissions consistent with production of anti-protons in DM annihilations within dSph, the corresponding bound on $\langle \sigma_{\rm ann} v \rangle$ coming from the AMS-02 measurements of anti-proton flux can be significantly strengthened [99] and is, over significant range of m_χ, even more constraining then the Fermi-LAT limits from the observations of dSphs, as shown in figure 1.7. Finally, it is worth noting that detection of non-relativistic (or mildly relativistic, depending on DM mass) anti-deuterium would be compelling evidence in favour of DM annihilations into final hadron

states. The vast majority of astrophysical anti-deuterium is expected to be produced in high-energy collisions of cosmic rays with interstellar gas, resulting in high particle momenta, while anti-deuterium produced in DM annihilations would necessarily have momenta well below the DM rest mass. No precise data regarding the anti-deuterium fluxes is yet available, however, in the near future AMS-02 and GAPS experiment should be able to provide first insights into its energy spectrum [100].

1.2.3 Direct detection

It has been shown that just like other galaxies, also Milky Way is nested in a massive DM halo. This allows us to study DM-nucleon interactions using sensitive terrestrial experiments since we should be surrounded by large amounts of DM particles. Such endeavors belong to the category of direct detection experiments, which originally proposed by Goodman & Witten [103] more then 30 years ago. The signal can be quantified as differential recoil rate:

$$\frac{\mathrm{d}R}{\mathrm{d}E_r} = \frac{1}{m_A m_\chi} \cdot \int_{|\vec{v}|>v_{\min}} d^3v \; f(\vec{x},\vec{v}) \cdot v \cdot \frac{d\sigma}{dE_r} \tag{1.9}$$

$$\text{with} \quad v_{\min} = \sqrt{\frac{m_A E_r}{2\mu_{A\chi}^2}} \quad , \quad \mu_{A\chi} = \frac{m_A m_\chi}{m_A + m_\chi} \; ,$$

where E_r the recoil energy, $m_{A/\chi}$ the nucleus/DM mass, $v = |\vec{v}|$ the velocity of DM particle in the detector (LAB) frame and $d\sigma/dE_r$ the corresponding differential cross-section. For spin-independent (SI) interactions the latter can be written as:

$$\frac{d\sigma}{dE_r} = \frac{m_A \sigma_n^{\mathrm{SI}}}{2\mu_{A\chi}^2 v^2} A^2 F^2(E_r) \; , \tag{1.10}$$

where σ_n^{SI} is the SI DM-nucleon cross-section at zero momentum transfer, A the mass number of target nucleus and $F(E_r)$ the corresponding (energy dependent) form factor. As can been seen from the above expression, SI differential cross-section introduces a factor of v^{-2} within the integral of equation (1.9), which also appears in the case of spin-dependent (SD) interactions, however, this is not always true for more general scattering operators. In either case, on can factorize equation (1.9) into a term determined by the specific particle physics model under consideration times an integral that is determined by the DM phase-space distribution, which for SI and SD case takes the following form:

$$g(v_{\min}) \equiv \frac{1}{\rho_\odot} \int_{|\vec{v}|>v_{\min}} d^3v \; \frac{f(\vec{x},\vec{v})}{v} \; . \tag{1.11}$$

When considering a broader range of effective elastic scattering operators, discussed in greater detain in section 3.3.1, leading order differential cross-section can be independent of the relative velocity and, therefore, it is useful to define also:

$$h(v_{\min}) \equiv \frac{1}{\rho_\odot} \int_{|\vec{v}|>v_{\min}} d^3v \;\; f(\vec{x},\vec{v}) \cdot v \; . \tag{1.12}$$

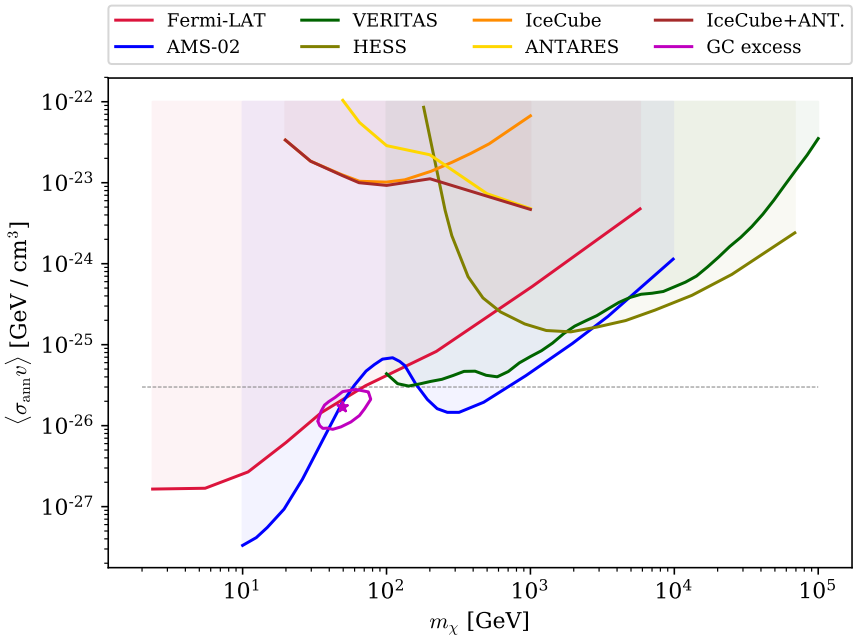

Figure 1.7: Compilation of constraints on the thermally averaged annihilation cross-section times velocity as a function of DM mass. Fermi-LAT stands for the limits obtained from recent analysis of 10 year γ-ray observations of Milky Way's dwarf satellite galaxies [82], assuming annihilations into $b\bar{b}$. Similarly, VERITAS [92] and H.E.S.S [91] stand for limits based on γ-ray emission in dwarfs and the galactic center. AMS-02 corresponds to recent bound obtained from the observed anti-proton spectrum [99], combined with the null results from Fermi-LAT observations. Limits from the analysis of neutrino telescopes, namely IceCube and ANTARES, and their combined constraints were taken from [101]. Finally, also the preferred parameter space for explanation of the galactic γ-ray excess by DM annihilations into $b\bar{b}$, as obtained by [102], is shown. The vertical dashed line marks the benchmark WIMP value of $\langle\sigma_{\rm ann}v\rangle = 3{\cdot}10^{-26}$ cm^3 / s.

It can be shown that the above functions, g and h, cover the velocity dependencies of all non-relativistic effective scattering operators, expanded up to the quadratic order in momentum transfer and relative velocity. Hence, their accurate determination is of great importance for understanding the direct detection constraints on DM-nucleus interactions. The phase-space modeling of DM distribution evidently has an important impact on the expected event rate. Foremost, it determines the velocity distribution of the scatterings, but also sets the maximum relative velocity between DM particles and target nuclei, which is crucial in the interpretation of results for light (sub-GeV) DM. In the past it has been often assumed that the local DM has Maxwell-Boltzmann velocity distribution, truncated at escape velocity ($v_{\rm esc}$):

$$P(v) = \mathcal{N} \exp\left(-\frac{v^2}{2\sigma^2}\right) \Theta\left(v_{\rm esc} - v\right) \ , \tag{1.13}$$
$$\text{where} \quad \mathcal{N}^{-1} = \left(2\pi\sigma^2\right)^{3/2} \left(\text{erf}\left(\frac{v_{\rm esc}}{\sqrt{2\sigma^2}}\right) - \sqrt{\frac{2}{\pi}} \frac{v_{\rm esc}}{\sigma} \exp\left(-\frac{v_{\rm esc}^2}{2\sigma^2}\right)\right) \ .$$

Such modelling, commonly known as the standard halo model (SHM), is however very rough and can be significantly improved in the light of modern astronomical data. A possible refined PSDF model, capable of describing axisymmetric systems, which is a reasonably good approximation for spiral galaxies, is presented in chapter 3, along with its implications for direct detection. Tabulated $g(v_{\rm min})$ and $h(v_{\rm min})$ functions are also provided, with their associated uncertainties derived from observations of dynamical traces within the Milky Way.

DM scatterings in target materials are expected to produce one additional characteristic feature; since the Earth is moving with respect to the Sun with a relatively large velocity, $|\vec{v}_\oplus| \approx 30$ km/s, one expects to see a yearly modulation of signal, as the direction of Earth's movement changes with respect to the rest frame of DM halo. Consequently, the expected signal modulation can vary significantly for different DM distribution models, which further highlights the need for accurate PSDF modelling. This effects will be addressed in greater detail in section 3.3.3.

In the remainder of this section, I briefly review the most stringent limits on DM-nucleus scattering cross-sections and present the existing controversies regarding detection claims. For more extensive recent reviews one can see, e.g., [104, 105]

Compilation of constraints

There exist numerous active experiments aimed at detecting nuclear recoils caused by scattering with DM. Target materials can vary between the setups and provide different sensitivities for different DM models. Typically either liquefied noble gas, such as Xenon, or highly pure scintillating crystals, e.g. NaI, are used. Currently some of the strongest reported limits were achieved by the Xenon1T collaboration, which used one ton-year exposure of liquid Xenon to obtain a bound on spin-independent (SI) and spin-dependent (SD) cross-sections of $\sigma_n^{\rm SI} \sim 10^{-47}$ and $\sigma_n^{\rm SD} \sim 10^{-42}$ cm^2 [106], correspondingly, assuming that DM mass is around the detectors maximum sensitivity, $m_\chi \sim 30$ GeV. This improved the previous Xenon100 results by more than an order of magnitude and slightly tightened the SI limits from LUX [107] and PandaX-II [108, 109] experiments,

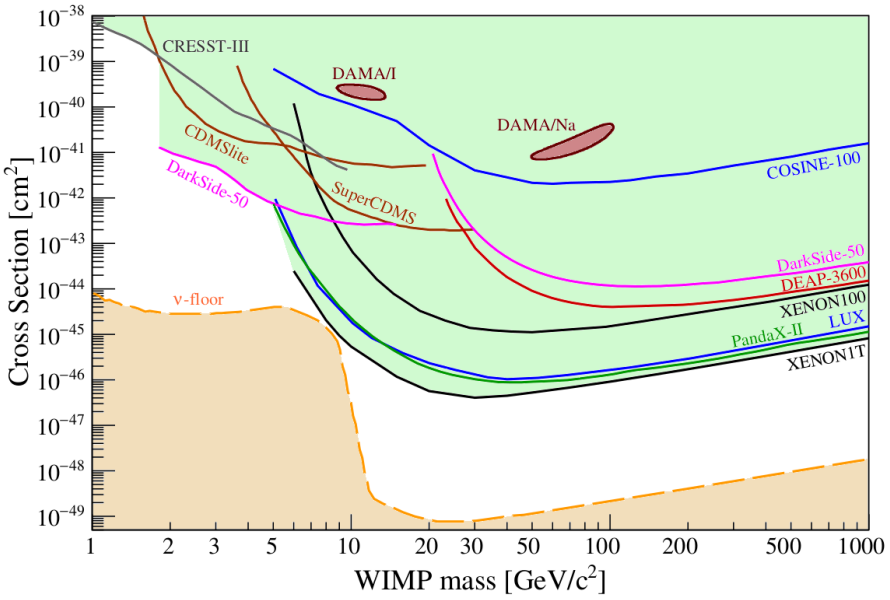

Figure 1.8: Compilation of constraints on the SI cross-section of DM with nucleons. Dark red contours mark the preferred parameter space for DM interpretation of DAMA results, while the orange region represents the neutrino floor. The figure were taken from [105].

which also use liquid Xenon targets. For DM with masses around GeV and below, the strongest limits on DM induced nuclear recoils come from DarkSide-50 experiment [110], which uses liquefied Argon target instead of Xenon. On the other hand, for SD scattering of DM with protons, the strongest constraints come from C_3F_8 and C_4F_{10} targets used by PICO-60 collaboration [111], which provide an order of magnitude stronger limit then the noble gas detectors. The corresponding limits on the SI and SD cross-section as a function of DM mass, along with several additional experiments, are combined in figures 1.8 and 1.9. In the near future, the bounds on σ_n^{SI} and σ_n^{SD} are expected to improve by an additional order of magnitude with the upcoming XenonNT and LZ experiments. Unfortunately, such improvements will only be possible until the detectors become sensitive to the *neutrino floor*, i.e. nuclear recoils sourced by astrophysical neutrinos, which will induce strong background signal and hence make further improvements of bounds on DM-nucleon cross-section extremely difficult.

Detection claims

In the past, there have been several claims of successful DM detection. The most notorious among them is probably the highly significant (12.9σ) measurement of the annual modulation of nuclear recoil rate, reported by the DAMA/LIBRA collaboration [112, 113]. The modulation signal is expected to be one of the key signatures for distinguishing DM induced recoils from various possible backgrounds and curiously enough the observed phase is perfectly consistent with the predictions based on Earth's orbit around the Sun. On

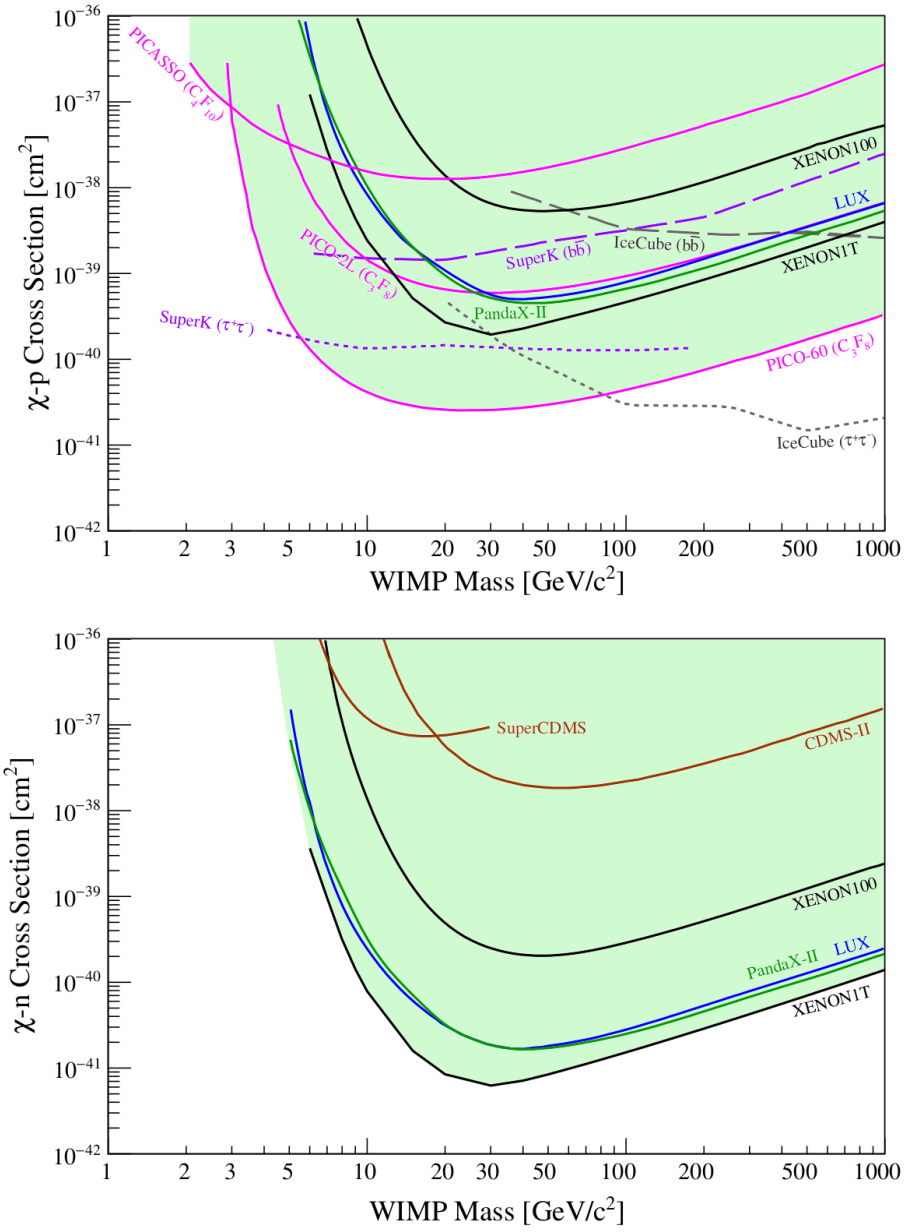

Figure 1.9: Compilation of constraints on the SD cross-section of DM with protons (above) and neutrons (below). The figures were taken from [105].

the other hand, the inferred DM-nucleus cross-section is in severe tension with other experiments, as shown figure 1.8 for SI interpretations of the scatterings. Due to this large discrepancy, dedicated experiments, such as COSINE-100 [114] and ANAIS-112 [115], have been launched with the purpose of replicating the DAMA/LIBRA results. They use the same target material, namely NaI scintillation crystals, to eliminate the uncertainties related nuclear physics that otherwise arises when comparing direct detection experiments based on different target nuclei. Other, but less significant, claims of DM induced events have been made by CDMS-II(Si) [116] and CoGeNT [117,118] experiments. However, their findings are inconsistent with other detection claims and, similarly as the DAMA annual modulation of the signal, strongly excluded by the null results of the most sensitive experiments.

The tensions discussed above are particularly sever under the standard approximations of SI/SD cross-section and Maxwellian velocity distribution. However, they can be somewhat lessened by allowing for more general DM-nucleus interactions or choosing a different velocity distribution for DM. In the light of providing more robust constraints, I will further address these assumptions in chapter 3, where a new modelling of DM velocity distribution for refined analysis of direct detection experiments is presented.

1.2.4 Other probes

Besides the above-described DM searches, there have been many alternative suggestions on how to learn more regarding the dark sector. While detection of DM in colliders or through (in)direct searches could provide essential insights into the DM particle properties, the absence of compelling signals lead to the proposals of numerous less direct, but still valuable probes. These range from cosmological, constraining DM through its effects on the structure formation and thermodynamical evolution of the Universe, astrophysical, which try to detect DM through its influence on known astrophysical processes, to gravitational observations, providing intricate new possibilities. While there exists a vast literature on the topic, see, e.g., [119] and references therein, I will restrict my attention to several most prominent suggestions.

Cosmological probes

CMB has proven itself to be indispensable experimental evidence in favour of the existence of DM, providing a precise determination of its cosmological abundance and firmly establishing its non-relativistic, particle-like, behaviour. At the same time it is also capable of putting significant constraints on its annihilation cross-section, see, e.g., [120], since additional energy injection into the visible sector around the time of recombination would drive the CMB away from the observed nearly perfect black-body spectrum. While the derived bounds are not as strong as the one obtained from indirect DM searches, they none-the-less provide an independent constraint coming from a significantly different environment. Furthermore, detailed studies of the CMB spectral distortions are capable of putting strong limits on the interaction between visible and dark sector for DM masses well below the sensitivity limit of direct detection experiments, for example discussed in [121,122]. Additionally, CMB provides also accurate measurement of the radiation energy density, which can be used to constrain the

presence of new light particles.

Another interesting probe of DM are the observations of Lymann-α forest. It is based on the fact that light emitted by distant quasars gets absorbed by neutral hydrogen, as it travels towards us, and produces a characteristic spectrum, exponentially sensitive to the neutral hydrogen density at different redshifts along the way. This, in turn, allows us to reconstruct the matter power spectrum, which is responsible for the formation of hydrogen over-densities, and can probe scales down to $k \sim 1/$ Mpc – for a recent review see [123]. As such, it provides an important insight into the DM, constraining models in which the collapse is halted at small scales, e.g. in models with warm, self-interacting or ultra-light bosonic DM.

Finally, in the near future radio astronomy, sensitive to the hydrogen 21-cm emission line, should provide us with new insights regarding the matter power spectrum over a broad range of scales and redshifts. Similarly as Lyman-α observations, it will be capable of further constraining the clustering properties of DM and finding possible deviations from the standard CDM hypothesis [124, 125], as well as improving the bounds on its annihilation rate [126]. It should also be able to rule out (or confirm) recent claims of EDGES experiment [127], concluding that the intergalactic medium cooled faster then it would be possible due to known physics and speculating that this could be explained by deposition of energy in the dark sector through baryons scattering with DM particles.

Gravitational probes

Similarly to the cosmological probes, several approaches based on purely gravitational effects have been suggested in order to constrain the small scale matter power-spectrum. Currently, the most stringent results rely on the gravitational lensing, which has independently confirmed the existence of DM on cluster and galactic scales, but as the quality of observations increases, it is becoming capable of addressing the small scale behaviour of DM. In fact, several spectacular lensed systems have been used to establish the presence of DM subhalos as small as $10^8 M_\odot$ [67,68], entering the phenomenologically interesting regime where the cold DM hypothesis is often challenged. Besides lensing, also other gravitationally based approaches were suggested within the literature, such as observations of tidal streams [128, 129] (i.e. stars stripped from globular clusters or dwarf galaxies due to tidal interactions with the Milky Way) or disruptions of bound structures [130]. Finally, with the recent improvements in the astrometric data provided by Gaia satellite, gravitational effects of DM substructure could also be searched in the galactic stellar field, which will be further explored in chapter 5.

Furthermore, with the detection of gravitational waves, a new window for exploration of the Universe has been opened. Among many other exciting applications, it also provides the means to study the nature DM. This can be either through its interplay with inspiraling of compact objects [131, 132], such as recently observed coalescences of black holes and neutron stars, putting constraints on the abundance of PBH [133,134], or even by detecting the primordial gravitational waves that could carry information regarding the physics responsible for inflation and reheating. Furthermore, DM composed of light bosons, such as axions or axion-like particles, could be constrained by arguments based on superradiance [135], which is a relativistic effect allowing radiation to extract the rotational energy from black holes. Superradiance becomes highly

efficient for specific black hole masses (at fixed value of the scalar or vector field mass), which would allow to constrain the existence of additional light boson fields through exploring the distribution of black hole spin parameter at different masses, without any need to assume that these bosons couple to the SM particles.

Astrophysical probes

Last but not least, one can also constrain the DM interaction rate with the ordinary matter by careful study of known astrophysical processes. One such example are the limits on DM-nucleus interactions derived from the cooling rate of neutron stars. Since the efficiency of cooling can be rather accurately determined within the known theories, additional dissipation of energy due to DM interactions with nuclei could lead to an observable increase in the cooling rates, as well as depend on the surrounding DM density, see, e.g., [136]. DM capture within white dwarfs could also lead to observable effects, such as premature ignition of supernovae (SNe) [137,138]. Another attractive possibility is the use of SNe as particle physics accelerators since they are capable of producing the most violent outbursts of energy known to mankind. While the exact mechanisms governing SNe explosions are still under research, they might be able to set interesting constraints regarding the existence of new fields beyond the SM in near future [139–141]. As of now, probably the most interesting limits are the ones concerning sterile neutrinos [142,143], in the presence of which the dynamics of SN explosions could be significantly modified.

2. Statistical description of Dark Matter

Statistical mechanics has proven itself to be essential when addressing systems with a large number of degrees of freedom. This is especially true for the evolution of particle species in the early Universe, where we are typically interested in gross quantities such as number density and temperature, while the details regarding individual particles are irrelevant. Similarly, the statistical description also turns out to be useful for describing DM or stars within galaxies, where again a large number of point-like objects makes it infeasible to consider individual trajectories. By expressing the state of the systems through distribution function parametrized by the appropriate phase-space coordinates, one can make use of the powerful Boltzmann transport equation, which is capable of describing equilibrium as well as out of equilibrium evolution and can be applied to either relativistic or non-relativistic settings.

Therefore, the Boltzmann equation often plays a pivotal role in addressing the phenomenon of DM in various settings. Most notably, by tracking the evolution of particle species throughout cosmic history, it provides an essential benchmark whether a given model fulfils the observational constraints on the energy budget of the Universe. Furthermore, the applicability of the Boltzmann equation to non-equilibrium systems turns out to be essential, since DM is typically expected to deviate from the thermal distribution during its decoupling from the primordial plasma. On the other hand, the Boltzmann equation can also be used to obtain the stationary distributions of particles in a given force field, which is particularly interesting in the study of present-day galactic DM. As the latter has been only partially investigated in the existing literature, a significant amount of this thesis will be dedicated to the study of various equilibrium phase-space distribution models, which crucially enter the predictions for direct as well as indirect DM searches.

The first part of this section will be devoted to a brief overview of key concepts behind the phase-space distribution function and the Boltzmann equation. This will be followed by a discussion of particular limits, which are often used when addressing the open questions regarding the DM phenomenon.

2.1 The Boltzmann equation

The fundamental object in statistical description of many-body systems is the *phase-space distribution function* (PSDF), commonly denoted as f. It can be

thought of as the expected number of indistinguishable point-like objects N in a given phase-space volume at some time t:

$$\mathrm{d}N(t,\vec{x},\vec{p}) = f(t,\vec{x},\vec{p})\ \mathrm{d}^3x\ \mathrm{d}^3p\,. \tag{2.1}$$

For the purpose of this work the phase-space variables $\{\vec{x},\ \vec{p}\}$ will simply correspond to position and momentum, while in general different choices for the canonical coordinates might be possible. From the above equation it immediately follows that the number density of particles $n(\vec{x})$ is given by:

$$n(\vec{x}) = \int \mathrm{d}^3p\ f(\vec{x},\vec{p})\ . \tag{2.2}$$

To obtain ensemble averages of physical quantities one simply needs to consider the product of f with the corresponding operator and integrate out the relevant degrees of freedom, as it is usually done when equipped with distribution functions. For example, the mean velocity and velocity dispersion of particle along i-th axis can be obtained by the following expressions:

$$\bar{v}_i = \frac{1}{n(\vec{x})}\int \mathrm{d}^3p\ \ f(\vec{x},\vec{p})\cdot v_i\ , \tag{2.3}$$

$$\sigma_i^2 = \frac{1}{n(\vec{x})}\int \mathrm{d}^3p\ \ f(\vec{x},\vec{p})\cdot (v_i-\bar{v}_i)^2\ . \tag{2.4}$$

This makes the PSDF extremely useful, since it encodes all the statistical information regarding a given system.

While f captures the state of the system, its evolution is dictated by the Boltzmann transport equation. It can account for external forces, diffusion, as well as collisions and conversions between various particle species. In the absence of particle interactions, the Liouville's theorem states that f is constant along the trajectories of the system, i.e. the phase-space flow is incompressible. This is not true any more for interacting particles and the change in the phase-space density can be ascribed to collisions. This constitutes the essence of Boltzmann equation, which can be compactly written in terms of the Liouville operator $\mathcal{L}$ and collision operator $\mathcal{C}$:

$$\mathcal{L}\,[f] = \mathcal{C}\,[f]\ . \tag{2.5}$$

The collision operator can contain several terms; they can be related to elastic scattering, which only redistributes the momenta of scattered particles, but also inelastic scatterings, that can produce new particles and/or transform one species to another. While $\mathcal{C}$ can be neglected when addressing stars or late-time DM, it becomes crucial in the high energy regime, as will be described later on in this section. The Liouville operator, appearing on the other side of equation (2.5), measures the change in phase-space density along a given trajectory and can be therefore expressed as the total derivative of f with respect to time t:

$$\mathcal{L}\,[f] = \frac{\mathrm{d}f}{\mathrm{d}t}\ . \tag{2.6}$$

Note, however, care must be taken if one wishes to apply it to non-Euclidean geometry, such as de-Sitter spacetime, which becomes important when considering

cosmological contexts. In the following section I will first discuss the collisionless non-relativistic limit, which is relevant for the study of DM distribution within galaxies, and then shortly discuss the more general form, that has to be used when computing the evolution of particle species in the early Universe.

2.1.1 Collisionless non-relativistic systems

In the non-relativistic limit, the Liouville operator takes a simple form. The total time derivative of the PSDF can be rewritten in terms of partial derivative with respects to time t, and corresponding chain derivatives of the phase-space coordinates $\vec{x}$ and $\vec{p}$:

$$\mathcal{L}[f] = \frac{\partial f}{\partial t} + \vec{\nabla}_{\vec{x}} f \cdot \frac{\vec{p}}{m} - \vec{\nabla}_{\vec{p}} f \cdot \vec{\nabla}_{\vec{x}} \Phi \,, \tag{2.7}$$

where Φ is the potential associated with the force field acting on particles. The non-relativistic systems considered in this work, namely galactic DM and stars, can be both very accurately approximated as collisionless point-like particles. Therefore, the phase-space density is conserved along the trajectories of the system, i.e. $\mathcal{L}[f] = 0$, while Φ is simply the total gravitational potential of the galaxy. In case Φ is sourced solely by the matter component described by f, one can use the Poisson equation to relate the two and such systems are commonly dubbed as *self-consistent*, however, in real galaxies one usually has multiple components contributing to the total mass, such as stars, gas and DM. An additional simplification, to which I will often resort in this work, can be achieved by assuming f is a stationary solution and hence does not explicitly depend on time, i.e. $\partial f/\partial t = 0$. Stationary PSDFs correspond to equilibrium configurations of the system and, therefore, serve as a good leading order approximation for the distribution of particles within objects whose dynamical times are much shorter than their age, which is typically true for galaxies. Together with an adequate amount of symmetry within the system (e.g. spherical symmetry), these assumptions allow for computing f, given a density distribution $n(\vec{x})$ and, if the system is not self-consistent, gravitational potential Φ. This makes distribution function modelling particularly interesting since both n and Φ can be constrained by observations of galaxies. One of the well-known prescriptions for computing the PSDF from density-potential pair is the Eddington's inversion formula, which will be discussed in more detail later on in this section.

Jeans theorems

Before turning our attention towards the solutions of the collisionless Boltzmann equation, it is useful to revise the Jeans theorems, which are extremely powerful in setting up equilibrium distribution function models for non-relativistic systems. There are two main formulations of the theorem with slightly different assumptions regarding the orbits of its constituents. They both relate integrals of motion, i.e. quantities conserved along any orbit of the system, to stationary solutions of the collisionless Boltzmann equation. More formally, any integral of motion $I(\vec{x}, \vec{p})$, which can always be written as a function of phase-space coordinates only, must fulfil the following condition:

$$\frac{\mathrm{d}I(\vec{x}, \vec{p})}{\mathrm{d}t} = \vec{\nabla}_{\vec{x}} I \cdot \frac{\vec{p}}{m} - \vec{\nabla}_{\vec{p}} I \cdot \vec{\nabla}_{\vec{x}} \Phi \,. \tag{2.8}$$

The above expression is, in fact, identical to the Liouville operator applied to stationary PSDF of collisionless system, as can be seen from equation (2.7). This led to the initial formulation of Jean's theorem, which states: "*Any steady-state solution of the collisionless Boltzmann equation depends on the phase-space coordinates only through integrals of motion in the given potential, and any function of the integrals yields a steady-state solution of the collisionless Boltzmann equation*" [144].

While the theorem stated above is very neat, it does not tell us much regarding the actual integrals of motions that should be used to parametrize f. In fact, in practice there can exist many integrals $I(\vec{x}, \vec{p})$, however, typically one is interested only in isolating ones, which are defined as those that can be used to reduce the dimensionality of phase-space trajectories. This motivated the formulation of a more restrictive strong Jeans theorem, which relies on time-averaged behaviour of particle orbits (for more details see, e.g., [145]). It states: "*The distribution function of a steady-state system, in which almost all orbits are regular with non-resonant frequencies, may be presumed to be a function only of three independent isolating integrals*". The power of strong Jeans theorem will be demonstrated several times thought this thesis, as it plays a crucial role in modelling galactic distribution functions.

Eddington's inversion formula

In classical physics one of the basic conserved quantities, in absence of external forces, is the energy. Therefore, it is natural to consider a simple case where the PSDF depends on a single integral of motion, the relative energy. In fact, it can be shown that for spherically-symmetric isotropic systems $f = f(\mathcal{E})$, where $\mathcal{E}$ is the relative energy, defined as:

$$\mathcal{E} \equiv \Psi(r) - \frac{v^2}{2} \,, \tag{2.9}$$

while r is the radial distance from the center of mass in the standard spherical coordinates and $\Psi(r) = \Phi_b - \Phi(r)$ is the relative gravitational potential with Φ_b being the value of potential $\Phi(r)$ at the boundary of the system. Such gauging ensures that only bound particles have positive relative energy and hence $f(\mathcal{E})$ is non-zero only for $\mathcal{E} > 0$. For stationary spherical systems $\Psi(r)$ is a monotonic function of r, which allows us to rewrite the fundamental equation (2.2) as:

$$\rho(\Psi) = \int_{|\vec{v}|<\sqrt{2\Psi}} d^3v \; f(\mathcal{E}) \,. \tag{2.10}$$

In the above equation the number density n was substituted by the more commonly used mass density $\rho(r) = m \cdot n(r)$, assuming that all particles (or stars) described by f have the same mass m, which can be absorbed in the definition of PSDF; such normalization of f will be used in the following whenever discussing the non-relativistic PSDFs. Starting from equation (2.10), one can take

a derivative with respect to Ψ, which leads to:

$$\begin{aligned}\frac{d\rho}{d\Psi} &= 4\pi \int_0^{\sqrt{2\Psi}} dv\, v^2\, \frac{df}{d\mathcal{E}} \\ &= 4\pi \int_0^{\Psi} d\mathcal{E}\, \sqrt{2(\Psi-\mathcal{E})}\, \frac{df}{d\mathcal{E}} \\ &= 4\pi \int_0^{\Psi} \frac{d\mathcal{E}}{\sqrt{2(\Psi-\mathcal{E})}}\, f(\mathcal{E})\,, \end{aligned} \tag{2.11}$$

where Leibniz's rule for integral derivative was used along with the fact that $f(0) = 0$ and $\partial\mathcal{E}/\partial\Psi = 1$ in the first line, the variable of integration was changed from v to $\mathcal{E}$ in the second and integration by parts was performed in the third. At this point one can make use of Abel transform, which relates two smooth function $g(x)$ and $h(y)$ through the following integral equations:

$$g(x) = \int_0^x \frac{dy}{(x-y)^\alpha}\, h(y) \tag{2.12}$$

$$h(y) = -\frac{\sin(\alpha\pi)}{\pi} \frac{d}{dy} \int_0^y \frac{dx}{(y-x)^{1-\alpha}}\, g(x)\,, \tag{2.13}$$

for $0 < \alpha < 1$. By identifying $h(x)$ as $f(\mathcal{E})$ and $g(x)$ as $d\rho/d\Psi$, while setting $\alpha = 1/2$, one can apply it to invert the equation (2.11) and obtain the Eddington's inversion formula [146]:

$$\begin{aligned} f(\mathcal{E}) &= \frac{1}{\sqrt{8}\pi^2} \frac{d}{d\mathcal{E}} \int_0^{\mathcal{E}} \frac{d\Psi}{\sqrt{\mathcal{E}-\Psi}} \frac{d\rho}{d\Psi} \\ &= \frac{1}{\sqrt{8}\pi^2} \left[\int_0^{\mathcal{E}} \frac{d\Psi}{\sqrt{\mathcal{E}-\Psi}} \frac{d^2\rho}{d\Psi^2} - \frac{1}{\sqrt{\mathcal{E}}} \left(\frac{d\rho_{\rm DM}}{d\Psi} \right) \Big|_{\Psi=0} \right]. \end{aligned} \tag{2.14}$$

There exists only few density-potential pairs for which $f(\mathcal{E})$ can be computed analytically, however, it is not hard to perform the above integral numerically for an arbitrary combination of $\rho(r)$ and $\Psi(r)$. On the other hand, the resulting PSDF is not necessarily positive definite, which needs to be explicitly checked after performing the inversion. In case f takes negative values for $\mathcal{E} > 0$, it means that for a given $\rho(r)$ and $\Psi(r)$ no ergodic stationary solution of collisionless Boltzmann equation exists. Similarly, one can check whether the solution is stable, which is the case if $df/d\mathcal{E} > 0$ for all $\mathcal{E} > 0$ [147]. The Eddington's inversion formula makes it relatively easy to model PSDFs of spherical systems and, therefore, it has been often used within the context of galactic dynamics and more recently also in DM searches.

Jeans modelling

In practice one often encounters the problem of incomplete/lacking data to constrain the full six dimensional PSDF. Therefore, it is worth noting that the solution of collisionless non-relativistic Boltzmann equation do not necessarily need to be searched on the level of f, since one can obtain relations for its moments by integrating out the appropriate powers of velocity. For example,

by adopting the standard spherical coordinates (r, θ, ϕ) one can rewrite equation (2.7) as:

$$\frac{\partial f}{\partial t} + p_r \frac{\partial f}{\partial r} + \frac{p_\theta}{r^2}\,\frac{\partial f}{\partial \theta} + \frac{p_\phi}{r^2 \sin^2\theta}\,\frac{\partial f}{\partial \phi} - \left(\frac{\partial \Phi}{\partial r} - \frac{p_\theta^2}{r^3} - \frac{p_\phi^2}{r^3 \sin^2\theta}\right)\frac{\partial f}{\partial p_r} - \left(\frac{\partial \Phi}{\partial \theta} - \frac{p_\phi^2 \cos\theta}{r^2 \sin^3\theta}\right)\frac{\partial f}{\partial p_\theta} - \frac{\partial \Phi}{\partial \phi}\,\frac{\partial f}{\partial p_\phi} = 0\ . \tag{2.15}$$

In case of spherical symmetry f and Φ have non-vanishing derivatives only along $\hat{r}$ direction, which significantly simplifies the above expression. By further assuming $\partial f/\partial t = 0$, multiplying the expression v_r^2 and integrating over the velocity one obtains the so called spherical Jeans equation:

$$\frac{\partial P_r}{\partial r} + \frac{2\beta(r)}{r} P_r(r) = -\rho(r)\frac{\partial \Phi}{\partial r}\ , \tag{2.16}$$

where I have defined the radial dynamical pressure $P_r(r) = \rho(r) \cdot \sigma_r^2(r)$ and orbital anisotropy parameter:

$$\beta(r) = 1 - \frac{\sigma_\theta^2(r) + \sigma_\phi^2(r)}{2\sigma_r^2(r)}\ , \tag{2.17}$$

with σ_x being the velocity dispersion along the $\hat{x}$ coordinate. Spherical Jeans equation turns out to be particularly useful in the study of dispersion supported systems, such as elliptical galaxies or dwarf spheroidals. It is not hard to derive similar Jeans equations under the assumption of axial symmetry, however, this comes at the price of additional degrees of freedom. Non-the less, axisymmetric Jeans equation also proved itself to be valuable in the context of galactic dynamics, as well as constraining the local DM density through the vertical motion stars.

2.1.2 Interacting particles and non-Euclidean spacetime

Most of this thesis is based on results stemming from the collisionless non-relativistic limit of the Boltzmann equation, which was discussed in the previous section. However, in the field of DM physics, the relativistic generalization plays an equally important role. It often represents the starting point for computing relic abundances in different DM models, but also serves as a tool for exploring their impact on the thermal evolution of the early Universe or processes like the Big Bang Nucleosynthesis. As could be foreseen, the more general form of Boltzmann equation differs from the non-relativistic limit in two crucial points: at high energy densities the collision operator can often no longer be neglected, and the geometry of spacetime needs to be taken into account. The latter can be achieved through the following Lorentz-invariant formulation of the Liouville operator:

$$\mathcal{L}[f] = p^\alpha \frac{\partial f}{\partial x^\alpha} - \Gamma^\alpha_{\beta\gamma} p^\beta p^\gamma \frac{\partial f}{\partial p^\alpha}\ , \tag{2.18}$$

where x^α and p^α are the position and momentum four-vectors, while $\Gamma^\alpha_{\beta\gamma}$ is the connection corresponding to the particular spacetime under consideration.

Since one is typically interested in the evolution of particle species over cosmological scales, it is useful to write it out explicitly for the Friedmann-Lemaître-Robertson-Walker (FLRW) metric and assume that the PSDF is homogeneous and isotropic, $f \equiv f(t, |\vec{p}|)$, i.e. following the standard cosmological principle:

$$\mathcal{L}[f] = E\frac{\partial f}{\partial t} - H|\vec{p}|^2\frac{\partial f}{\partial E}\,, \tag{2.19}$$

where $H = \dot{a}/a$ is the Hubble expansion rate and E is the particle's energy.

On the other hand, the collision term is highly model dependent and requires the knowledge of microscopic properties of the particles. For a general process $\chi_1 + \chi_2 + ... \leftrightarrow \psi_1 + \psi_2 + ...$, where χ_1 is the particle species under consideration, one can express $\mathcal{C}\left[f_{\chi_1}\right]$ as:

$$\begin{aligned}\mathcal{C}\left[f_{\chi_1}\right] =& \frac{1}{E_{\chi_1}}\int d\Pi_{\chi_2}...\int d\Pi_{\psi_1}\int d\Pi_{\psi_2}...\ \ |M(p_{\chi_1}, p_{\chi_2}, ..., p_{\psi_1}, p_{\psi_2}, ...)|^2 \\ &\cdot\left[f_{\chi_1}f_{\chi_2}...(1 \pm f_{\psi_1})(1 \pm f_{\psi_2})... - f_{\psi_1}f_{\psi_2}...(1 \pm f_{\chi_1})(1 \pm f_{\chi_2})...\right] \\ &\cdot(2\pi)^4\delta^4(p_{\chi_1} + p_{\chi_2} + ... - p_{\psi_1} - p_{\psi_2} - ...)\end{aligned} \tag{2.20}$$

where $p_{\rm X}$, $E_{\rm X}$, and $f_{\rm X}$ are the four-momentum, energy and PSDF corresponding to particle species X (in the square brackets + sign applies to bosons and − to fermions), $|M|^2$ is the absolute square of the relevant scattering matrix [1], while $d\Pi_{\rm X}$ is the Lorentz-invariant differential three-momentum:

$$d\Pi_{\rm X} = \frac{d^3p_{\rm X}}{(2\pi)^3\ 2E_{\rm X}}\,. \tag{2.21}$$

In case of interactions between different particle species, the collision operator couples their distribution functions and the solutions often need to be computed numerically. In the following, however, I will sketch the typical WIMP scenario, for which evolution of number density is particularly easy to obtain, yet it provides one of the most compelling explanations for the origin of DM.

2.2 Boltzmann equation and the WIMP miracle

WIMPs are characterized by their large mass and coupling to the Standard Model states with the cross-section similar to typical weak force processes. By simply assuming that WIMPs were initially in thermal equilibrium with primordial plasma, the subsequent evolution surprisingly leads to the correct DM relic abundance, which is entirely determined by dynamics around the time of decoupling.

An equation tracking the number density of particles can be obtained by integrating the Boltzmann equation over the three-momenta appearing in the PSDF, as could be expected from equation (2.2) (in the relativistic limit single particle distribution function with a different normalization of number density is conventionally used, namely a factor of $\frac{g}{(2\pi)^3}$ is usually kept explicit on right hand side of equation (2.2), where g is the number of internal degrees of freedom

[1] Here I assumed that the scattering is CP invariant. If these is not the case two different scattering matrices enter the expression, one corresponding to $\chi_1 + \chi_2 + ... \to \psi_1 + \psi_2 + ...$ and the other to the inverse process, multiplying the appropriate PSDFs in the square bracket.

for a given particle species). By using the above equation (2.19) for $\mathcal{L}$ in FLRW Universe one obtains:

$$\frac{\partial n_\chi}{\partial t} + 3Hn_\chi = \frac{g}{(2\pi)^3}\int \frac{d^3p}{E}\,\mathcal{C}[f_\chi]\,. \tag{2.22}$$

From the above expression it can be seen that the number of density varies on account of two effects; scatterings can transform particles of one species to another, while the expansion of the Universe gradually dilutes its content. When considering the standard WIMP scenario, the collision term defined in equation (2.20) can be significantly simplified. Firstly, one can disregard the blocking or stimulated emission factors in the square brackets, i.e. $1 \pm f_i \approx 1$, as particles are expected to be far from the degenerate state, and, by neglecting the chemical potentials, approximate $f_i \approx \exp(-E_i/T)$. Furthermore, by focusing on a single 2-to-2 pair-annihilation/creation process, namely $\chi\bar{\chi} \leftrightarrow \psi\bar{\psi}$ with matrix element $M_{\chi\bar{\chi}\text{-}\psi\bar{\psi}}$, where ψ is the SM fields to which DM field χ couples, and using the energy part of δ-function, which implies $E_\psi + E_{\bar{\psi}} = E_\chi + E_{\bar{\chi}}$, one can show that the equilibrium distribution functions of the two particles species obey:

$$f_\psi^{\rm eq} f_{\bar{\psi}}^{\rm eq} = \exp\left(-\frac{E_\psi + E_{\bar{\psi}}}{T}\right) \overset{!}{=} \exp\left(-\frac{E_\chi + E_{\bar{\chi}}}{T}\right) = f_\chi^{\rm eq} f_{\bar{\chi}}^{\rm eq}\,, \tag{2.23}$$

By defining the thermally averaged annihilation cross-section times velocity as:

$$\begin{aligned}\langle \sigma_{\chi\bar{\chi}\text{-}\psi\bar{\psi}}\, v\rangle = \frac{1}{(n_\chi^{\rm eq})^2}\int d\Pi_\chi \int d\Pi_{\bar{\chi}} \int d\Pi_\psi \int d\Pi_{\bar{\psi}}\ \ |M_{\chi\bar{\chi}\text{-}\psi\bar{\psi}}|^2 \\ \cdot f_\chi^{\rm eq} f_{\bar{\chi}}^{\rm eq} \cdot (2\pi)^4\delta^4\left(p_\chi + p_{\bar{\chi}} - p_\psi - p_{\bar{\psi}}\right)\,,\end{aligned} \tag{2.24}$$

and noting that the SM particles remain in thermal equilibrium even after DM decouples, one can bring the equation (2.22) into the familiar form:

$$\frac{\partial n_\chi}{\partial t} + 3Hn_\chi = \langle \sigma_{\chi\bar{\chi}\text{-}\psi\bar{\psi}}\, v\rangle \left((n_\chi^{\rm eq})^2 - n_\chi^2\right)\,. \tag{2.25}$$

The above expression is often generalized to an arbitrary combination of annihilation processes by defining the total thermally averaged cross-section times velocity as a sum over individual channels with final states, $\langle \sigma_{\rm ann} v\rangle \equiv \sum_i \langle \sigma_{\chi\bar{\chi}\text{-}F_i} v\rangle$, where F_i can contain any number of daughter particles which, however, have to be in thermal equilibrium with the primordial plasma. As already mentioned in the discussion of WIMPs, the resulting evolution of number density for various cross-sections and DM masses is shown in figure 1.4. One recovers the correct present-day DM abundance for particles that decouple non-relativistic with thermally averaged cross-section $\langle \sigma_{\rm ann} v\rangle \sim 3 \cdot 10^{26}$ cm^3/s, which is comparable to the typical weak-force processes, while the result only slightly depends on DM mass, which can vary from GeV up to TeV scale. From the expression (2.25) one can approximate the freeze-out yield, which is commonly expressed in terms of number density normalized to the entropy density, $Y_\chi \equiv n_\chi/s$, as:

$$Y_\chi^{\rm FO} \approx \frac{x_{\rm FO}}{\langle \sigma_{\rm ann} v\rangle\, M_{\rm P}}\,, \tag{2.26}$$

where $x \equiv m_\chi/T$ and at the time of freeze-out typically takes values between $x_{\rm FO} \sim 20 - 30$. For detail numerical treatment of the freeze-out mechanism see, e.g., [45] and references therein.

As could be seen from the above discussion, several assumptions regarding the standard WIMP scenario can be called into question. For example, DM can have a much more complicated set of interactions, which can include processes like co-annihilations, conversions or even decays, provided that multiple fields are present in the dark sector. Furthermore, there can also be a non-negligible asymmetry between χ and $\bar{\chi}$ particles, in which case one needs to keep track of chemical potentials in the distribution functions, or, if DM annihilation/creation processes are CP-violating, two distinct squared matrix elements need to be considered in the corresponding collision terms. Since the simplest picture of WIMPs, discussed above, is becoming disfavored by experiments, many studies were done in the direction of relaxing these assumptions. The exact modification of the DM evolution is highly model-dependent and exhaustive analysis falls beyond the scope of this work; however, there exist few general categories in terms of DM detection prospects, which will be briefly mentioned in section 4.1.

3. Relaxed Dark Matter in spiral galaxies

The galactic phase-space distribution of DM plays a vital role in the interpretation of direct as well as indirect searches. In the past, crude approximations were often used, for example the combination of simulation-motivated NFW density profile and truncated Maxwell-Boltzmann velocity distribution. While such simplified models are usually computationally friendly and can provide the correct order of magnitude estimates, they do not correspond to an equilibrium solution of the collisionless Boltzmann equation. Furthermore, they are also difficult to link to dynamical observables within galaxies, making them less favourable in the light of newly available astronomical observations. Several refined models based on Eddington's inversion formula have been applied to the study of the Milky Way, however, they are hindered by the assumption of spherical symmetry. The latter is perhaps justifiable for dwarf spheroidals or elliptical galaxies, but evidently provides an inadequate description of spiral galaxies, which are characterized by their flattened stellar disks. Furthermore, rapidly improving astronomical observations allow us to perform increasingly detailed mass decompositions of galaxies, constraining their baryonic as well as DM components. This is especially true for our Milky Way, which is currently being mapped by the Gaia satellite, providing a new perspective on its dynamics, which is expected to improve even further with next-generation telescopes such as LSST and ELT. Additional information regarding the galactic DM distribution can also be obtained from state-of-the-art numerical simulations of structure formation, which have reached impressive accuracy in replicating the observed galaxies. While they can not be used to study particular objects, they can provide crucial information regarding the correlations between baryons and underlying DM content, as well as quantify the deviations from equilibrium, over large samples of simulated galaxies.

This chapter will be devoted to possible improvements in the modelling of spiral galaxies and the impact they may have on DM searches. The first section provides an overview of axisymmetric phase-space distribution models and their applicability to the study of DM. I will present in detail a computationally efficient method for obtaining axisymmetric equilibrium distribution functions, which was for the first time applied in the context of DM in our recent work [148], as well as most notable alternative approaches that can be found within the literature. This will be followed by a careful analysis of the differences in velocity distribution between spherically symmetric approaches and the axisymmetric generalization, as well as several deviations from the equilibrium solutions that

one generically expects to find in real galaxies will be mentioned. The second section is devoted to our galaxy, beginning with a review of recent observational insights and subsequent analysis of available measurements to provide updated constraints on the DM distribution within the Milky Way. These findings will be then used in the final section, where implications for the direct DM searches will be discussed. In particular, the focus will be on the general case of DM-nucleus interactions, considering the entire set of possible effective non-relativistic scattering operators, which might play a crucial role in interpreting the outcomes of experimental searches.

3.1 Axisymmetric distribution models

Within the field of galactic dynamics disk galaxies occupy a special place. Despite their abundance and long observational history, the exact mechanisms responsible for the emergence and evolution of their spiral structure are still topics of active research. In contrast with dispersion supported objects, such as elliptical or dwarf spheroidal galaxies, that can be reasonably well described via the spherical Jeans modelling introduced in section 2.1.1, disk galaxies require more careful treatment. Most notably, their shape is far from spherically symmetric. Furthermore, due to features like the spiral arms and/or central bars, even axisymmetric modelling seems to be inadequate to account fully for its dynamics. Significant advances in triaxial modelling have been made through the use of action-angle coordinates native to the system, which exploit the full power of strong Jeans theorem. There have also been attempts to build distribution models from a superposition of test particle orbits, often referred to as Schwartzschild modelling. However, these turn out to be much more computationally demanding and can have highly degenerate solutions. Unfortunately, the applicability of above methods to DM is additionally problematic due to the lack of directly observable quantities, such as the rotational velocity or velocity dispersion, that are typically used to constrain the dynamics of stellar populations. Therefore, the simplification to cylindrical symmetry (i.e. axisymmetry) can be often justified, since the existing data is insufficient to constrain the additional degrees of freedom that arise in more sophisticated models. Axisymmetric models are still capable of including the flattening of gravitational potential due to baryonic disk, which is felt by DM particles and leaves an imprint on DM velocity distribution, even if they reside in a perfectly spherical halo. Therefore, axisymmetric PSDFs provide a significant improvement over previous models that assume spherical symmetry. Apart from flattening, axisymmetric PSDFs can also self-consistently describe the rotation of galactic components, which is particularly important from the point of view of direct DM searches, where the signals can be strongly enhanced or suppressed, depending on the assumed rotational properties of the DM halo.

The latest astronomical surveys are providing us with a wealth of new information, making it possible to study the dynamics within galaxies with unprecedented precision. By combining observations of various dynamical tracers, it is possible to reconstruct the total gravitational potentials of galaxies, while photometric and radio observations allow us to determine the morphology and extent of baryonic components. Using these observations, mass decomposition of galaxies can be performed, which gives us also an estimate on the spatial

distribution of dark matter within the studied objects. In turn, these precise determinations of the total gravitational potential Φ and the density profile ρ can be exploited to reconstruct the full phase-space distribution of relaxed collisionless components in spiral galaxies by finding stationary solutions of the Boltzmann equation, in analogy to the spherically symmetric case discussed in section 2.1.1. Evaluation of such equilibrium solution will be one of the key topics of this section, paying particular attention to a computationally efficient method developed by Hunter & Qian [149, 150], which was, however, up to now applied only to stellar systems. Finally, I will mention several expected deviations of the actual galactic DM distribution from the previously discussed equilibrium solutions and explore possible ways of including them in the modelling.

3.1.1 Computational approaches

In the case of spherically symmetric and isotropic systems, a unique stationary solution for f can be obtained through Eddington's inversion formula (2.11). By imposing the less constraining assumption of axial symmetry, the situation becomes more complicated and several possible methods for reconstructing the PSDF exist, each with its limitations.

In the following, I will first describe an approach which assumes the absence of other continuous symmetries apart from rotations around the central axis. This, in turn, implies a two-integral PSDF, namely $f = f(\mathcal{E}, L_z)$, where $\mathcal{E}$ is the relative energy as defined in (2.9) and L_z is the angular momentum around the axis of symmetry. In this case, a generalization of the Eddington's inversion formula can be obtained, allowing to compute unique $f(\mathcal{E}, L_z)$ for an arbitrary axisymmetric density-potential pair. I will devote particular attention to a numerically friendly approach developed by Hunter & Qian, that relies on theoretical foundations previously lied out by Lynden-Bell [151]. This will be followed by a short overview of other computational methods that are capable of obtaining the PSDF in an even more general setting. Perhaps the most notable among them is an approach based on angle-action coordinates, which provide a particularly convenient description of the system in light of the strong Jeans theorem. While such modelling applies to any stationary PSDF, allowing for the presence of all three integrals of motion and also triaxial configurations, the transformation between action-angle and real-space coordinates is often very complicated and has, therefore, been successfully applied only to a limited set of analytically favourable galactic potentials. Furthermore, besides the gravitational potential and density distribution additional observational input is required to fully constrain such models, which can be done for certain stellar systems, however, is currently infeasible in the case of DM.

The Hunter-Qian method

According to the strong formulation of Jeans theorem, for a system with regular non-resonant orbits, any steady-state solution of the collisionless Boltzmann equation in a given stationary gravitational potential depends on up to three independent integrals of motion. For an axisymmetric configuration, the isolating integrals are the energy $\mathcal{E}$, usually defined as in equation (2.9), the component of the angular momentum parallel to the axis of symmetry, L_z, and a so-called

non-classical third integral I_3, which however takes an analytic expression only in very few specific cases. Hence, most often, PSDFs for axisymmetric systems have been assumed to depend on the first two only; while this is a limitation of the following method, such approach is actually favourable for addressing DM, as more general models often invoke degrees of freedom that can not be constrained by observations.

Under the two-integral-of-motion assumption, the PSDF can be decomposed in two parts, f_+ that is even in L_z and the f_- that is odd:

$$f(\mathcal{E}, L_z) = f_+(\mathcal{E}, L_z) + f_-(\mathcal{E}, L_z) \,. \tag{3.1}$$

The even part contains information regarding the density distribution, while the odd part describes the rotational properties of the considered system, given that:

$$\begin{aligned} \rho(R,z) &\equiv \int_{|\vec{v}|<\sqrt{2\Psi(R,z)}} \mathrm{d}^3 v \; f(\mathcal{E}, L_z) \\ &= \frac{2\pi}{R} \int_0^{\Psi(R,z)} \mathrm{d}\mathcal{E} \int_{-R\sqrt{2(\Psi(R,z)-\mathcal{E})}}^{R\sqrt{2(\Psi(R,z)-\mathcal{E})}} \mathrm{d}L_z \; f_+(\mathcal{E}, L_z) \,, \end{aligned} \tag{3.2}$$

$$\begin{aligned} \left(\rho\bar{v}_\phi\right)(R,z) &\equiv \int_{|\vec{v}|<\sqrt{2\Psi(R,z)}} \mathrm{d}^3 v \; |\vec{v}| \cdot f(\mathcal{E}, L_z) \\ &= \frac{2\pi}{R^2} \int_0^{\Psi(R,z)} \mathrm{d}\mathcal{E} \int_{-R\sqrt{2(\Psi(R,z)-\mathcal{E})}}^{R\sqrt{2(\Psi(R,z)-\mathcal{E})}} \mathrm{d}L_z \; L_z \cdot f_-(\mathcal{E}, L_z) \,. \end{aligned} \tag{3.3}$$

In the formulas above $\bar{v}_\phi$ is the rotational velocity profile around the symmetry axis, while R and z are the radial distance and vertical height in the usual cylindrical coordinate frame.

Analogously to Eddington's formula, the two-integral-of-motion PSDFs can be reconstructed via an inversion of equations (3.2) and (3.3). The approach described below was proposed by Hunter & Qian [149] and will be therefore in the following referred to as "HQ method". One starts with the analytic continuation of the density $\rho(R,z)$ and relative gravitational potential $\Psi(R,z)$ into the complex plane; restricting to models which are symmetric with respect to the equatorial plane, and provided that Ψ decreases monotonically with increasing z, one can replace the cylindrical coordinates R and z with the variables R^2 and Ψ. Hunter & Qian [149, 150] then showed that the L_z-even part of PSDF can be computed as:

$$f_+(\mathcal{E}, L_z) = \frac{1}{4\pi^2 i\sqrt{2}} \oint_{C(\mathcal{E})} \frac{\mathrm{d}\xi}{\sqrt{\xi - \mathcal{E}}} \left. \frac{\mathrm{d}^2\rho(R^2,\Psi)}{\mathrm{d}\Psi^2} \right|_{\substack{\Psi=\xi \\ R^2=\frac{L_z^2}{2(\xi-\mathcal{E})}}} \,, \tag{3.4}$$

where $C(\mathcal{E})$ is an appropriate path which tightly wraps around the real axis between the value of the potential at infinity, Ψ_∞, and a characteristic value Ψ_{env}, which, for any given value of the relative energy $\mathcal{E}$, is the value of the relative potential corresponding to the position on the galactic plane at which a circular orbit of radius R_c has relative energy $\mathcal{E}$, namely $\Psi_{\mathrm{env}}(\mathcal{E}) = \Psi\left(R = R_c(\mathcal{E}), z = 0\right)$.

The authors propose, as useful way to parametrize the contour, to define an ellipse in terms of a real variable $\theta \in [0, 2\pi]$:

$$\xi(\theta) = \frac{\Psi_{\mathrm{env}}(\mathcal{E})}{2}(1 + \cos\theta) + i\,h\sin\theta\,, \tag{3.5}$$

$$\xi(\theta) = \Psi_{\mathrm{env}}(\mathcal{E}) + l(1 - \sec\frac{\theta}{2}) + i\,h\sin\theta\,, \tag{3.6}$$

where the first expression should be used in case of finite Ψ_∞ and the second one in case of $\Psi_\infty \to -\infty$. The parameter h controls the width of the contour in the imaginary plane, while l is relevant only for infinite potentials and determines where the contour reaches its maximum width. In practice it is good to keep h small to avoid including possible additional singularities that arise from the analytical continuation of ρ, however large enough to maintain good numerical convergence. Having this, the crucial point becomes the evaluation of the second derivative of the density with respect to the potential. In most cases one cannot perform the change of variables explicitly, and is forced to use the implicit derivation in cylindrical coordinates:

$$\begin{aligned}\frac{\mathrm{d}^2\rho(R^2,\Psi)}{\mathrm{d}\Psi^2} = \frac{\mathrm{d}^2\rho(R^2,z^2)}{\mathrm{d}(z^2)^2}\left(\frac{\mathrm{d}\Psi(R^2,z^2)}{\mathrm{d}z^2}\right)^{-2} \\ - \frac{\mathrm{d}\rho(R^2,z^2)}{\mathrm{d}z^2}\frac{\Psi(R^2,z^2)}{\mathrm{d}(z^2)^2}\left(\frac{\mathrm{d}\Psi(R^2,z^2)}{\mathrm{d}z^2}\right)^{-3}\,,\end{aligned} \tag{3.7}$$

evaluated at $R^2 = \frac{L^2}{2(\xi-\mathcal{E})}$ and z^2 such that $\Psi(R^2, z^2) = \xi$. Values of z^2 fulfilling the latter equality typically need to be found via numerical minimization routines. Further difficulties might arise if $\Psi(R^2, z^2)$ contains a branch cut along the contour, inducing a discontinuity in the Jacobian of the coordinate transformation; this typically happens for certain values of $\mathcal{E}$ and L_z for a system embedded in very flattened potential and requires a proper adjustment of $C(\mathcal{E})$ and of the method in which the numerical integral is performed (this technical issue and its possible solutions are discussed in Appendix A). Finally, one can simplify the contour integral by using the Schwarz reflection principle, which implies that the values of integral above and below the real axis must be complex conjugates of each other. Therefore one can shrink the domain of integration to $\theta \in [0, \pi]$, compute only the real part and multiply the final result by factor of 2. The L_z-odd part of PSDF can be computed analogously, using the following expression:

$$f_-(\mathcal{E}, L_z) = \frac{\mathrm{sign}(L_z)}{8\pi^2 i}\oint_{C(\mathcal{E})}\frac{\mathrm{d}\xi}{\xi-\mathcal{E}}\left.\frac{\mathrm{d}^2\left(\rho\bar{v}_\phi\right)}{\mathrm{d}\Psi^2}\right|_{\substack{\Psi=\xi \\ R^2=\frac{L_z^2}{2(\xi-\mathcal{E})}}}\,. \tag{3.8}$$

It is important to note that in order to evaluate f_- one needs to specify also $\bar{v}_\phi(R^2, z^2)$, which is unfortunately often unknown. To surmount this one can either assume a parametric form for $\bar{v}_\phi$ or construct the PSDF using only f_+. This issue will be addressed in greater detail in the following section.

Similarly as Eddington's inversion, the HQ method can be in principle used to compute the PSDF for any choice of axisymmetric $\rho(R^2, z^2)$, $\Psi(R^2, z^2)$ and $\bar{v}_\phi(R^2, z^2)$, however there is no guarantee that the resulting PSDF will be positive definite (i.e. physical). This needs to be checked explicitly after performing

the contour integrals. At this point, we also note that one can check the accuracy of resulting PSDF by, for example, plugging it back in equation (3.2), which should reproduce the initially assumed density distribution. When performing the analysis, I found my implementation of the algorithm capable of reconstructing the initial density within a few per cent accuracy over the entire region of interest for all the studied cases.

Action-angle coordinates

An alternative approach of modelling PSDF that is applicable to any stationary configuration composed of regular orbits is based on the exploitation of action-angle coordinates. Instead of the usual parametrization of phase-space through $\{\vec{x}, \vec{p}\}$, one can use the actions, $\vec{J}$, that coincide with the isolating integrals of a given system and are hence conserved along trajectories Γ_α, and their corresponding conjugate coordinates $\vec{\theta}$:

$$J_i = \frac{1}{2\pi} \oint_{\Gamma_\alpha} d\vec{p} \cdot \vec{x} \,, \tag{3.9}$$

$$\theta_i = \theta_i(0) + \frac{\partial \theta_i}{\partial t} \cdot t \quad \text{where} \quad \frac{\partial \theta_i}{\partial t} = \frac{\partial H}{\partial J_i} \,. \tag{3.10}$$

According to the strong Jeans theorem, any stationary solution of the collisionless Boltzmann equation, which consists of regular orbits, has to be a function of a maximum three isolating integrals and hence independent of θ_i. As a consequence, any regular orbit can be written as a periodic function of the latter, which are therefore commonly known angles. Furthermore, it can be shown that PSDFs parametrized with action-angle coordinates are adiabatically invariant and therefore particularly suitable for slowly evolving systems like galaxies. On the other hand, the mapping between the action-angle coordinates and real phase-space often turns out unduly complicated and can be tackled only at a great numerical expense. Several analytically traceable choices of galactic potentials and corresponding actions exist, typically relying on spherical symmetry and power-law potential, or more generally axisymmetric potentials of Stäckel form. However, these do not cover important phenomenologically motivated functional forms that yield a fairly good description of galactic dynamics. In practice, several parametric solutions for the PSDF are known, and while their applicability to realistic spiral galaxies has remained limited, they can be refined by iterative methods. The latter, however, again come at a great computational expense as the actions need to be evaluated through numerical integration. More details regarding the action-angle approach can be found, e.g., in [145, 152] and references therein.

Orbital superposition

Another possible approach, which is often referred to as Schwartzschild modelling, relies on superimposing single-particle orbits native to the system. Given some gravitational potential, one can pre-compute all the regular orbits, which can be either done numerically or by knowing the appropriate set of actions, $\vec{J}$. These can then be used to construct their superposition and tune the corresponding coefficients to reproduce the observational features of a given system.

Several implementations of this algorithm have been proposed, see for example [153, 154]. In this approach, there is no clear guidance for the choice of the coefficients, and therefore the construction of PSDF is typically very computationally demanding. Furthermore, there can be severe degeneracies between the solutions, since several PSDFs can lead to the same density distribution or kinematic features. For DM, this is particularly problematic, since current observations are capable of constraining only the density distribution, while the kinematic properties remain uncertain, leading to poor constraints on the orbital coefficients.

3.1.2 Spherical vs axial symmetry

The HQ method, described in the previous section, turns out to be indispensable for determining the phase-space distributions within spiral galaxies. The method can be applied to the DM halo, but also stars or any other component that is well approximated by a steady-state axial distribution of collisionless point-like particles. In the following a representative model of a spiral galaxy will be used to outline the main features in DM velocity distribution that differ from the spherically symmetric modelling, namely the effect of flattened gravitational potential and flattening or rotation of DM halo itself.

Galactic potential and DM distribution

To obtain f_+ for the component of interest, one needs to specify its density profile, as well as the total gravitational potential. Spiral galaxies are typically composed of a stellar disk with a bulge/bar structure in the centre, embedded in large DM halo. In this section, I will consider a toy model with: *i)* a Myamoto-Nagai (MN) disk, whose potential is given by:

$$\Psi_{\text{MN}}(R^2, z^2) = \frac{GM_d}{\sqrt{R^2 + (a_d + \sqrt{z^2 + b_d^2})^2}} \,, \tag{3.11}$$

and parametrized in terms of its mass M_d, characteristic radius a_d and characteristic height b_d; *ii)* a spherically symmetric Hernquist bulge (we are not going to discuss results regarding regions where the bulge is the dominant component, hence this specific choice is not crucial), with potential:

$$\Psi_{\text{H}}(R^2, z^2) = \frac{GM_b}{\sqrt{R^2 + z^2} + a_b} \,, \tag{3.12}$$

parameterized by its mass M_b and characteristic radius a_b; and *iii)* a spheroidal DM halo with an oblate or prolate NFW density profile [155]:

$$\rho_{\text{sNFW}}(m) = \frac{\rho_s}{m/r_s \cdot (1 + m/r_s)^2} \quad \text{where} \quad m^2 = R^2 + z^2/q^2 \,, \tag{3.13}$$

parameterized by the scale density ρ_s, the scale radius r_s and the "flattening" parameter q. For spherical halos, obtained by setting $q = 1$, the corresponding gravitational potential can be computed analytically:

$$\Psi_{\text{NFW}}(r) = 2\pi G \rho_s r_s^2 \cdot \frac{\log(1 + r/r_s)}{r/r_s} \quad \text{where} \quad r = \sqrt{R^2 + z^2} \,, \tag{3.14}$$

while for oblate ($q < 1$) or prolate ($q > 1$) halos, a numerical evaluation of the following integral is required:

$$\Psi_{\rm NFW}(R^2, z^2) = \pi G q \int_0^\infty \frac{{\rm d}u}{(1+u)\sqrt{q^2+u}} \int_U^\infty \rho(m^2){\rm d}m^2 \qquad (3.15)$$

$$\text{where} \qquad U = \frac{R^2}{1+u} + \frac{z^2}{q^2+u} \, .$$

The above model involves a set of free parameters that need to be inferred from observations. In this section a set of sample values will be used, which is in rough agreement with what is typically found in spiral galaxies [12, 156–158]:

$$M_b(r_{2.2}) = 0.05 M_{2.2} \quad , \quad M_d(r_{2.2}) = 0.45 M_{2.2} \, , \qquad (3.16)$$

$$a_b = \frac{a_d}{3} \quad , \quad b_d = \frac{a_d}{10} \quad , \quad r_s = 5 a_d \, , \qquad (3.17)$$

where $M_{2.2}$ is the total mass of the object within a radius equal to 2.2 disk lengths. This characteristic scale was recognized to be particularly useful as a benchmark distance for determining the fraction of DM mass in a given galaxy [159]. We use the corresponding circular velocity $\hat{V}_c \equiv V_c(R = 2.2 a_d)$ as a normalization scale in the rest of this section.

From spherical to flattened systems

When connecting the model to observations, one needs to fit the total relative gravitational potential $\Psi_{\rm tot}$, which is the sum of the bulge, disk and halo components, to reproduce the observed circular velocity profile in the galactic plane $V_c(R)$:

$$V_c^2(R) = -2R^2 \cdot \left. \frac{{\rm d}\Psi_{\rm tot}(R^2, z^2)}{{\rm d}R^2} \right|_{z=0} \, . \qquad (3.18)$$

It is evident that spherical, as well axisymmetric, modelling can reproduce a given $V_c(R)$. Hence, spherically symmetric models were used in the past to compute PSDF of halos using the Eddington's inversion. We demonstrate that such simplification can drastically affect the PSDF and the axisymmetric HQ method should be used instead. To illustrate the difference, we used a combination of spherical NFW potential for the halo and a linear combination of MN and Plummer potential (a spherical approximation of MN potential, obtained by setting $a_d \to 0$ and $b_d \to a_d$) for the disk:

$$\Psi_{\rm disk}(R^2, z^2) = x_{\rm axi} \Psi_{\rm MN}(R^2, z^2) + (1 - x_{\rm axi}) \Psi_{\rm P}(R^2 + z^2) \, , \qquad (3.19)$$

while for the moment we omit the sub-dominant bulge component. In figure 3.1 we present the comparison of radial and azimuthal velocity distributions, as well as the residuals with respect to the spherical limit, for various values of $x_{\rm axi} \in [0, 1]$. As the admixture of the axisymmetric potential increases, the radial velocity distribution becomes shifted towards higher velocities, while the azimuthal component gains power at low velocities. This results in skewed velocity distributions that can not be accurately modelled within the spherical approximation, nor using a Gaussian profile. The differences are most significant in the central part of the halo and gradually diminish with increasing

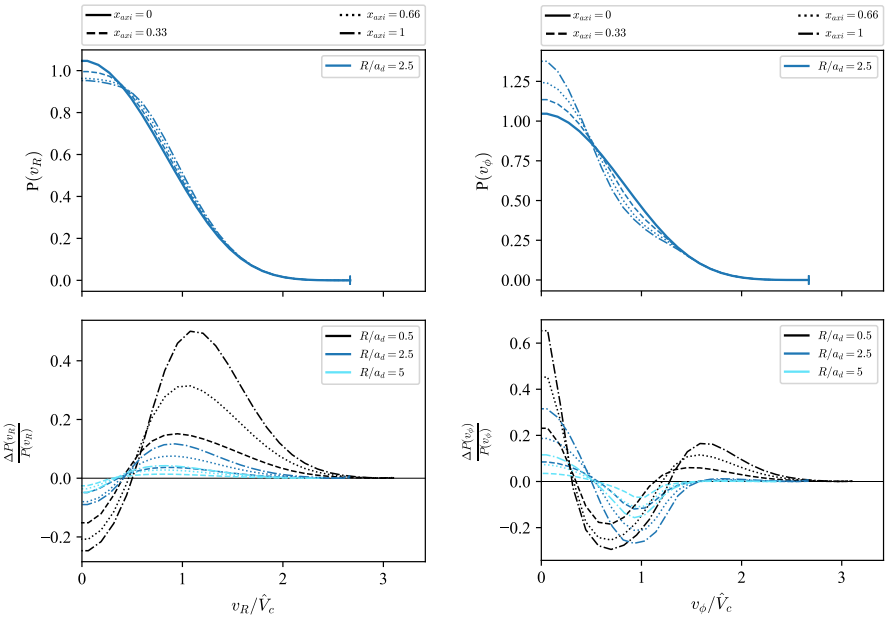

Figure 3.1: Radial (left) and azimuthal (right) velocity distributions in the galactic plane for various fraction of the axisymmetric component, parametrized by $x_{\rm axi}$. In lower panels we show the relative difference with respect to the $x_{\rm axi} = 0$ case, computed at different radii.

distance from the centre, as the effect of disk component becomes negligible. The changes in the velocity distributions naturally lead also to changes in the velocity dispersion $\sigma^2(R, z)$, as well as in a velocity anisotropy. Analogously to spherical systems, for which the anisotropy is usually described in terms of radial anisotropy parameter defined as the ratio of velocity second moments in the tangential and radial direction, we introduce here the following quantity, better suited for describing axial systems:

$$\beta_\ominus(R, z) \equiv \frac{1}{2} - \frac{\sigma^2_\phi(R^2, z^2)}{\sigma^2_M(R^2, z^2)} \,, \tag{3.20}$$

where σ^2_ϕ is the velocity dispersion in azimuthal direction, while $\sigma^2_M = \sigma^2_R + \sigma^2_z$ is the velocity dispersion in meridional plane (note that for $f(\mathcal{E}, L_z)$ the velocity dispersion in meridional plane is isotropic, i.e. $\sigma^2_R = \sigma^2_z$, by construction). On the right-hand side of figure 3.2 we show that the velocity anisotropy in the galactic plane, $\beta_\ominus(R, 0)$, becomes positive as the admixture of axisymmetric potential increases, with the radial velocity dispersion increasing and the azimuthal component diminishing. In the plot on left hand side of same figure 3.2, we show the total velocity dispersion ($\sigma^2 = 2\sigma^2_R + \sigma^2_\phi$), which also increases with $x_{\rm axi}$. These effects are, however, again limited only to the central part of the galaxy, where the influence of disk is significant, and slowly diminish as one moves towards the outskirts of the system.

Similarly, one can check how the PSDF of the halo particles changes if one varies the relative weight of axisymmetric disk and spherical halo components,

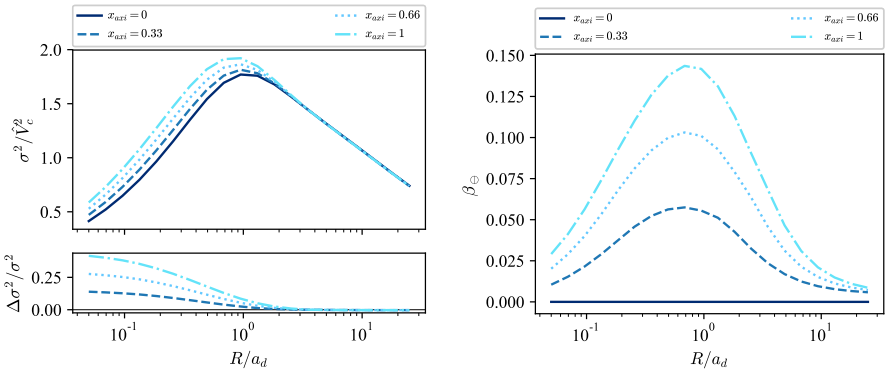

Figure 3.2: Total velocity dispersion (left) and velocity anisotropy (right) in the galactic plane as a function of radial distance for various fractions of axisymmetric component, parametrized by $x_{\rm axi}$. In the lower left panel we show the relative difference of the velocity dispersion with respect to the $x_{\rm axi}=0$ case.

while keeping the characteristic circular velocity $\hat{V}_c$ unchanged:

$$\hat{V}_c = -2 \cdot \left[R^2 \left(x_{\rm disk} \cdot \frac{{\rm d}\Psi_{\rm MN}(R^2,z^2)}{{\rm d}R^2} + (1-x_{\rm disk}) \cdot \frac{{\rm d}\Psi_{\rm NFW}(R^2,z^2)}{{\rm d}R^2} \right) \right] \Bigg|_{\substack{R=2.2a_d \\ z=0}} \tag{3.21}$$

In figure 3.3 we show the comparison of radial and azimuthal velocity distributions for various values of $x_{\rm disk}$. The span of values displayed go from $x_{\rm disk}=0$, in which case one has only spherical NFW halo, to values that are representative of minimal/average/maximal disk models for spiral galaxies. The trends are similar as when varying $x_{\rm axi}$, since also $x_{\rm disk}$ interpolates between spherically symmetric and increasingly axisymmetric configurations. However, an important difference is the fact that the local escape velocity, $v_{\rm esc}=\sqrt{2\Psi(R^2,z^2)}$, decreases with increasing $x_{\rm disk}$, since smaller amount of total mass is needed to produce the same $\hat{V}_c$. Therefore the corresponding velocity distributions become suppressed at high velocities with respect to the halo-only case. This effect is somewhat compensated by the aforementioned shift of power in the radial velocity distribution towards higher v, which occurs in presence of flattened disk. The differences are again most significant in the central part of the galaxy, where the disk component dominates, but remain noticeable even at large radii due to the change in $v_{\rm esc}$. The interplay of these effects again highlights the need for careful modelling that goes beyond the standard approximations.

Degeneracies in mass model decompositions sometimes make it hard to infer the DM density profile precisely. Besides the well-known cusp/core problem, one often faces large uncertainties in inferring the halo scale radius r_s. In figure 3.4 we show the velocity probability distributions for three different r_s/a_d ratios, which cover a range of values typical for the Milky-Way [160]. We find that for large r_s/a_d the velocity distributions contains features that can not be encaptured by a simple Gaussian curve, while decreasing the ratio leads to increasingly Maxwellian distribution. An important difference with respect to varying the admixture of disk component is that both radial and azimuthal ve-

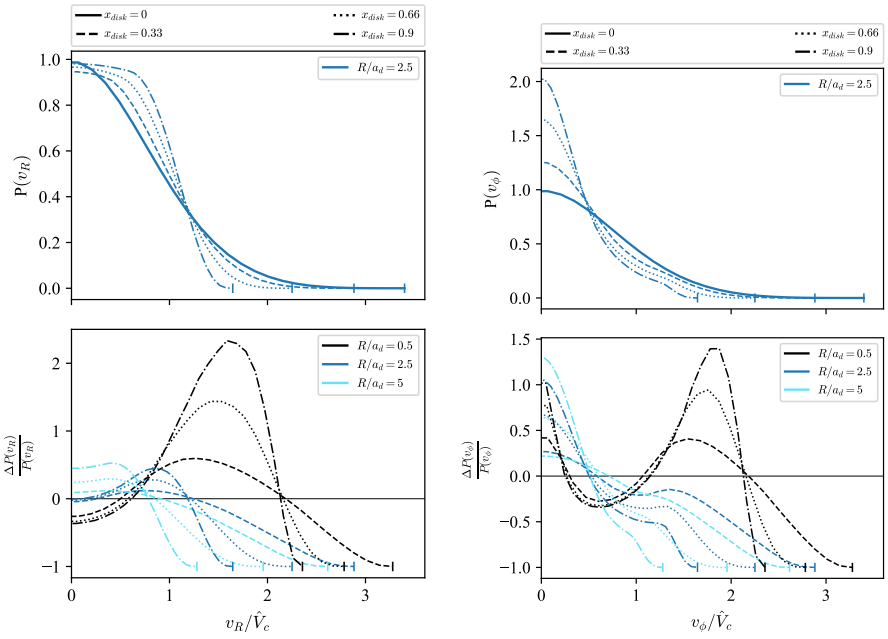

Figure 3.3: Radial (left) and azimuthal (right) velocity distributions in the galactic plane for various fractions of the stellar disk component, parametrized by $x_{\rm disk}$. In the lower panels we show the relative difference with respect to the $x_{\rm disk} = 0$ case, computed at different radii.

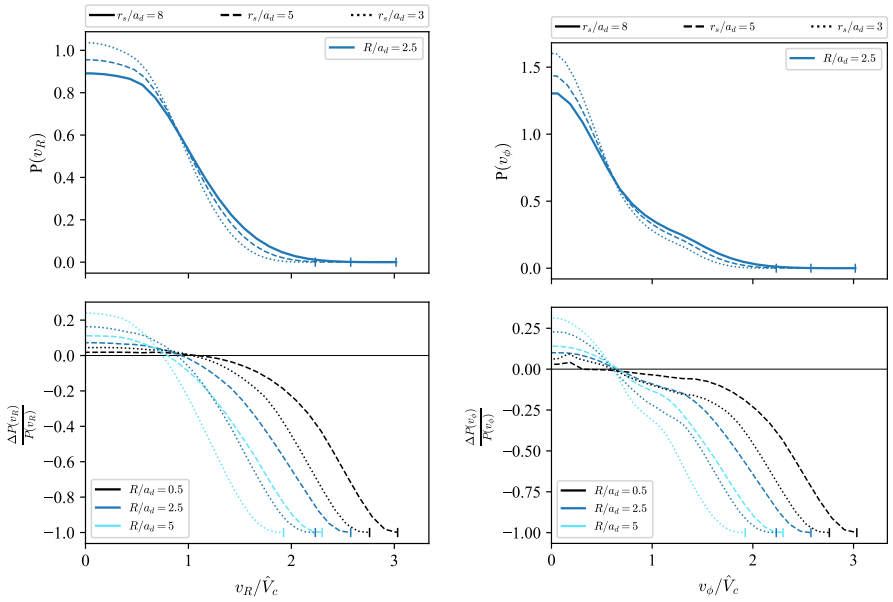

Figure 3.4: Radial (left) and azimuthal (right) velocity distributions in the galactic plane for various ratios of r_s/a_d. In the lower panels we show the relative difference with respect to the $r_s/a_d = 8$ case, computed at different radii.

locity distributions get shifted towards lower velocities as r_s decreases, which leads to "colder" halos at $R \gtrsim a_d$. This can also be seen from the corresponding velocity dispersion, shown in the plot on the left-hand side of figure 3.5. In the right-hand side plot of the same figure 3.5, we show the resulting velocity anisotropy in the galactic plane for same r_s/a_d ratios, which demonstrates that decreasing r_s leads to a relative increase of the velocity dispersion in the meridional plane with respect to the azimuthal component.

Finally, we note that the effects of the stellar disk on the halo particles soften more rapidly as one moves along the z-axis, as compared to the radial direction. This can be seen from figure 3.6, where we plot the radial and azimuthal velocity probability distributions for various heights above the galactic plane. As one moves towards larger values of z, the radial velocity distribution gets shifted back to lower velocities, while the azimuthal components get more power at high velocities. These trends are the opposite as one finds for increasing the amount of disk component. However, at $z \gg b_d$ the velocity distribution deviates from the one found in the spherically symmetric case, which is most evident for $R \lesssim a_d$.

Halo flattening

Using the HQ method, one can also study the effect of flattening or elongation of the DM halo along the axis of symmetry. As disused before, the sphericity of halo is controlled by parameter q, where $q < 1$ corresponds to oblate and $q > 1$ to prolate configurations. Even though some recent studies suggest that

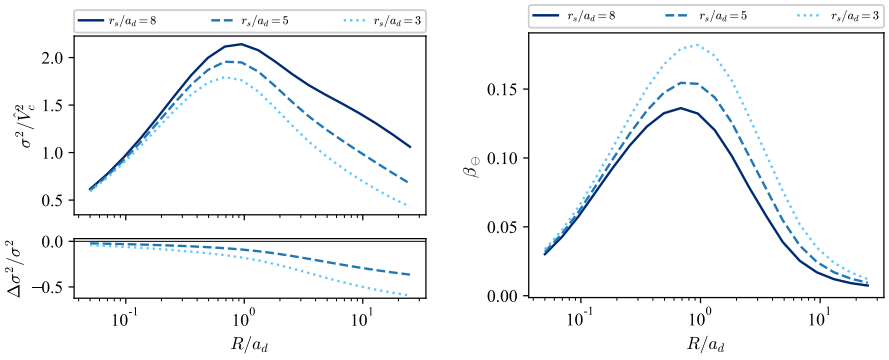

Figure 3.5: Total velocity dispersion (left) and velocity anisotropy (right) in the galactic plane as a function of radial distance for various ratios of r_s/a_d. In the lower left panel we show the relative difference of velocity dispersion with respect to the $r_s/a_d = 8$ case.

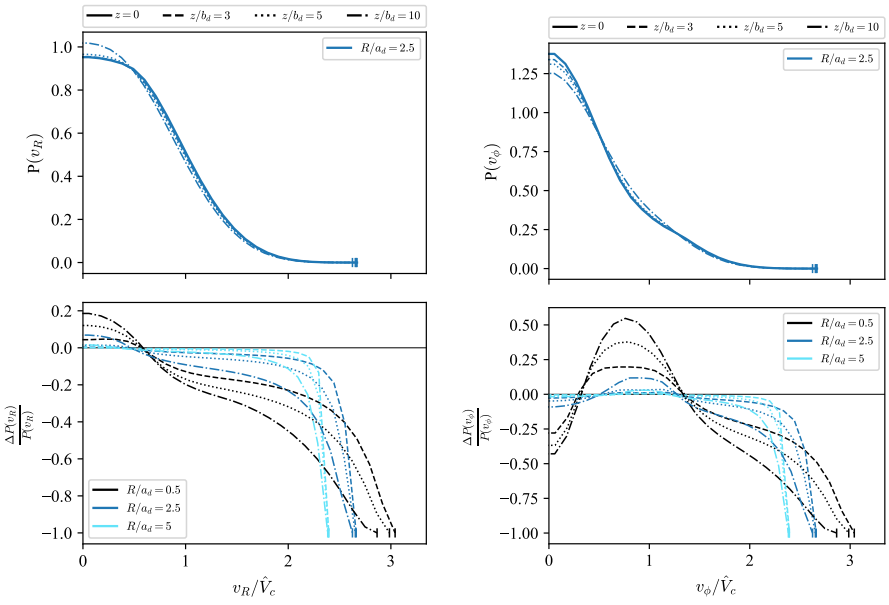

Figure 3.6: Radial (left) and azimuthal (right) velocity distributions for various heights z above the galactic disk, normalized to the disk height b_d. In the lower panels we show the relative difference respect to the $z = 0$ case, computed at different radii.

the Milky Way halo is very close to spherical [161], there exist claims in favour of a highly flattened DM sub-component coming from past mergers, see [162] and references therein. Furthermore, hydrodynamical simulations of structure growth, which include baryons, generically predict oblate halos [15, 20] with a significant spread in the q parameter, whose value is strongly influenced by the formation history of the particular object. figure 3.7 shows the halo velocity distributions obtained for a range of typical q values while keeping the baryonic component and $\hat{V}_c$ fixed. We find that for oblate halos the radial velocity distribution gets shifted towards smaller velocities, while the azimuthal velocity distribution is more sharply peaked at intermediate velocities. The morphology of the halo also affects the depth of the gravitational potential when keeping $\hat{V}_c$ unchanged, which in turn leads to lower $v_{\rm esc}$ for $q < 1$, while changes are in the opposite direction in case of prolate halos. By comparing with figures 3.1 and 3.3 we can see that flattening has roughly the opposite effect of increasing the disk component. However, the velocity distributions in the presence of both features are still poorly described by the Gaussian or spherical approximation. The corresponding velocity dispersion, portrayed in the left-hand side plot of figure 3.8, is consistent with the changes in the velocity probability distributions, as it decreases (increases) for oblate (prolate) halos. The effect remains significant at all radii since the halo is the largest component of the galaxy and extends way beyond the stellar disk. The velocity anisotropy in the galactic plane showed in the right-hand side plot of figure 3.8, remains radially biased in the central part for oblate and prolate halos, however, in the outskirts we see different behaviours. Oblate halos generically lead to negative, i.e. circularly biased, velocity anisotropy, while for prolate halos we find increasing radial bias at large galactocentric distances.

Halo rotation

In order to compute the L_z-odd part of PSDF one needs to additionally specify halo rotation profile $\bar{v}_\phi(R^2, z^2)$. While it can be, at least in principle, measured for stars or other baryonic components of galaxy, we presently have no way of inferring the rotational properties of galactic DM. Therefore, to address the uncertainty arising from various possible realizations of f_- one can adopt the following parametrization:

$$f_-(\mathcal{E}, L_z) = \alpha(\mathcal{E}, L_z) f_+(\mathcal{E}, L_z) \,, \tag{3.22}$$

where α is an arbitrary functions of the two integrals that takes values in the range of $[-1, 1]$ and is odd in L_z. One of the simplest choices is $\alpha(L_z) = \alpha_0 \cdot \mathrm{sign}(L_z)$, which has been used in context of modelling stellar components of elliptical galaxies [145], however, it introduces a discontinuity in $f(\mathcal{E}, L_z)$ at $L_z = 0$. The corresponding velocity distribution $\mathrm{P}_{\alpha_0}(v_\phi)$ is simply obtained by scaling the result obtained from f_+ (i.e. for $\alpha_0 = 0$) by a constant factor:

$$\mathrm{P}_{\alpha_0}(v_\phi) = \mathrm{P}_{\alpha_0=0}(v_\phi) \cdot \begin{cases} 1 + \alpha_0 \,; & v_\phi > 0 \\ 1 - \alpha_0 \,; & v_\phi < 0 \end{cases} . \tag{3.23}$$

To avoid the discontinuity at $v_\phi = 0$ one could choose, e.g., $\alpha(L_z) = L_z / L_{z,\max}$. While the resulting velocity distribution is smooth, it is not clear whether such $\bar{v}_\phi$ profile describes a likely configuration for DM particles or not. Therefore, it

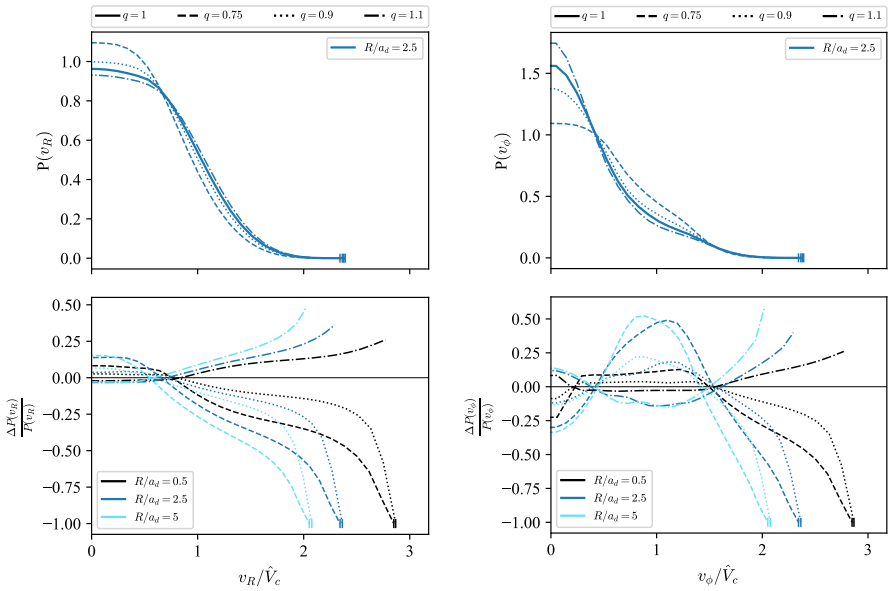

Figure 3.7: Radial (left) and azimuthal (right) velocity distributions in the galactic plane for various halo shapes, parametrized by q. In the lower panels we show the relative difference with respect to the spherical halo, computed at different radii.

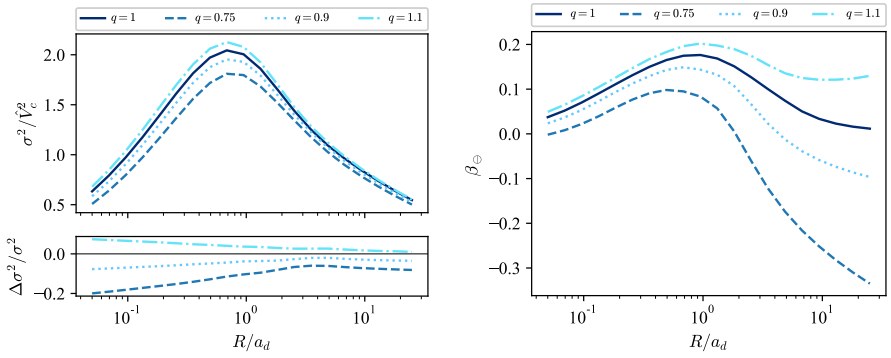

Figure 3.8: Total velocity dispersion (left) and velocity anisotropy (right) in the galactic plane as a function of radial distance for various halo shapes, parametrized by q. In the lower left panel we show the relative difference of velocity dispersion with respect to the spherical halo.

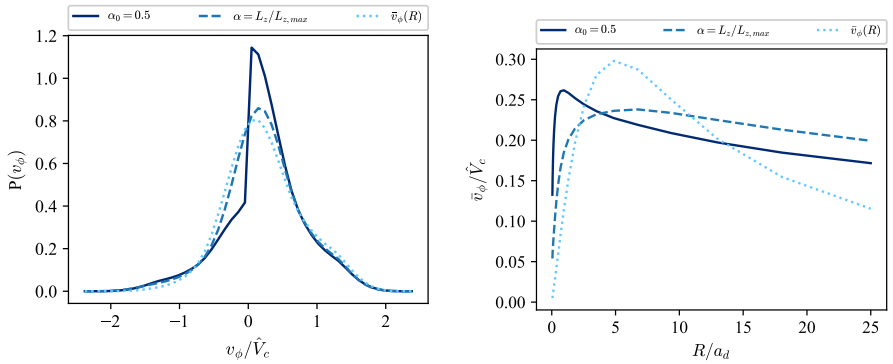

Figure 3.9: Azimuthal velocity probability distribution at $R = 2.2a_d$ (left) and average azimuthal velocity as a function of R (right) for PSDF with $f_- = \alpha f_+$ and f_- computed from $\bar{v}_\phi(R)$ as defined in (3.24), using $r_a = r_s$ and ω such that that the spin parameter $\lambda(r_{200}/4) = 0.05$.

is worthwhile considering another option, where we assume a functional form for $\bar{v}_\phi(R, z)$. A simple choice, that was considered in the past [145], is the following:

$$\bar{v}_\phi(R) = \frac{\omega R}{1 + R^2/r_a^2} \ . \tag{3.24}$$

It corresponds to a configuration where the system is spinning "on cylinders", as the expression in equation (3.24) is independent of z (and this is convenient, since the implicit derivation of $\rho\bar{v}_\phi$ with respect to Ψ in equation (3.8) does not produce additional terms). Physically, it resembles a core with solid-body rotation that diminishes towards the outskirts as $\bar{v}_\phi \propto 1/R$ for $R \gg r_a$. The comparison of $\bar{v}_\phi(R)$ and $\mathrm{P}(v_\phi)$ for various rotating models is shown in figure 3.9. As can be seen from the plots, the azimuthal velocity probability distributions for models with $\alpha \propto L_z$ and rotational profile defined in (3.24) are quite similar at the benchmark radial distance $R = 2.2a_d$ (roughly corresponding to the solar galactocentric distance in Milky Way) while constant α induces a sharp jump at $v_\phi = 0$, as could have be anticipated from equation (3.23). On the other hand, the azimuthal rotational profiles of all the considered models are noticeably different.

Since numerical simulations are essentially the only source of information regarding halo rotation, we follow their convention and normalized the above f_- models in terms of the spin parameter:

$$\lambda(r) = \frac{J(r)}{\sqrt{2} r M_{\mathrm{DM}}(r) V_c(r)} \ , \tag{3.25}$$

where $J(r)$ and $M_{\mathrm{DM}}(r)$ are the total angular momentum and DM mass within radius r. The values of spin parameter typically found in hydrodynamic simulations range between $\lambda(r_{200}/4) \sim 0.03 - 0.08$ [20] for Milky Way-like galaxies, where r_{200} is the virial radius, defined as distance at which the average halo density is 200 times the critical density. Throughout this work $\lambda(r_{200}/4) = 0.05$ will be assumed.

3.1.3 Deviations from equilibrium

All of the above-discussed methods are derived upon the assumption that the distribution function is stationary, i.e. in dynamical equilibrium. However, in practice, there is compelling evidence that this is at some level violated for most of the galaxies. While their dynamical times are small enough that they could have reached equilibrium configurations, this is most probably at some level violated due to interactions of nearby galaxies and their merging, or by violent baryonic processes, such as supernovae explosions. This picture is strongly confirmed by state-of-the-art numerical simulations, where it is rare to have isolated structures, and the inclusion of baryonic effects proved crucial for replicating various features of the observed galaxies. Furthermore, under the assumption of cold DM, the theory of structure formation, as well as the simulations, predicts a halo mass function which grows nearly quadratically with decreasing halo mass and results in roughly scale-invariant hierarchically clustered DM structures. Therefore, cold DM halos are probably not smooth, as it is commonly assumed, but contain a large number of subhalos, whose number density increases with their decreasing mass. Such deviations from the assumptions used in our modelling can have a profound effect on the expected signals in direct, as well as indirect, DM searches.

While this section will be far from a complete review on the topic, several recent developments will be discussed, along with possible ways of accounting for the perturbations on top of the equilibrium models. First, I will focus on the effect of DM subhalos, which will be followed by effects arising from tidal disruption and merging of galaxies.

DM subhalos

The cold DM hypothesis is capable of providing an explanation for a wide range of astronomical and cosmological observations, which can not be accounted for within conventional theories. All the relevant observations, however, measure the gravitational effects of DM on relatively large scales, while the properties of its clustering on sub-galactic scales remain poorly constrained. As already stated above, within the standard cold DM lore, one expects to find an increasing amount of structure with decreasing mass [155, 163, 164]. This can be intuitively understood by the fact that small halos form first, since larger scales take longer time to collapse, but also start growing with a delay as they enter the event horizon later. The details of DM distribution on small scales also crucially depend on the assumed DM candidate, how it was produced in the early Universe and how resilient the substructure is in subsequent non-linear evolution, during which it could be partially washed out by effects such as tidal forces or baryonic feedback. Therefore, it is rather unclear whether modelling of galactic DM as smooth equilibrium component, as assumed in previous sections, is a reasonably accurate description of real galaxies or not.

It has been long understood that the presence of substructures can have an important effect on indirect as well as direct DM detection experiments. For indirect searches presence of subhalos generically increases the expected signal, since the astrophysical J-factors are sensitive to the square of DM density and, therefore, presence of additional clumps within a given DM halo leads to larger predicted signals, as has been noted in numerous studies [165–169]. On the other

hand, the impact on direct detection searches highly depends on the distribution of DM in our local neighbourhood, which could be drastically increased by the presence of subhalo or include DM streams from disrupted structures [170–173]. Partitioning the total DM in a smooth component and subhalos has been suggested, since the equilibrium PSDF for smooth halo can be used to establish the lower bound on the expected signal, while substructure can lead to significant boosts, provided that one of these clumps finds itself near to the Earth. Since we currently have no means to probe whether we find ourselves within one of these structures or not, this has to be included as an additional source of systematic error in our predictions. The fraction of DM in subhalos, and hence the probability to find one in Earth's neighbourhood, can be estimated by various semi-analytic models [169, 174–177] or by extracting their statistical abundance from simulations [178–180]. Fortunately, several recent studies suggest that not more then few percents of galactic mass can be in the form of subhalos at solar galactocentric distance [169, 178], which implies that majority of DM indeed finds itself in virialised and relatively smooth halo that can be addressed through the equilibrium PSDF, $f_0(\mathcal{E}, L_z)$, obtained, e.g., through the HQ method. Provided that the subhalo probability distribution $P_{\rm sub}(\vec{\theta})$ is known, where $\vec{\theta}$ is a set of relevant parameters (e.g. subhalo mass, concentration, position, velocity, etc.), one can build the total PSDF by adding up the smooth component and appropriately weighted PSDF of the substructure:

$$f(\mathcal{E}, L_z) = f_0(\mathcal{E}, L_z) + \int d^n\theta \; P_{\rm sub}(\vec{\theta}) \; f_{\rm sub}(\mathcal{E}'; \vec{\theta}) \; . \tag{3.26}$$

In the above expression, it was assumed that the PSDF of subhalos, $f_{\rm sub}(\mathcal{E}')$, with $\mathcal{E}'$ being the relative energy of DM particles bound to a given substructure in its rest frame, can be approximated by means of Eddington's inversion formula (2.14). This is probably a good approximation in the central part of the subhalos, where the bulk of the associated DM particles resides, while in the outskirts tidal forces induced by the gravitational potential of the host galaxy become important and such simple modelling becomes inadequate, but affects only a smaller fraction of DM particles.

Tidal effects and merging of galaxies

According to the modern understanding of structure formation within the Universe, galaxies can hardly be considered as isolated systems. Typical spiral galaxies reproduced in simulations undergo several significant mergings with nearby smaller galaxies during their formation [181–183]. There is also an increasing amount of experimental evidence, which points towards several important merging events in the history of our Milky Way [184–187], while in the future it is expected to coalesce with galaxies in the local group [188–190]. Such intergalactic interactions can drive the DM particles away from equilibrium configuration, through either inducing tidal forces or by depositing new non-thermalized material into the existing halo.

The problem of non-linear halo growth and galactic merging has been extensively studied through numerical simulations. According to a recent work [191], it is useful to split the accumulated DM within galaxies in three categories: *i*) early accreted DM, which is to a good degree in dynamical equilibrium, *ii*) debris flow from recent mergers, that is partially phase-mixed, however, not yet

reach an equilibrium distribution and *iii*) streams of particles that are being stripped through tidal forces in ongoing mergers. For most galaxies, the majority of DM is expected to be in the form of smooth component, which can be directly modelled by an appropriate equilibrium distribution. On the other hand, a significant amount of DM (the exact fraction can vary greatly among different galaxies) can be in the form of debris flow, i.e. accreted through recent mergers but not yet thermalized, despite completing several orbits within the host. It has been recently suggested [191, 192] that the kinematic properties of simultaneously accreted DM and stars are similar, which provides us with a window into the phase-space distribution of debris DM component. Using the observations of accreted stars, as was done in [193, 194], one can deduce the phase-space distribution of DM debris flow, $f_{\rm DF}(\mathcal{E}, L_z)$, and combine it with the thermalized component, $f_0(\mathcal{E}, L_z)$, computed through, e.g., HQ method, to obtain the total DM distribution function:

$$f(\mathcal{E}, L_z) = f_0(\mathcal{E}, L_z) + f_{\rm DF}(\vec{x}, \vec{v}) \ , \tag{3.27}$$

Unfortunately, no such handle exists for treating DM streams, coming from ongoing or very recent tidal stripping of smaller objects. Since they became part of the host galaxy only very recently, their kinematic properties still closely resemble those they had in the accreted object, where DM and stars are expected to have significantly different distributions. Luckily, an only small fraction of DM is expected to be found in streams and can noticeably boost the direct detection signal only if these particles are passing through Earth with high velocities compared to the smooth DM component, while the effects on indirect detection are expected to be negligible. Possible new insights could come in the near future from precision astronomy, that might be able to discover ongoing disruptions of dwarf galaxies within Milky Way and provide us with accurate orbits of their tidal streams. Additional information regarding the properties of streams could also come from refined simulations, as their resolution increases sufficiently to resolve small accreted structures. Similarly, treating the DM distribution during the merging of galaxies with comparable masses or the perturbations induced by their flybys remains an open question.

3.2 Dark Matter in the Milky Way

One of the most direct observational motivations in favour of the DM hypothesis are the rotation curves of galaxies. This is equally true in the case of Milky Way, for which it has be established that a DM halo with local density of roughly $\rho_\odot \sim 0.005 - 0.02$ $\mathrm{M}_\odot$ pc^{-3} is needed to explain the observed circular velocities [12, 158, 195–201]. This has been independently confirmed by studies of vertical motion of stars in the solar neighborhood, however, often requiring values of $\rho_\odot$ at the upper limit of what has been inferred from rotation curve measurements [202–206]. Since in direct detection experiments the local DM density is linearly proportional with the expected nuclear recoil rate, its accurate determination plays an important role in establishing constraints on DM-nucleus cross-section. Good estimates of DM distribution are even more important in indirect searches, as the annihilation signal is proportional to the DM density squared and integrated along the line of sight. Furthermore, to construct realistic DM phase-space models, the determination of DM profile is

needed over the entire galaxy, since the HQ method, discussed in the previous section, relies on the knowledge of density-potential pair throughout the entire system. Recent observations provide us with data that makes it feasible to reconstruct the PSDF of galactic DM, which will be the main goal of this section.

I will begin by proving a short overview of recent studies addressing the rotation curve and vertical force field of Milky Way, which make use of the latest astronomical observations. Subsequently, I will use their results to perform the mass decomposition of our galaxy, with the goal of constraining DM density distribution and total gravitational potential, which are the essential quantities for determining the PSDF of galactic DM. These results will be essential for the next section, where the implications for direct detection experiments will be discussed.

3.2.1 Dynamical traces

In recent year we have witnessed drastic improvements in the quality of astronomical observations. These include: the second data release of the Gaia satellite [207], which provided us with accurate measurements of positions and proper motions of billions of stars within the galaxy; improved surveys of optical transients, such as OGLE-IV [208], capable of constraining the central galactic stellar density from microlensing events, as well as providing insights into galactic circular velocities through tracking of variable stars; a highly precise determination of solar galactocentric distance by the Gravity collaboration [209]; and many others. Therefore, it is timely to reassess the Milky Way mass composition by taking advantage of these new observations.

Galactic rotation curve

For the purpose of constraining the galactic DM content, the most interesting information comes from the measurements of circular velocities of stars and gas, which is related to the radial variation of the gravitational potential in the galactic plane:

$$V_c^2(R) = R \cdot \left.\frac{\partial \Psi_{\rm tot}(R,z)}{\partial R}\right|_{z=0} . \tag{3.28}$$

In light of recent observations, the most significant improvements come from precise determination of stellar velocities by the Gaia satellite, which mapped positions and proper motions of nearly a billion of stars within the Milky Way, and OGLE observations of variable Cepheid stars, whose brightness can be predicted from their periodicity and therefore serve as standard candles, allowing accurate distance determination. While these measurements mostly focus on galactocentric distances from few up to 25 kpc, somewhat older determinations of circular velocities from halo giant stars, which were mapped up to distances of 100 kpc by SDSS-III/SEGUE survey, play an equally important role. Finally, additional information can be gained from circular velocities of gas, masers, globular cluster and other tracers, which have accumulated throughout the literature in the last decades. The studies I chose to include in our analysis are:

- **Eilers et al. (2019)** [200]: The authors combine spectral data from APOGEE survey with photometric information from WISE, 2MASS, and

Gaia observations to derive the rotation curve based on 23000 red-giant stars at galactocentric distances between 5 and 25 kpc. Their analysis relies on solving the Jeans equation in the axisymmetric limit, assuming that stellar number density profile is given by $\nu(R) \propto \exp(-R/R_{\rm exp})$ with $R_{\rm exp} = 3$, while the radial and azimuthal velocity dispersions are estimated from ensemble averages in radial bins. For the solar galactocentric distance they adopt the recent determination of Gravity collaboration [209], $R_\odot = 8.122$ kpc, while for the peculiar velocity of the Sun they assume the standard values $(U, V, W) = (-11.1, 245.8, 7.8)$ km/s [210]. In the axisymmetric Jeans equation, they neglect the tilt term, which according to their estimate induces a systematic uncertainty of $\sim 1\%$. The main contribution to the systematic error arises from the assumed $\nu(R)$; they estimate it to be $\sim 2\%$ when varying $R_{\rm exp}$ by 30% and roughly $\sim 3\%$ when substituting the exponential profile with a power law. Other systematic errors (namely deviations from axisymmetry, assumed $R_\odot$ and peculiar motion of the Sun) are claimed to play only a minor role and are estimated to $\lesssim 1\%$. In total they estimate the systematic errors to be $\sim 2-5\%$ at galactocentric distances $5-20$ kpc, while they become significantly larger at $R \gtrsim 20$ kpc due to an insufficient number of stars.

- **Mroz et al. (2019)** [211]: The authors use OGLE observations of 773 Classical Cepheids coupled with radial velocities determined by Gaia to obtain rotation curve for galactocentric distances from 5 to 20 kpc. They perform Bayesian likelihood analysis, constraining three possible parameterizations of the rotation curve: *i*) constant circular velocity, $V_c(R) = V_{c,0}$, *ii*) linearly varying rotation curve, $V_c(R) = V_{c,\odot} + dV_c/dR(R_\odot)\cdot(R - R_\odot)$ and *iii*) Persic model [10]. For the peculiar motion of the Sun and its galactocentric distance they adopt Gaussian priors with $(U_\odot, V_\odot, W_\odot) = (-11.1 \pm 1.3, 12.2 \pm 2.1, 7.3 \pm 1.3)$ km/s [210] and $R_\odot = 8.122 \pm 0.031$ kpc [209], that is consistent with the choice of Eilers et al.. They find that $V_c(R) = V_{c,0}$ model provides significantly worse fit then the other two models. While the Persic's model gives slightly better fit then the linear approximation, the authors note that it is inconsistent with previous results of Soufe et al. [212] at small R. Therefore, they adopt the median values of $R_\odot, V_c(R_\odot)$ from the linear model to construct the final rotation curve of the Chepeids. They consistently propagate the uncertainties sourced by peculiar (non-circular) motions of stars and their distance measurements, however, do not comment on other possible sources of systematics.

- **Huang et al. (2016)** [213]: The authors derive the rotation curve out to ~ 100 kpc using 6000 primary red clump giants (PRCGs) in the outer disk, selected from the LAMOST Spectroscopic Survey of the Galactic Anticentre (LSS-GAC) and the Sloan Digital Sky Survey (SDSS)-III/APOGEE survey, combined with 5700 halo K giants (HKGs), selected from the SDSS-III/SEGUE survey. For PRCGs, covering the range from 8 to 17 kpc, they use Oort-like modelling that includes asymmetric drift correction [145] and perform Bayesian likelihood analysis. Possible systematics arise due to the choice of solar galactocentric distance, $R_\odot = 8.34 \pm 0.16$ kpc, and azimuthal velocity, $V_{\phi,\odot}/R_\odot = 30.24 \pm 0.11$ km s^{-1} kpc^{-1}, as

well as in modelling asymmetric drift due to uncertainties and assumptions regarding azimuthal and radial velocity dispersions and disk scale length, however, they estimate all of these effects amount to errors $\lesssim 2\%$. For HKGs, spanning the range between 8 and 100 kpc, they adopt spherical Jeans modelling, assuming broken power-law for stellar distribution, parametric form for the radial velocity dispersion (including Dehnen's correction [214]) and adopting particular values of orbital anisotropy. They estimate the systematics coming from the power-law slope of the HKGs number densities to be $\sim 10\%$, while they only comment on possible further systematics due to distinct halo populations, deviations from spherical symmetry and choices of orbital anisotropy, without addressing them quantitatively. While these uncertainties are significantly larger than the ones associated with PRCGs (and other works discussed above), they none-the-less provide highly valuable information regarding large galactocentric distance, which is crucial for bracketing the DM content of the Milky Way.

- **Galkin (1978-2013)** [215]: Compilation of circular velocities, as inferred from 25 different studies, based on various tracers, ranging from stars, gas, masers and globular clusters. The provided data covers the galactocentric distances between 2 and 20 kpc and can be simply rescaled to the preferred value of solar distance and peculiar motion, which were often chosen differently in the original studies. While most of the included surveys are somewhat older and come with relatively large errors, they all together still provide valuable input due to the diversity of available tracers.

While Eilers et al. and Huang et al. provide binned data, Mroz et al. estimate V_c for each star separately and, therefore, has to be binned to be on the same footing as the other two studies. I also chose to bin the Galkin data, since the complete compilation contains more than 2700 data points and includes surveys with uncompetitively large error bars. To perform the binning, I split the relevant datasets in $\sqrt{N}$ bins, where N is the total number of points, chosen such that each bin contains the same number of elements, and computed the median, 16th and 84th percentile of each bin, as the corresponding central value and its standard deviations. Comparison of the discussed rotation curves can be found in figure 3.10.

Vertical motion of stars

The vertical motion of stars has been long known to provide a powerful tool for constraining the amount of DM in the solar neighbourhood. Most analyses rely on the Jeans modelling, introduced in section 2.1.1, recast in the galactic cylindrical coordinates. By focusing only on the vertical direction (i.e. perpendicular to the disk), the following relation can be obtained:

$$\frac{1}{\nu}\frac{\partial}{\partial z}(\nu\sigma_z^2) + \frac{1}{R\nu}\frac{\partial}{\partial R}\left(R\nu\sigma_{Rz}^2\right) = \frac{\partial\Psi_{\rm tot}(R,z)}{\partial z}\ , \tag{3.29}$$

where $\nu(R,z)$ is the number density of the tracer stars and $\sigma_z(R,z)$ is their velocity dispersion along the vertical axis. As can be seen by comparing equations (3.28) and (3.29), the observations of circular velocity and vertical motion

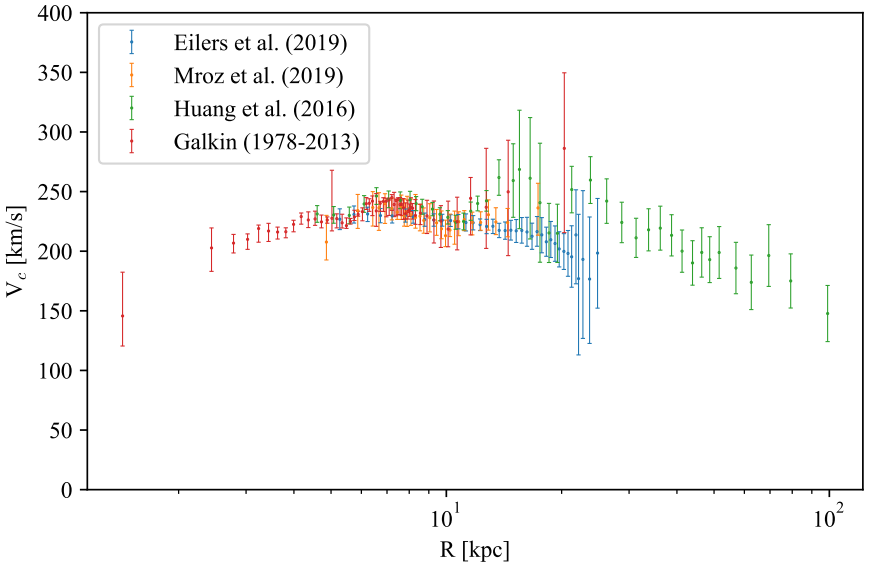

Figure 3.10: Circular velocity as a function of galactocentric distance within the Milky Way, as inferred by various studies used in this work.

of stars probe the galactic gravitational potential, $\Psi_{\rm tot}(R, z)$, in orthogonal directions, as the former is proportional to its derivative along the $\hat{R}$ and the latter along $\hat{z}$ coordinate, and, therefore, provide complementary information. In particular, the vertical motion is very useful in breaking the degeneracy between spherically symmetric and flattened mass components that typically occurs when relying only on rotation curve data. There have been several recent studies, focusing on the thin stellar populations [205, 206] that span up to few hundred pc above the disk, as well as thick populations [203,204] that probe the galactic potential up to $z \approx 1.5$ kpc. In our work we chose to use the findings of Hagen & Helmi [204], since their results are largely consistent with previous works, but also directly provide the inferred vertical force $K_z(z) = \partial\Psi_{\rm tot}/\partial z$. On the other hand, I chose not to include the studies focused on thin disk only, since they are somewhat controversial, finding evidence for an additional highly flattened component, which is speculated to be either underestimated gas disk or dark disk, but could also be due to departure from equilibrium, e.g. perturbations of the disk that were recently discovered by Gaia satellite [216–218].

An alternative approach of studying the vertical force is to use the full 6D stellar phase-space information. This has been done by Bovy & Rix [202], where they derived $K_z(z = 1.1$ kpc) at various galactocentric radii in the range from $4-9$ kpc. Their analysis assumes that each mono-abundance population of stars (i.e. the population of stars characterized by given [Fe/H] and [α/Fe]) follows a quasi-isothermal distribution function (qDF) based on action-angle modelling, where the latter was briefly introduced in section 3.1.1. They perform an elaborate fitting of the qDF parameters in several sample gravitational potentials for 43 distinct mono-abundance stellar populations and for each of them they derive $K_z(z = 1.1$ kpc), (as well as the stellar surface density within 1.1 kpc)

at specific galactocentric radius, where the uncertainty is expected to be the smallest. Similarly, the choice of $z = 1.1$ kpc is driven by the fact that it represents the mode of stellar mid-plane-distance in the dataset and, therefore, the latter should be the most constraining at that value of z. This allows them to derive 43 distinct measurements of $K_z(z = 1.1 \text{ kpc})$ at various R with rather high accuracy. Possible systematic errors are discussed in detail; they conclude that their estimates are robust against the changes of the gravitational potential, namely rotation curve normalization $V_c(R_\odot)$ and its deviation from flatness ($\partial V_c/\partial R \neq 0$), as well as changes in the assumed disk scale hight. They also remove the dependence of their results on the choice of solar galactocentric distance $R_\odot$ by providing their results in terms of $\tilde{R} = R - R_\odot$.

The final compilation of $K_z(R, z)$ measurements used in the analysis is shown in figure 3.11. As already mentioned, these measurements do not drive the constraints on galactic DM distribution, but rather serve as additional information to break the degeneracy between disk and DM mass.

Other constraints

Additional constraints might come from other studies, such as the estimates of galactic escape velocities [219–221], motions of globular clusters and Milky Way satellites [222–226] or estimates of virial mass calibrated against numerical simulations [227]. On the other hand, these constraints are typically less stringent then the circular velocity measurements and implicitly depend on the galactic mass modelling. Therefore, I restrain from using them in the analysis, while I explicitly checked that the obtained results are consistent also with these measurements.

3.2.2 Galactic mass decomposition

The presence of DM has so far been inferred only through its gravitational effects, which are essential also for determining its galactic distribution. In the non-relativistic limit, which is well justified when addressing galactic dynamics, the gravitational potential of the system is related to the underlying matter density through the Poisson's equation. Since the latter is linear in density, the Laplacian of total gravitational potential can be written as a sum of density distributions of various galactic components:

$$\nabla^2 \Psi_{\text{tot}}(\vec{r}) = -4\pi G \sum_i \rho_i(\vec{r}) \,, \tag{3.30}$$

and represents the fundamental equation in galactic mass decomposition. The total potential, as discussed in the previous section, as well as the density distribution of baryonic matter, can be constrained by independent observations, which in turn also allow constraining the unknown DM distribution. In practice, precise determination of baryonic mass turns out problematic, and one can directly constrain only the morphology of its distribution, while the overall normalizations need to be fit along with the DM distribution, to correctly reproduce the observables related to the gravitational potential, such as galactic rotation curve and vertical motion of stars.

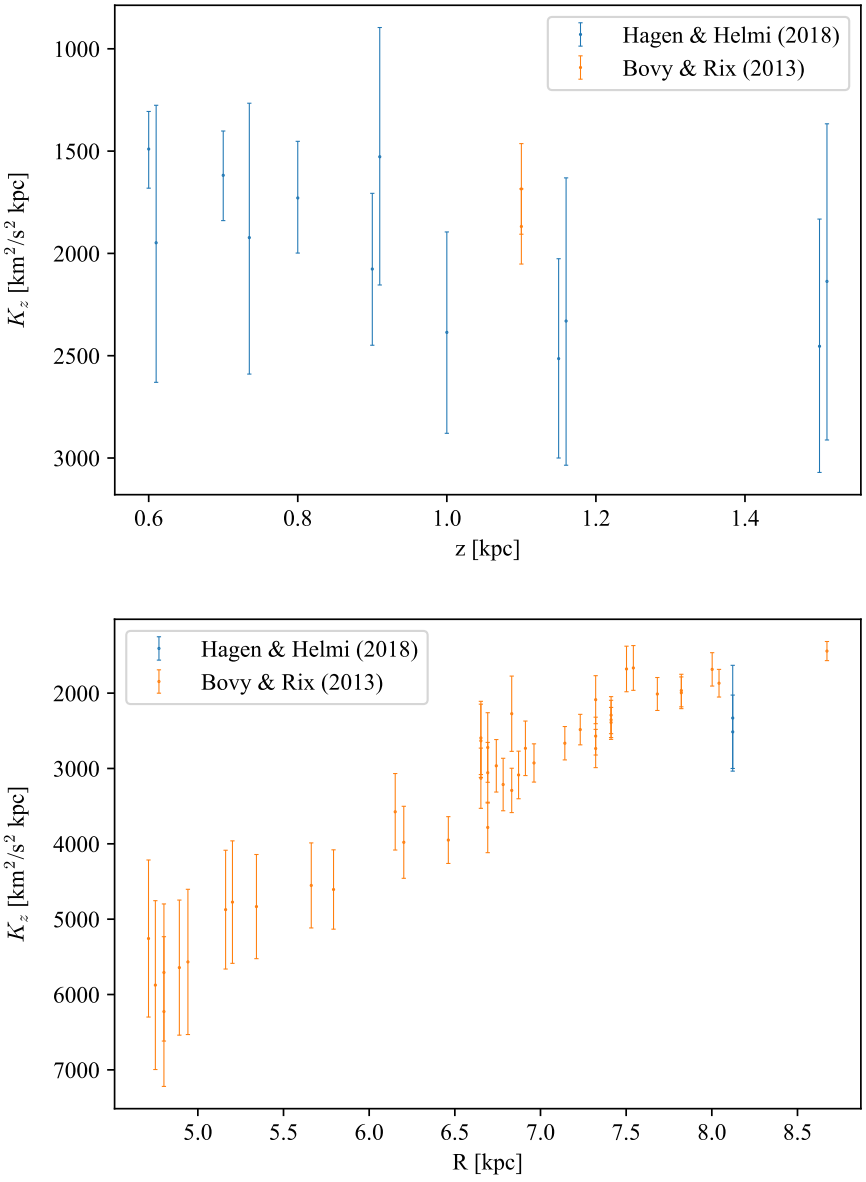

Figure 3.11: Vertical force estimates as a function of height above the galactic midplane at $R \sim R_\odot$ (above) and as a function of radial distance at $z \sim 1.1$ kpc (below).

Baryonic modelling

Despite significant improvements in observational data, the distribution of baryons within the Milky Way is still subjected to large uncertainties. This is mainly due to the fact that we are viewing our own galaxy from within, which makes it hard to resolve the extent and precise shape of the stellar disks, but also its central structure. In the following, I will shortly review the current status and describe the simplified modelling used in my analysis – for more complete works on the topic see, e.g., [228, 229] and references therein.

The galactic bulge has been often approximated by spheroidal power-law distribution, flattened along the central axis, with exponential truncation in the outskirts. Since truncation radius has been estimated to lie at $r_{\rm trunc} \approx 1.8$ kpc, which is below the innermost reliable measurements of the galactic rotation curve, the exact details of its morphology are not important for the analysis at hand. Therefore, in the attempt to marginalize over the baryonic uncertainties I will simply assume that its potential corresponds to the Hernquist ansatz, given in equation (3.12), with appropriately small scale radius, i.e. $a_d \lesssim 1$ kpc. Regarding its mass, the situation is slightly better, however, still significant uncertainties are present due to its overlap with galactic disks. One of the strongest constraints come from microlensing observations of stars, performed by OGLE survey, which is capable of estimating the optical depth that can serve as a proxy of its total mass. Most of the recent studies point towards $M_b \sim 1.4{-}1.8{\cdot}10^{10} M_\odot$, which however includes also the disk stars, and therefore smaller masses, e.g. $M_b \sim 8.9 \cdot 10^9 M_\odot$ in [158], have been often assumed in combination with appropriate disk models. For this reasons I will only use an upper prior on the bulge mass, i.e. $M_b \leq 1.8 \cdot 10^{10} M_\odot$ and fix its scale length to $a_b = 0.5$ kpc.

Regarding the galactic disks, there are several caveats, which again makes it hard to draw strong conclusions. Throughout the literature, presence of thin and thick disk was often assumed, both having a double exponential profile:

$$\rho_{\rm disk} = \frac{\Sigma_0}{2 z_d} \exp\left(-\frac{R}{R_d} - \frac{|z|}{z_d} \right) , \tag{3.31}$$

where R_d and z_d are the scale length and scale hight, while Σ_0 is corresponding surface density. The thick disk was believed to have $z_d \approx 0.9$ kpc and smaller-scale length, $R_d \approx 2.5$ kpc, while the thick disk was often modelled as having $z_d \approx 0.3$ kpc and $R_d \approx 3.5$ kpc. The ratio between their surface densities was estimated as $f_\Sigma \sim 0.12$ (with rather large uncertainties due to their overlap), with the thin disk being the dominant one. These definitions of galactic disks were based on morphological and/or kinematic properties. However, recent studies have shown it is more appropriate to talk about disks composed of α-rich and α-poor stars. Unfortunately, these new definitions are largely inconsistent with the traditional interpretation, as in light of the new data both of the disks have roughly the same mass. The observed α-rich is significantly thicker, $z_d \sim 1$ kpc, and can be traced up to the solar radius, while α-poor disk has a larger, but poorly constrained, radial extent and varying height, with $z_d \sim 0.3$ in the central part and slowly increasing towards the outskirts where it "flares" and reaches thickness comparable or even greater then the α-rich disk. Furthermore, it has been pointed out by several authors that even further distinctions can be made by looking at other element ratios within the stars. Due

to the lack of a coherent picture and well-constrained disk parameters I chose to model the galactic disk, in which I also include the subdominant gas, as a single Myiamoto-Nagai component, whose potential can be written analytically, see equation (3.11). The validity of such modelling is supported by noticing that combining several exponential disks (whose potential needs to be computed numerically and are therefore quite computationally expensive) with various scale lengths leads to a total potential, which can be fairly well approximated with the MN expression [1]. Furthermore, since in this work I am primarily interested in bracketing the uncertainties related to the DM distribution, such modelling performs sufficiently well in marginalizing over the baryonic uncertainties. For these reasons I will only make use of conservative mass estimate on the total disk mass, $10^{10} M_\odot < M_{\rm disk} < 1.5 \cdot 10^{11} M_\odot$, as well as its scale length and scale height, $a_{\rm disk} < 5$ kpc and $b_{\rm disk} < 1.5$ kpc.

Bayesian analysis

In order to constrain the DM distribution within the Milky Way, I used the Bayesian approach based on Monte Carlo Markov Chain (MCMC) exploration of the parameter space, given the set of observations constraining the total gravitational potential of the galaxy. For baryonic modelling, a combination of Hernquist potential (3.12), describing the bulge, and MN potential (3.11), approximating the stellar disks and galactic gas, was used, as discussed above. On the other hand, for the DM, I assumed two different phenomenologically motivated density profiles, namely the cuspy NFW profile [155]:

$$\rho_{\rm NFW}(r) = \frac{\rho_s}{r/r_s(1+r/r_s)^2} \ , \tag{3.32}$$

and cored Burkert profile [230]:

$$\rho_{\rm BUR}(r) = \frac{\rho_s}{(1+r/r_s)(1+r^2/r_s^2)} \ , \tag{3.33}$$

where ρ_s and r_s are the corresponding scale densities and radii. While in general also a spheroidal realization of the DM halo could be considered, as was done in section 3.1.2, there exists compelling new evidence that Milky Way's halo is close to spherical at the relevant galactocentric distances [161, 231] and, therefore, spheroidal generalizations of the above DM densities will not be considered, as they are much more demanding from the computational point of view, since the corresponding potentials need to be evaluated numerically. Such modelling of the Milky Way in total contains 6 free parameters, namely:

$$\vec{\theta} = \{M_b, M_d, a_d, b_d, \rho_s, r_s\} \ , \tag{3.34}$$

where the first four are related to the baryonic distribution that we wish to marginalized over, while the last two describe the DM density profile. For all the parameters describing baryonic distributions I use broad non-informative (i.e.

[1] I explicitly checked that for the combination of exponential thin and thick disk, that were traditionally used within the literature, a Miyamoto-Nagai approximation of the total gravitational potential could be found, which deviates less then 15% from the true one for any value of R and z. An even better match can be found by restricting to $R \gtrsim 2$ kpc, which is the relevant range for present analysis.

flat) priors, which can be safely established according to the existing literature, as described above (for a more comprehensive review see, e.g., [228]):

$$\begin{aligned} 0 \leq \quad & M_b \quad \leq 1.8 \cdot 10^{10} M_\odot \ , \\ 10^{10} M_\odot \leq \quad & M_d \quad \leq 1.5 \cdot 10^{11} M_\odot \ , \\ 1 \text{ kpc} \leq \quad & a_d \quad \leq 5 \text{ kpc} \ , \\ 0.1 \text{ kpc} \leq \quad & b_d \quad \leq 1.5 \text{ kpc} \ . \end{aligned} \tag{3.35}$$

On the other hand, for DM parameters I used the most generous range of priors, i.e. demanding $\rho_s, r_s > 0$ and imposed that the scale radius is within the range of data, namely $r_s \leq 100$ kpc, since for larger values it becomes fully degenerate with ρ_s. Additionally, the scale density was sampled in the logarithmic space, expressed in terms of variable $\tilde{\rho}_s \equiv \log_{10}\left(\rho_s / M_\odot \text{pc}^{-3}\right)$. The analysis was then performed using the following likelihood function:

$$\begin{aligned} \mathcal{L}_{\text{MW}} \equiv & \prod_{k=1}^{\text{N}_{V_c}} \frac{1}{\sqrt{2\pi}\,\sigma^{\pm}_{V_c,k}} \exp\left[-\frac{1}{2} \left(\frac{V_{c,k} - V_c(R_k;\vec{\theta})}{\sigma^{\pm}_{V_c,k}} \right)^2 \right] \\ & \cdot \prod_{l=1}^{\text{N}_{K_z}} \frac{1}{\sqrt{2\pi}\,\sigma^{\pm}_{K_z,l}} \exp\left[-\frac{1}{2} \left(\frac{K_{z,l} - K_z(R_l, z_l;\vec{\theta})}{\sigma^{\pm}_{K_z,l}} \right)^2 \right] \ , \end{aligned} \tag{3.36}$$

where $V_{c,i}$ (K_z, i) are the binned rotation curve (vertical force) measurements, with total of N_{V_c} (N_{K_z}) points, and $\sigma^{\pm}_{V_c,i}$ ($\sigma^{\pm}_{K_z,i}$) the corresponding upper/lower standard deviations, while $V_c(R_i;\vec{\theta})$ ($K_z(R_i, z_i;\vec{\theta})$) are the predictions of our model at the radial distance of the bin R_i (and its vertical height z_i), given parameters $\vec{\theta}$. For the exploration of parameter space I used a Python implementation of Goodman & Weare's affine invariant MCMC Ensemble sampler, delivered in *emcee* package [232]. The sampling was done using 200 walkers, where each of them evolved for 20000 steps. The first half of each chain was discarded as part of burn-in period.

The resulting posterior distributions of the parameters, as well as their pairwise correlations, for the two considered DM profiles are presented in figure 3.12. The results give a good fit to the data, as can be seen in figure 3.13 for NFW and 3.14 for Burkert case. The latter shows a preference for somewhat larger disk mass, while the rest of baryonic parameters show reasonable agreement and fall within the inferred uncertainties. The corresponding DM parameters match fairly well with the results of other recent studies, see, e.g., [12, 158, 200, 201], establishing the following local DM densities for the two considered parametric profiles:

$$\rho_{\text{NFW}}(R_\odot) = 7.4^{+1.3}_{-1.3} \cdot 10^{-3} \ M_\odot/\text{pc}^3 \ , \tag{3.37}$$

$$\rho_{\text{BUR}}(R_\odot) = 5.0^{+1.7}_{-1.1} \cdot 10^{-3} \ M_\odot/\text{pc}^3 \ . \tag{3.38}$$

The derived values are somewhat lower with respect to the ones found in older studies, see, e.g., [195, 196, 198, 199], which is most probably driven by recent measurements of circular velocity that systematically yield lower and faster declining $V_c(R)$, as can also been seen from figure 3.10. Furthermore, the local DM

density inferred solely from rotation curve measurements can be significantly affected by the assumptions regarding the baryonic modelling, as pointed out in [201]. On the other hand, in our study we additionally make use of vertical force measurements, which together with latest determinations of $V_c(R)$ lead to baryonic modelling that agrees fairly well with recent galactic microlensing observations [233], pointing towards the "maximal disk" in Milky Way. The inferred baryonic parameters are also in good agreement with the modelling suggested by [234] on the basis of recent observations of galactic stellar populations.

3.3 Implications for the direct detection

Direct detection (DD) experiments provide a unique probe of a possible coupling between baryons and DM. As already described in section 1.2.3, the key idea is to measure nuclear recoils in target materials that are caused by scattering with the galactic DM. Unlike indirect detection, they are performed in controlled laboratory setups and, therefore, subjected to significantly smaller uncertainties due to possible backgrounds. Consequently, for a fixed particle physics model, they provide robust bounds on the interaction rate between DM and nucleons, where typically the largest source of uncertainty is the local DM density and its velocity distribution. For this reason, precise modelling of galactic DM phase-space distribution is crucial for accurate interpretation of experimental results and legitimate exclusion of relevant parts of the parameter space in various DM models. Furthermore, it was recently recognized that different velocity dependences of the scattering operators might arise in the effective non-relativistic description of DM-nucleon scattering, additionally motivating the need for accurate modelling of the DM velocity distribution. As of now, most of the DD experiments still cite their results on DM-nucleon cross-section assuming truncated Maxwell-Boltzmann velocity distribution, however, the latter, as well as approximations based on other spherically symmetric models [147, 235–238], are most likely a poor approximation of the actual DM velocity distribution in disk galaxies, as was shown in the comparison with a axisymmetric modelling of a sample disk galaxy in section 3.1.2. To overcome this issue, several recent works suggested a halo-independent approach [239–242], expressing the DD constraints as a product of the relevant cross-section times astrophysical factor, which must be common to all the experiments, or by modelling DM velocity distribution as a sum of streams [243–245] that minimize/maximize the astrophysical factors. While such techniques are fruitful in comparing possible tensions among various DD experiments, they are not suitable for providing the most stringent constraints on the DM-nucleon cross-section, since they do not use the full power of astronomical observations that provide us with the information regarding DM velocity distribution. In this work, I consider an alternative approach, where a refined PSDF is invoked to describe the DM distribution and carefully calibrated against the observables constraining dynamics within the Milky Way.

In the following, I will first briefly review the theory behind hypothetical DM-nucleon scattering, starting with the standard spin-independent and spin-dependent cases and then turn my attention to the full set of possible non-relativistic effective operators. This will be followed by a comparison of limits on different DM-nucleus couplings, marginalized over the uncertainties related

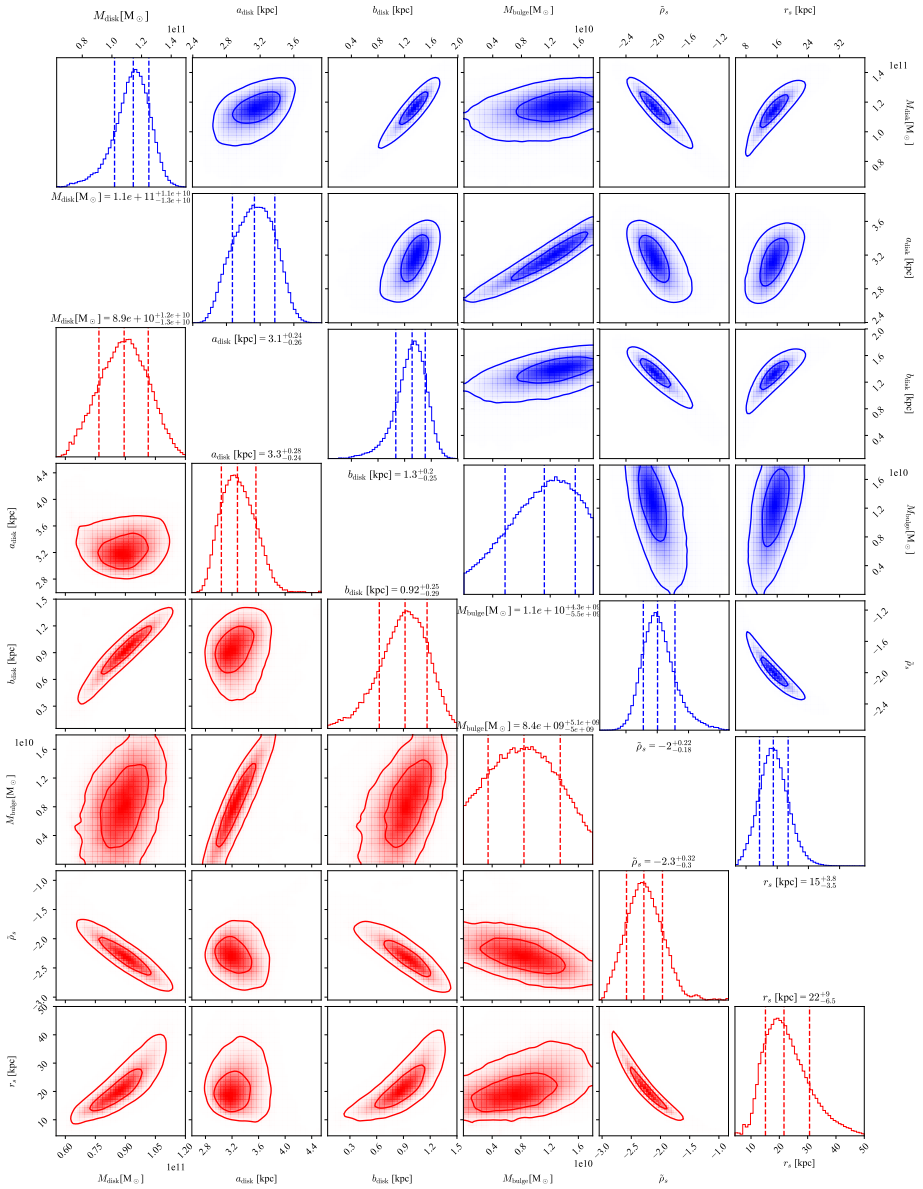

Figure 3.12: Single parameter posterior distributions and their pairwise correlations as obtained in the MCMC sampling for NFW (red) and Burkert (blue) DM density profile. The vertical lines in the posteriors mark median as well the 68% h.p.d. interval, while the contours correspond to 68% and 95% h.p.d. regions.

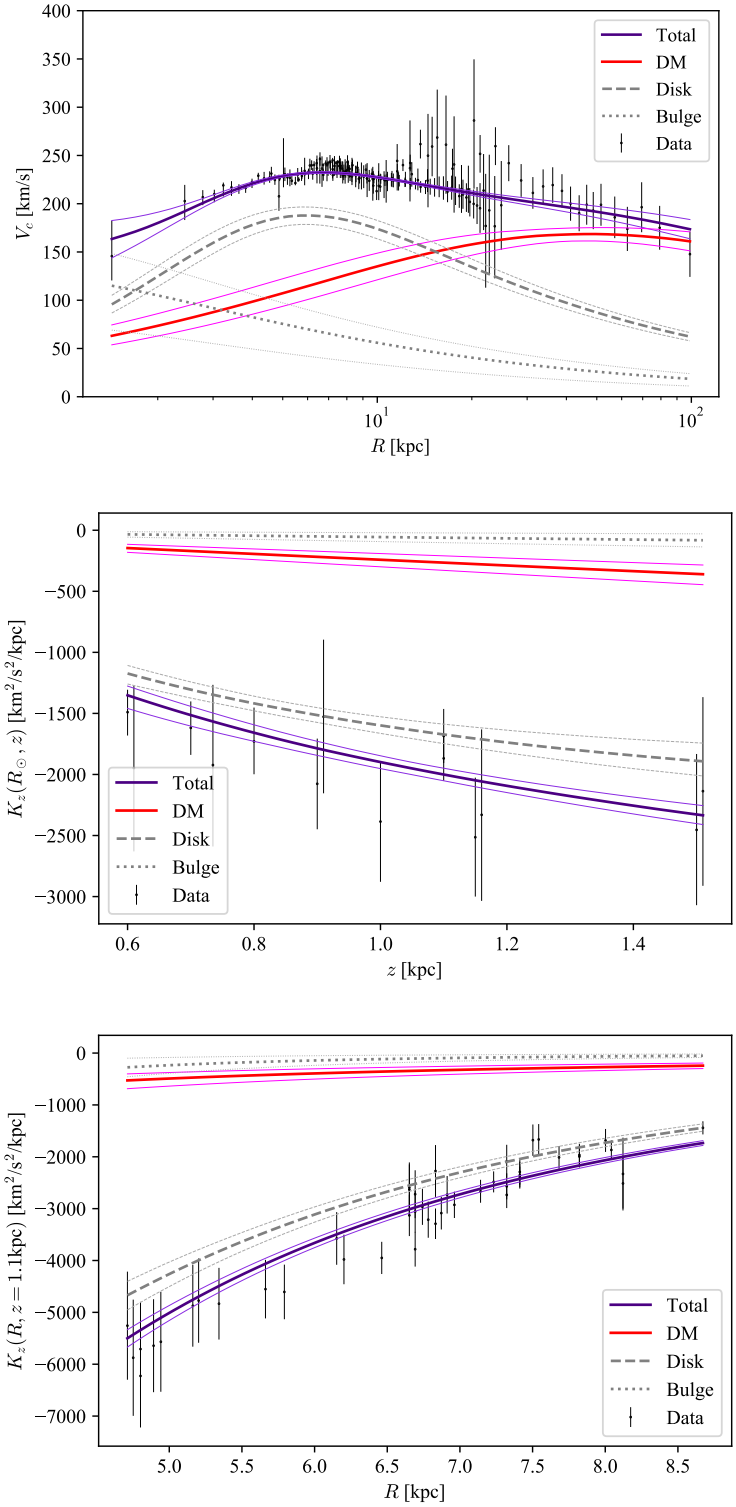

Figure 3.13: Observational data and the corresponding posterior distributions obtained in the MCMC sampling of the galactic model with NFW DM density profile. The thin lines correspond to 68% h.p.d. region.

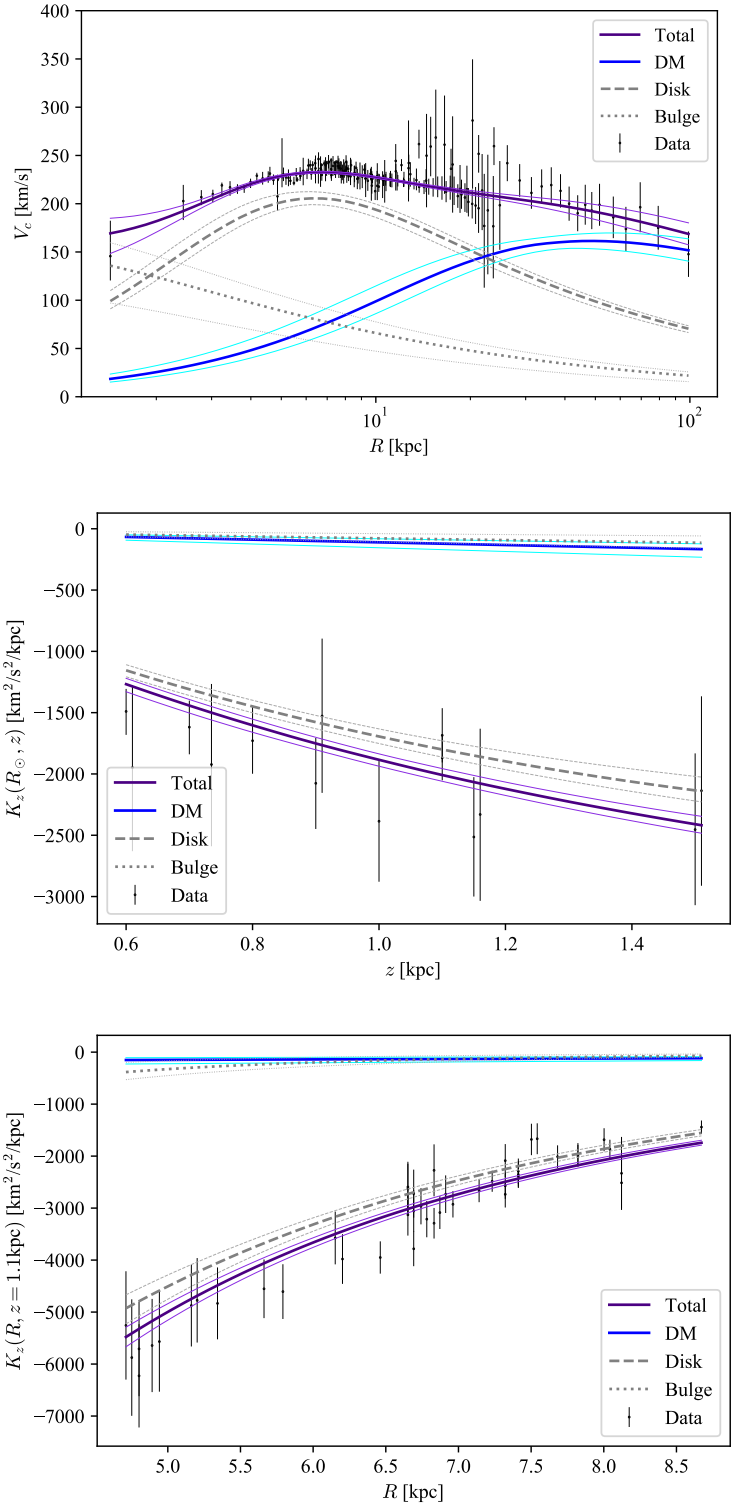

Figure 3.14: Observational data and the corresponding posterior distributions obtained in the MCMC sampling of the galactic model with Burkert DM density profile. The thin lines correspond to 68% h.p.d. region.

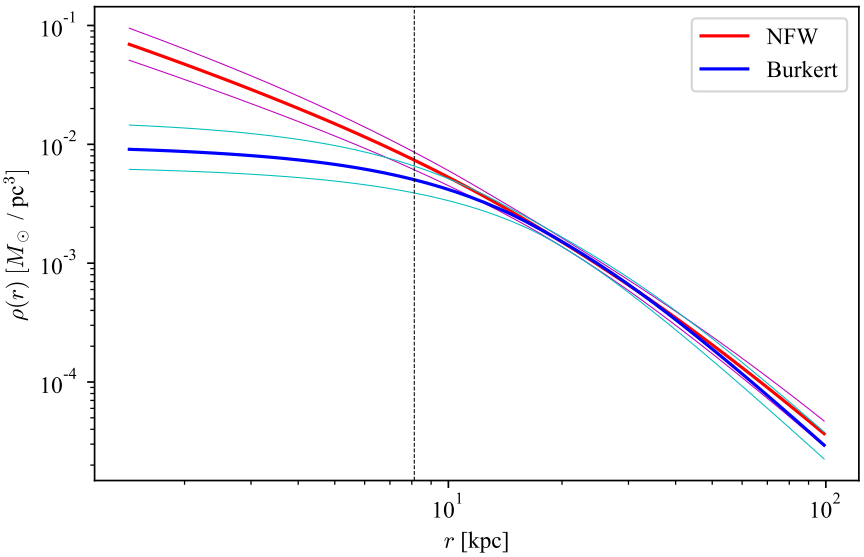

Figure 3.15: The inferred DM density as a function of galactocentric distance with its 68% h.p.d. interval. The vertical dashed line marks the solar distance $R_\odot$.

to the DM distribution. Finally, I will comment on implications for the annual signal modulation, which is a characteristic signature of DM induced interactions and exhibits a particularly strong dependence on the galactic DM velocity distribution.

3.3.1 DM-nucleon scattering

It seems reasonable to assume that at some level baryons couple to DM, possibly leading to detectable nuclear recoil rates in direct detection experiments. Due to their relatively cheap design, at least compared to colliders or satellite missions, numerous highly sensitive detectors have been constructed, which are capable of probing DM-nucleus cross-sections as small as 10^{-47}cm^2 for spin-independent interactions, while for spin-dependent cross-section the bound is only a few orders of magnitude weaker. Consequently, the absence of undisputed detections of DM induced events puts stringent limits on various phenomenological DM models and motivates the exploration of alternative scenarios, where leading order velocity independent cross-sections are parametrically suppressed or absent.

In the following, I will briefly review the standard lore of DM-nucleon scattering, which assumes that the leading order interactions are mediated either through spin-independent (SI) or spin-dependent (SD) operators. However, these do not exhaust all the possibilities, and other conceivable operators exist, which can become important in the absence of strong parametric suppression of the SI and SD interactions. It has been recently recognized that in the non-relativistic limit of elastic scattering a total of 16 distinct effective operators can arise up to the quadratic order in the momentum transfer and scattering

velocity. While their derivation is rather a laborious task, I will only provide a brief overview and discuss their implications.

Spin (in)dependent cross-section

Elastic scattering of DM on target nuclei is commonly assumed to be mediated through either SI or SD interactions, depending on the microphysics of the DM candidate. In general, one can write the interaction term of the Lagrangian as:

$$\mathcal{L}_{\rm int} = \lambda_q(\bar{\chi}\Gamma^\alpha\chi)(\bar{q}\Gamma_\alpha q) \ , \tag{3.39}$$

where λ_q is the relevant quark coupling constant, χ is the DM field and q the relevant quark field to which it couples, while Γ^α is the appropriate 4×4 matrix corresponding to the interaction, namely $\mathbb{1}_4$ (γ^μ) in case of SI interactions mediated by scalar (or vector) particle and $\gamma^\mu\gamma_5$ for SD interactions mediated by pseudo-vector particle. While in general also other Γ^α can appear, they are typically velocity or mass suppressed and only relevant in case of vanishing SI or SD interactions. The scattering matrix element can be obtained by inserting $\mathcal{L}_{\rm int}$ between the initial and final states:

$$\begin{aligned}\mathcal{M} &= \lambda_q \ \langle\chi_f; A_f|\ (\bar{\chi}\Gamma^\alpha\chi)(\bar{q}\Gamma_\alpha q)\ |\chi_i; A_i\rangle \\ &= \lambda_q \ \langle\chi_f|\ \bar{\chi}\Gamma^\alpha\chi\ |\chi\rangle\ \langle A_f|\langle N_f|\ \bar{q}\Gamma_\alpha q\ |N_i\rangle|A_i\rangle\end{aligned} \tag{3.40}$$

where $|A_{i/f}\rangle$ is the relevant nucleus states build from nucleon states $|N_{i/f}\rangle$. Using the explicit expression for Dirac spinors and applying the non-relativistic limit, in which $\vec{p} \ll p^0 \approx m$, one can show that:

$$\bar{u}^r(p)u^s(p) = 2m\ \delta_{r,s} \ , \tag{3.41}$$

$$\bar{u}^r(p)\gamma^\mu u^s(p) \approx 2m\ \delta_{0,\mu}\ \delta_{r,s} \ , \tag{3.42}$$

$$\bar{u}^r(p)\gamma^\mu\gamma_5 u^s(p) = 4m\ s^i\ \delta_{\mu,i}\ \delta_{r,s} \ . \tag{3.43}$$

where m is the particle mass and $\vec{s}$ its spin. From the above expressions it is clear that in the first two cases the resulting matrix element must be spin independent, while for pseudo-vector it depends on particle spins. The first bra-ket term in equation (3.40) can therefore be written as:

$$\langle\chi_f|\bar{\chi}\Gamma^\mu\chi|\chi_i\rangle = \begin{cases} 2m_\chi \ ; & \Gamma^\mu = \mathbb{1} \\ 2m_\chi\ \delta_{0,\mu}\ ; & \Gamma^\mu = \gamma^\mu \\ 2m_\chi\langle\vec{S}_\chi\rangle\delta_{\mu,i}\ ; & \Gamma^\mu = \gamma^\mu\gamma_5 \end{cases} , \tag{3.44}$$

where n_χ is the DM number density and $\langle S^i_\chi\rangle$ its spin expectation value,

The nuclear part of the computation is somewhat more complicated. In the zero momentum transfer limit, i.e. $q = p_{\chi,f} - p_{\chi,i} \to 0$, one can show that in the scalar and axial case one simply gets a coherent scattering on all nucleons, while for pseudo-vector case it depends on the spin structure of the nucleus:

$$\langle A_f|\langle N_f|\ \bar{q}\Gamma_\mu q\ |N_i\rangle|A_i\rangle = \begin{cases} [Zf_p + (A-Z)f_n]\ \bar{A}A\ ; & \Gamma_\mu = \mathbb{1} \\ [Zf_p + (A-Z)f_n]\ \bar{A}\gamma_\mu A\ ; & \Gamma_\mu = \gamma_\mu \\ \left[a_p\langle\vec{S}_p\rangle + a_n\langle\vec{S}_n\rangle\right]\ |\vec{J}|^{-1}\langle A_f|J^i|A_i\rangle\ \delta_{\mu,i}\ ; & \Gamma_\mu = \gamma_\mu\gamma_5 \end{cases} \tag{3.45}$$

In the above expression Z and A are the atomic and mass numbers of the nucleus, while f_p and f_n are the appropriate combinations of quark coupling constants. In the expression for axial interaction $a_{p/n}$ are constants determined from the nuclear spin structure, $\langle \vec{S}_{p/n} \rangle$ the expected values of the spin content of the protons/nucleons in the nucleus and $\vec{J}$ is the total angular momentum of the nucleus. This lead to the standard SI and SD cross-sections in the zero momentum transfer, i.e. $q = 0$, limit:

$$\tilde{\sigma}^{\rm SI}_{A\chi} = \frac{4\mu^2_{A\chi}}{\pi}[Z f_p + (A-Z) f_n]^2 \,, \tag{3.46}$$

$$\tilde{\sigma}^{\rm SD}_{A\chi} = \frac{16\mu^2_{A\chi}}{\pi}\frac{J+1}{J}[a_p\langle \vec{S}_p \rangle + a_n \langle \vec{S}_n \rangle]^2 \,, \tag{3.47}$$

where $\mu_{A\chi}$ is the reduced DM-nucleus mass. To account for non-zero momentum transfer one needs to correct the above cross-section by the appropriate form factors $|F(E_r)|^2$. In the case of SI scattering, they can be simply approximated by an exponential [246]:

$$|F_{\rm SI}(E_r)|^2 = \exp(-E_r/E_0) \quad \text{where} \quad E_0 = \frac{3}{2m_A R_0^2} \,. \tag{3.48}$$

Above m_A is the nucleus mass, while R_0 is its effective size. For SD interactions the form factors take more complicated form and need to be computed from nuclear shell models. Combining everything together one finds:

$$\frac{d\sigma^{\rm SI}_{A\chi}}{dE_r} = \frac{m_A \tilde{\sigma}^{\rm SI}_{A\chi}}{2v^2\mu^2_{A\chi}}|F_{\rm SI}(E_r)|^2 \,, \tag{3.49}$$

$$\frac{d\sigma^{\rm SD}_{A\chi}}{dE_r} = \frac{m_A \tilde{\sigma}^{\rm SD}_{A\chi}}{2v^2\mu^2_{A\chi}}|F_{\rm SD}(E_r)|^2 \,, \tag{3.50}$$

where v is the magnitude of DM-nucleus relative velocity and $\mu_{A\chi}$ is the DM-nucleus reduced mass:

$$\mu_{A\chi} = \frac{m_A\, m_\chi}{m_A + m_\chi} \,. \tag{3.51}$$

Complete set of effective operators

The SI and SD interactions, discussed above, are usually expected to be the leading order terms in DM-nucleus scattering. This is motivated by the fact that other operators vanish in the limit of zero momentum transfer. However, they can become the leading order terms if the SI and SD cross-sections are parametrically suppressed or vanish. This can occur, e.g., in models where DM is a Majorana fermion coupled through anapole moment to a massive dark photon field A'_μ that undergoes kinetic mixing with the SM photon, or if DM is a composite neutral particle, but its constituents are charged under A'_μ. Furthermore, under the assumption of SI and SD interactions there exists severe tensions between several DD experiments claiming successful detections and others yielding null results, which can be reduced by considering certain combinations of more general scattering operators. These generically depend on momentum transfer, as well as relative velocity between DM and nucleus, which additionally highlights the need for careful DM velocity distribution modelling.

In recent works [247–250] all possible non-relativistic effective operators for elastic scattering were systematically studied in order to produce a general framework for the analysis of DD experimental results. Imposing Galilean invariance and requiring that the operators are Hermitian, the relevant quantities for scattering reduce to:

$$i\vec{q}\,, \quad \vec{v}^{\perp} \equiv \vec{v} + \frac{\vec{q}}{2\mu_{N\chi}}\,, \quad \vec{S}_{\chi}\,, \quad \vec{S}_{N}\,. \tag{3.52}$$

It can be shown that in total 16 independent elastic scattering operators can be constructed from these quantities, by keeping terms up to second order in momentum transfer $\vec{q}$ and relative velocity $\vec{v}$. Additionally, upon acting on nuclear states, six different response functions can appear. As anticipated in the introductory discussion regarding direct detection in section 1.2.3, all of these operators are characterized by one of the two possible v dependences, which need to be convoluted with the DM velocity distribution, namely the one appearing in equation (1.11), which arises for relative velocity independent operators, such as the standard SI and SD ones, as well as the one appearing in equation (1.12), which is relevant for operators with additional power of v^2. In general, also higher-order operators could be considered; however, they are further suppressed in the non-relativistic limit and have a negligible contribution. The precise mapping between the UV and non-relativistic operators, which includes running of the couplings, can be found in [251].

In this work, I will consider only eight further scattering operators, in addition to the SI and SD ones, which cover all the possible couplings of fermionic DM to quarks through a spin-0 or spin-1 mediator. These are:

$$\begin{aligned}
&\mathcal{O}_3 = i\vec{S}_N \cdot \left(\frac{\vec{q}}{m_N} \times \vec{v}^{\perp}\right) \quad , && \mathcal{O}_5 = i\vec{S}_{\chi} \cdot \left(\frac{\vec{q}}{m_N} \times \vec{v}^{\perp}\right) \,, \\
&\mathcal{O}_6 = \left(\vec{S}_{\chi} \cdot \frac{\vec{q}}{m_N}\right)\left(\vec{S}_N \cdot \frac{\vec{q}}{m_N}\right) \quad , && \mathcal{O}_7 = \vec{S}_N \cdot \vec{v}^{\perp} \,, \\
&\mathcal{O}_8 = \vec{S}_{\chi} \cdot \vec{v}^{\perp} \quad , && \mathcal{O}_9 = i\vec{S}_{\chi} \cdot \left(\vec{S}_N \times \frac{\vec{q}}{m_N}\right) \,, \\
&\mathcal{O}_{10} = i\vec{S}_N \cdot \frac{\vec{q}}{m_N} \quad , && \mathcal{O}_{11} = i\vec{S}_{\chi} \cdot \frac{\vec{q}}{m_N} \,.
\end{aligned} \tag{3.53}$$

3.3.2 Differential event rates

DM is expected to produce a characteristic energy spectrum of nuclear recoils, which is being actively searched for in many direct detection experiments. As can be seen from equation (1.9), the differential recoil rate depends on the particle physics parameters, namely the DM and nucleus mass, their differential cross-section and DM phase-space distribution. In order to constrain the particle nature of DM, one needs to accurately determine its distribution, which can be conveniently encoded in terms of functions $g(v_{\min})$ and $h(v_{\min})$, defined in equations (1.11) and (1.12). These functions cover all the velocity dependences of the cross-section that can arise up to the second order in momentum transfer and relative velocity, convoluted with the DM PSDF. Going beyond the standard modelling approach, which relies on simplistic Maxwellian velocity distribution, I evaluated $g(v_{\min})$ and $h(v_{\min})$ using the two-integral axisymmetric PSDF for

1000 randomly picked samples from the MCMC scan of the galactic mass models, described in section 3.2.2. This allowed me to compute a posterior distribution of $g(v_{\rm min})$ and $h(v_{\rm min})$, derived directly from the observational constrains on galactic kinematics. To consistently include also the uncertainty stemming from the local DM density itself, I did not normalize $g(v_{\rm min})$ and $h(v_{\rm min})$ by $\rho_\odot$ as determined by particular parameters of the sample under consideration, but rather by its median value over the entire set of samples. As such, the obtained $g(v_{\rm min})$ and $h(v_{\rm min})$, presented in figure 3.16, provide a novel insight into the uncertainty regarding DM phase-space distribution, which has been previously done only through rough estimates, either assuming standard halo model (SHM), where the local DM density, velocity dispersion and escape velocity are treated as independent, as for example in [162, 252, 253] and used by most experimental collaborations, or relying on spherical symmetry [235–238]. On the contrary, results presented here are built on a fair assumption that the galactic DM can be described by axisymmetric equilibrium PSDF, parametrized by two integrals of motion, namely relative energy and angular momentum around the axis of symmetry. As can be seen from the plots, assuming cored Burkert profile leads to a larger number of high velocity particles, as $g(v_{\rm min})$ is enhanced (suppressed) at large (small) $v_{\rm min}$ and $h(v_{\rm min})$ takes larger values over the entire range of $v_{\rm min}$, relative to the cuspy NFW profile. Furthermore, the latter yields smaller spread in the local DM density and, therefore, also bands corresponding to the 68% h.p.d. regions of $g(v_{\rm min})$ and $h(v_{\rm min})$ are significantly narrower and, at small $v_{\rm min}$, fall inside the bracketing of Burkert profile. Additionally, the axisymmetric modelling used in these work allows for self-consistent treatment of rotating halos and results for mildly co-rotating DM with the baryonic disk are shown, assuming typical spin parameter found in simulations, $\lambda = 0.05$, and azimuthal velocity profile defined in equation (3.24). For co-rotating halos the corresponding $g(v_{\rm min})$ and $h(v_{\rm min})$ are suppressed at large $v_{\rm min}$ and fall to zero quicker, since the relative velocity between DM particles and the detector is reduced, while $g(v_{\rm min})$ is enhanced at low $v_{\rm min}$. For the convenience of future analyses the tabulated values of obtained astrophysical factors are available on my website [2].

Having $g(v_{\rm min})$ and $h(v_{\rm min})$ the corresponding differential nuclear rate can be easily evaluated. In figure 3.17 I present the results for SI scattering on ^{131}Xe, assuming DM with mass $m_\chi = 100$ GeV and $\tilde{\sigma}_n^{\rm SI} = 10^{-46}{\rm cm}^2$, as obtained for the two-integral PSDF in case of NFW and Burkert density profiles with no rotation, as well as mildly co-rotating halos. From the plots one can see that the results for NFW profile lead to noticeably larger differential event rates over the entire recoil energy range, which is a consequence of the fact that it is associated with larger local DM density. The difference is most significant at low E_r, leading to a larger total number of expected events and correspondingly stronger limits on the coupling between DM and nuclei for large m_χ.

Using the tabulated values of $g(v_{\rm min})$ one can easily obtain the limits on standard SI and SD cross-section through the use of existing tools, such as DDCalc [254]. In figure 3.18, I present the upper limits obtained from Xenon1T null results for the discussed axisymmetric PSDF models along with the reference SHM, used in the original interpretation of data by Xenon collaboration [106]. While the differences between various models seem small due to the logarithmic

[2] https://people.sissa.it/∼mpetac/

scale, there can be significant deviations, especially at low DM masses, where the bounds derived from SHM are typically over-constraining due to the thick tail of the velocity distribution around $v_{\rm esc}$. By using the lower 95% confidence values of $g(v_{\rm min})$, the bounds on cross-section at $m_\chi \lesssim 5$ GeV are relaxed by a factor of 4 for non-rotating halos and almost two orders of magnitude for co-rotating halos, where the relative velocity between the target and DM particles is reduced. The difference between results obtained for NFW and Burkert profiles is much smaller, however, it is most significant just below the DM masses corresponding to the peak sensitivity of the detector, $m_\chi \sim 30$ GeV, where Burkert profile leads to roughly 15% stronger limits then the NFW one. For large DM masses, $m_\chi \gtrsim 100$ GeV, SHM again leads to over-constraining limits, which can be relaxed by roughly a factor of 1.5 for NFW and 2 for Burkert density profile.

The differences between various DM distribution models also shows up when one considers the general set of non-relativistic effective scattering operators, for which also function $h(v_{\rm min})$ becomes important. To illustrate the effect, I show in figure 3.19 the expected number of events in Xenon1T and CDMSlite experiments (where the former is currently most constraining detector for $m_\chi \gtrsim 5$ GeV while the latter has significantly lower recoil energy threshold and is, therefore, more sensitive at lower DM masses) for several operators with distinct scattering velocity dependences, assuming the aforementioned DM distribution models. Similarly as for the SI case, the co-rotating halos show strong suppression of the event rate at low DM masses, while the non-rotating Burkert halo can lead to significant enhancement of recoil rate at $m_\chi \sim 10$ GeV for Xenon1T experiment and $m_\chi \sim 3$ for CDMSlite. At large DM masses, all of the considered models predict lower scattering rates compared to the SHM, while the exact amount of suppression depends on the considered operator and target material.

3.3.3 Annual signal modulation

As already mentioned in the introduction, a hallmark signature of DM-nucleon interactions in direct detection experiments is expected in the form of an annual modulation of the nuclear recoil rate. Since the Earth is on a circular orbit around the Sun with a significant velocity, which amounts to more than 10% of the movement speed of the local standard of rest, one needs to account for it appropriately when mapping the DM phase-space distribution into the detector's rest frame – for more details see, e.g., [255]. Upon successful detection of DM induced recoils, a sinusoidal modulation of the signal with a period of one year should appear, clearly distinguishing it from any conceivable background noise. Further interest for this phenomena comes from the well established DAMA/LIBRA measurement of signal modulation [112, 113], which is, however, virtually impossible to reconcile with null results of other direct detection experiments. As could be expected, the amplitude of modulation crucially depends on the velocity distribution of DM, which again stresses the need for accurate modelling of the galactic DM halo. In figure 3.20 I present the annual modulation rate as obtained for the considered benchmark models, namely the PSDFs computed through the HQ method for NFW and Burkert DM density profiles with and without halo co-rotation. As can be seen from the plot, NFW case leads to significantly larger modulation amplitude than the Burkert one, while the rotation of halo along with the disk leads to suppression of the mod-

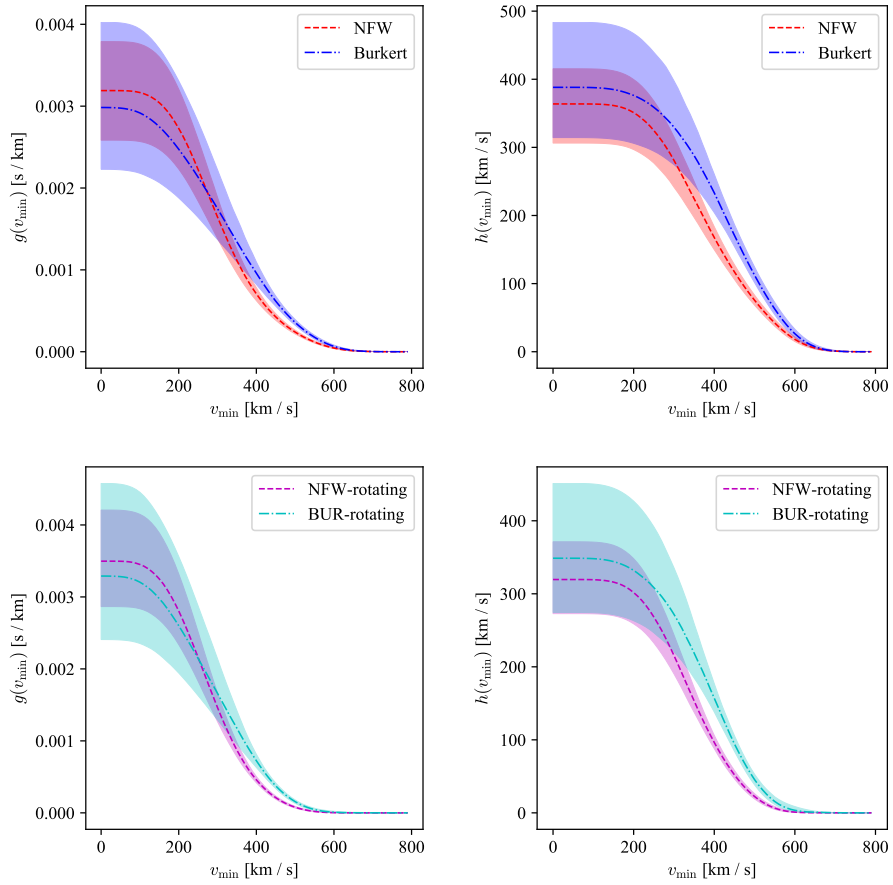

Figure 3.16: Astrophysical factor entering differential event rate in direct detection experiments as a function of the minimum scattering velocity for the two relevant velocity dependences of the cross-section, defined in equations (1.11) and (1.12). Lines show the median value, while the bands correspond to 68% credibility regions, as derived from the sampling of galactic mass decomposition, which was presented in section 3.2. The results are shown for NFW and Burkert density profiles, assuming non-rotating halos, as well as rotating ones with spin parameter $\lambda = 0.05$ and azimuthal velocity profile given by equation (3.24).

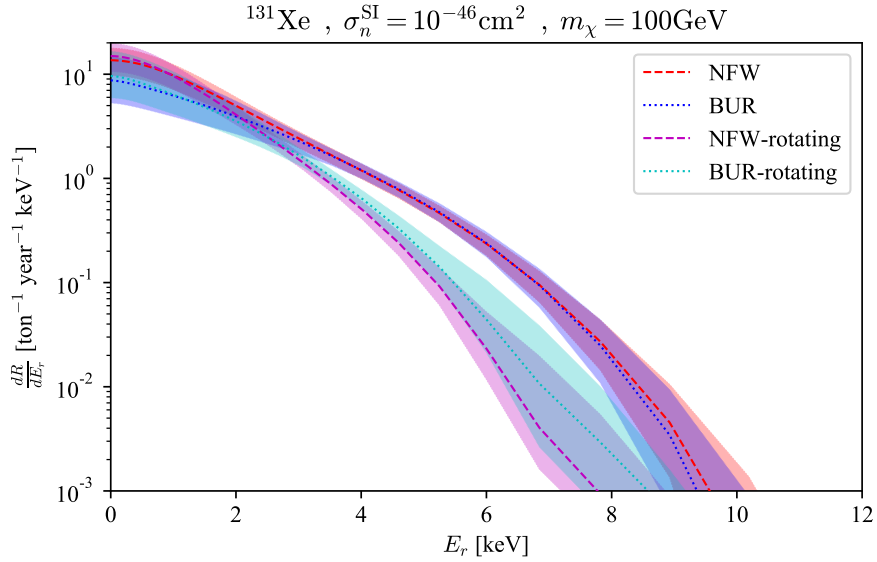

Figure 3.17: Expected differential event rate obtained for ^{131}Xe target, assuming SI scattering with zero momentum transfer cross-section $\tilde{\sigma}_n^{\rm SI} = 10^{-46}$ cm^2 and DM mass $m_\chi = 100$ GeV. Lines show median values for non-/co-rotating halos with NFW and Burkert density profile, while the bands correspond to 68% credibility regions.

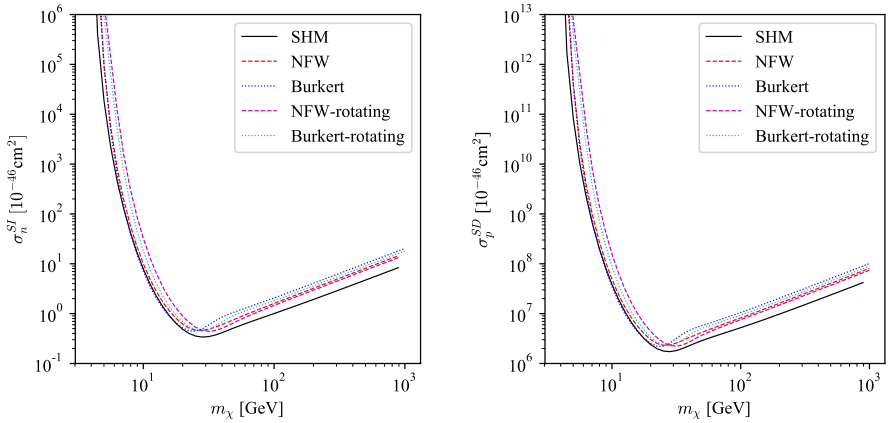

Figure 3.18: The Xenon1T upper limits on SI (left) and SD (right) cross-section, as obtained for the SHM [106] and non-/co-rotating axisymmetric models fit to the kinematic data using NFW and Burkert density profile. For the latter, exclusion limits corresponding to the lower 95% credibility bound on g are shown.

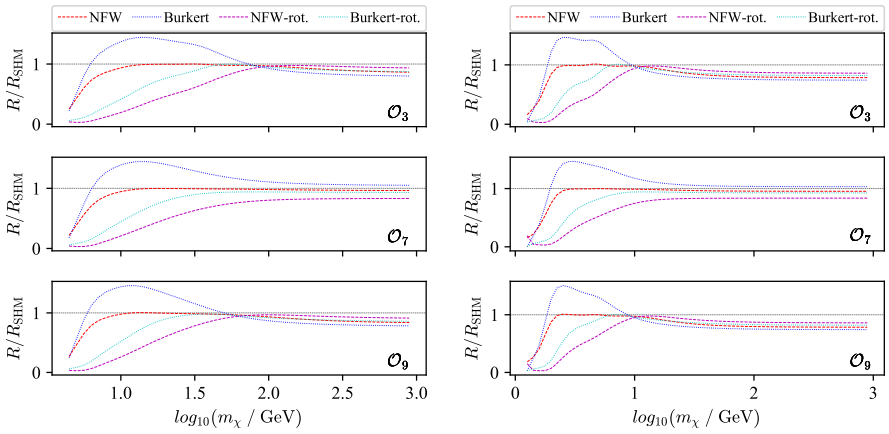

Figure 3.19: The expected event rates as a function of DM mass in Xenon1T (left) and CDMSlite (right) experiments for non-/co-rotating axisymmetic models, normalized to the SHM rates. The results are shown for distinct velocity dependences appearing in non-relativistic effective operators listed in equations (3.53).

ulation signal for both density profiles. On the other hand, larger spread in the DM parameters, found in the case of Burkert profile, lead to larger uncertainties in the amplitude of modulation. Non-the-less, the two considered DM densities still yield results that are distinguishable within the 68% confidence regions.

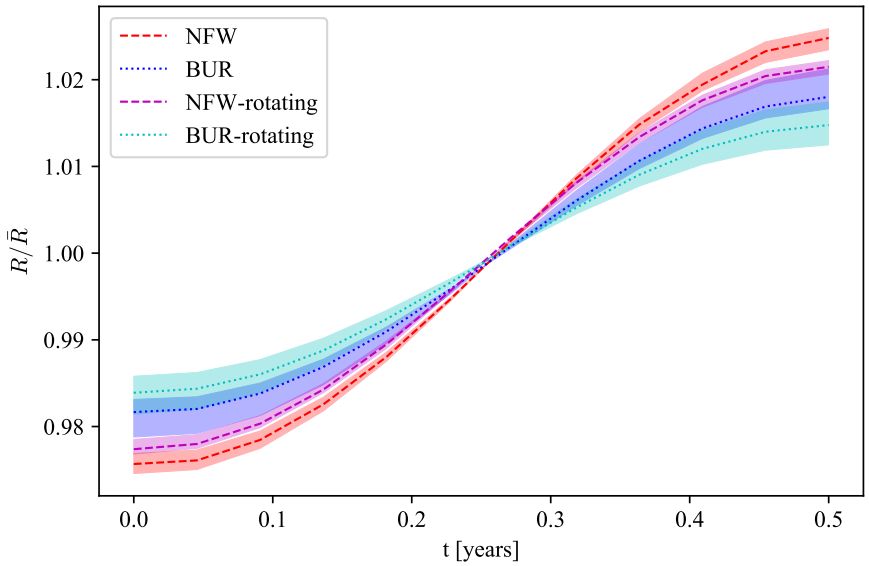

Figure 3.20: The annual modulation rate as obtained for different galactic DM phase-space models, normalized by the yearly average. The bands mark the 68% confidence region as obtained from the MCMC sampling of the galactic potential and DM density distribution. The minimum/maximum recoil rates, corresponding to $t = 0$ and $t = 0.5$ year, respectfully, is expected in beginning of June/December.

4. Annihilating Dark Matter

With the accumulation of the evidence for the existence of DM, significant research efforts were dedicated to exploring its particle nature. It was soon realized that one of the most promising channels for observing its non-gravitational signatures is through its annihilation [256, 257] or decay products in environments with high DM density, found in the centres of galaxies. While DM decays are strongly constrained by the fact that vast majority of DM survived from very early times until today, implying that its lifetime must be greater than the age of Universe, DM annihilations are generally allowed in a wide range of phenomenological models and the inverse processes (i.e. pair-creation) can be used to explain the production of DM within the early Universe, along with visible matter. Furthermore, in many well-motivated extensions of the SM, DM annihilations into SM particles can occur at tree-level, which typically leads to appreciable annihilation signals in dense DM environments, even if the responsible coupling is relatively small compared to the known forces. In practice, a key requirement for successful detection is that the daughter particles carry a characteristic feature in the spectrum, which can be successfully distinguished from emissions generated by various astrophysical processes taking place in the central regions of galaxies.

As already discussed in section 1.2.2, efforts to detect products of DM annihilations fall within the domain of indirect searches and can be pursued through various channels, among which γ-rays play the central role, however, with rapid advancements in the precision measurements of anti-matter and neutrino fluxes, even these are becoming increasingly relevant. This chapter will be devoted to the reassessment of the experimental bounds on DM annihilation cross-section, focusing primarily on the γ-ray fluxes from dwarf spheroidal satellites of the Milky Way, which currently provide the strongest and most robust constraints. In the following I will first mention few possible modifications of the simplest WIMP paradigm, which was introduced in sections 1.1.2 and 2.2, focusing in particular on non-perturbative Sommerfeld enhancement effect, which can substantially increase the expected DM annihilation rate. This will be followed by the analysis of different phase-space distribution models that can be used for describing galactic DM, paying particular attention to spherical systems, with the intention of addressing the Milky Way's dwarf satellite galaxies. In the final part of the chapter, the expected signals from the latter will be scrutinized in detail, with the purpose of marginalizing the astrophysical uncertainties in the expected annihilation flux that stem from DM phase-space distribution within

these objects. Special care will be given to boosts in the signal due to the presence of non-perturbative Sommerfeld enhancement.

4.1 Model dependence of DM annihilation rates

The standard WIMP paradigm leaves us with little freedom regarding DM properties. This was initially seen as a virtue of the model, leading to concrete and testable predictions, however, today it is becoming increasingly constrained by various experimental results. Furthermore, given the complexity of the standard model of elementary particles, it seems perhaps over-simplistic to assume that the DM consists of a single particle species. This led to numerous generalizations of the WIMP paradigm and paved way to new, but equally successful, models of describing the origin of the dark sector. One of the possible generalizations are the scenarios, in which several interacting dark fields are present, see e.g. [258–263], allowing for additional processes, such as conversions, semi-annihilations and/or co-annihilations, which can have important implications for the parameter space resulting in the correct DM abundance. Another possibility is the presence of particle-antiparticle asymmetry in the dark sector, analogous to the observed baryon asymmetry, which can allow for substantially larger $\langle \sigma_{\rm ann} v \rangle$, as discussed, for example, in [264, 265]. Additional possible differences in the relic abundance computation might arise due to modified thermal history of the Universe [266–268], that could be caused either by early phase of matter domination or increase in the Hubble expansion rate before the onset of radiation dominated era, encountered in various inflationary models and/or modifications of General Relativity. Furthermore, one can also drop the assumption regarding thermal equilibrium between visible and dark sector within the early Universe, which allows for an alternative DM production mechanism known as freeze-in [269], that has important similarities, but also differences, with respect to the standard freeze-out picture. Finally, changes in the expected annihilation signals within the late Universe can also occur, either due to the absence (or suppression) of velocity independent s-wave annihilations or onset of Sommerfeld enhancement, which is a non-perturbative effect that generically arises in the non-relativistic limit of annihilations mediated by light force carrier. In particular, the latter will be further scrutinized in the context of DM annihilations signals coming from dwarf spheroidal galaxies, as it can lead to several orders of magnitude stronger exclusion limits on the DM annihilation cross-section.

4.1.1 Sommerfeld enhancement

Above I have mentioned various classes of phenomenological DM models, which can lead to significant departures from the standard WIMP annihilation cross-section. With the possible exception of strongly coupled DM, which can be realized in case of large dark asymmetry or dominant co-annihilations, where the late-time annihilations are halted by depletion of a relevant dark component, most of the models rely on the perturbative description of particle interactions. This indeed sounds reasonable, given the existing evidence for smallness of coupling between dark and visible sectors. In the following, however, I will address an important non-perturbative effect, which generically arises in the

non-relativistic limit of theories with a light force mediator and an attractive potential. In the context of DM, it can lead to a strong enhancement of late time annihilation cross-section (i.e. for highly non-relativistic DM) and can, therefore, have a profound effect on the indirect detection signals. Furthermore, it makes the expected annihilation flux strongly dependent on the full DM phase-space distribution and not just the density profile, as it is often approximated for s-wave annihilations. Due to these reasons, particular attention will be paid to the so-called Sommerfeld enhancement [270], and its interplay with the DM phase-space modelling will be further scrutinized throughout this chapter.

The enhancement effect is quantum in its nature and stems from distortion of the wave-function of incoming particle states due to the exchange of a mediator sufficiently light to establish a regime of long-range interactions [271, 272]. Sommerfeld enhanced cross-sections for DM particle χ that can annihilate through the mediator ϕ, with $m_\chi \gg m_\phi$, can be computed by solving a non-relativistic Schrödinger equation with a potential related to long-range forces or by resummation of ladder ϕ-exchanges in the diagrammatic field theory approach [273, 274]. The induced enhancement of cross-section is linearly proportional to the absolute square of the ratio of wave functions in presence and absence of the long-ranged force, i.e. $S = |\chi(0)/\chi(\infty)|^2$ where $\chi(\infty)$ is the unperturbed wave-function at spatial infinity, effectively quantifying the distortions induced by long-range interactions. In the following I will restrain myself from making assumptions regarding the nature of the new force; however, the coupling of Yukawa type will be used as the reference case, while the other possible interactions follow analogously. In general there is no analytical solution for scattering in presence of the Yukawa potential, but the latter can be very well approximated by Hulten's potential [275, 276], for which one finds:

$$S(v_{\rm rel};\,\xi) = \frac{\pi\alpha_\chi}{v_{\rm rel}} \frac{\sinh\left(\frac{12 v_{\rm rel}}{\pi\alpha_\chi \xi}\right)}{\cosh\left(\frac{12 v_{\rm rel}}{\pi\alpha_\chi \xi}\right) - \cos\left(2\pi\sqrt{\frac{6}{\pi^2\xi} - \left(\frac{6 v_{\rm rel}}{\pi^2\alpha_\chi\xi}\right)^2}\right)}\,, \tag{4.1}$$

where $\xi \equiv m_\phi/(\alpha_\chi m_\chi)$ and the long-range force strength dictated by the coupling constant α_χ. The above expression provides an enhancement of the DM annihilation rate for small $v_{\rm rel}$ and ξ, while it becomes negligible at large velocities or when $m_\phi \gtrsim \alpha_\chi m_\chi$, leading to $S \approx 1$. In the case of vanishing mediator mass, which is often referred to as the Coulomb regime due to its analogy with the electromagnetic force, one finds:

$$S(v_{\rm rel};\,\xi \ll 1) \approx \frac{\pi\alpha_\chi}{v_{\rm rel}}. \tag{4.2}$$

A different limiting behavior occurs at resonant values of ξ, where the enhancement becomes even stronger for low relative velocities. From equation (4.1) one finds the following:

$$S\left(v_{\rm rel}\,;\,\xi_{\rm res} = \frac{6}{\pi^2 n^2}\right) \approx \frac{\alpha_\chi^2}{v_{\rm rel}^2 n^2} \quad \text{where} \quad n \in \mathbb{N}\,. \tag{4.3}$$

In practice, when addressing annihilation signals coming from galactic DM, one needs to convolute $S(v_{\rm rel};\xi)$ with the PSDF of annihilating particles, as

dictated by equation (1.5), where $v_{\rm rel} = |\vec{v}_1 - \vec{v}_2|$ is their relative velocity. As will be discussed in the last part of the chapter, this can lead to several orders of magnitude larger annihilation fluxes compared to the non-enhanced case.

The possibility of enhancing annihilation signals in the non-relativistic limit has several important phenomenological motivations. In the context of DM, it was initially conceived as a way of boosting the annihilation rates in the non-relativistic limit to explain the galactic positron excess, as observed by PAMELA and later confirmed by Fermi-LAT and AMS-02 data, without significantly modifying the evolution of WIMPs in the early Universe [277]. Today, astrophysical explanations of the positron excess are preferred due to the lack of associated diffuse γ-ray emissions [278]. However, Sommerfeld enhancement is still a generic prediction of many popular DM models. For example, in many concrete realizations of Supersymmetry, it can have a significant impact on the behaviour of DM candidates, not only affecting the late time signals, but also the course of its decoupling from primordial plasma [279]. Analogously, one needs to be careful to correctly account for Sommerfeld enhancement in all DM models, where DM couples to light force mediator with attractive potential, fulfilling the criterion $\xi \lesssim 1$.

4.2 DM distribution models

The expected DM annihilation signal in indirect experiments crucially depends on DM distribution, as can be seen from equation (1.6). While in case of s-wave annihilations only the spatial distribution is relevant, this is no longer true in more general settings, where the annihilation cross-section times relative velocity can no longer be approximated as a constant and hence also the velocity distribution of DM becomes important. In the past Maxwell-Boltzmann velocity distribution was often assumed for DM, which however corresponds to the equilibrium solution of the Boltzmann equation only for DM isothermal sphere with $\rho(r) \propto r^{-2}$. In recent studies, it was recognized that Eddington's inversion formula (2.14) is capable of providing much more accurate description of the velocity distribution for realistic DM profiles, particularly in the central part of galaxies. On the other hand, Eddington's inversion still assumes fully isotropic DM orbits, while the actual orbital anisotropy of DM within halos remains unknown.

Following our recent publication [280], I will provide a comparison of Maxwell-Boltzmann approximation of the PSDF and solutions of the Eddington's inversion for cuspy and cored DM density distributions. Furthermore, I will also compare the resulting velocity distributions of isotropic models with several anisotropic generalizations of Eddington's approach, which can provide a handle on the effect of DM orbital anisotropy. Since the Milky Way's dwarf spheroidal satellites, described in greater detail in section 4.3.1, represent one of the prime targets for indirect detection, I will mainly focus on spherical modelling which is a reasonable approximation for these dispersion supported objects. In the final part of the section, few implications of axisymmetric models, discussed in section 3, will be addressed. This can be relevant in the light of claims for γ-ray excess in the centre of Milky Way and Andromeda galaxies, where p-wave annihilating DM could reconcile these observations with null signals from dwarf satellites.

4.2.1 Spherical systems

Numerous analyses of indirect detection signals for velocity-dependent cross-sections have been preformed assuming Maxwell-Boltzmann velocity distribution, as partially motivated by the isothermal sphere model. The latter is defined by a constant velocity dispersion and results in Maxwellian velocity distribution at all radii. While the assumption of constant velocity dispersion is in general too crude for modern analysis, given the wealth of observational data, one can readjust it to a dynamical model at hand by applying the spherical Jean's equation for the second moment (2.16). For isotropic DM, i.e. $\beta(r) = 0$, one can express the radially-dependent velocity dispersion for arbitrary density distribution $\rho(r)$ and total gravitational potential $\Phi(r)$ as:

$$\sigma^2(r) = \frac{1}{\rho(r)} \int_r^\infty dr' \rho(r') \frac{d\Phi}{dr'} \,. \tag{4.4}$$

The corresponding PSDF can be then written in the following form:

$$f_{\rm MB}(r, v) = \frac{\rho(r)}{(2\pi\sigma^2(r))^{3/2}} \cdot \exp\left(-\frac{v^2}{2\sigma^2(r)}\right) \,, \tag{4.5}$$

where v is the modulus of the velocity. One must note, however, that such PSDF does not represent a stationary solution of the collisionless Boltzmann equation, so it can not describe the relaxed galactic DM. As discussed in the following, exact equilibrium configurations for spherical systems can be obtained through Eddington's inversion or its generalizations, applicable to certain anisotropic systems.

Isotropic modelling

Eddington's inversion formula, introduced in section 2.1.1, provides a unique stationary solution of collisionless Boltzmann equation for an ergodic (i.e. spherically symmetric and isotropic) system with a given density distribution and total gravitational potential. The resulting PSDF is a function of single integral of motion, usually expressed as relative energy $\mathcal{E}$, and can be in principle computed for any density-potential pair. However, the solution is not automatically guaranteed to be physical; the resulting $f_{\rm Edd}(\mathcal{E})$ has to be checked a posteriori for positive definiteness. Additionally, it has to be monotonic in $\mathcal{E}$ to be a stable solution.

In practice further complications in evaluation of $f_{\rm Edd}(\mathcal{E})$ might arise due to the second term in the second line of equation (2.14), which might lead to a singularity if the derivative of $d\rho/d\Psi$ does not approach 0 quickly enough in the limit $\Psi \to 0$. While this is generally not a concern for infinite systems, a non-vanishing derivative usually appears for finite objects. This is indeed the case when reconstructing the phase-space distribution in Milky Way dwarf satellites since the latter are embedded in a much stronger gravitational potential of the host galaxy, which strips the dwarfs of any matter beyond the truncation radius $r_{\rm t}$ through tidal forces. In this case, the issue might be mitigated by adopting a smooth truncation function for the density profile:

$$\rho(r) \to \rho(r) \cdot \begin{cases} 1 \,; & r < r_{\rm c} \\ s(r) \,; & r_{\rm c} \leq r < r_{\rm t} \\ 0 \,; & r > r_{\rm t} \end{cases} \,, \tag{4.6}$$

where r_c is the innermost point at which the smoothing has an effect, while $s(r)$ must satisfy:

$$s(r_c) = 1, \quad s(r_t) = 0, \quad \left.\frac{ds}{dr}\right|_{r_c} = 1 \quad \& \quad \left.\frac{ds}{dr}\right|_{r_t} = 0 \,. \tag{4.7}$$

The lowest order polynomial function satisfying these conditions is:

$$s(r) = 3\,\frac{(r_t - r)^2}{(r_t - r_c)^2} - 2\,\frac{(r_t - r)^3}{(r_t - r_c)^3} \,. \tag{4.8}$$

Choosing r_c too close to r_t might lead to non-positive definite $f(\mathcal{E})$, however, in most cases a reasonably large r_c can be found to not significantly modify the density profile, but as the same time provide a well behaved PSDF function.

Anisotropic PSDFs

Going beyond the standard lore, one should also consider spherical models which do not rely on the assumption of isotropic DM velocity distribution. In fact, similar approaches to Eddington's inversion allow to reconstruct DM phase-space distributions with non-vanishing anisotropy profiles [145] and can lead to significantly different velocity distributions, then the one found for the isotropic model.

For spherically symmetric systems, Jean's theorem implies that the PSDFs can be parametrized in terms of two integrals of motion, namely the relative energy $\mathcal{E}$ and the magnitude of angular momentum L, i.e. $f = f(\mathcal{E}, L)$. The DM particles in such distributions follow orbits that can be either radially or tangentially biased, determining the sign of orbital anisotropy parameter $\beta(r)$, defined in (2.17). Since the latter can not be inferred from observations, we have very limited information regarding this quantity. N-body simulations within the ΛCDM paradigm find only modest net departure from the isotropic limit [281–286], with slight preference for radial orbits in the outskirts, however, this can greatly vary from galaxy to galaxy and depends on the particular merging history of the object. There exists also the *cusp slope-central anisotropy* theorem, which states that at the center of a system $2\beta \leq -\,\mathrm{d}\ln\rho/\mathrm{d}\ln r$ [287], prohibiting radially biased orbits in the center of cored systems and imposing $\beta \leq 1/2$ for NFW density profile. With these guidelines in mind, one can hope to account for the systematic uncertainty entering the astrophysical J-factors due to the unknown DM orbital anisotropy.

In the following section, radially biased anisotropy will be studied by adopting the so-called *Osipkov-Meritt model* [288, 289]. This choice corresponds to a halo that is isotropic in the centre, while the DM orbits become increasingly radial in the outskirt:

$$\beta(r) = \frac{r^2}{r^2 + r_a^2} \,, \tag{4.9}$$

where r_a is the anisotropy scale radius. Even in this case the PSDF still depend on a single integral of motion, namely the variable $Q \equiv \mathcal{E} - L^2/(2r_a^2)$ and consequently equation (2.10) can be inverted analogously to the Eddington's

case [288, 289]:

$$f_{\rm OM}(Q) = \frac{1}{\sqrt{8}\pi^2}\frac{d}{dQ}\int_0^Q \frac{d\Psi}{\sqrt{Q-\Psi}}\frac{d\rho_{\rm Q}}{d\Psi} = \frac{1}{\sqrt{8}\pi^2}\left[\int_0^Q \frac{d\Psi}{\sqrt{Q-\Psi}}\frac{d^2\rho_{\rm Q}}{d\Psi^2} - \left(\frac{1}{\sqrt{Q-\Psi}}\frac{d\rho_{\rm Q}}{d\Psi}\right)\Big|_{\Psi=0}\right], \quad (4.10)$$

where the rescaled density $\rho_{\rm Q}(r) \equiv \rho(r)\cdot(1+r^2/r_a^2)$ was introduced.

Finally, unique solutions exist also for DM particles following tangentially biased orbits. Here the central anisotropy theorem is automatically fulfilled for all phenomenologically motivated density profiles, and one can adopt the simplifying assumption of constant velocity anisotropy $\beta(r) = \beta_c$, with $\beta_c < 0$. A simple choice for such a setup is the one in which the PSDF can be factorized as [145]:

$$f_{\beta_c}(\mathcal{E}, L) = g_{\beta_c}(\mathcal{E}, L_0)\cdot\left(\frac{L}{L_0}\right)^{-2\beta_c}. \quad (4.11)$$

The procedure to invert equation (2.10) is again similar to the one of Eddington's formula. It becomes particularly simple for $\beta_c = -1/2$, when g_{β_c} takes the following form:

$$g_{-\frac{1}{2}}(\Psi, L_0) = \frac{L_0}{2\pi^2}\frac{\mathrm{d}^2}{\mathrm{d}\Psi^2}\left(\frac{\rho}{r}\right). \quad (4.12)$$

Analytic solutions can be derived also for other half-integer values of β_c, while the inversion could even be performed numerically for an arbitrary constant value using Abel integral transform (2.12). In this work we, however, focus only on the case of $\beta_c = -1/2$, since this choice proves sufficient for exploring the trends and, at the same time, stronger deviations from the isotropic configuration seem unlikely. Indeed significant J-factor boosts are found, compared to the isotropic case, already by considering such moderate values of orbital anisotropy, while we explicitly checked that by going to lower values of β_c one finds even larger enhancements.

Comparison of velocity distributions

The four PSDF models listed above are all based on a given DM density profile and its corresponding gravitational potential. Therefore, one should obviously recover the same initial $\rho(r)$ after applying equation (2.10). However, the differences among them can be appreciated by looking at the corresponding velocity probability distributions:

$$\mathrm{P}(v; r) = \frac{v^2}{\rho_{\rm DM}(r)}\int d\Omega_v f_{\rm DM}(r, \vec{v}), \quad (4.13)$$

where $d\Omega_v$ denotes the integral over the direction of the velocity vector $\vec{v}$ (it reduces to a factor of 4π for isotropic PSDFs). In figure 4.1 I show $\mathrm{P}(v; r)$ for the four PSDFs under assumption of the two parametric density profiles (NFW on the left panel and Burkert on the right) at a fixed ratio of $r/r_s = 0.3$, chosen as representative radius, since in both cases a significant contribution

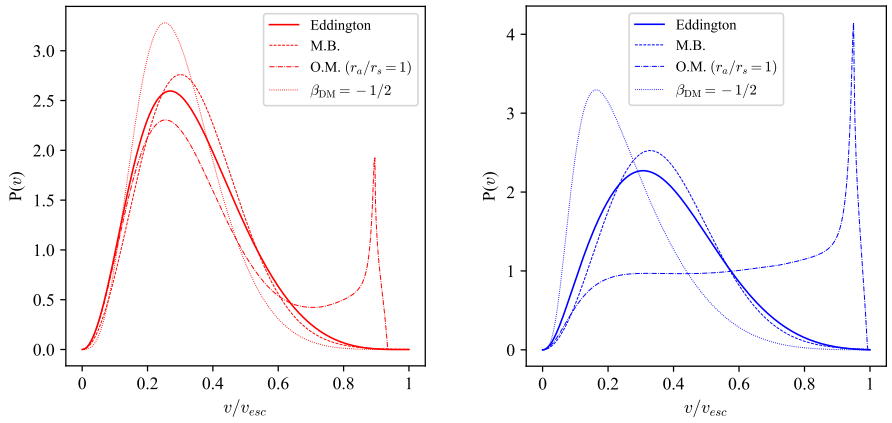

Figure 4.1: Velocity probability distribution in sample dSph for various PSDF models. The left (right) plot corresponds to a NFW (Burkert) DM density profile; in both cases results are shown for $r/r_s = 0.3$, with r_s being the scale radius. The velocities are normalized to the escape velocity $v_{\rm esc}$.

towards the total J-factor originates around this portion of the density profile, as will be demonstrated in the following section. We can see that the standard isotropic modelling, using Eddington's inversion formula or Maxwell-Boltzmann approximation, yields similar $\mathrm{P}(v;r)$, with the MB approach typically predicting somewhat warmer particles. The difference gets more pronounced at smaller r/r_s, which leads to greater enhancement of J-factors for cuspy profiles, since there the contribution towards total annihilation flux peaks at $r = 0$. On the other hand, anisotropic PSDFs have distinct velocity distributions, deviating significantly from the isotropic case for both $\rho(r)$ considered. Osipkov-Merritt model yields velocity distributions with more power at high velocities[1], which can be heuristically understood by the fact that particles on radial orbits reach their terminal velocities at the centre of the halo. On the contrary, for $\beta(r) = -1/2$, where the orbits are circularly biased, one finds significantly colder central velocity distribution. This can be elucidated by the fact that circular velocity scales as $v_{\rm circ} \propto r^{(3-\gamma)/2}$ for a density profile with the central slope γ (i.e. $\rho(r) \propto r^{-\gamma}$ for $r \ll r_s$) and therefore leads to diminishing tangential velocities as $r \to 0$ for any realistic density profiles.

The trends sketched here for single-particle velocity distributions are to some extent representative also of the scalings with the relative velocity in particle pairs, which is the relevant quantity when addressing J-factors in the presence of velocity-dependent annihilation cross-sections. In the following section, we apply our analysis to observational data of dSphs and examine the implications of various phase-space distribution models.

[1] The secondary peak close to $v_{\rm esc}$ arises in connection to the radial truncation of the profile. A sharp peak in the plots appears when the smoothing function (4.8) is introduced, while it would be less pronounced for (ill-defined) sharp cut-off. Due to the nature of Sommerfeld enhancement, this truncation artefact at high velocities has, however, no sizeable impact on the results.

4.2.2 Axisymmetric systems

While the above discussion was centred around spherical objects, its natural to wonder how the situation changes in the case of flatted systems, such as spiral galaxies. This is particularly interesting in the light of γ-ray excess in the centre of Milky Way and Andromeda galaxies, which is, however, inconsistent with observations of dSphs under the assumptions of velocity independent WIMP annihilations. To accurately predict signals from velocity-dependent annihilations careful phase-space modelling becomes important and refined approaches, like the HQ method discussed in chapter 3, have to be used, as can be seen from the velocity distributions plotted in figure 4.2. The results are shown at galactocentric radius $r/r_s = 0.1$ for spherical PSDFs and at corresponding points along $\hat{R}$ and $\hat{z}$ directions for the axisymmetric model (i.e. at $\{R = r_s/10,\ z = 0\}$ and $\{R = 0,\ z = r_s/10\}$), assuming either NFW or Burkert DM density profile and sample baryonic setup introduced in section 3.1.2. The standard halo model (SHM) can be seen to provide a distorted shape of the velocity distribution in the central part of the system with respect to the other more realistic models; for NFW case the truncation occurs relatively close to the peak of the distribution and predicts much larger abundance of high-velocity particles compared to the other two PSDF models, while for Burkert case the peak of distribution is shifted to significantly lower velocities, resulting in higher abundance of slow particles. On the other hand, Eddington's inversion and HQ method predict much more similar velocity distributions. However, some differences are still present, especially when considering the particles above/below the disk (i.e. at $\{R = 0,\ z = r_s/10\}$). There the peaks of $\mathrm{P}(v)$ obtained through the HQ method are shifted to noticeably lower velocities compared to the spherical modelling, and in the case of Burkert profile, the resulting distribution is also broader. These differences naturally affect the predictions for velocity-dependent annihilations, which are determined by a convolution of two single-particle velocity distribution, presented here, with the appropriate function of the relative velocity of the annihilating particles. The exact impact of the axisymmetric PSDF modelling on the astrophysical J-factors will not be discussed further within this thesis, leaving the precise analysis for future works.

4.3 Reassessment of J-factors and the Sommerfeld enhancement

In the previous section, differences in the single-particle velocity distributions of various PSDF models were demonstrated. This can naturally lead to important changes in the anticipated DM annihilation flux for velocity-dependent $(\sigma_{\mathrm{ann}}v)$. In the light of Sommerfeld enhancement, this is expected to be particularly important in the analysis of dwarf galaxies, since they are typically associated with low DM velocities due to their small dynamical masses. Furthermore, recent observations allow us to constrain the DM content of these objects with unprecedented accuracy, which, together with the rapidly improving sensitivity of indirect DM searches, drives the need for refined modelling.

In the following, I will briefly present Milky Way's dwarf spheroidal satellites (dSphs) and demonstrate how Jean's analysis, introduced in section 2.1.1, can be used to connect the observations of stellar kinematics with the underlying

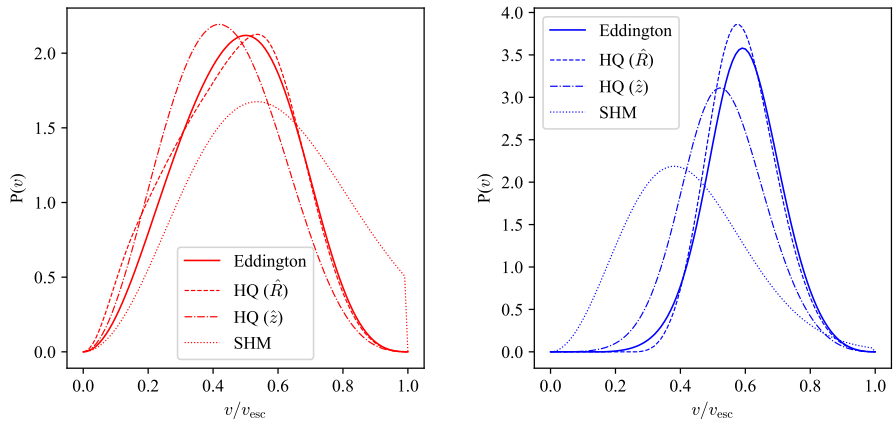

Figure 4.2: Velocity probability distribution in sample disk galaxy for various PSDF models. The left (right) plot corresponds to a NFW (Burkert) DM density profile; in both cases results are shown for $r/r_s = 0.1$ in case of spherical models and points $\{R = r_s/10,\ z = 0\}$ and $\{R = 0,\ z = r_s/10\}$ for HQ model (denoted as HQ $(\hat{R})$ and HQ $(\hat{z})$, respectfully), with r_s being the scale radius. The velocities are normalized to the corresponding escape velocity $v_{\rm esc}$.

DM density profile. This will be followed by Bayesian inference of the DM distribution within the classical dSphs, which host a sufficiently large number of stars for performing Jean's analysis, using recent measurements of their stellar line-of-sight velocity dispersion profiles. The fits will be performed for two different density profiles, namely the cuspy NFW and cored Burkert parametric forms, while a highly general ansatz for stellar anisotropy will be used, allowing for marginalization over this poorly constrained quantity. Once the posterior distributions of DM density parameters are obtained, the above-described models will be used to construct the full 6D phase-space distribution of DM. This will then allow us to derive the corresponding posterior distribution of the J-factors, which are essential for the interpretation of indirect DM searches in dSphs, based either on γ-ray and/or neutrino fluxes.

4.3.1 The Milky Way's dwarf satellites

The cold DM paradigm predicts the existence of the nearly scale-invariant cosmic web, in which small structures are hierarchically embedded into larger ones. This is indeed consistent with the observations of galaxies and galaxy clusters. However, the sub-galactic structures have proven difficult to detect, since they often host negligible amounts of visible matter. Classical dwarf satellites of the Milky Way fall on the lower end of the mass spectrum at which star formation is still possible and are, therefore, DM dominated systems, with mass-to-light ratio typically more than an order of magnitude larger than in spiral galaxies. Recently several ultra-faint satellites of Milky Way were discovered, which are expected to provide even larger mass-to-light ratios. However, precise analysis of these objects turns out to be problematic, since they host only very few stars, making it very difficult to determine their mass and its distribution accurately.

Therefore, we restrict our attention to the classical dwarf satellites, as they pose as a unique laboratory for observing signatures of DM annihilations; their low baryonic content and negligible star formation rates guarantee small contamination of the signal with backgrounds related to astrophysical processes, while their stellar content still allows for robust determination of their mass.

In the following, I will first present the details of statistical analysis, performed on the available kinematic dataset of eight Milky Way classicals in order to constrain the DM halo density profile in dSphs. For this purpose Bayesian Monte Carlo Markov Chain (MCMC) approach was used along with two phenomenologically different functional forms for the DM density, namely cuspy NFW and cored Burkert profiles, given by equations (3.32) and (3.33) respectfully, which are both parametrized by scale density ρ_s and scale radius r_s. In the second part of the section, posterior distributions of DM density profiles will be used to evaluate the corresponding J-factors. The results for standard velocity independent case, as well as for Sommerfeld enhanced annihilations, will be presented. For velocity dependent cross-sections, special attention will be given to different possible choices of the PSDF modelling, and novel results for anisotropic DM configurations will be discussed.

Analysis of stellar kinematics

The moderate ellipticities and the lack of evidence in favour of tidal disruption in the eight classical dSphs give reasonable support to the assumptions of spherical symmetry and dynamical equilibrium. This allows one to apply standard spherical Jeans modelling, introduced in section 2.1.1, to study these objects. Starting with equation (2.16), one can show that the formal solution for $P_\star(r)$ (where I have introduced subscript $\star$ to distinguish quantities related to the stellar component from the DM ones) takes the following form:

$$P_\star(r) = G\int_r^\infty dx\,\frac{\rho_\star(x)M_{\rm tot}(x)}{x^2}\exp\left[2\int_r^x dy\,\frac{\beta_\star(y)}{y}\right], \tag{4.14}$$

with G being the gravitational constant. At this point one can approximated total mass profile of the system with the one of DM component only, $M_{\rm tot}\simeq M_{\rm DM}$, given the large mass-to-light ratio exhibited by dSphs. To make connection with the actual measurements, namely the stellar line-of-sight (l.o.s.) velocity dispersion profiles $\sigma_{\rm los}(R)$, equation (4.14) is projected along the l.o.s. according to:

$$\sigma^2_{\rm los}(R) = \frac{1}{\Sigma_\star(R)}\int_{R^2}^\infty \frac{dr^2}{\sqrt{r^2-R^2}}\left(1-\beta_\star(r)\frac{R^2}{r^2}\right)p_{r\,\star}(r)\,, \tag{4.15}$$

where we have introduced the surface brightness profile of the system, $\Sigma_\star(R)$. Note that the stellar density can be traced via an Abel transform of the surface brightness under the approximation of a constant luminosity profile for the stars in the galaxy. Once equation (4.14) is plugged into equation (4.15), such normalization drops out. For an adequate description of the surface brightness profile of the classical dwarfs, we rely on the Plummer model [290, 291], characterized by the projected half-light radius $R_{1/2}$, which provides good fits to the available photometric dataset for these objects [292]:

$$\Sigma_\star(R)\propto\left(1+(R/R_{1/2})^2\right)^{-2}\quad\Leftrightarrow\quad\rho_\star(r)\propto 3/(4R_{1/2})\left(1+(R/R_{1/2})^2\right)^{-5/2}. \tag{4.16}$$

In the study we included two independent sources of uncertainty lying in the observational determination of $R_{1/2}$ (which is to a very good approximation given by $R_{1/2} \simeq \alpha_{1/2} D$), namely the error from determination of the heliocentric distance of the object, D, and the one from analysis of the photometric data when determining the angular half-light distance, $\alpha_{1/2}$. The nominal values $\overline{D}$, $\overline{\alpha}_{1/2}$ and corresponding estimated errors ΔD, $\Delta\alpha_{1/2}$ were adopted from the compilation of ref. [293].

In order to predict l.o.s. velocity dispersion profiles, equations (4.14) and (4.15) require the modelling of the stellar orbital anisotropy and the DM halo mass. In an attempt to derive conservative bounds on DM halo parameters, we avoid the use of over-simplified stellar anisotropy profiles, e.g. a spatially constant parameter [294–296]. In light of the poor indications concerning $\beta_\star(r)$ in dSphs, both from the side of N-body simulations [297, 298] and present observations [299], we rather advocate a 3-parameter fiducial model of the form:

$$\beta_\star(r) = \frac{\beta_0 + \beta_\infty (r/r_\beta)^2}{1 + (r/r_\beta)^2} \,, \tag{4.17}$$

i.e. the Baes-Van Hese parametrization [300], characterized by a transition from an inner regime governed by β_0 to an outer one set by β_∞, with characteristic scale r_β and slope $\eta_\beta = 2$, which we for simplicity kept constant throughout our analysis.

The adopted combination of stellar Plummer model, stellar velocity dispersion anisotropy in equation (4.17), and the cuspy/cored DM halo profile defined in equations (3.32) and (3.33), fully characterize our study of dSph galactic dynamics with the spherical Jeans equation. The test-statistic we define in order to perform our analysis on the measured stellar kinematics in MW satellites reads as follows:

$$\mathcal{L}_{\rm kin} \equiv \prod_{k=1}^{\rm N} \frac{1}{\sqrt{2\pi}\,\Delta\sigma_{{\rm los}\,(k)}\left(\alpha_{(k)}\right)} \exp\left[-\frac{1}{2} \left(\frac{\overline{\sigma}_{{\rm los}\,(k)} - \sigma_{\rm los}\left(\alpha_{(k)}\right)}{\Delta\sigma_{{\rm los}\,(k)}\left(\alpha_{(k)}\right)} \right)^2 \right] \,. \tag{4.18}$$

The above likelihood is suitable for a binned data analysis of dSph kinematics, as for instance previously done in [301]. For each bin $k \leq N$, with angular annulus $\alpha_{(k)} \simeq R_{(k)}/D$, we can compare theory predictions, $\sigma_{\rm los}\left(\alpha_{(k)}\right)$, against spectroscopic measurements, denoted here by $\overline{\sigma}_{{\rm los}\,(k)}$; in doing so, we also take into account the observational uncertainty on the dataset binning, namely:

$$\Delta\sigma_{{\rm los}\,(k)}\left(\alpha_{(k)}\right) \equiv \sqrt{\left(\delta\sigma_{{\rm los}\,(k)}\right)^2 + \frac{1}{4}\left[\sigma_{\rm los}\left(\alpha_{(k)} + \Delta\alpha_{(k)}\right) - \sigma_{\rm los}\left(\alpha_{(k)} - \Delta\alpha_{(k)}\right)\right]^2}, \tag{4.19}$$

where $\delta\sigma_{{\rm los}\,(k)}$ corresponds to the observational error stemming from the spectroscopic measurement of the l.o.s. velocity dispersion, while $\Delta\alpha_{(k)}$ stands for the angular distance uncertainty associated with the k-th bin. Equipped with equation (4.18), we performed a Markov Chain Monte Carlo (MCMC) analysis exploiting the stellar kinematic dataset presented in [296].[2] The full model

[2] We are deeply grateful to M.G. Walker, who has provided us stellar l.o.s. velocity dispersions for the classical MW satellites in bins of angular annuli. We wish to refer to [296, 302] and more specifically to [303–306] for the details on the compilation of the spectroscopic measurements characterizing the dataset analysed in this work.

under scrutiny by means of Bayesian inference is defined by seven parameters:

$$\vec{\theta} = \{\rho_s, r_s, r_\beta, \beta_0, \beta_\infty, \alpha_{1/2}, D\} \,. \tag{4.20}$$

We explored the model parameter space restricted to the following set of ranges:

$$\begin{aligned}
-5 \leq \quad & \tilde{\rho}_s \equiv \log_{10}\left(\rho_s/[\text{GeV cm}^{-3}]\right) && \leq 5\,, \\
-5 \leq \quad & \tilde{r}_s \equiv \log_{10}\left(r_s/[\text{kpc}]\right) && \leq 2\,, \\
-3 \leq \quad & \tilde{r}_\beta \equiv \log_{10}\left(r_\beta/[\text{kpc}]\right) && \leq 1\,, \\
1 \leq \quad & b_0 \equiv 2^{\beta_0/(\beta_0-1)} && \leq 1.95\,, \\
0 \leq \quad & b_\infty \equiv 2^{\beta_\infty/(\beta_\infty-1)} && \leq 1.95\,.
\end{aligned} \tag{4.21}$$

Non-informative (i.e. flat) prior distributions were assigned on the set of parameters $\{\tilde{\rho}_s, \tilde{r}_s, \tilde{r}_\beta, b_0, b_\infty\}$, according to the intervals reported in equation (4.21), while for the heliocentric distance D and the half-light angle $\alpha_{1/2}$ Gaussian prior with mean and standard deviation matching the corresponding observational information available, i.e. $\overline{D} \pm \Delta D$ and $\overline{\alpha}_{1/2} \pm \Delta\alpha_{1/2}$, were assumed.

In light of the well-known mass-anisotropy degeneracy plaguing the spherical Jeans analysis [307–310], some comments on the ranges appearing in equation (4.21) are in order. First, we note that the adopted prior on $\tilde{r}_s$ involves a quite conservative upper-bound in relation to the size of halos in dSph, which are expected to be within $\mathcal{O}(10)$ kpc, while for what concerns the lower-bound, smaller radii than that fall way below the resolution of data. We remained quite agnostic also on the normalization of the DM halo, assigning a range to $\tilde{\rho}_s$ that covers ten dex in ρ_s. For what regards the orbital anisotropy parameters, by definition $\beta_\star(r) \leq 1$ and the central-cusp anisotropy theorem [287] further restricts the physical range of β_0. We also exploited the parametrization of limiting orbital anisotropies by $b_{0,\infty}$, introduced in equation (4.21), in order to equally weight tangential-like and radial-like stellar motion, however, delimit the description of tangential orbits to values $\beta_{\star\,0,\infty} \gtrsim -25$ due to numerical limitations. Finally, we found it reasonable to restrict r_β to the range essentially probed by the stellar kinematic dataset, namely $\mathcal{O}(1)$ pc–$\mathcal{O}(10)$ kpc.

To perform our MCMC analysis, we make usage of the *emcee* package [232], which implements the affine invariant algorithm of ref. [311] as the basic tool to build up the proposal distribution for the random walk of the chains. For each of the eight considered galaxies, we let 500 walkers evolve for 2000 steps, starting from a neighbourhood of the best-fit point in the seven-dimensional parameter space, collecting a total of 10^6 samples. We remove the first half of them to account for the burn-in period and further check the auto-correlation length of the parameters in order to assess convergence. As a final validation of our numerical analysis, we test the possible appearance of multi-modal solutions, which are challenging to sample within an ordinary MCMC sampling algorithm. In order to do that, we repeat the full analysis of the eight objects by applying the default nested sampling method available with the *pymultinest* library [312], which implements the importance sampling algorithm proposed in ref. [313]. We used 1000 live points subjected to the same prior distributions as discussed above and adopted the default tolerance of 0.5 for the estimated remaining evidence as a stopping criterion. For all the NFW and Burkert fits, we found a remarkable agreement between the affine-invariant ensemble MCMC and the important nested sampling analyses, resulting in nearly identical posterior distributions.

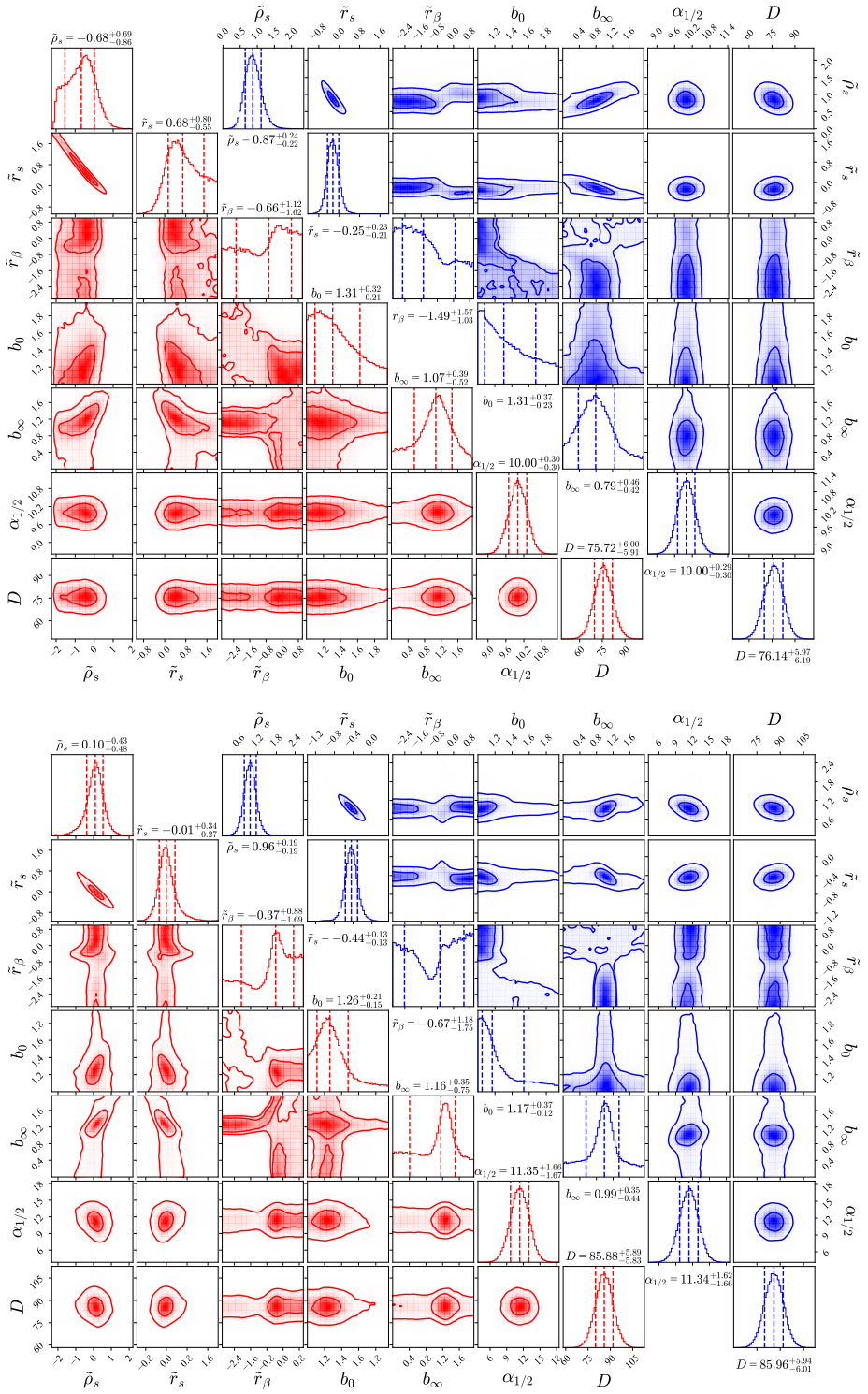

Figure 4.3: MCMC output of the estimated parameters from NFW and Burkert fits, respectively red and blue triangle plots, for Draco (upper panel) and Sculptor (lower panel). For each parameter, we report with dashed lines the 16-th, 50-th, 84-th percentile on the histogram of the marginalized posterior distribution. Correlations among the seven model parameters are also shown with the corresponding 68% and 95% highest probability regions. The parameter labels are defined as follows: $\tilde{\rho}_s = \log_{10}(\rho_s/\mathrm{GeVcm}^{-3})$, $\tilde{r}_x = \log_{10}(r_x/\mathrm{kpc})$ and $b_x = 2^{\beta_x/(\beta_x-1)}$, while $\alpha_{1/2}$ and D are in units of arcmin and kpc respectively.

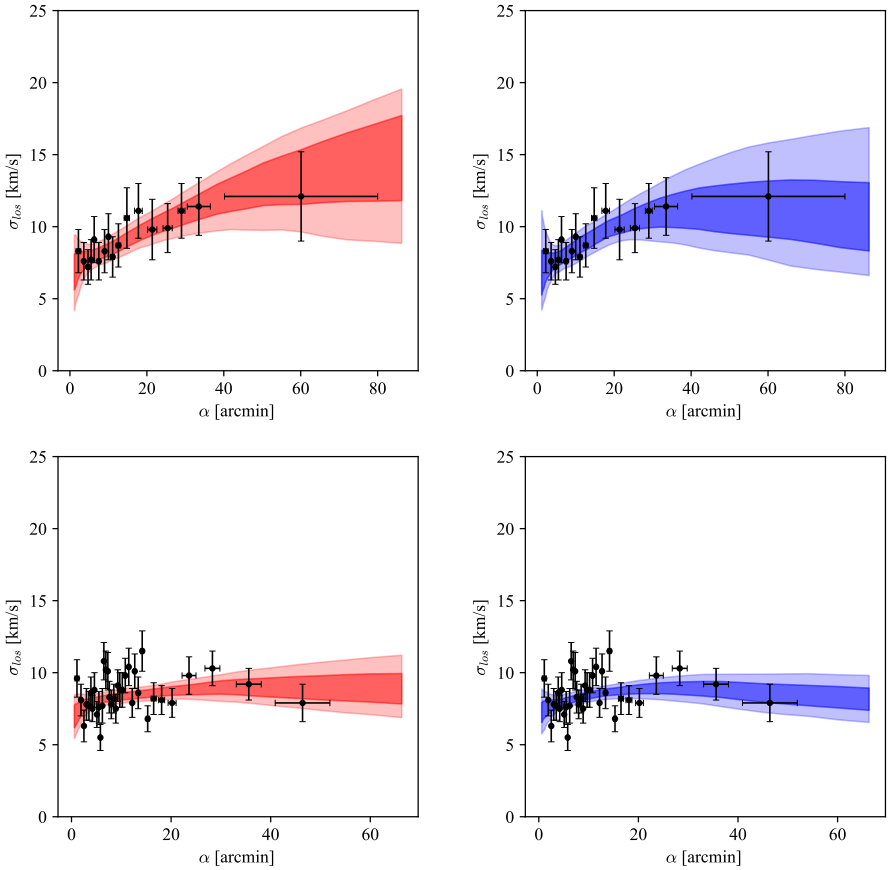

Figure 4.4: Predicted l.o.s. velocity dispersion profile and related kinematic data for Draco (upper panels) and Sculptor (lower panels) in terms of the angular distance from the centre of the dSph galaxy. In dark (light) colour we show respectively the 68% (95%) highest density probability region obtained assuming a NFW (left panels) or a Burkert (right panels) halo profile when fitting the spectroscopic measurements.

In figure 4.3 the outcome of our Bayesian fit on Sculptor and Draco datasets is shown, describing the underlying DM halo with the NFW (red triangle plot) or with the Burkert (blue triangle plot) profile. We report the one-dimensional marginalized posterior p.d.f. for each of the estimated parameters, highlighting the 16-*th*, 50-*th*, 84-*th* percentiles, and their joint probability distribution with the 68% and 95% highest probability density (h.p.d.) contours. While a strong correlation between the DM halo parameters emerges in all our fits, we can observe for the case of Draco and Carina that the NFW scenario is sensitive to the physically motivated upper-limit assigned on r_s. As a general trend, we find in NFW fits a non-negligible correlation among DM halo parameters and $\beta_{0,\infty}$, while for the fits with Burkert profile the correlation of the halo parameters with the inner trend of the stellar anisotropy gets substantially milder. Heliocentric distance and half-light angle show overall mild correlations in the bi-dimensional joint distributions with the rest of the fitted parameters. Finally, to provide a qualitative picture of the goodness of our fits, in figure 4.4 the 68% and 95% h.p.d. intervals for the predicted l.o.s. velocity dispersion profile in Draco and Sculptor are shown, together with their binned data points. As has been noted by previous authors, see, e.g., [295, 301, 314], both cuspy and cored profiles can provide an optimal description of the present stellar kinematics in MW classical dwarfs, if one allows for a flexible enough stellar anisotropy profile.

Bracketing the uncertainties

The main motivation for this research project was to accurately predict the expected prompt γ-ray emission from DM annihilations in a general setting, where the relevant cross-section can be velocity dependent. As already motivated in the introduction, the net effect can be nicely captured in a velocity-averaged enhancement factor:

$$\langle S(v_{\rm rel})\rangle(r) = \frac{1}{\rho^2_{\rm DM}(r)} \int d\vec{v}_1 f_{\rm DM}(r,\vec{v}_1) \int d\vec{v}_2 \; f_{\rm DM}(r,\vec{v}_2) S(|\vec{v}_{\rm rel}|) \; , \qquad (4.22)$$

which crucially enters the expression for generalized J-factor, as defined in equation (1.6), and simply reduces to 1 in case of velocity-independent annihilations. The concrete scenario that was addressed applies to models in which Sommerfeld effect is present, motivated by numerous DM phenomenological models, see e.g. [315–317], while arbitrary velocity dependence of the annihilation cross-section could be addressed in analogous manner. In this perspective, the key feature is the strong enhancement of the annihilation cross-section for highly non-relativistic (slow) particles that are charged under a force with light or massless mediator. In correspondence to these three regimes a subscript notation for the J-factors will be used, where $J_{\alpha-{\rm X}}$ denotes its value in the $S \propto v_{\rm rel}^{-\alpha}$ regime for phase-space model abbreviated by X (E for Eddington's inversion, MB for Maxwell-Boltzmann approximation, OM for Osipkov-Merritt model and β_c for the $\beta_{\rm DM}(r) = -1/2$ case). As an additional note, all of the results below were computed for $\alpha_\chi = 1/100$ and aperture of $\alpha = 0.5^\circ$ in the instrument acceptance cone $\Delta\Omega$, unless stated otherwise.

Figure 4.5 shows the dependence of J-factors on the combination of particle physics parameters ξ. The two panels refer again to the case of Draco (left panel) and Sculptor (right panel), while the three bands displayed are all computed under the assumption of isotropic velocities for PSDF given by Eddington's

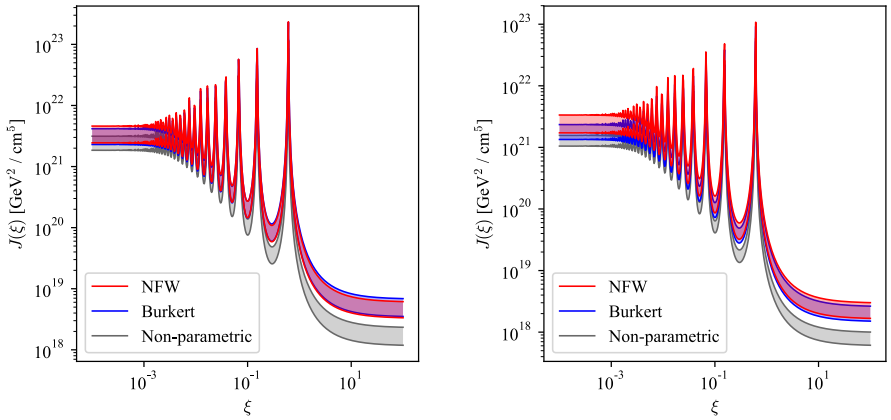

Figure 4.5: J-factor dependence on the parameter $\xi \equiv m_\phi / (\alpha_\chi m_\chi)$; the bands displayed correspond to the 68% highest density probability region obtained assuming a NFW, a Burkert or a non-parametric halo profile in case of Draco (left panel) and Sculptor (right panel).

inversion formula: they correspond to the 68% h.p.d. interval, derived from the above statistical analysis for the NFW and Burkert parametric profiles and by consistently propagating the errors on $R_{1/2}$ and D. The same plot also contains the results for "non-parametric" DM profile, which was obtained via Jean's inversion procedure under the assumption of flat stellar l.o.s. velocity dispersion and in the limit of circular stellar orbits, $\beta_\star \to -\infty$; more details regarding the derivation of this profile can be found in [318]. Each of the three bands in the plots shows the three limiting regimes of the Sommerfeld effect: for large values of ξ the standard, non-enhanced, values of J-factors are recovered. By decreasing ξ one first encounters the resonance peaks, at which huge boost can be obtained, up to factors of $\mathcal{O}(10^5)$, with the peak at the largest ξ (i.e. the one corresponding to $n = 1$ in equation (4.3)) providing the largest enhancement. By going to even lower values of ξ one enters the Coulomb limit, where the enhancement saturates at factors of $\mathcal{O}(10^3)$; while the corresponding boost is notably smaller than on the resonances, this regime requires less fine-tuning on particle physics parameters. In the same plot, the three bands clearly exhibit slight differences that arise among the considered density profiles. For both, Draco and Sculptor, we see larger net enhancement for cuspy density profiles (i.e. the NFW and reference non-parametric case), since they typically imply deeper potential wells and therefore these halos host colder particle populations at their centres. At the same time, the effect one finds for a given dwarf cannot be rigidly applied to another object since details of the enhancement depend on the preferred region in the parameter space. In general the larger the halo concentration, the larger the flux increase: e.g., in Draco we found that the fit in case of the NFW profile points to significantly larger r_s and lower ρ_s than for Sculptor, see figure 4.3, while for the Burkert profile the preferred regions in parameter space are closer one to the other; correspondingly we find a smaller relative boost in the NFW versus Burkert comparison for Draco, while it is appreciably more significant for Sculptor.

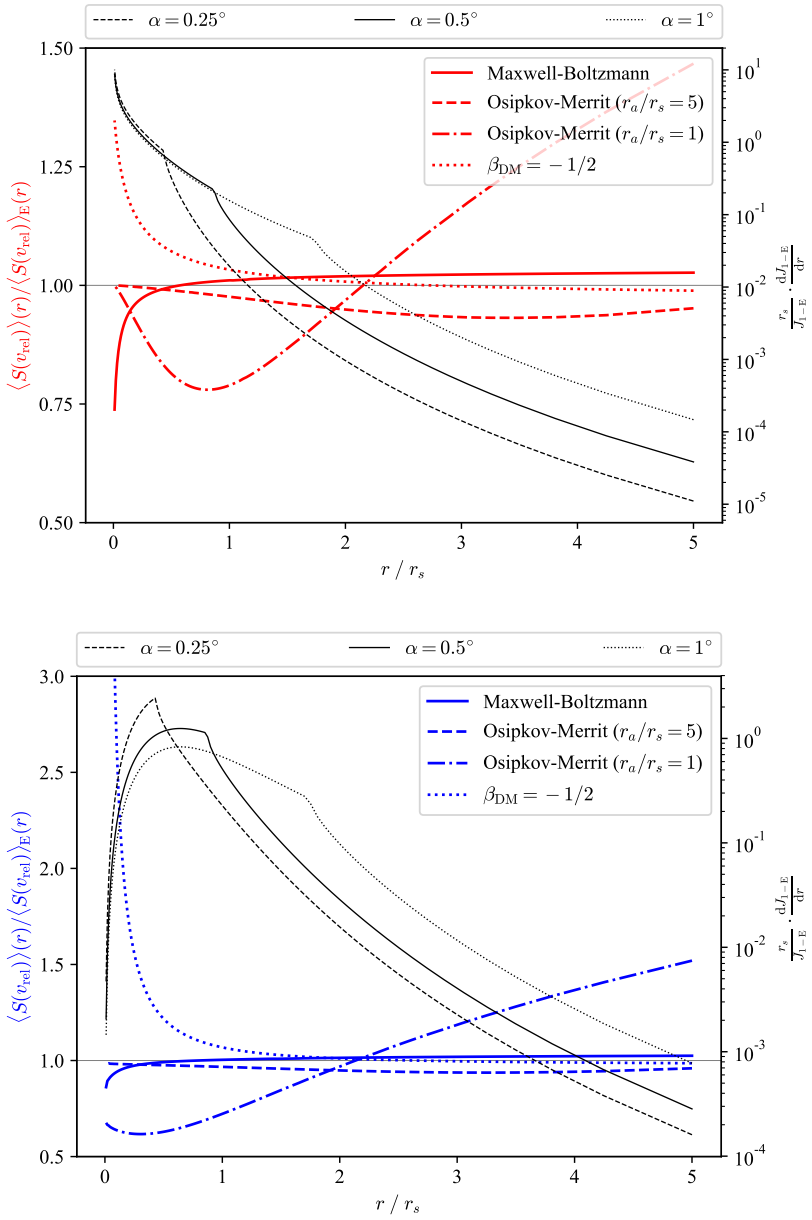

Figure 4.6: Rescaling of the velocity dependent factor $\langle S(v_{\rm rel})\rangle$ in case of a given PSDF with respect to the result obtained assuming Eddington's inversion formula, as a function of the radial distance r from the centre of the halo (thick coloured curves). To illustrate where such rescalings are relevant, we also show the normalized integrands in the formula for the J-factor, assuming the Eddington's model and the Coulomb regime for the Sommerfeld-enhancement, when the J-factor for an instrument pointing towards the centre of a spherical object is rewritten in terms of an integral over r; three different instrument angular apertures α are considered, having fixed the ratio of the object distance D to the scale length r_s to 100 (thin black lines). The upper (lower) panel assumes an NFW (Burkert) density profile for the DM halo.

As illustrated in the following, the choice of phase-space modelling also has a significant impact on the extrapolated enhancements, both when considering an approximation to the isotropic case, such as for the MB model introduced above, and even more drastically when one allows for anisotropic velocity distributions. In figure 4.6 we consider the ratio $\langle S(v_{\rm rel})\rangle(r)/\langle S(v_{\rm rel})\rangle_{\rm E}(r)$, comparing the velocity averaged enhancement of a given PSDF to the Eddington's case at the radial distance r from the centre of halo. The angular and line-of-sight integrals appearing in the definition of J-factor, see equation (1.6), when pointing towards the centre of a spherical object, can be reduced to an integral on r, while performing the other integrals analytically, as shown in the appendix of [318]. After rewriting J as $J = \int_0^{r_b} dr\, dJ/dr(r)$, where r_b is the outer truncation radius, the appropriately normalized ratio dJ/dr over J, assuming the Eddington's PSDF and the Coulomb regime for the Sommerfeld-enhancement, is plotted in figure 4.6 with thin black lines (with corresponding vertical axis scale at the r.h.s. of the plots; note that this scale is logarithmic). The three lines in each plot are for three different apertures α of the instrument acceptance cone $\Delta\Omega$. The curves for the NFW profile peak all at $r = 0$, while for the Burkert profile the largest contribution to J shifts towards $r \approx r_s$; analogous trends, but sharper, would also appear in the resonant regime of the Sommerfeld enhancement. This check provides visual guidance to the plots, indicating the intervals in r over which there is a significant impact on the expected annihilation flux, would a different DM velocity distribution provide a significantly different $\langle S(v_{\rm rel})\rangle(r)$. In figure 4.6 thick lines show this quantity as computed for the MB, OM, β_c PSDF over the result for the Eddington's case (now the vertical reference scale is on the l.h.s. of the plots). From the plot one can see that, for the NFW profile, the Maxwell-Boltzmann approximation gives a systematic (but numerical-friendly) underestimate of the true result in the isotropic case, since the corresponding curve is smaller than 1 at the peak of the contribution to J_1 (and even more so for J_2), while it gets marginally above 1 at large radial distances that are, however, practically unimportant for the J-factors. On the contrary, MB approximation performs much better for Burkert profile and, as will be shown later, provides very accurate estimates of the J-factors in both regimes of enhancement. Regarding the anisotropic PSDFs, one sees that even the very small bias on circular velocity introduced by the model with $\beta_{\rm DM}(r) = -1/2$, which increases the abundance of slow particles at the centre of the systems, leads to a significant boost of $J_{1,2-\beta_c}$ for both density profiles. Finally, for what regards Osipkov-Merritt model, $J_{1,2}$ tend to be smaller then in the isotropic case, which however becomes significant only when the suppression in $\langle S(v_{\rm rel})\rangle(r)$, which is maximized at r slightly below r_a, gets within the radial range relevant for the computation of $J_{1,2}$, namely if we consider r_a close to r_s for Burkert and $r_a \lesssim r_s$ for NFW profile.

With the general trends delineated in figure 4.6, we can now quantify the effect of Sommerfeld enhancement on annihilation fluxes coming from Milky Way classical dSphs for various DM phase-space models. From the samples obtained in the MCMC analysis described in section 4.3.1, the J-factor posterior distributions can be computed. Note that evaluation requires the non-trivial computational task of performing multidimensional integration for each of the recorded MCMC steps. In order to make the demanding numerics feasible, we resorted to the scaling relations explained in greater detail in appendix B. In figure 4.7 we show the J-factor p.d.f. for our benchmark galaxies, Draco and

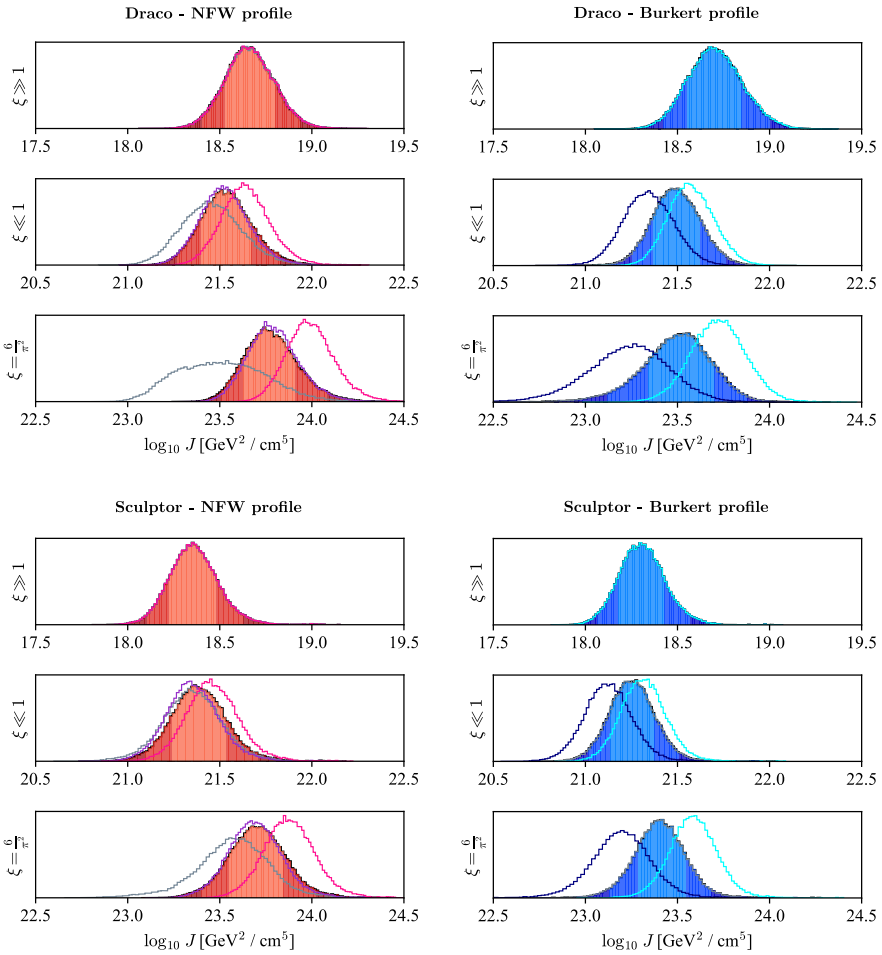

Figure 4.7: Posterior distributions of J-factors in the three regimes of enhancement. The upper and lower figures are respectively representing the study cases of Draco and Sculptor under the assumption of NFW (left) and Burkert (right) DM density profiles. The histograms with coloured 68% and 95% highest density probability regions were obtained using Eddington's inversion. Also, we report with grey lines the posterior related to the Maxwell-Boltzmann scenario, while with dark (purple for NFW and dark blue for Burkert) coloured lines the Osipkov-Merritt model, while we show with light coloured lines (pink for NFW and cyan for Burkert) the case of $\beta_{\rm DM} = -\frac{1}{2}$ modelling.

Sculptor. The foreseen trend from figure 4.6 is nicely met in our findings for J-factors, applied to dSph kinematic data. We see significant shifts in the peak of the distributions for the β_c model, and for the MB model with NFW profile, as well as the for OM model in the Burkert case. We also note that the width of distributions depends on the PSDF under consideration, most clearly visible by the increased spread for MB approximation in NFW case and OM model in the Burkert case. On the contrary, β_c model yields slightly narrower distributions, as the enhancement effect is dominated by the centre of halo resulting in lesser dependence on the structural parameters.

Most importantly, a summary of all the results is presented in figure 4.8. The obtained J-factors for the eight classical dSphs in the non-enhanced (left panel), as well as the enhanced regimes (right panel) are displayed. In the figure 68% h.p.d. intervals are shown, as extracted from the marginalized posterior distribution, while their exact numerical values, as well as 95% h.p.d. intervals, are given in table 4.1. In the left panel of figure 4.8, we also compare our results in the non-enhanced regime to some recent results in the literature; the good agreement with these — despite the several sources of differences concerning the parametrization of the stellar surface brightness profile, of the stellar anisotropy profile and the choice DM parametric profile, together with the prior adopted in the corresponding MCMC studies — comes as further validation of our analysis, as well as provides an illustration of the impact which these modelling assumptions can have. The results obtained for the non-parametric profile, derived under the assumption of circular orbits for stars, are reported in the plot as 68% lower limits since it was shown in [318] that this DM profile could be used to extrapolate conservative lower limit on (non-enhanced) J-factors. From the right panel of figure 4.8 we can read off the following trends: for NFW fits the difference between isotropic and OM model tends to be small, especially for objects that prefer large r_s (in particular, Draco and Carina), which we also adopted as the characteristic scale for the velocity anisotropy, i.e. $r_a = r_s$, to avoid the introduction of additional length scale that can not be constrained by observations. On the other hand, for the Burkert profile, we find stronger dependence on the PSDF anisotropy, which stands out in the same fashion for all the eight objects. In this respect, the prime targets for detection among the eight classical dSphs remain essentially the same as in the non-enhanced case, with slight improvement for Sculptor and Sextans, which we find to have more concentrated DM halos.[3] The effect of phase-space modelling turns out to be significant, as it is comparable to, or in some cases even exceeds, other uncertainties in the spherical Jeans equation approach and can be summarized as follows: when considering the Sommerfeld enhancement regimes, the OM model may indeed induce up to $\sim 30\%$ decrease in J-factors, compared to estimates with Eddington's inversion formula, while $\beta_{\rm DM} = -1/2$ can lead up to 50% increase. The use of MB approximation implies, in general, an underestimate of the flux, particularly in the case of singular or very concentrated DM profiles, while it is reasonably accurate for DM cores. Finally regarding the non-

[3]Regarding the peculiar shape of J_2 errors for Sextans assuming a NFW profile we need to underline that in this case our results are actually affected by choice of the inner cut-off radius $r_{\rm min}$ we need to introduce for numerical convergence: a significant number points in the MCMC chain end up at $r_s < r_{\rm min}$, leading to nearly identical J-factors; this results in central values lying right at the upper boundary of the 68% h.p.d. region, with the exception of OM model for which the contribution around r_s is suppressed.

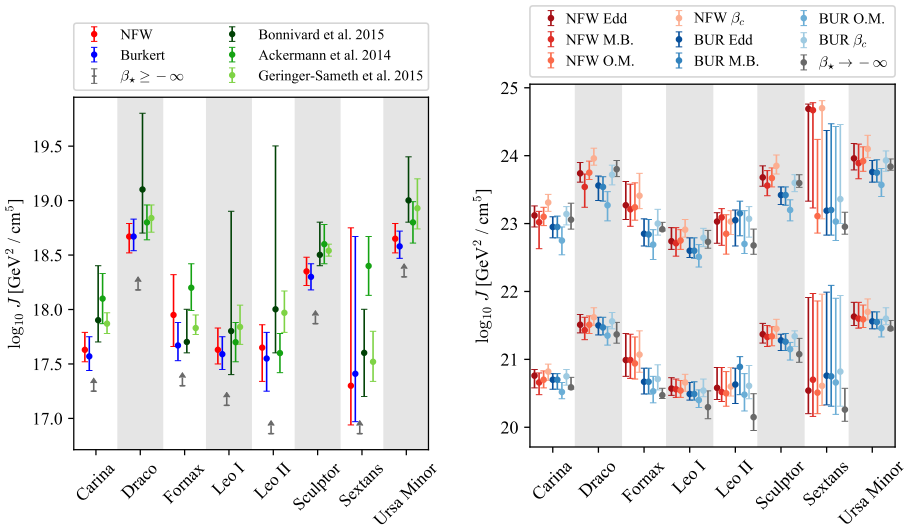

Figure 4.8: *Left*: comparison of our results for non-enhanced J-factors with previous works. *Right*: results for Sommerfeld-enhanced J-factors for different PSDF under consideration in the Coulomb regime (lower points) and resonant regime (upper points).

parametric approach of ref. [318], 68% h.p.d. intervals are shown in the right panel of figure 4.8, for which only the isotropic PSDF modelling was considered. Note that these do not correspond anymore to the most conservative cases for the extrapolated J_1 and J_2, which is due to the fact that this profile is still singular towards the centre and therefore receives a prominent gain in the expected flux from the Sommerfeld effect, compared to the cored profile. A more general analysis would be needed to find the new conservative lower limits in the two enhanced regimes; this is technically and numerically very challenging and beyond the scope of this work. Another flaw of this density profile is the fact that we cannot actually exploit the OM model to treat radially anisotropic DM configurations since one finds positive-definite PSDF only for $r_a/r_s \gtrsim 10$, being essentially equivalent to the Eddington's case. For this reasons we mostly find the lowest J-factors in the enhanced regime for the Burkert profile, which has a flatter central gravitational potential and can be eventually even further suppressed by adopting Osipkov-Merritt's DM orbital anisotropy. As for what regards β_c models in the context of non-parametric density profile, they are physical and can be computed, however, would yield higher J-factor, irrelevant for what concerns the problem of addressing conservative upper bound on the DM pair annihilation cross-section.

dSph	$\log_{10} J_0$	$\log_{10} J_{1-\mathrm{E}}$	$\log_{10} J_{1-\mathrm{MB}}$	$\log_{10} J_{1-\mathrm{OM}}$	$\log_{10} J_{1-\beta_c}$	$\log_{10} J_{2-\mathrm{E}}$	$\log_{10} J_{2-\mathrm{MB}}$	$\log_{10} J_{2-\mathrm{OM}}$	$\log_{10} J_{2-\beta_c}$
Carina	$17.63^{+0.16(0.29)}_{-0.11(0.23)}$	$20.76^{+0.09(0.24)}_{-0.18(0.30)}$	$20.66^{+0.14(0.31)}_{-0.18(0.31)}$	$20.70^{+0.13(0.26)}_{-0.12(0.24)}$	$20.82^{+0.11(0.25)}_{-0.13(0.24)}$	$23.12^{+0.14(0.32)}_{-0.17(0.27)}$	$23.02^{+0.16(0.35)}_{-0.39(0.58)}$	$23.10^{+0.14(0.31)}_{-0.13(0.24)}$	$23.31^{+0.12(0.28)}_{-0.13(0.23)}$
Draco	$18.67^{+0.12(0.26)}_{-0.15(0.27)}$	$21.51^{+0.15(0.31)}_{-0.12(0.24)}$	$21.43^{+0.19(0.36)}_{-0.14(0.28)}$	$21.51^{+0.13(0.28)}_{-0.13(0.25)}$	$21.62^{+0.14(0.28)}_{-0.12(0.24)}$	$23.74^{+0.16(0.34)}_{-0.13(0.24)}$	$23.54^{+0.19(0.42)}_{-0.30(0.45)}$	$23.75^{+0.17(0.33)}_{-0.10(0.22)}$	$23.96^{+0.15(0.30)}_{-0.10(0.21)}$
Fornax	$17.95^{+0.37(1.19)}_{-0.29(0.43)}$	$20.99^{+0.39(1.08)}_{-0.24(0.37)}$	$20.99^{+0.38(1.09)}_{-0.27(0.40)}$	$20.94^{+0.39(1.05)}_{-0.23(0.37)}$	$21.07^{+0.35(1.00)}_{-0.26(0.40)}$	$23.27^{+0.35(0.89)}_{-0.21(0.31)}$	$23.21^{+0.37(0.95)}_{-0.25(0.37)}$	$23.24^{+0.36(0.85)}_{-0.19(0.34)}$	$23.41^{+0.33(0.82)}_{-0.19(0.29)}$
Leo I	$17.63^{+0.20(0.43)}_{-0.13(0.24)}$	$20.57^{+0.16(0.36)}_{-0.10(0.21)}$	$20.56^{+0.15(0.36)}_{-0.12(0.24)}$	$20.54^{+0.15(0.34)}_{-0.10(0.20)}$	$20.66^{+0.12(0.30)}_{-0.13(0.23)}$	$22.74^{+0.20(0.39)}_{-0.12(0.25)}$	$22.71^{+0.23(0.46)}_{-0.19(0.46)}$	$22.75^{+0.16(0.34)}_{-0.13(0.25)}$	$22.91^{+0.15(0.31)}_{-0.11(0.22)}$
Leo II	$17.65^{+0.21(0.43)}_{-0.31(0.54)}$	$20.58^{+0.30(0.48)}_{-0.17(0.35)}$	$20.52^{+0.36(0.54)}_{-0.14(0.33)}$	$20.50^{+0.32(0.62)}_{-0.19(0.32)}$	$20.60^{+0.28(0.46)}_{-0.14(0.31)}$	$23.03^{+0.13(0.24)}_{-0.32(0.57)}$	$23.09^{+0.13(0.23)}_{-0.41(0.86)}$	$22.85^{+0.28(0.79)}_{-0.30(0.41)}$	$23.03^{+0.16(0.28)}_{-0.19(0.37)}$
Sculptor	$18.35^{+0.13(0.27)}_{-0.13(0.26)}$	$21.37^{+0.16(0.34)}_{-0.13(0.28)}$	$21.33^{+0.17(0.35)}_{-0.14(0.31)}$	$21.34^{+0.14(0.31)}_{-0.14(0.28)}$	$21.45^{+0.14(0.30)}_{-0.14(0.27)}$	$23.68^{+0.17(0.34)}_{-0.13(0.29)}$	$23.56^{+0.22(0.40)}_{-0.15(0.42)}$	$23.67^{+0.15(0.32)}_{-0.13(0.27)}$	$23.85^{+0.16(0.31)}_{-0.12(0.25)}$
Sextans	$17.30^{+1.45(2.49)}_{-0.36(0.38)}$	$20.54^{+1.37(2.15)}_{-0.34(0.39)}$	$20.70^{+1.27(2.02)}_{-0.54(0.64)}$	$20.51^{+1.35(2.17)}_{-0.31(0.38)}$	$20.61^{+1.35(2.08)}_{-0.29(0.34)}$	$24.69^{+0.07(0.09)}_{-1.36(1.92)}$	$24.67^{+0.11(0.18)}_{-1.44(2.20)}$	$23.11^{+1.13(1.78)}_{-0.25(0.39)}$	$24.70^{+0.11(0.33)}_{-1.63(1.70)}$
Ursa Minor	$18.65^{+0.14(0.34)}_{-0.13(0.26)}$	$21.63^{+0.21(0.44)}_{-0.13(0.28)}$	$21.60^{+0.24(0.48)}_{-0.14(0.34)}$	$21.59^{+0.21(0.44)}_{-0.12(0.24)}$	$21.70^{+0.19(0.42)}_{-0.12(0.24)}$	$23.96^{+0.22(0.41)}_{-0.17(0.35)}$	$23.89^{+0.28(0.49)}_{-0.23(0.63)}$	$23.92^{+0.21(0.42)}_{-0.15(0.28)}$	$24.10^{+0.20(0.38)}_{-0.13(0.26)}$

dSph	$\log_{10} J_0$	$\log_{10} J_{1-\mathrm{E}}$	$\log_{10} J_{1-\mathrm{MB}}$	$\log_{10} J_{1-\mathrm{OM}}$	$\log_{10} J_{1-\beta_c}$	$\log_{10} J_{2-\mathrm{E}}$	$\log_{10} J_{2-\mathrm{MB}}$	$\log_{10} J_{2-\mathrm{OM}}$	$\log_{10} J_{2-\beta_c}$
Carina	$17.57^{+0.18(0.40)}_{-0.13(0.25)}$	$20.70^{+0.09(0.23)}_{-0.14(0.27)}$	$20.70^{+0.09(0.22)}_{-0.14(0.27)}$	$20.52^{+0.14(0.28)}_{-0.10(0.24)}$	$20.75^{+0.10(0.23)}_{-0.13(0.24)}$	$22.95^{+0.15(0.35)}_{-0.16(0.40)}$	$22.95^{+0.16(0.36)}_{-0.16(0.40)}$	$22.75^{+0.20(0.42)}_{-0.21(0.52)}$	$23.14^{+0.11(0.28)}_{-0.16(0.32)}$
Draco	$18.67^{+0.16(0.32)}_{-0.13(0.25)}$	$21.50^{+0.12(0.26)}_{-0.14(0.26)}$	$21.47^{+0.15(0.29)}_{-0.11(0.22)}$	$21.35^{+0.13(0.27)}_{-0.14(0.27)}$	$21.56^{+0.13(0.26)}_{-0.11(0.22)}$	$23.56^{+0.14(0.31)}_{-0.22(0.46)}$	$23.54^{+0.15(0.32)}_{-0.21(0.45)}$	$23.27^{+0.20(0.41)}_{-0.23(0.48)}$	$23.72^{+0.14(0.30)}_{-0.15(0.29)}$
Fornax	$17.67^{+0.21(0.80)}_{-0.14(0.30)}$	$20.67^{+0.20(0.78)}_{-0.18(0.32)}$	$20.67^{+0.20(0.78)}_{-0.18(0.32)}$	$20.53^{+0.22(0.81)}_{-0.17(0.33)}$	$20.71^{+0.21(0.77)}_{-0.16(0.32)}$	$22.85^{+0.22(0.76)}_{-0.18(0.35)}$	$22.84^{+0.22(0.76)}_{-0.18(0.36)}$	$22.69^{+0.22(0.86)}_{-0.22(0.40)}$	$23.00^{+0.21(0.73)}_{-0.17(0.33)}$
Leo I	$17.59^{+0.16(0.38)}_{-0.14(0.26)}$	$20.49^{+0.17(0.37)}_{-0.09(0.21)}$	$20.49^{+0.18(0.37)}_{-0.09(0.21)}$	$20.40^{+0.15(0.37)}_{-0.11(0.22)}$	$20.54^{+0.17(0.36)}_{-0.09(0.21)}$	$22.60^{+0.19(0.47)}_{-0.10(0.21)}$	$22.60^{+0.19(0.46)}_{-0.11(0.21)}$	$22.51^{+0.18(0.50)}_{-0.15(0.27)}$	$22.79^{+0.14(0.38)}_{-0.13(0.23)}$
Leo II	$17.55^{+0.24(0.47)}_{-0.30(0.51)}$	$20.63^{+0.24(0.43)}_{-0.28(0.47)}$	$20.89^{+0.15(0.26)}_{-0.41(0.70)}$	$20.48^{+0.31(0.53)}_{-0.24(0.43)}$	$20.61^{+0.30(0.47)}_{-0.19(0.40)}$	$23.05^{+0.15(0.27)}_{-0.38(0.64)}$	$23.15^{+0.18(0.24)}_{-0.33(0.69)}$	$22.70^{+0.49(0.66)}_{-0.14(0.41)}$	$23.07^{+0.18(0.31)}_{-0.27(0.50)}$
Sculptor	$18.30^{+0.12(0.26)}_{-0.12(0.24)}$	$21.28^{+0.09(0.23)}_{-0.15(0.27)}$	$21.26^{+0.12(0.24)}_{-0.13(0.25)}$	$21.15^{+0.10(0.23)}_{-0.16(0.29)}$	$21.34^{+0.08(0.21)}_{-0.15(0.27)}$	$23.42^{+0.12(0.27)}_{-0.14(0.30)}$	$23.42^{+0.12(0.26)}_{-0.15(0.30)}$	$23.20^{+0.15(0.33)}_{-0.16(0.33)}$	$23.60^{+0.12(0.25)}_{-0.13(0.28)}$
Sextans	$17.41^{+1.26(2.27)}_{-0.44(0.52)}$	$20.76^{+1.23(1.97)}_{-0.43(0.69)}$	$20.75^{+1.34(2.13)}_{-0.44(0.67)}$	$20.66^{+1.24(2.03)}_{-0.47(0.77)}$	$20.82^{+1.12(1.89)}_{-0.51(0.68)}$	$23.19^{+1.18(1.70)}_{-0.36(0.81)}$	$23.20^{+1.27(1.79)}_{-0.37(0.80)}$	$23.03^{+1.40(1.91)}_{-0.28(0.95)}$	$23.36^{+1.10(1.54)}_{-0.36(0.72)}$
Ursa Minor	$18.58^{+0.14(0.30)}_{-0.11(0.23)}$	$21.56^{+0.14(0.33)}_{-0.11(0.22)}$	$21.55^{+0.15(0.33)}_{-0.10(0.21)}$	$21.46^{+0.13(0.32)}_{-0.13(0.26)}$	$21.60^{+0.16(0.34)}_{-0.09(0.20)}$	$23.76^{+0.17(0.40)}_{-0.15(0.31)}$	$23.75^{+0.19(0.41)}_{-0.14(0.31)}$	$23.57^{+0.24(0.50)}_{-0.17(0.37)}$	$23.93^{+0.14(0.37)}_{-0.16(0.28)}$

Table 4.1: J-factors with 1σ (2σ) errors for the 8 dSph with NFW and Burkert density profile.

5. Hunt for Dark Matter substructures

One of the characteristic predictions of the cold (i.e. heavy non-relativistic and collisionless) DM paradigm is its hierarchical clustering. Observations, spanning scales from several Gpc down to a fraction of Mpc, give an excellent match to the matter power spectrum predicted within the standard cosmological model, as can be seen from figure 1.3. However, the study of galactic DM distribution turns out to be much more demanding, since it, on one side, requires highly precise astronomical measurements and, on the other, dealing with non-linear structure growth and baryonic processes. None-the-less, constraining the behaviour of DM on small scales seems a promising way of obtaining new insights into the particle properties of DM, since many alternatives to the cold DM hypothesis involve suppression of DM clustering on small scales, among which most prominent examples are warm [46, 319, 320], self-interacting [321] or fuzzy DM [62, 63]. Additionally, the study of DM through its gravitational effects has proven to be essential, given that no undisputed detection has been achieved so far in direct and indirect searches or particle colliders, despite decades of efforts. At the same time, a better understanding of sub-galactic DM distribution could help further improving the constraints on its non-gravitational interactions with ordinary matter, either through improved DM modelling in direct detection or discovering new prime targets for indirect searches.

Significant progress in addressing the DM clustering properties on small scales has been recently made through strong lensing observations, sensitive to substructures down to $10^8 M_\odot$ [67, 68]; this is expected to improve even further in the near future with upcoming sky surveys [322, 323]. Similarly, valuable new astrometric data opened novel opportunities for studying DM distribution within the Milky Way. In section 3.2 a compilation of recently updated stellar kinematics was used to constrain two sample phenomenological DM density profiles. The latter assume smooth DM distribution over the entire galaxy, which is, however, in disagreement with the prediction of the cold DM paradigm. Thanks to the significant improvements in observations, new insights came from various probes, ranging from searches for gravitationally bound groups of metal-poor stars [324–326], as was traditional done to identify dwarf satellite galaxies and/or globular clusters, to more recently proposed techniques, such as analysis of gaps in stellar streams left behind accreted objects [128, 129], searching for wakes in the distribution of stars [327, 328] or detecting tidal heating of bound structures [130].

This chapter will be devoted to a novel approach in the efforts to shed light on

galactic DM substructure. Similarly to the techniques mentioned above, it relies on gravitational signatures left by DM subhalos in the distribution of surrounding stars. As it was already noted in [327], subhalos with masses $M_{\rm sub} \gtrsim 10^7 M_\odot$ should induce observable features in the phase-space distribution of galactic stellar populations. With the recent release of Gaia's astrometric data [329], it has become possible to search for subhalo signatures over a significant portion of our galactic neighbourhood with unprecedented precision. Additionally, new modern tools for reducing large and complex datasets have been developed, which allow us to go step further than the standard likelihood analyses. For the problem at hand perhaps the most interesting progress comes from the field of computer vision, where highly efficient convolutional neural network (CNN) models have been introduced, allowing for incredibly sophisticated extraction of information from image-like data – for a review on the topic see, e.g., [330,331]. After briefly discussing the DM properties that could be addressed through the study of DM subhalo abundance, I will explore the possibility to detect dark substructure in the galactic stellar field through the use of CNNs. While further research is required in order to apply it to real observations, the study of mock datasets, presented at the end of this chapter, indicates good prospects for such an approach.

5.1 Particle properties encoded in small scale distribution of DM

Non-linear gravitational clustering of cold DM particles is expected to produce self-similar structure over a vast range of scales [332, 333]. While the size of the largest perturbations is effectively set by the Hubble scale, since super-horizon modes are protected from gravitational collapse, their minimal size is in many models determined by the temperature of DM, establishing a scale below which the DM is expected to "free-stream". Furthermore, any DM structure existing below the free-streaming length is expected to be washed out by the thermal motion of DM particles, which would results in a sharp cut-off in the matter power spectrum below that scale. For standard WIMPs the dynamics of thermal decoupling typically implies existence of DM subhalo with masses well below $M_{\rm sub} = 10^{-4} M_\odot$ [334, 335], which is much smaller then the foreseeable accuracy of astronomical measurements. On the other hand, in models of hot DM, which is assumed to decouple ultra-relativistic and became non-relativistic only in the matter-dominated era, the free-streaming length can be estimated as [336]:

$$\lambda_{\rm FS} \approx 36 \text{ kpc } \cdot g_d^{-1/3} \left(\frac{\text{keV}}{m_\chi} \right) , \tag{5.1}$$

where g_d is the number of relativistic degrees of freedom at the time of decoupling. While hot DM has already been ruled out, warm DM, which decoupled relativistic and became non-relativistic soon thereafter, is still in agreement with observations. While the latter requires more careful treatment in order to obtain the corresponding $\lambda_{\rm FS}$, the effect on structure formation is analogous to the one of hot DM and typically leads to the suppression of matter power spectrum below the scales ranging from several to a fraction of kpc. These estimates are,

however, valid only for thermally produced DM. On the contrary, in the case of non-thermally produced light bosons, the formation of condensates generally allows them to be consistent with cold DM predictions even at much lower DM masses. As already mentioned in the introduction, this changes for $m_\chi \lesssim 10^{-22}$ eV, where the quantum effects start dominating the behaviour on kpc scales. The minimal possible clustering size for such ultra-light bosons can be estimated to lie around the corresponding de-Brogli wave-length, give by equation (1.4). Additionally, the small scale properties of DM clustering could also be affected by elastic scatterings within the dark sector. In particular, such self-interactions could lead the central part of DM halos, which reach sufficiently large densities, to form isothermal cores. In this work, I will avoid addressing the vast range of concrete scenarios that could be realized in nature – a comprehensive approach for mapping different classes of particle physics models into the corresponding matter power spectrum has, for example, been formulated within the framework of Effective Theory of Structure Formation (ETHOS) [337].

Besides the microphysics of DM, the small scale matter power spectrum also crucially depends on the resilience of substructure against tidal disruption and violent baryonic processes, which are both expected to dominate the subhalo abundance in the central parts of galaxies. Dedicated high-resolution numerical simulations suggest that cuspy DM subhalos can survive tidal shocks caused by the gravitational potential of host halo and/or baryonic disks [175, 179, 338], even though they lose the majority of their mass during the successive crossings of the perihelion. The predicted mass and number densities of DM subhalos in the Milky Way for a recently suggested model [169], assuming cold DM with minimum halo mass $M_{\rm sub} = 10^{-4} M_\odot$, is shown in figure 5.1, for two extreme cases of tidal disruption efficiencies (the latter is defined as the ratio between the corresponding tidal and scale radius, $\epsilon = r_t/r_s$, at which the object is considered as disrupted; "fragile subhalos" are defined to be disrupted when $\epsilon \leq 1$, while "resilient subhalos" are defined to survive until $\epsilon \leq 0.01$). On the contrary, cored DM subhalos tend to be disrupted much more easily and their abundance in Milky Way-like galaxies is expected to be strongly suppressed within the galactocentric distance of $D \sim 10 - 20$ kpc – see, e.g., [178, 180, 339], where unresolved central structure effectively makes the subhalos behave as cored [179, 338]. Consequently, the detection of sub-galactic DM structures would be a strong indicator in favour of cold DM hypothesis, casting doubt on a wide range of alternative candidates, ranging from sterile neutrinos, ultra-light bosons to self-interacting DM models, which all predict DM cores. Furthermore, potential newly discovered nearby subhalos could serve as excellent indirect detection targets due to their proximity and weak gravitational field, harbouring minimal amounts of baryonic contaminants. Detection of nearby DM subhalos could also provide essential corrections to the models of local DM distribution, used in the interpretation of direct detection experiments, implying larger local DM density and modifications in its velocity distribution.

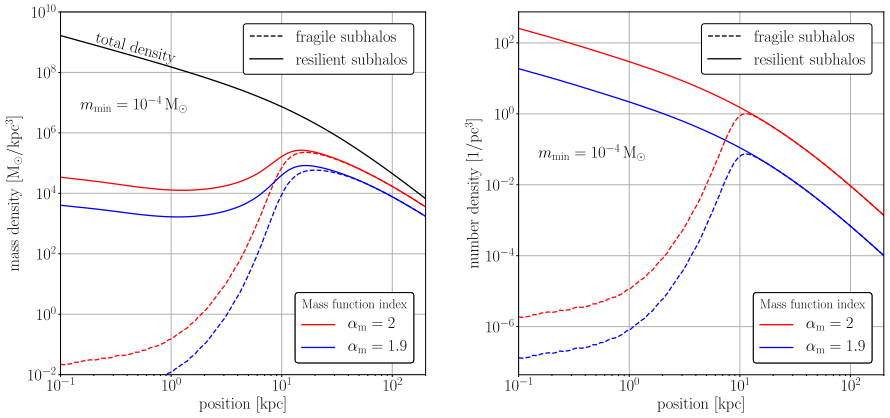

Figure 5.1: The predicted mass (left plot) and number (right plot) densities of subhalos as a function of galactocentric radius, assuming cold DM with minimum mass of subhalos $M_{\rm sub} = 10^{-4} M_\odot$ and two different mass function indices. The full line corresponds to subhalos, which are highly resilient to tidal disruption effects (defined as bound until tidal radius reaches 1/100 of their scale radius), while the dashed line shows the result for halos fragile subhalos (considered disrupted when the tidal radius becomes equal to halo's scale radius). The results are taken from [169]

.

5.2 A look at the galactic stellar field through computer vision

Recent Gaia's second data release (DR2) allows for unprecedented precision in the study of Milky Way's stellar field. The improvements over previous catalogues are two-fold: primarily, it provides the largest dataset ever compiled, covering several millions of stars in our galactic neighbourhood, and secondly, it provides the most accurate global measurements of stellar positions and parallaxes, typically reducing the uncertainty by order of magnitude compared to older surveys. Gaia-era data, therefore, grants us a new window into the details of dynamics and evolution of our galaxy.

While the importance of the Gaia mission for astrophysics has been well recognized, its possible implications for the studies of DM have received lesser attention. Interesting claims have been made in the context of Milky Way formation, by identifying several populations of stars that were most probably accreted through past mergers. Based on numerical simulations, it was argued that these stars should exhibit similar kinematic properties as the DM that was accreted along with them [191,192]. Apart from this, several attempts have been made to asses the amount of DM subhalos through the study of tidal streams of globular clusters [340,341], however, such approaches had limited results, since they are sensitive only to relatively small volume around the stream and perturbations similar to the ones sourced by DM subhalos could be produced by various other galactic structures. In this section, I will explore the possibility of inferring information about DM substructure by means of full 6D stellar phase-

space measurements. Such possibility was previously considered by Buschmann et al. [328]. However, their proposed analysis relies on the assumptions that DM subhalos have a cored Plummer density profile and that the surrounding stellar field is homogeneous with isotropic Gaussian velocity distribution, which are very restraining approximations. Instead, the approach advocated here is applicable to the number density and velocity distributions as measured by Gaia satellite, as well as an arbitrary DM density distribution within the subhalos. Furthermore, in contrast with the work of Buschmann et al., which relied on likelihood-based analysis of the data, I will instead make use of the state-of-the-art computer vision tools, which allow for highly accurate extraction of features from extensive datasets at a relatively small computational cost. In particular, the ability of deep CNNs to recognize the characteristic subhalo-induced patterns in spatial and velocity distributions of stars will be explored. As it is typically the case in virtually all practical applications of machine learning, the success crucially depends on the quality of training data. Since the results presented here are only the first step in the exploration of possibilities that CNNs offer in this particular context, a simplified problem will be addressed, where additional perturbations of the stellar field due to, e.g., globular clusters or giant molecular clouds will be neglected. Furthermore, only homogeneous stellar field with Gaussian velocity distribution will be considered, however, a generalization to an arbitrary stellar distribution can be easily achieved.

In the following, I will first discuss the feasibility of detecting small perturbations in stellar kinematics sourced by DM substructures. This will be followed by a discussion of the algorithm for generating the mock realizations of the stellar catalogue in presence/absence of DM subhalos, which will serve as training data for the CNN. This will be followed by details regarding the implementations of a simple classifier network, designed to detect the number of subhalos in a specific mass range within a sample dataset. Finally, an empirical criterion for the detectability of substructure with CNN will be proposed, estimating the smallest DM subhalo mass that can be found in a stellar field with a given number density and velocity dispersion.

5.2.1 Detectability of subhalos

The existence of DM, and our present knowledge about it, was inferred from various observations that are sensitive to its gravitational influences, while its coupling to other forces remains elusive. Therefore, exploring the possibilities of detecting perturbations induced by DM substructure in the galactic stellar field seems a promising way of learning new insights into the nature of DM particles. There is a number of factors that determine whether such signatures can actually be found in observational data. Evidently, the mass of the subhalo plays a crucial role, since it is directly proportional to the force exerted on surrounding stars. However, stellar number density and kinematic properties are also important, as they determine the sample size and noise level for studying the perturbations. Finally, when addressing real observations, one needs to take into account also measurement errors, which make convincing detections even more difficult.

To get an estimate of the gravitational perturbation caused by a DM subhalo, one can simply compute the variation in stellar kinetic energy in the vicinity of

a compact clump with mass $M_{\rm sub}$:

$$\delta T = \frac{GM_{\rm sub}}{\Delta r} \qquad \text{with} \qquad \Delta r^{-1} = r_{\rm min}^{-1} - r_{\rm max}^{-1} \,, \tag{5.2}$$

where $r_{\rm min}$ and $r_{\rm max}$ are the minimal and maximal distance of the considered star to the centre of subhalo, while G is the gravitational constant. To detect the perturbation of size δT the signal must be at least of the same order as the noise. Given a stellar population with velocity dispersion $\sigma_\star$ and typical measurement error $\delta v_\star$, one can estimate the uncertainty in kinetic energy:

$$\delta T \sim \sigma_\star \cdot \delta v_\star \,. \tag{5.3}$$

Since the velocities of individual stars are just random samples from their overall probability distribution, not much can be learned from the trajectories of single star. Observations become useful only when nearby stars are binned together and local variations of kinematic properties are studied. This, however, induces additional shot noise due to extracting average quantities from a finite sample. For a Gaussian distribution, one can show that the variance in inferred velocity dispersion equals to:

$$\mathrm{Var}(\sigma_\star) = \frac{2\sigma_\star^4}{N_b - 1} \,, \tag{5.4}$$

where N_b is the number of stars in a given bin. Therefore, by demanding that the signal is of the same order as the combined noise of measurement errors and binning in volume elements with characteristic length δr, one obtains:

$$\frac{GM_{\rm sub}}{\delta r} \sim \sigma_\star \cdot \delta v_\star + \sigma_\star^2 \cdot \sqrt{\frac{2}{N_b - 1}} \,, \tag{5.5}$$

$$\Rightarrow \hat{M}_{\rm sub} \sim \frac{\sigma_\star \cdot \delta r}{G} \left(\delta v_\star + \sigma_\star \sqrt{\frac{2}{N_b - 1}} \right) \,. \tag{5.6}$$

The above expression provides an order-of-magnitude estimate for the minimum subhalo mass, $\hat{M}_{\rm min}$, that could be detected in a particular catalogue of stars. Furthermore, from the above expression one can also obtain an estimate for the optimal bin size δr in the corresponding stellar field with average mapped number density $n_\star$:

$$\delta r \sim \left(\frac{\sigma_\star}{\sqrt{2n_\star}\, \delta v_\star} \right)^{2/3} \,, \tag{5.7}$$

where the number of stars per bin in equation (5.6) was approximated by $N_b \approx n_\star \cdot \delta r^3$. Note that for successful application of the suggested method δr must be smaller then extent of the mapped stellar field. Gaia's second data release provides us with accurate 6D phase-space measurements for several million stars within a radius of nearly 10 kpc from Earth, which amounts to average stellar density $n_\star \sim 10^3$ kpc^{-3}, with the accuracy of velocity measurements $\delta v_\star \sim 5$ km/s, while the typical velocity dispersion of galactic stars is in the range of $\sigma_\star \sim 50$ km/s. This implies:

$$\delta r \sim 0.4 \text{ kpc} \cdot \left(\frac{\sigma_\star}{50 \text{ km/s}} \right)^{2/3} \left(\frac{\delta v_\star}{5 \text{ km/s}} \right)^{-2/3} \left(\frac{n_\star}{10^3 \text{kpc}^{-3}} \right)^{-1/3} \,, \tag{5.8}$$

$$\hat{M}_{\rm min} \sim 10^7 \, M_\odot \cdot \left(\frac{\sigma_\star}{50 \text{ km/s}} \right)^{5/3} \left(\frac{n_\star}{10^3 \text{kpc}^{-3}} \right)^{-1/3} \left(\frac{\delta v_\star}{5 \text{ km/s}} \right)^{1/3} \,. \tag{5.9}$$

As can be seen from the above estimates, there is good hope to detect DM subhalos with masses down to $10^7\ M_\odot$ through the high quality data that has recently became available. Successful detection of a single subhalo in this mass range could rule out many alternatives to the cold DM hypothesis, while the absence of compelling signals would be harder to interpret due to large uncertainties in the expected abundance of subhalos and their distribution within the Milky Way. Fortunately, significant improvements in the coverage and accuracy of observations are expected with the future Gaia data releases [342], but also upon combining their results with other surveys such as the ones planned for LSST [323,343] and other large telescopes [69], increasing the probability to encounter a subhalo with $M_{\rm sub} \gtrsim \hat{M}_{\rm sub}$ in the mapped stellar field. On the other hand, from equation (5.9) one can see that the smallest detectable subhalo mass strongly depends on the $\sigma_\star$ and hence studying cold stellar populations, such as α-rich disk stars, could lead to significantly lower $\hat{M}_{\rm sub}$. However, this comes at the cost of reducing the probed region of the galaxy and hence lower probability to find a subhalo in the considered volume, while the corresponding decrease in the number of tracer stars with respect to the entire catalogue should have a sub-dominant effect due to the weak (inverse cubic root) dependence of $\hat{M}_{\rm sub}$ on $n_\star$.

5.2.2 Generation of mock data

The Gaia mission provides stellar positions, parallaxes and proper motions for several hundred millions of stars. However, to pursue our goal, the full 6D phase-space information of the stellar field is needed. The latter is unfortunately available only for a subset of stars, for which also the radial velocities are determined. This amounts to roughly 7 million objects, most of which lie within 10 kpc of Earth. There are several publicly available catalogues, e.g. the official Gaia DR2 online archive [1], a catalogue with computed galactocentric distances and velocities in the standard galactic coordinates, compiled by Marchetti et al. [344], or the one by Sanders et al. [345], which combines Gaia DR2 astrometry and spectroscopic measurements of APOGEE, GALAH, LAMOST, RAVE and SEGUE.

In order to produce mock stellar field, which contains dark subhalos with known abundance and properties, there are several possible approaches. Buschmann et al. [328] derived an equilibrium distribution function for stars in the vicinity of a DM subhalo with Plummer density profile. However, their solution assumes homogeneously distributed stars with isotropic Gaussian velocity distribution. For the task at hand, I will make use of a different approach, in which the distribution of stars can be similar to the one inferred from observations. Such mock dataset can be constructed by dividing the observed volume of the galaxy in bins, where each of them is populated with stars following some given net properties, namely the number density and velocity distribution, at the corresponding location. These can be inferred from the observations, however, they need to be averaged over scales much larger than the expected size of DM perturbation, in order to avoid including unknown structures in the synthetic stellar field. In practice, this can be achieved by binning the mapped stars in relatively large spatial bins and then smoothly interpolating the number den-

[1] https://gea.esac.esa.int/archive/

sity and moments of velocity distribution over the finer grid that is used for constructing the mock dataset. Such smoothed stellar field then needs to be endowed by DM substructure and its phase-space distribution updated according to the gravitational effects of the inserted subhalos. This can be done in the following steps: first one picks the subhalo position, $\vec{r}_{\rm sub}$, velocity, $\vec{v}_{\rm sub}$ and mass, $M_{\rm sub}$, which allows one to determine the characteristic radius, r_g, at which the gravitational potential of the subhalo is comparable to the typical uncertainty in stellar velocity. Making use of the relation (5.5), one can define:

$$r_g \equiv \frac{G M_{\rm sub}}{\sigma_\star \left(\delta v_\star + \sigma_\star \sqrt{\frac{2}{N_b - 1}} \right)} \,, \tag{5.10}$$

which is to be used for determining whether a given star at position $\vec{r}_\star$ is considered as perturbed or the gravitational effects of the subhalo can be neglected. While such criterion guarantees that the change in stellar kinetic energy is below the typical measurement error, one could worry that there is a non-negligible effect on the direction of its velocity, if the star passed sufficiently close to the subhalo in the past. The probability for such a close encounter, however, falls of as $(\vec{r}_\star - \vec{r}_{\rm sub})^{-2}$ and can also be safely neglected. On the other hand, stars that are within the characteristic radius (i.e. $|\vec{r}_\star - \vec{r}_{\rm sub}| < r_g$) receive non-negligible correction, which can be computed according to the standard results for scattering in a central potential. For each such stars first the elapsed time, t_0, and the corresponding position, $\vec{r}_{0,\star}$, since entering the radius of influence of the subhalo is determined:

$$|\vec{r}_{\rm rel} + t_0 \cdot \vec{v}_{\rm rel}| = r_g \quad \text{where} \quad \vec{r}_{\rm rel} = \vec{r}_\star - \vec{r}_{\rm sub} \quad \text{and} \quad \vec{v}_{\rm rel} = \vec{v}_\star - \vec{v}_{\rm sub}$$

$$\Rightarrow \; \vec{r}_{0,\star} = \vec{r}_\star - t_0 \cdot \vec{v}_\star \,, \tag{5.11}$$

$$t_0 = \frac{1}{v_{\rm rel}^2} \left(\vec{r}_{\rm rel} \cdot \vec{v}_{\rm rel} \pm \sqrt{(\vec{r}_{\rm rel} \cdot \vec{v}_{\rm rel})^2 + v_{\rm rel}^2 (r_g^2 - r_{\rm rel}^2)} \right) \,. \tag{5.12}$$

From the point $\vec{r}_{0,\star}$ one can then compute the stellar trajectory under the influence of an arbitrary gravitational potential $\Phi(r)$. The problem can be simplified by moving to the scattering plane, where the trajectory becomes two dimensional and can be described in terms of the azimuthal angle ϕ and time t as a function of radial distance r (i.e. distance from the center of the potential) [346]:

$$\phi(r) = b \int_{r_{\rm min}}^{r} \frac{{\rm d}x}{x^2 \sqrt{1 - b^2/x^2 + \Psi(x)}} \,, \tag{5.13}$$

$$t(r) = \frac{1}{|\vec{v}_\star - \vec{v}_s|} \int_{r_{\rm min}}^{r} \frac{{\rm d}x}{\sqrt{1 - b^2/x^2 + \Psi(x)}} \,, \tag{5.14}$$

$$\text{where} \quad b = |\vec{r}_{0,\star} \times \vec{v}_{\rm rel}| \,/\, |\vec{v}_{\rm rel}| \quad \text{and} \quad r_{\rm min} = \frac{G M_{\rm sub}}{v_{\rm rel}^2} \left(\sqrt{1 + \left(\frac{b\, v_{\rm rel}^2}{G M_{\rm sub}} \right)^2} - 1 \right)$$

are the impact parameter and the distance of closest approach, respectively. By evaluating this solutions for the elapsed time since entering in the gravitational range, r_g, and mapping it back to the galactic coordinate frame, one can then

determine the actual position and velocity of each perturbed star. For a Keplerian potential (i.e. subhalos approximated by a point-mass) the above integrals admit an analytical solution, while the modified stellar positions and velocities can be obtained numerically for an arbitrary spherical gravitational potential. Additionally, this procedure of synthesizing the Milky Way stellar field is relatively robust against the inhomogeneities in fiducial distribution, provided that they correspond to scales sufficiently larger then r_g. Furthermore, it is also capable of accounting for spacial dependence of the stellar velocity distribution, which does not need to be Gaussian nor isotropic. Note that none of these features are possible in the analytical approach developed by Buschmann et al. [328]. In the following, however, the simplified case of homogeneous stellar field with Gaussian velocity distribution will be considered for the sake of comparing the generated datasets to the analytical solution. An example of the produced dataset is presented in figure 5.2, along with predictions of the analytical model.

Search for DM subhalo signatures using CNN

Identifying gravitational perturbations induced by DM subhalos traversing the stellar field turns out to be a rather complicated task. The observations, as well as faithful mocks, form a 6D phase-space populated with millions of individual stars. There are several possible approaches for detecting subtle patterns in such datasets. In astronomy, the wavelet transform was probably one of the most extensively used techniques and represents the standard tool for identifying globular clusters and dwarf satellite galaxies from photometric images, see, e.g., [347–349], however, as such is sensitive only to stellar number density. Another possibility are algorithms designed to detect clusters in the higher-dimensional parameter spaces, e.g., Gaussian mixture models or their refined variations such as extreme deconvolution [350]. On the other hand, modern techniques of machine learning have recently lead to major advances in the analysis of such high-dimensional datasets. For the task at hand, CNNs are particularly convenient as they are highly efficient for detecting characteristic features in noisy input data and exhibit translational invariance (for recent reviews see, e.g., [330, 331]). Furthermore, the machine learning algorithms use training data to teach themselves what are the relevant patterns, while in case of the wavelet transform or Gaussian mixture models additional manual input and/or further assumptions are often required.

The CNN used in this study is constructed in such a way that it takes stellar number density distribution and first two moments of the velocity distribution as its input and returns the probabilities for a given dataset to contain a certain number of subhalos. Since not more then a few detectable DM clumps are expected within the portion of galaxy mapped by Gaia, one can use a classifier network, where each output class corresponds to a fixed number of subhalos contained in the given volume. The input data, therefore, comprises of seven 3D grids, which can be from the machine learning perspective interpreted as images, and correspond to spatially binned information regarding the stellar number density, as well as average velocities and velocity dispersions along the three coordinate axes. These seven grids are referred to as channels, since in the conventional application of CNNs to images they represent different colour channels of the image. An especially useful feature of CNNs is the fact that

Layer	Output shape	Number of parameters
Conv3D	(20,20,20,32)	6080
BatchNormalization	(20,20,20,32)	80
Dropout	(20,20,20,32)	0
MaxPooling	(10,10,10,64)	0
Conv3D	(8,8,8,32)	27680
BatchNormalization	(4,4,4,32)	16
Dropout	(20,20,20,32)	0
MaxPooling	(4,4,4,32)	0
Flatten	64	0
Dense	64	131136
Dense	32	2080
Dense	3	99

Table 5.1: Simple CNN used for classifying the amount of DM subhalos in a give stellar field. The expected inputs are seven $22 \times 22 \times 22$ grids, containing the spacial information regarding the stellar number density and the three components of the first two moments of the velocity distribution. In total the model has 167091 trainable parameters.

they simultaneously cross-correlate the signals at a given spatial position in the image across all the channels, which results in surprisingly high sensitivity for the characteristic patterns exhibited by the stellar field perturbed by the DM subhalos. Furthermore, the translational invariance of CNNs greatly reduces the number of required training samples, since the spatial position of signals becomes irrelevant, and the network is automatically capable of recognizing it anywhere within the grid. Besides just extracting the number of dark subhalos in a given dataset, there is good hope to transform the described neural network from a classifier into a regression model, able of quantifying the mass of perturber, as well as its location and velocity. In this preliminary study I, however, consider only the simpler case of classification network, since regression models can be constructed only for a known fixed number of embedded subhalos and would, therefore, serve as second step in the analysis of data.

The above network was constructed through Python implementation of Keras library [351]. It uses 3D convolutional layers, each followed by batch normalization, drop-out and max-pooling layer, which then connect to final dense layers. Each convolutional layer contains a number of filters, which are trained to produce positive signals when convoluted with the part of the stellar field that contains the sought-after pattern. By stacking multiple convolution layers, one increases the robustness and the range of features that can be learned. The subsequent normalization and drop-out layers are used to assure effective training, while the max-pooling is used to reduce the amount of data passing through each step of convolution. The latter is necessary in order to end up with a manageable amount of weights in the dense layers, which are responsible for final classification of the inputs. Precise summary of the network layout is presented in table 5.1. For training of the network Keras implementation ADAM optimizer with learning rate `lr` $= 10^{-4}$ was used, along with the categorical cross-entropy metric. 20% of the input samples served as a validation set, while the rest 80% was used for training.

5.2.3 Results

Addressing the actual stellar field, as mapped by Gaia satellite, is a complex task. Besides non-trivial, position-dependent, phase-space distribution of stars, the data contains numerous features which are not sourced by DM substructure, such as spiral arms, globular clusters, giant molecular clouds, etc. Therefore, in the first step of applying computer vision for detecting DM subhalos, I will focus on a simplified case, assuming homogeneous stellar field with Gaussian velocity distribution and neglect the possibility of non-DM induced perturbations. Relaxing these assumptions naturally requires much more careful generation of training data, but also makes the extraction of DM signatures more difficult. However, the perturbations induced by DM substructure are fortunately rather unique and can not be easily mimicked by any other galactic structure or perturber, due to the expected spheroidal morphology and high central density of the surviving DM subhalos. In principle, this makes it possible for the CNNs to distinguish them even in presences of other phase-space features over the scales of interest, but to obtain quantitative results for such realistic datasets further improvements in the generation of mock stellar fields will be needed. In the simplified setting used here, each dataset can be characterized by the number of embedded subhalos, their masses and velocities, and additionally the stellar number density and velocity dispersions along with the three spatial directions. A sample realization of the stellar field with a single DM subhalo with $M_{\rm sub} = 10^7 M_\odot$, moving in positive $\hat{x}$ direction with $|\vec{v}_{\rm sub}| = 100$ km/s through stellar field with $n_\star = 10^3$ kpc^{-3} and $\sigma_{\star,x} = \sigma_{\star,y} = \sigma_{\star,z} = 10$ km/s, is shown in figure 5.3. As can be seen, the features induced by the presence of DM subhalo are very subtle and nearly impossible to spot by eye.

To test the efficiency of CNNs in extracting the number of subhalos in a given stellar field, I first generated 32000 training samples, which contained between 0 and 2 point-mass subhalos with $M_s = 10^7 M_\odot$ and velocity drawn from isotropic Gaussian distribution with $\sigma_{\rm sub} = 50$ km/s. The stars were then binned in 22 bins per spatial dimension and corresponding 3D maps of number density and velocity moments were created. Finally, the obtained maps were used to train the CNN, which typically took about 20 epochs (i.e. iterations through the entire set of maps). The network's loss function and accuracy versus the number of training epochs are shown in figure 5.4. Once the training of network converged, I used it to extract the number of subhalos from a collection of independent stellar field realization, which was not used in the training procedure, serving as a test dataset. The network reached an accuracy of more than 99.9%, miss-classifying one sample out of several thousand.

With decreasing $M_{\rm sub}$, it becomes increasingly difficult to detect the signatures of substructure, since both, the magnitude of perturbations and effected number of stars, decrease. However, after repeating the training procedure with stellar fields containing subhalos with $M_{\rm sub} = 5 \cdot 10^6 M_\odot$ the network reached only slightly worse accuracy of 99.8%. Similar results were found for $M_{\rm sub} = 3 \cdot 10^6 M_\odot$, while the network failed to train when $M_{\rm sub} \lesssim 2 \cdot 10^6 M_\odot$. The efficiency of CNNs to recognize substructure of a given mass is nicely captured in receiver operating characteristic (ROC) curves, measuring the rate of correct classification versus the rate of false classifications as the threshold value of signal needed for assigning it to a certain category is being varied. They are shown in figure 5.5 for networks trained with datasets containing aforementioned

mono-chromatic subhalo masses, as well as a network trained on dataset with uniformly distributed subhalo masses in the range $M_{\rm sub} \in [3 \cdot 10^6, 10^7]\ M_\odot$, which is a step closer to the realistic setting, since galactic DM substructures are expected to vary in mass. As can be seen from the plot, CNN performed well in all the cases where $M_{\rm sub} \geq 3 \cdot 10^6 M_\odot$, yielding the worst performance for datasets with varying subhalo masses, but still reaching decent accuracy of 97.1%. Interestingly enough, the network was not able to train on datasets with $M_{\rm sub} < 3 \cdot 10^6 M_\odot$ and exhibited a behaviour reminiscent of a phase-transition, reaching precision better than 97% above the threshold value of $M_{\rm sub}$ and failed to train below it.

To further explore the dependence of subhalo detection efficiency on the $M_{\rm sub}$, but also stellar parameters, I trained CNNs for several combinations of $M_{\rm sub}/\sigma_\star^2$, characterizing the strength of the signal, and $n_\star$, determining noisiness of the data. Results are shown in figure 5.6, where the green crosses mark parameter values at which network trained successfully, reaching accuracy above 95%, and red crosses where it failed, resulting in accuracy $\sim 33\%$, which equals to random guessing between the three possible answers regarding the number of contained subhalos. In the same plot also the sensitivity threshold estimate from equation (5.5) is shown, where $\delta v_\star$ was set to 0 since the mock datasets did not include measurement uncertainties in the stellar velocities. As can be seen from the figure 5.6, the derived estimate leads to better expected sensitivity then the one found in practice, which implies that the perturbations in stellar distribution need to be somewhat larger then the shot noise induced by binning of the stars, in order for the CNN do detect them. At intermediate values of $GM_{\rm sub}/\sigma_\star^2 \sim 0.2$, for which the δr that was used for binning the stellar field is near the optimal choice, a correction factor of less then 2 is needed, however, the discrepancy gets more sever at larger and smaller values of $GM_{\rm sub}/\sigma_\star^2$. This could be perhaps mitigated by choosing more appropriate δr, but that would also imply changing either the sizes of network layers or the considered stellar field volume.

Finally, also the case of anisotropic stellar velocity distributions was explored by setting different velocity dispersions along the three spatial directions. In this case, I found that the sensitivity mostly depends on the smallest velocity dispersion component, denoted by $\sigma_{\star,3}$, yielding only slightly worse accuracy than in isotropic setting with similar velocity dispersion along all three spatial components, i.e. $\sigma_\star \sim \sigma_{\star,3}$. This result is particularly important for the application of the discussed technique to real data, as it tells us that it is probably best to look for the perturbations in thin disk stars (or more accurately speaking, the α-rich population), which are typically characterized by small velocity dispersion in the direction perpendicular to the galactic disk, allowing for detection of smaller $M_{\rm sub}$ then through thick disk and/or halo stars.

In summary, the results presented here show good prospects for detecting dark subhalos with $M_{\rm sub} \gtrsim 10^7 M_\odot$ through the gravitational imprints they leave in the distribution of surrounding stars using CNNs. Astrometric data of adequate quality for such analyses has only recently become available, however, in the near future even more extensive and accurate catalogues are expected to be released. This opens a new window into the distribution of DM on the sub-galactic scales, which could contain valuable hints for the particle nature of DM. For detection of the smallest DM clumps, the cold stellar populations (i.e. the ones with small velocity dispersion), such as the galactic α-rich stars, are

particularly important, since they offer the best signal-to-noise ratio. On the other hand, before addressing the real data, still significant improvements are needed in the generation of mock stellar catalogues to include possible features, which are not directly sourced by DM substructure. Furthermore, improvements are also possible on the side of the deployed neural network models. In future research, it would also be interesting to explore the possibilities of applying regression CNNs for extracting the mass, location and velocity of a given subhalo or directly inferring quantities related to the DM mass function on sub-galactic scales.

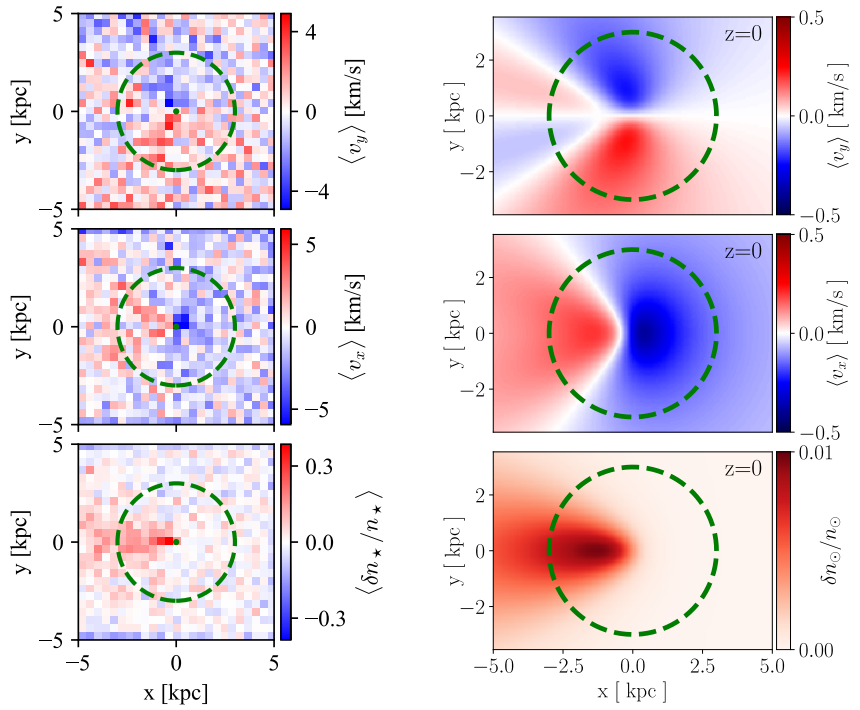

Figure 5.2: Stellar number density perturbation ($\langle \delta n_\star / n_\star \rangle$) and average velocities perpendicular ($\langle v_y \rangle$) and parallel ($\langle v_x \rangle$) to the subhalo's movement direction. In the plots on left hand side, generated according to the procedure described section 5.2.2, DM subhalo is assumed to have a mass of $M_{\rm sub} = 5 \cdot 10^7 M_\odot$ and $|\vec{v}_{\rm sub}| = 100$ km/s along $\hat{x}$ direction, while for stars $n_\star = 10^4$ kpc^{-3} and $\sigma_x = \sigma_y = \sigma_z = 30$ km/s were chosen. On the right hand side the results obtained by Buschmann et al. [328] using the analytical expression are shown, with the difference that $M_{\rm sub} = 2 \cdot 10^7 M_\odot$ and $|\vec{v}_{\rm sub}| = 200$ km/s was assumed, along with $n_\star = 5 \cdot 10^3$ kpc^{-3} and $\sigma_x = \sigma_y = \sigma_z = 100/\sqrt{2}$. Larger $M_{\rm sub}$, $n_\star$ and lower $\sigma_\star$ were chosen in generated stellar maps to emphasize the features, since these contain shot noise due to the binning procedure, which makes its harder to observe the characteristic patterns by eye. The green dashed circle (and dot in the left hand side plot) only serve as a guidance for the location of the subhalo, whose center lies at $x = 0$ and $y = 0$.

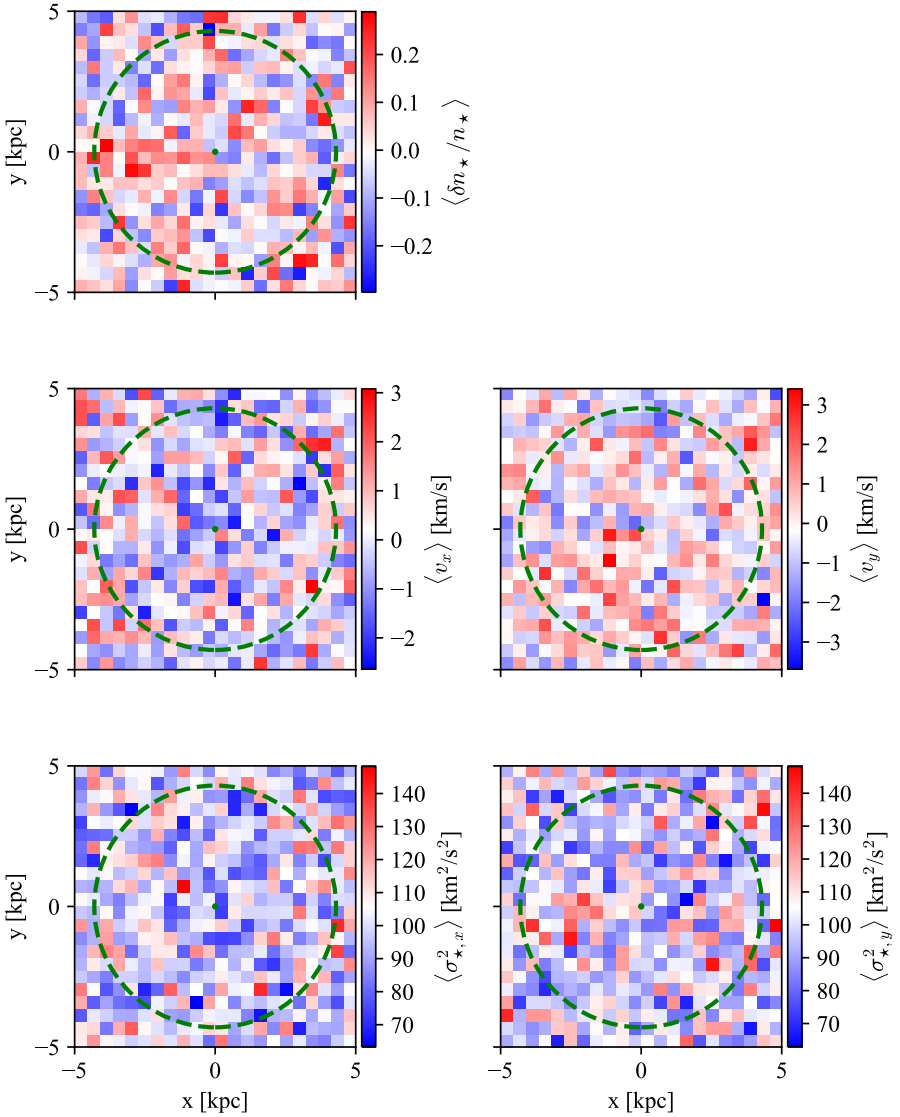

Figure 5.3: Bin-averaged stellar number density and first two moments of their velocity distribution obtained from a mock catalog with a single DM subhalo of $M_{\rm sub} = 10^7 M_\odot$, moving in the positive $\hat{x}$ direction with 100 km/s. The fiducial values of stellar parameters are $n_\star = 10^3$ kpc^{-3} and $\sigma_\star = 10$ km/s, while green circle marks the subhalos range of influence, r_g.

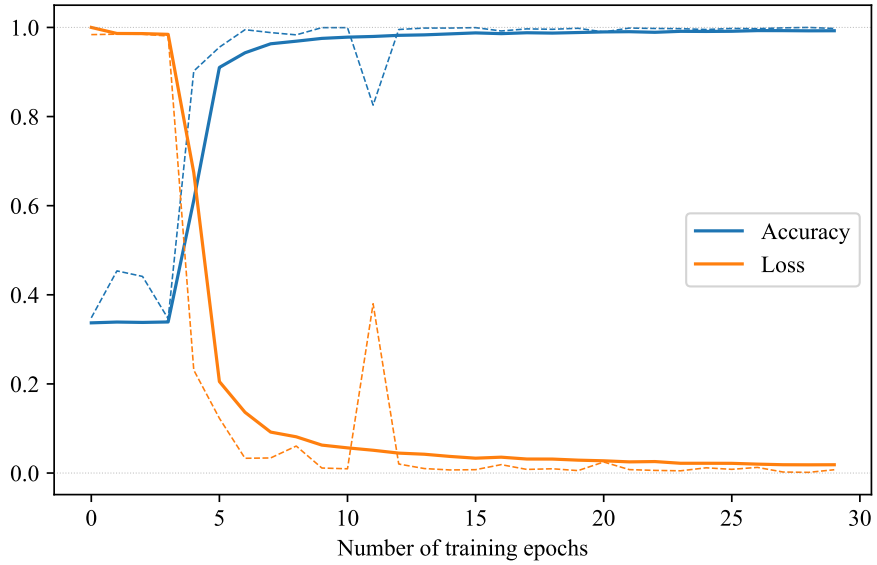

Figure 5.4: CNN accuracy and normalized loss function for training (solid lines) and validation (dashed lines) datasets as a function of elapsed training epochs. The above results were obtained for homogeneous isotropic stellar field with $n_{\rm sub} \in [0, 2]$ point-masses of $M_{\rm sub} = 10^7 M_\odot$ and stellar field with $n_\star = 10^3$ kpc^{-3} and $\sigma_\star = 10$ km/s.

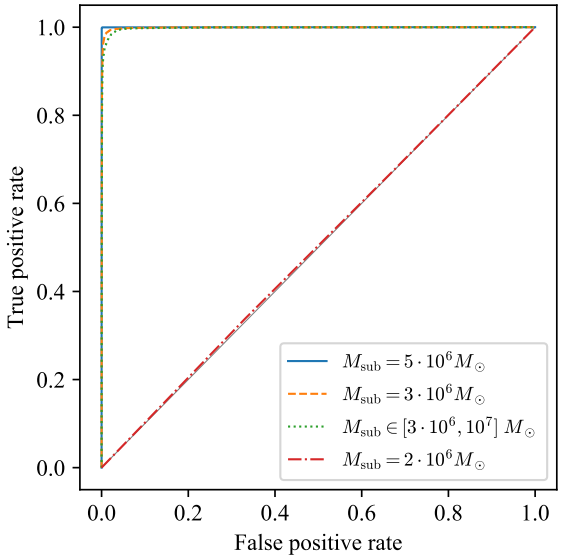

Figure 5.5: ROC (receiver operating characteristic) curves for CNNs trained on datasets with different subhalo masses $M_{\rm sub}$, but same fiducial stellar field parameters, namely $n_\star = 10^3$ kpc^{-3} and $\sigma_\star = 10$ km/s.

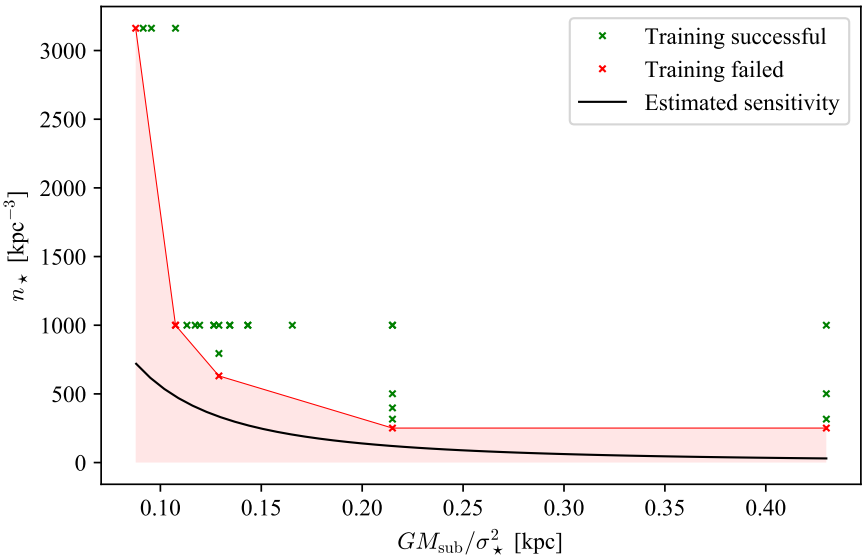

Figure 5.6: The ability of CNN to successfully train at given point in the subhalo mass over stellar velocity dispersion, $GM_{\rm sub}/\sigma^2_\star$, versus stellar number density, $n_\star$, plane. Green crosses mark the points where network successfully trained and reach accuracy above 95%, while red crosses mark the points where network failed to train, resulting in accuracy $\sim 33\%$. The red region marks the part of parameter space, where the CNN approach is expected to fail, while the black line denotes the sensitivity threshold estimate from equation (5.5), assuming $\delta v_\star \ll \sigma_\star/\sqrt{N_b}$.

6. Closing remarks

The endeavour of understanding and successfully detecting DM remains a bustling field of research. In this thesis I provide several novel results regarding the DM phase-space distributions within galaxies and explore their impacts on the direct and indirect searches. Such refined analyses are particularly welcome in the light of latest astronomical observations, which allows us to asses the dynamics within galaxies with unprecedented precision, but also needed for the legitimate exclusion of relevant parameter space in various particle physics models.

In chapter 3 a sophisticated method for modelling equilibrium phase-space distribution functions in axisymmetric systems was invoked and for the first time applied to the DM component of spiral galaxies. The differences between axisymmetric method and previous approaches, relying on spherical symmetry, were carefully examined, along with additional features that can be consistently included in the refined approach, such as flattening of the DM halo and its rotation. Significant deviations were found on the level of the velocity distribution of DM particles, even when keeping the same density profile in all of the considered models, which are most notable in the central parts of systems, where the impact of flattened stellar disk is the largest. Furthermore, I also briefly presented possible ways how to extend the equilibrium modelling, which tacitly assumes smooth DM halo, to more realistic setups, where also DM substructure and non-thermalized DM component accreted with recent mergers can be included. The axisymmetric modelling of DM was then applied to Milky Way through a careful mass decomposition of our galaxy, taking into account most recent measurements of circular velocity and vertical motion of stars. An important advantage of this approach, with respect to the traditional modelling, is the fact that phase-space distribution of DM encodes all the information regarding the system, correlating the local DM density with velocity distribution and corresponding escape velocity, which were previously often treated as independent. Finally, the obtained PSDFs for two phenomenologically motivated DM density profiles, namely the cuspy NFW and cored Burkert, were used to investigate their impact on the interpretation of direct detection experiments. Additionally, the universal astrophysical factors entering the analysis were computed and made available for the convenience of future analyses. As it was shown for the case of detectors based on liquefied Xenon, the refined approach can lead to significantly weaker bounds on the DM-nucleon cross-sections at low (sub-GeV) DM masses, where the difference can be larger then an order of magnitude, while it reduces to a factor of a few for larger DM masses. Furthermore, also the impact on annual modulation of the recoil rates was explored, where different models were shown to induce notable changes in the amplitude of signal modulation.

Subsequently, in chapter 4, the prospects of indirect detection of DM through its annihilation products was discussed. In particular, I focused on classical dwarf satellites of the Milky Way, which provide one of the most promising and robust targets for indirect searches in the γ-ray band. While most of the existing studies were performed under the assumption of velocity independent $\langle\sigma_{\rm ann}v\rangle$, the analysis presented in this work was done for a general setting, where non-trivial dependences on the relative velocity of annihilating particles can be included. Special attention was paid to the Sommerfeld enhancement of the perturbative cross-section, which generically arises in the non-relativistic limit of models where DM annihilates through a light force mediator. Similarly, as in the case of Milky Way, recent measurements of stellar kinematics were used to constrain the distribution of DM within the dwarf satellites, which was then utilised to construct phase-space models needed for computing the astrophysical factors entering the predictions for DM annihilation fluxes. A good match with previous works was obtained for the velocity independent annihilations, while novel results were presented for the case of Sommerfeld enhancement. It was shown that the DM velocity anisotropy, which is entirely unconstrained by observations, can have a significant impact on the expected signals and induces uncertainties, which are of the same magnitude as the ones stemming from observations of stellar velocity dispersion, leading to uncertainty in the amount of DM within these objects. On the other hand, the ordering of prime targets for detection remains the same as in the non-enhanced case, however, the expected signals are significantly enhanced, namely by three orders of magnitude in the Coulomb regime and up to five orders of magnitude for resonant values of particle physics parameters.

Finally, in chapter 5 I discussed an alternative approach to gain new insights into the nature of DM through careful study of the galactic stellar field. More precisely, cold DM is expected to form structure down to very small scales, which should also be present within our galaxy and could cause detectable perturbations in the kinematic properties of the surrounding stars. Such studies have only recently become possible thanks to the new generation of precise astrometric surveys, such as the Gaia mission, on the one hand, but also sophisticated tools for their analysis, on the other. I explored the possibilities of applying supervised machine learning through the use of deep convolutional neural networks to detect the subtle patterns in the distribution of stars caused by DM subhalo flybys. For a simplified setup, where the presence of additional structures, such as spiral arms or giant molecular clouds, was neglected, the network performed surprisingly well, reaching accuracy above 97% in classifying the number subhalos included in a given stellar field. My findings give substantial support to estimates that such approach could be sensitive to subhalo masses of $M_{\rm sub} \gtrsim 10^7 M_\odot$, entering regime where the amount of substructure is expected to be modified with respect to the standard cold DM hypothesis in many alternative models, such as warm, self-interacting or ultra-light bosonic DM. Furthermore, thin disk stars were identified as a prime target in such searches, since they exhibit particularly low velocity dispersion in the direction perpendicular to the disk, allowing for easier recognition of the characteristic perturbations. On the other hand, further improvements in the modelling of mock stellar fields, used for training of convolutional networks, are needed before it could be applied to the actual observations.

A. Closing the contour integral

The HQ method is rather efficient in numerically computing phase-space distribution functions for isolated self-gravitating populations, i.e. when the gravitational potential $\Psi(R^2, z^2)$ is self-consistently generated by the system density profile $\rho(R^2, z^2)$. In this case, the proposal by Hunter & Qian, as reproduced in Eqns. (3.5) and (3.6), for the contour $C(\mathcal{E})$, entering critically in the evaluation of the integral in Eqn. (3.4), is a good choice. The reason for which it works well is that it generally avoids the inclusion of additional singularities and/or crossing of branch cuts which the analytic continuation of $\frac{\mathrm{d}\rho}{\mathrm{d}\Psi}$ in the complex plane may introduce (see the discussion in [149] for details). However, when addressing configurations in which the total gravitational potential is not entirely sourced by the density under consideration, but there are also additional contributions from other components, the method may encounter difficulties. For example, in the case considered in this paper of a DM halo combined with an external Myamoto-Nagai potential, Eqn (3.11), an additional branch cut in $\Psi(R^2, z^2)$ occurs along the real axis at $z^2 < -b_d^2$. As a consequence the Jacobian for the change of variables from $\rho(R^2, z^2)$ to $\rho(R^2, \Psi)$ contains a discontinuity, due to which it is not always possible to invert the potential at every point $\xi(\theta)$ along the contour in Eqns. (3.5) or (3.6). The inverse for $\xi(\theta = 0)$ does exist by construction, however for larger values of θ, there is no guarantee that one can find z^2 such that:

$$\xi(\theta) = \Psi\left(\frac{L_z^2}{2(\xi(\theta) - \mathcal{E})}, z^2\right) \ . \tag{A.1}$$

This indeed does not happen for certain values of $\mathcal{E}$ and L_z, depending also on the choice of the "thickness" of the contour h. It is sometimes possible to mitigate the problem by adjusting the value of h, or by choosing a different contour shape, in order to avoid values of ξ for which the inversion breaks down. For finite potentials an alternative choice of the upper half of the contour is a boxy path parametrized by:

$$\xi_1(s) = \psi_{\mathrm{env}} + i\, h\, s \ , \tag{A.2}$$

$$\xi_2(s) = \psi_{\mathrm{env}}\,(1 - s) + i\, h \ , \tag{A.3}$$

$$\xi_3(s) = i\, h\,(1 - s) \ , \tag{A.4}$$

with $s \in [0, 1]$. Again, by tuning the parameter h one can try to avoid the values of ξ where the inversion fails. If this is not possible even along this second path (e.g. it requires again such a small h that one faces loss of numerical

precision when integrating around the pole), an approximate solution is to pick out h in such a way that the discontinuity occurs along $\xi_3(s)$. Indeed, it turns out that the contribution to the integral along $\xi_3(s)$ is negligible, being orders of magnitude smaller then the ones from $\xi_1(s)$ and $\xi_2(s)$, as it approaches the value of potential at infinity (i.e. $\Re\left[\xi_3(s)\right] = 0$, $\forall s$), where $\rho(R^2, z^2)$ and it's derivatives vanish. We explicitly checked that $f(\mathcal{E}, L_z)$ computed through this approximation successfully reproduces the initial density. Furthermore, in practice the error of neglecting the $\xi_3(s)$ contribution is much smaller then the errors coming from the numerical integration along the rest of the contour.

B. Scaling relations of J-factors

Precise evaluation of J-factors turns out to be too computationally demanding to run it for all the samples produced by the MCMC walkers, even when using the shortcut discussed in previous section. Therefore we resort to scaling relations which allow us to extrapolate the values to arbitrary halo parameters without the need of recomputing the nested numerical integrals in Eq. (**??**). More precisely, it is possible to obtain exact scaling relations for a change in the DM scale density $\rho_s \to \mu\rho_s$ and physical length scale $r \to \lambda r$, which also applies to all distance parameters e.g. r_s and D. For all spherically symmetric density profiles of the form $\rho_{\rm DM}(r; \rho_s, r_s) = \rho_s \cdot f(r/r_s)$, where $f(x)$ is an arbitrary function, it is possible to show the following relation:

$$J(r_s/D\ ;\ \mu\rho_s, \lambda r_s, \lambda D) = J(r_s/D\ ;\ \rho_s, r_s, D) \times \begin{cases} \mu^2\lambda & \text{for } \xi \gg 1\ , \\ \mu^{3/2} & \text{for } \xi \ll 1\ , \\ \mu/\lambda & \text{for } \xi = 6/\left(\pi^2 n^2\right)\ . \end{cases} \tag{B.1}$$

While the effect of varying ρ_s is quite clear, the scaling with λ is somewhat less expected and is in fact broken by the radial cut-offs which we kept constant. We numerically checked the deviations from the above relation and found excellent agreement except for resonantly enhanced NFW profile where we found scaling exponent of ~ -0.8 instead of -1. This is a consequence of using static inner cut-off which removes an increasingly significant amount of the DM cusp for decreasing values of λ. We present the comparison of power-law scalings with the numerical results in Fig. B.1. Some deviations also arise at small/large values of λ where the effect of cut-offs again becomes noticeable, however when considering dSphs one mostly deals with $\lambda \sim \mathcal{O}(1)$. Using this shortcut the J-factors can be thought of as only a function of r_s/D for which however we found no analytical form. Instead we interpolated $J(r_s/D)$ which, together with scaling relations, allowed us to compute accurate J-factor posterior distributions from the entire MCMC sample.

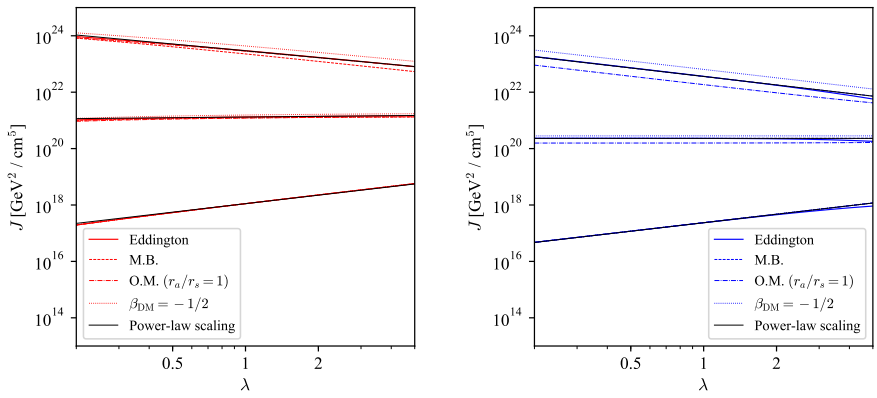

Figure B.1: J-factor scaling under change of physical length $r \to \lambda r$ for NFW and Burkert profiles with nominal values of $r_s = 1$ kpc, $D = 100$ kpc and $\rho_s = 1$ GeV/cm^3.

Bibliography

[1] F. Zwicky. Die Rotverschiebung von extragalaktischen Nebeln. *Helvetica Physica Acta*, 6:110–127, 1933.

[2] F. Zwicky. On the Masses of Nebulae and of Clusters of Nebulae. *The Astrophysical Journal*, 86:217, October 1937.

[3] Vera C. Rubin and W. Kent Ford. Rotation of the Andromeda Nebula from a Spectroscopic Survey of Emission Regions. *The Astrophysical Journal*, 159:379, February 1970.

[4] V. C. Rubin, W. K. Ford, and N. Thonnard. Rotational properties of 21 SC galaxies with a large range of luminosities and radii, from NGC 4605 /R = 4kpc/ to UGC 2885 /R = 122 kpc/. *The Astrophysical Journal*, 238:471–487, June 1980.

[5] K. C. Freeman. On the Disks of Spiral and S0 Galaxies. *The Astrophysical Journal*, 160:811, June 1970.

[6] P. de Bernardis, P. a. R. Ade, J. J. Bock, et al. A flat Universe from high-resolution maps of the cosmic microwave background radiation. *Nature*, 404(6781):955, April 2000.

[7] D. N. Spergel, R. Bean, O. Doré, et al. Three-Year Wilkinson Microwave Anisotropy Probe (WMAP) Observations: Implications for Cosmology. *The Astrophysical Journal Supplement Series*, 170(2):377, June 2007.

[8] William Thomson and Baron Kelvin. *Baltimore lectures on molecular dynamics and the wave theory of light: founded on Mr. A.S. Hathaway's stenographic report of twenty lectures delivered in Johns Hopkins University, Baltimore, in October 1884: followed by twelve appendices on allied subjects*. Cambridge Universiy Press, London, 2010. OCLC: 850752756.

[9] A. Bosma. The distribution and kinematics of neutral hydrogen in spiral galaxies of various morphological types. *Ph.D. Thesis*, 1978.

[10] Massimo Persic, Paolo Salucci, and Fulvio Stel. The universal rotation curve of spiral galaxies — I. The dark matter connection. *Monthly Notices of the Royal Astronomical Society*, 281(1):27–47, July 1996.

[11] Yoshiaki Sofue and Vera Rubin. Rotation Curves of Spiral Galaxies. *Annual Review of Astronomy and Astrophysics*, 39(1):137–174, 2001.

[12] Yoshiaki Sofue. Rotation and mass in the Milky Way and spiral galaxies. *Publications of the Astronomical Society of Japan*, 69(1), February 2017.

[13] Paolo Salucci. Dark Matter in Galaxies: evidences and challenges. *arXiv:1807.08541 [astro-ph]*, July 2018.

[14] S. M. Faber and R. E. Jackson. Velocity dispersions and mass-to-light ratios for elliptical galaxies. *The Astrophysical Journal*, 204:668–683, March 1976.

[15] Kun Ting Eddie Chua, Annalisa Pillepich, Mark Vogelsberger, and Lars Hernquist. Shape of dark matter haloes in the Illustris simulation: effects of baryons. *Monthly Notices of the Royal Astronomical Society*, 484(1):476–493, March 2019.

[16] M. Girardi, A. Biviano, G. Giuricin, F. Mardirossian, and M. Mezzetti. Velocity dispersions in galaxy clusters. *The Astrophysical Journal*, 404:38–50, February 1993.

[17] Jubee Sohn, Margaret J. Geller, H. Jabran Zahid, et al. The Velocity Dispersion Function of Very Massive Galaxy Clusters: Abell 2029 and Coma. *The Astrophysical Journal Supplement Series*, 229(2):20, April 2017.

[18] D. Walsh, R. F. Carswell, and R. J. Weymann. 0957 + 561 A, B: twin quasistellar objects or gravitational lens? *Nature*, 279(5712):381, May 1979.

[19] Frédéric Courbin, Dante Minniti, R. Beig, et al., editors. *Gravitational Lensing: An Astrophysical Tool*, volume 608 of *Lecture Notes in Physics*. Springer Berlin Heidelberg, Berlin, Heidelberg, 2002.

[20] S. E. Bryan, S. T. Kay, A. R. Duffy, et al. The impact of baryons on the spins and shapes of dark matter haloes. *Monthly Notices of the Royal Astronomical Society*, 429(4):3316–3329, March 2013.

[21] Ran Li, Carlos S. Frenk, Shaun Cole, et al. Constraints on the identity of the dark matter from strong gravitational lenses. *Monthly Notices of the Royal Astronomical Society*, 460(1):363–372, July 2016.

[22] Kevin E. Andrade, Quinn Minor, Anna Nierenberg, and Manoj Kaplinghat. Detecting dark matter cores in galaxy clusters with strong lensing. *Monthly Notices of the Royal Astronomical Society*, 487(2):1905–1926, August 2019.

[23] Surhud More, Hironao Miyatake, Rachel Mandelbaum, et al. The Weak Lensing Signal and the Clustering of BOSS Galaxies II: Astrophysical and Cosmological Constraints. *The Astrophysical Journal*, 806(1):2, June 2015.

[24] H. Hildebrandt, M. Viola, C. Heymans, et al. KiDS-450: cosmological parameter constraints from tomographic weak gravitational lensing. *Monthly Notices of the Royal Astronomical Society*, 465(2):1454–1498, February 2017.

[25] Douglas Clowe, Anthony Gonzalez, and Maxim Markevitch. Weak-Lensing Mass Reconstruction of the Interacting Cluster 1e 0657–558: Direct Evidence for the Existence of Dark Matter*. *The Astrophysical Journal*, 604(2):596, April 2004.

[26] M. Markevitch, A. H. Gonzalez, D. Clowe, et al. Direct Constraints on the Dark Matter Self-Interaction Cross Section from the Merging Galaxy Cluster 1e 0657–56. *The Astrophysical Journal*, 606(2):819, May 2004.

[27] R. K. Sachs and A. M. Wolfe. Perturbations of a Cosmological Model and Angular Variations of the Microwave Background. *The Astrophysical Journal*, 147:73, January 1967.

[28] Planck Collaboration, N. Aghanim, Y. Akrami, et al. Planck 2018 results. VI. Cosmological parameters. *arXiv e-prints*, page arXiv:1807.06209, July 2018.

[29] Volker Springel, Simon D. M. White, Adrian Jenkins, et al. Simulations of the formation, evolution and clustering of galaxies and quasars. *Nature*, 435(7042):629, June 2005.

[30] Mark Vogelsberger, Shy Genel, Volker Springel, et al. Introducing the Illustris Project: simulating the coevolution of dark and visible matter in the Universe. *Monthly Notices of the Royal Astronomical Society*, 444(2):1518, October 2014.

[31] Glennys R. Farrar. Stable Sexaquark. *arXiv e-prints*, page arXiv:1708.08951, August 2017.

[32] Lars Bergström. Non-baryonic dark matter: observational evidence and detection methods. *Reports on Progress in Physics*, 63(5):793–841, April 2000.

[33] Gianfranco Bertone, Dan Hooper, and Joseph Silk. Particle dark matter: evidence, candidates and constraints. *Physics Reports*, 405(5):279–390, January 2005.

[34] Katherine Garrett and Gintaras Duda. *Dark Matter: A Primer*. 2011.

[35] Martin Bauer and Tilman Plehn. Yet Another Introduction to Dark Matter. *arXiv e-prints*, page arXiv:1705.01987, May 2017.

[36] John Ellis, J. S. Hagelin, D. V. Nanopoulos, K. Olive, and M. Srednicki. Supersymmetric relics from the big bang. *Nuclear Physics B*, 238(2):453–476, June 1984.

[37] G. L. Kane, Chris Kolda, Leszek Roszkowski, and James D. Wells. Study of constrained minimal supersymmetry. *Physical Review D*, 49(11):6173–6210, June 1994.

[38] Gerard Jungman, Marc Kamionkowski, and Kim Griest. Supersymmetric dark matter. *Physics Reports*, 267(5):195–373, March 1996.

[39] Stephen P. Martin. A supersymmetry primer. In *Perspectives on Supersymmetry*, volume Volume 18 of *Advanced Series on Directions in High Energy Physics*, pages 1–98. WORLD SCIENTIFIC, July 1998.

[40] Carlos Muñoz. Models of Supersymmetry for Dark Matter. *EPJ Web of Conferences*, 136:01002, 2017.

[41] Graham G Ross. *Grand unified theories*. Benjamin/Cummings Publ. Co., Menlo Park, 1984. OCLC: 441636763.

[42] Giorgio Arcadi. Dark matter phenomenology of GUT inspired simplified models. *Journal of Physics: Conference Series*, 718:042003, May 2016.

[43] Géraldine Servant and Tim M. P. Tait. Is the lightest Kaluza–Klein particle a viable dark matter candidate? *Nuclear Physics B*, 650(1):391–419, February 2003.

[44] Dan Hooper and Stefano Profumo. Dark matter and collider phenomenology of universal extra dimensions. *Physics Reports*, 453(2):29–115, December 2007.

[45] Gary Steigman, Basudeb Dasgupta, and John F. Beacom. Precise relic WIMP abundance and its impact on searches for dark matter annihilation. *Physical Review D*, 86(2):023506, July 2012.

[46] Scott Dodelson and Lawrence M. Widrow. Sterile neutrinos as dark matter. *Physical Review Letters*, 72(1):17–20, January 1994.

[47] Takehiko Asaka, Steve Blanchet, and Mikhail Shaposhnikov. The νMSM, dark matter and neutrino masses. *Physics Letters B*, 631(4):151–156, December 2005.

[48] Takehiko Asaka and Mikhail Shaposhnikov. The νMSM, dark matter and baryon asymmetry of the universe. *Physics Letters B*, 620(1):17–26, July 2005.

[49] Ernest Ma. Verifiable radiative seesaw mechanism of neutrino mass and dark matter. *Physical Review D*, 73(7):077301, April 2006.

[50] Peter Minkowski. $mu \rightarrow$ e γ at a rate of one out of 109 muon decays? *Physics Letters B*, 67(4):421–428, April 1977.

[51] Tsutomu Yanagida. Horizontal Symmetry and Masses of Neutrinos. *Progress of Theoretical Physics*, 64(3):1103–1105, September 1980.

[52] Rabindra N. Mohapatra and Goran Senjanović. Neutrino Mass and Spontaneous Parity Nonconservation. *Physical Review Letters*, 44(14):912–915, April 1980.

[53] J. Schechter and J. W. F. Valle. Neutrino masses in SU(2) $\bigotimes$ U(1) theories. *Physical Review D*, 22(9):2227–2235, November 1980.

[54] Marco Drewes. The phenomenology of right handed neutrinos. *International Journal of Modern Physics E*, 22(08):1330019, August 2013.

[55] R. Adhikari, M. Agostini, N. Anh Ky, et al. A White Paper on keV Sterile Neutrino Dark Matter. *Journal of Cosmology and Astroparticle Physics*, 2017(01):025–025, January 2017. arXiv: 1602.04816.

[56] A. Boyarsky, M. Drewes, T. Lasserre, S. Mertens, and O. Ruchayskiy. Sterile neutrino Dark Matter. *Progress in Particle and Nuclear Physics*, 104:1–45, January 2019.

[57] Esra Bulbul, Maxim Markevitch, Adam Foster, et al. Detection of an Unidentified Emission Line in the Stacked X-Ray Spectrum of Galaxy Clusters. *The Astrophysical Journal*, 789:13, July 2014.

[58] A. Boyarsky, O. Ruchayskiy, D. Iakubovskyi, and J. Franse. Unidentified Line in X-Ray Spectra of the Andromeda Galaxy and Perseus Galaxy Cluster. *Physical Review Letters*, 113(25):251301, December 2014.

[59] A. Boyarsky, D. Iakubovskyi, O. Ruchayskiy, and D. Savchenko. Surface brightness profile of the 3.5 keV line in the Milky Way halo. *arXiv e-prints*, page arXiv:1812.10488, December 2018.

[60] Leanne D. Duffy and Karl van Bibber. Axions as dark matter particles. *New Journal of Physics*, 11(10):105008, October 2009.

[61] Gordon Kane, Kuver Sinha, and Scott Watson. Cosmological moduli and the post-inflationary universe: A critical review. *International Journal of Modern Physics D*, 24(08):1530022, June 2015.

[62] Wayne Hu, Rennan Barkana, and Andrei Gruzinov. Fuzzy Cold Dark Matter: The Wave Properties of Ultralight Particles. *Physical Review Letters*, 85(6):1158–1161, August 2000.

[63] Lam Hui, Jeremiah P. Ostriker, Scott Tremaine, and Edward Witten. Ultralight scalars as cosmological dark matter. *Physical Review D*, 95(4):043541, February 2017.

[64] Vid Iršič, Matteo Viel, Martin G. Haehnelt, James S. Bolton, and George D. Becker. First Constraints on Fuzzy Dark Matter from Lyman-α Forest Data and Hydrodynamical Simulations. *Physical Review Letters*, 119(3):031302, July 2017.

[65] Matteo Nori, Riccardo Murgia, Vid Iršič, Marco Baldi, and Matteo Viel. Lyman-α forest and non-linear structure characterization in Fuzzy Dark Matter cosmologies. *Monthly Notices of the Royal Astronomical Society*, 482(3):3227–3243, January 2019.

[66] Olof Nebrin, Raghunath Ghara, and Garrelt Mellema. Fuzzy dark matter at cosmic dawn: new 21-cm constraints. *Journal of Cosmology and Astroparticle Physics*, 2019(04):051–051, April 2019.

[67] Simona Vegetti and L. V. E. Koopmans. Statistics of mass substructure from strong gravitational lensing: quantifying the mass fraction and mass function. *Monthly Notices of the Royal Astronomical Society*, 400(3):1583–1592, December 2009.

[68] D. Bayer, S. Chatterjee, L. V. E. Koopmans, et al. Observational constraints on the sub-galactic matter-power spectrum from galaxy-galaxy strong gravitational lensing. 2018.

[69] Joshua Simon, Simon Birrer, Keith Bechtol, et al. Testing the Nature of Dark Matter with Extremely Large Telescopes. *Bulletin of the American Astronomical Society*, 51(3):153, May 2019.

[70] P. Sikivie. Experimental Tests of the "Invisible" Axion. *Physical Review Letters*, 51(16):1415–1417, October 1983.

[71] Peter W. Graham, Igor G. Irastorza, Steven K. Lamoreaux, Axel Lindner, and Karl A. van Bibber. Experimental Searches for the Axion and Axion-Like Particles. *Annual Review of Nuclear and Particle Science*, 65(1):485–514, October 2015.

[72] S. J. Asztalos, G. Carosi, C. Hagmann, et al. SQUID-Based Microwave Cavity Search for Dark-Matter Axions. *Physical Review Letters*, 104(4):041301, January 2010.

[73] B. J. Carr and S. W. Hawking. Black Holes in the Early Universe. *Monthly Notices of the Royal Astronomical Society*, 168(2):399–415, August 1974.

[74] Bernard Carr, Florian Kühnel, and Marit Sandstad. Primordial black holes as dark matter. *Physical Review D*, 94(8):083504, October 2016.

[75] Fabio Capela, Maxim Pshirkov, and Peter Tinyakov. Constraints on primordial black holes as dark matter candidates from capture by neutron stars. *Physical Review D*, 87(12):123524, June 2013.

[76] Hiroko Niikura, Masahiro Takada, Naoki Yasuda, et al. Microlensing constraints on primordial black holes with Subaru/HSC Andromeda observations. *Nature Astronomy*, 3(6):524–534, June 2019.

[77] Nicolò Trevisani. Collider Searches for Dark Matter (ATLAS + CMS). *Universe*, 4(11):131, November 2018.

[78] Jan Conrad. Indirect Detection of WIMP Dark Matter: a compact review. *arXiv e-prints*, page arXiv:1411.1925, November 2014.

[79] Tracy R. Slatyer. TASI Lectures on Indirect Detection of Dark Matter. *arXiv:1710.05137 [astro-ph, physics:hep-ph]*, October 2017.

[80] M. Ackermann and others. Searching for dark matter annihilation from Milky Way dwarf spheroidal galaxies with six years of Fermi Large Area Telescope data. *Physical review letters*, 115(23):231301, 2015.

[81] The Fermi-LAT, D. E. S. Collaborations, A. Albert, et al. Searching for Dark Matter Annihilation in Recently Discovered Milky Way Satellites with Fermi-LAT. *The Astrophysical Journal*, 834(2):110, January 2017.

[82] Sebastian Hoof, Alex Geringer-Sameth, and Roberto Trotta. A Global Analysis of Dark Matter Signals from 27 Dwarf Spheroidal Galaxies using Ten Years of Fermi-LAT Observations. *arXiv e-prints*, page arXiv:1812.06986, December 2018.

[83] Lisa Goodenough and Dan Hooper. Possible Evidence For Dark Matter Annihilation In The Inner Milky Way From The Fermi Gamma Ray Space Telescope. *arXiv:0910.2998 [hep-ph]*, October 2009.

[84] Dan Hooper and Lisa Goodenough. Dark matter annihilation in the Galactic Center as seen by the Fermi Gamma Ray Space Telescope. *Physics Letters B*, 697(5):412–428, March 2011.

[85] M. Ackermann, M. Ajello, A. Albert, et al. Observations of M31 and M33 with the Fermi Large Area Telescope: a galactic center excess in Andromeda? *The Astrophysical Journal*, 836(2):208, 2017.

[86] Francesca Calore, Ilias Cholis, and Christoph Weniger. Background model systematics for the Fermi GeV excess. *Journal of Cosmology and Astroparticle Physics*, 2015(03):038–038, March 2015.

[87] Tansu Daylan, Douglas P. Finkbeiner, Dan Hooper, et al. The Characterization of the Gamma-Ray Signal from the Central Milky Way: A Compelling Case for Annihilating Dark Matter. *Physics of the Dark Universe*, 12:1–23, June 2016.

[88] Richard Bartels, Suraj Krishnamurthy, and Christoph Weniger. Strong Support for the Millisecond Pulsar Origin of the Galactic Center GeV Excess. *Physical Review Letters*, 116(5):051102, February 2016.

[89] Mattia Di Mauro, Xian Hou, Christopher Eckner, Gabrijela Zaharijas, and Eric Charles. Search for γ-ray emission from dark matter particle interactions from the Andromeda and Triangulum galaxies with the Fermi Large Area Telescope. *Physical Review D*, 99(12):123027, June 2019.

[90] Oscar Macias, Chris Gordon, Roland M. Crocker, et al. Galactic bulge preferred over dark matter for the Galactic centre gamma-ray excess. *Nature Astronomy*, 2(5):387, May 2018.

[91] H. Abdallah, A. Abramowski, F. Aharonian, et al. Search for Dark Matter Annihilations towards the Inner Galactic Halo from 10 Years of Observations with H.E.S.S. *Physical Review Letters*, 117(11):111301, September 2016.

[92] S. Archambault, A. Archer, W. Benbow, et al. Dark matter constraints from a joint analysis of dwarf Spheroidal galaxy observations with VERITAS. *Physical Review D*, 95(8):082001, April 2017.

[93] Andrzej Hryczuk, Krzysztof Jodłowski, Emmanuel Moulin, et al. Testing dark matter with Cherenkov light - prospects of H.E.S.S. and CTA for exploring minimal supersymmetry. *arXiv e-prints*, page arXiv:1905.00315, May 2019.

[94] M. G. Aartsen, K. Abraham, M. Ackermann, et al. Search for dark matter annihilation in the Galactic Center with IceCube-79. *The European Physical Journal C*, 75(10):492, October 2015.

[95] The ANTARES collaboration. Search of dark matter annihilation in the galactic centre using the ANTARES neutrino telescope. *Journal of Cosmology and Astroparticle Physics*, 2015(10):068–068, October 2015.

[96] M. Cirelli. Dark matter phenomena. *34th International Cosmic Ray Conference (ICRC2015)*, 34:14, July 2015.

[97] Mathieu Boudaud, Yoann Génolini, Laurent Derome, et al. AMS-02 antiprotons are consistent with a secondary astrophysical origin. *arXiv e-prints*, page arXiv:1906.07119, June 2019.

[98] Carmelo Evoli, Roberto Aloisio, and Pasquale Blasi. Galactic cosmic rays after the AMS-02 observations. *Physical Review D*, 99(10):103023, May 2019.

[99] Ming-Yang Cui, Xu Pan, Qiang Yuan, Yi-Zhong Fan, and Hong-Shi Zong. Revisit of cosmic ray antiprotons from dark matter annihilation with updated constraints on the background model from AMS-02 and collider data. *Journal of Cosmology and Astro-Particle Physics*, 2018(6):024, June 2018.

[100] Kerstin Perez, Philip von Doetinchem, Tsuguo Aramaki, et al. Astro 2020 Science White Paper: Cosmic-ray Antinuclei as Messengers for Dark Matter. *arXiv e-prints*, page arXiv:1904.05938, April 2019.

[101] Juan Antonio Aguilar Sánchez, Nadège Iovine, Christoph Tönnis, Juan de Dios Zornoza Gómez, and on behalf of the IceCube and ANTARES Collaboration. Combined Search for Neutrinos from Dark Matter Annihilation in the Galactic Center using IceCube and ANTARES. In *Proceedings of 35th International Cosmic Ray Conference — PoS(ICRC2017)*, volume 301, page 911. SISSA Medialab, August 2018.

[102] Fermi-LAT Collaboration, C. Johnson, R. Caputo, et al. Search for gamma-ray emission from p-wave dark matter annihilation in the Galactic Center. *Physical Review D*, 99(10):103007, May 2019.

[103] Mark W. Goodman and Edward Witten. Detectability of certain dark-matter candidates. *Physical Review D*, 31(12):3059–3063, June 1985.

[104] Tongyan Lin. TASI lectures on dark matter models and direct detection. *arXiv:1904.07915 [astro-ph, physics:hep-ph]*, April 2019. arXiv: 1904.07915.

[105] Marc Schumann. Direct Detection of WIMP Dark Matter: Concepts and Status. *arXiv:1903.03026 [astro-ph, physics:hep-ph, physics:physics]*, March 2019.

[106] E. Aprile, J. Aalbers, F. Agostini, et al. Dark Matter Search Results from a One Ton-Year Exposure of XENON1t. *Physical Review Letters*, 121(11):111302, September 2018.

[107] L. U. X. Collaboration, D. S. Akerib, S. Alsum, et al. Limits on spin-dependent WIMP-nucleon cross section obtained from the complete LUX exposure. *Physical Review Letters*, 118(25), June 2017.

[108] Jingkai Xia, Abdusalam Abdukerim, Wei Chen, et al. PandaX-II constraints on spin-dependent WIMP-nucleon effective interactions. *Physics Letters B*, 792:193, May 2019.

[109] G. Arcadi, C. Döring, C. Hasterok, and S. Vogl. Inelastic dark matter nucleus scattering. *arXiv:1906.10466 [astro-ph, physics:hep-ph]*, June 2019.

[110] The DarkSide Collaboration, P. Agnes, I. F. M. Albuquerque, et al. Low-Mass Dark Matter Search with the DarkSide-50 Experiment. *Physical Review Letters*, 121(8):081307, August 2018.

[111] C. Amole, M. Ardid, I. J. Arnquist, et al. Dark matter search results from the complete exposure of the PICO-60 c_3f_8 bubble chamber. *Physical Review D*, 100(2):022001, July 2019.

[112] R. Bernabei, P. Belli, A. Di Marco, et al. DAMA/LIBRA results and perspectives. *EPJ Web of Conferences*, 136:05001, 2017.

[113] R. Bernabei, P. Belli, A. Bussolotti, et al. First model independent results from DAMA/LIBRA-phase2. *arXiv:1805.10486 [astro-ph, physics:hep-ex, physics:physics]*, May 2018.

[114] COSINE-100 Collaboration, G. Adhikari, P. Adhikari, et al. Search for a dark matter-induced annual modulation signal in NaI(Tl) with the COSINE-100 experiment. *arXiv:1903.10098 [astro-ph, physics:hep-ex, physics:physics]*, March 2019.

[115] J. Amaré, S. Cebrián, I. Coarasa, et al. First results on dark matter annual modulation from ANAIS-112 experiment. *arXiv:1903.03973 [astro-ph, physics:hep-ex, physics:physics]*, March 2019.

[116] CDMS Collaboration, R. Agnese, Z. Ahmed, et al. Silicon Detector Dark Matter Results from the Final Exposure of CDMS II. *Physical Review Letters*, 111(25):251301, December 2013.

[117] CoGeNT Collaboration, C. E. Aalseth, P. S. Barbeau, et al. Results from a Search for Light-Mass Dark Matter with a *p*-Type Point Contact Germanium Detector. *Physical Review Letters*, 106(13):131301, March 2011.

[118] CoGeNT Collaboration, C. E. Aalseth, P. S. Barbeau, et al. Search for an Annual Modulation in a p-Type Point Contact Germanium Dark Matter Detector. *Physical Review Letters*, 107(14):141301, September 2011.

[119] Bing-Lin Young. A survey of dark matter and related topics in cosmology. *Frontiers of Physics*, 12(2):121201, October 2016.

[120] Masahiro Kawasaki, Kazunori Nakayama, and Toyokazu Sekiguchi. CMB constraint on dark matter annihilation after Planck 2015. *Physics Letters B*, 756:212–215, May 2016.

[121] Kimberly K. Boddy, Vera Gluscevic, Vivian Poulin, et al. Critical assessment of CMB limits on dark matter-baryon scattering: New treatment of the relative bulk velocity. *Physical Review D*, 98(12):123506, December 2018.

[122] Jens Chluba, A. Kogut, S. P. Patil, et al. Spectral Distortions of the CMB as a Probe of Inflation, Recombination, Structure Formation and Particle Physics. *Bulletin of the American Astronomical Society*, 51(3):184, May 2019.

[123] Matthew McQuinn. The Evolution of the Intergalactic Medium. *Annual Review of Astronomy and Astrophysics*, 54(1):313–362, 2016.

[124] Michael Sitwell, Andrei Mesinger, Yin-Zhe Ma, and Kris Sigurdson. The imprint of warm dark matter on the cosmological 21-cm signal. *Monthly Notices of the Royal Astronomical Society*, 438(3):2664–2671, March 2014.

[125] Isabella P. Carucci, Francisco Villaescusa-Navarro, Matteo Viel, and Andrea Lapi. Warm dark matter signatures on the 21cm power spectrum: intensity mapping forecasts for SKA. *Journal of Cosmology and Astroparticle Physics*, 2015(07):047–047, July 2015.

[126] Sergio Colafrancesco, Marco Regis, Paolo Marchegiani, et al. Probing the nature of Dark Matter with the SKA. *arXiv:1502.03738 [astro-ph]*, January 2015.

[127] Judd D. Bowman, Alan E. E. Rogers, Raul A. Monsalve, Thomas J. Mozdzen, and Nivedita Mahesh. An absorption profile centred at 78 megahertz in the sky-averaged spectrum. *Nature*, 555(7694):67–70, March 2018.

[128] Denis Erkal and Vasily Belokurov. Properties of dark subhaloes from gaps in tidal streams. *Monthly Notices of the Royal Astronomical Society*, 454(4):3542–3558, December 2015.

[129] Nilanjan Banik, Gianfranco Bertone, Jo Bovy, and Nassim Bozorgnia. Probing the nature of dark matter particles with stellar streams. *Journal of Cosmology and Astroparticle Physics*, 2018(07):061–061, July 2018.

[130] Jorge Peñarrubia. Stochastic tidal heating by random interactions with extended substructures. *Monthly Notices of the Royal Astronomical Society*, 484(4):5409–5436, April 2019.

[131] Xiao-Jun Yue, Wen-Biao Han, and Xian Chen. Dark Matter: An Efficient Catalyst for Intermediate-mass-ratio-inspiral Events. *The Astrophysical Journal*, 874(1):34, March 2019.

[132] Lisa Randall and Zhong-Zhi Xianyu. A Direct Probe of Mass Density near Inspiraling Binary Black Holes. *The Astrophysical Journal*, 878(2):75, June 2019.

[133] N. Bartolo, V. De Luca, G. Franciolini, et al. Primordial Black Hole Dark Matter: LISA Serendipity. *Physical Review Letters*, 122(21):211301, May 2019.

[134] Paul H. Frampton. Dark matter gravity waves at LIGO and LISA. *Modern Physics Letters A*, 34(16):1950124, April 2019.

[135] Masha Baryakhtar, Robert Lasenby, and Mae Teo. Black hole superradiance signatures of ultralight vectors. *Physical Review D*, 96(3):035019, August 2017.

[136] Wen-Bo Ding, Zi Yu, Yan Xu, Chun-Jian Liu, and Tmurbagan Bao. Neutrino Emission and Cooling of Dark-Matter-Admixed Neutron Stars. *Chinese Physics Letters*, 36(4):049701, April 2019.

[137] Peter W. Graham, Ryan Janish, Vijay Narayan, Surjeet Rajendran, and Paul Riggins. White dwarfs as dark matter detectors. *Physical Review D*, 98(11):115027, December 2018.

[138] Javier F. Acevedo and Joseph Bramante. Supernovae Sparked By Dark Matter in White Dwarfs. *arXiv:1904.11993 [astro-ph, physics:hep-ph]*, April 2019.

[139] William DeRocco, Peter W. Graham, Daniel Kasen, Gustavo Marques-Tavares, and Surjeet Rajendran. Observable signatures of dark photons from supernovae. *arXiv:1901.08596 [astro-ph, physics:hep-ph]*, January 2019.

[140] William DeRocco, Peter W. Graham, Daniel Kasen, Gustavo Marques-Tavares, and Surjeet Rajendran. Supernova signals of light dark matter. *arXiv:1905.09284 [astro-ph, physics:hep-ph]*, May 2019.

[141] Allan Sung, Huitzu Tu, and Meng-Ru Wu. New constraint from supernova explosions on light particles beyond the Standard Model. *arXiv:1903.07923 [astro-ph, physics:hep-ph]*, March 2019.

[142] MacKenzie L. Warren, Matthew Meixner, Grant Mathews, Jun Hidaka, and Toshitaka Kajino. Sterile neutrino oscillations in core-collapse supernovae. *Physical Review D*, 90(10):103007, November 2014.

[143] Carlos A. Argüelles, Vedran Brdar, and Joachim Kopp. Production of keV sterile neutrinos in supernovae: New constraints and gamma-ray observables. *Physical Review D*, 99(4):043012, February 2019.

[144] J. H. Jeans. On the theory of star-streaming and the structure of the universe. *Monthly Notices of the Royal Astronomical Society*, 76:70–84, December 1915.

[145] J. Binney and S. Tremaine. *Galactic Dynamics: Second Edition*. Princeton University Press, 2008.

[146] A. S. Eddington. The Distribution of Stars in Globular Clusters. *Monthly Notices of the Royal Astronomical Society*, 76(7):572–585, May 1916.

[147] Thomas Lacroix, Martin Stref, and Julien Lavalle. Anatomy of Eddington-like inversion methods in the context of dark matter searches. *Journal of Cosmology and Astroparticle Physics*, 2018(09):040–040, September 2018.

[148] Mihael Petač and Piero Ullio. Two-integral distribution functions in axisymmetric galaxies: Implications for dark matter searches. *Physical Review D*, 99(4):043003, February 2019.

[149] C. Hunter and Edward Qian. Two-integral distribution functions for axisymmetric galaxies. *Monthly Notices of the Royal Astronomical Society*, 262:401–428, May 1993.

[150] E. E. Qian, P. T. de Zeeuw, R. P. van der Marel, and C. Hunter. Axisymmetric galaxy models with central black holes, with an application to M32. *Mon.Not.Roy.Astron.Soc.*, 274:602, 1995.

[151] D. Lynden-Bell. Stellar dynamics: Exact solution of the self-gravitation equation. *Monthly Notices of the Royal Astronomical Society*, 123:447, 1962.

[152] Jason L. Sanders and James Binney. A review of action estimation methods for galactic dynamics. *Monthly Notices of the Royal Astronomical Society*, 457(2):2107, April 2016.

[153] N. Cretton, P. Tim de Zeeuw, Roeland P. van der Marel, and Hans-Walter Rix. Axisymmetric Three-Integral Models for Galaxies. *The Astrophysical Journal Supplement Series*, 124(2):383, October 1999.

[154] Eugene Vasiliev. A new code for orbit analysis and Schwarzschild modelling of triaxial stellar systems. *Monthly Notices of the Royal Astronomical Society*, 434(4):3174, October 2013.

[155] Julio F. Navarro, Carlos S. Frenk, and Simon D. M. White. A Universal Density Profile from Hierarchical Clustering. *The Astrophysical Journal*, 490(2):493–508, December 1997.

[156] P. Salucci, A. Lapi, C. Tonini, et al. The universal rotation curve of spiral galaxies - II. The dark matter distribution out to the virial radius. *Monthly Notices of the Royal Astronomical Society*, 378(1):41–47, June 2007.

[157] Stephane Courteau and Aaron A. Dutton. On the Global Mass Distribution in Disk Galaxies. *The Astrophysical Journal*, 801(2):L20, March 2015.

[158] Paul J. McMillan. The mass distribution and gravitational potential of the Milky Way. *Monthly Notices of the Royal Astronomical Society*, 465(1):76–94, February 2017.

[159] Stephane Courteau and Hans-Walter Rix. Maximal Disks and the Tully-Fisher Relation. *The Astrophysical Journal*, 513(2):561, March 1999.

[160] Yoshiaki Sofue. Rotation Curve Decomposition for Size-Mass Relations of Bulge, Disk, and Dark Halo in Spiral Galaxies. October 2015.

[161] Jo Bovy, Anita Bahmanyar, Tobias K. Fritz, and Nitya Kallivayalil. The Shape of the Inner Milky Way Halo from Observations of the Pal 5 and GD–1 Stellar Streams. *The Astrophysical Journal*, 833(1):31, 2016.

[162] N. Wyn Evans, Ciaran A. J. O'Hare, and Christopher McCabe. SHM^{++}: A Refinement of the Standard Halo Model for Dark Matter Searches in Light of the Gaia Sausage. *arXiv:1810.11468 [astro-ph, physics:hep-ex, physics:hep-ph]*, October 2018.

[163] William H. Press and Paul Schechter. Formation of Galaxies and Clusters of Galaxies by Self-Similar Gravitational Condensation. *The Astrophysical Journal*, 187:425–438, February 1974.

[164] Ravi K. Sheth and Giuseppe Tormen. Large-scale bias and the peak background split. *Monthly Notices of the Royal Astronomical Society*, 308(1):119–126, September 1999.

[165] George Lake. Detectability of γ-rays from clumps of dark matter. *Nature*, 346(6279):39–40, July 1990.

[166] Felix Stoehr, Simon D. M. White, Volker Springel, Giuseppe Tormen, and Naoki Yoshida. Dark matter annihilation in the halo of the Milky Way. *Monthly Notices of the Royal Astronomical Society*, 345(4):1313–1322, November 2003.

[167] Savvas M. Koushiappas, Andrew R. Zentner, and Terrence P. Walker. Observability of gamma rays from neutralino annihilations in the Milky Way substructure. *Physical Review D*, 69(4):043501, February 2004.

[168] Shin'ichiro Ando, Tomoaki Ishiyama, and Nagisa Hiroshima. Halo substructure boosts to the signatures of dark matter annihilation. *arXiv:1903.11427 [astro-ph]*, March 2019.

[169] Martin Stref, Thomas Lacroix, and Julien Lavalle. Remnants of Galactic subhalos and their impact on indirect dark matter searches. *arXiv:1905.02008 [astro-ph, physics:hep-ph]*, May 2019.

[170] Katherine Freese, Paolo Gondolo, Heidi Jo Newberg, and Matthew Lewis. Effects of the Sagittarius Dwarf Tidal Stream on Dark Matter Detectors. *Physical Review Letters*, 92(11):111301, March 2004.

[171] Rafael F. Lang and Neal Weiner. Peaked Signals from Dark Matter Velocity Structures in Direct Detection Experiments. *JCAP*, 1006:032, 2010.

[172] Chris W. Purcell. The Sagittarius Impact on Light and Dark Structure in the Milky Way. *ASP Conf.Ser.*, 480:3, 2014.

[173] Michael S. Petersen, Neal Katz, and Martin D. Weinberg. Dynamical response of dark matter to galaxy evolution affects direct-detection experiments. *Phys.Rev.*, D94(12):123013, December 2016.

[174] Veniamin Berezinsky, Vyacheslav Dokuchaev, and Yury Eroshenko. Small-scale clumps in the galactic halo and dark matter annihilation. *Physical Review D*, 68(10):103003, November 2003.

[175] Jorge Peñarrubia and Andrew J. Benson. Effects of dynamical evolution on the distribution of substructures. *Monthly Notices of the Royal Astronomical Society*, 364(3):977–989, December 2005.

[176] Richard Bartels and Shin'ichiro Ando. Boosting the annihilation boost: Tidal effects on dark matter subhalos and consistent luminosity modeling. *Physical Review D*, 92(12):123508, December 2015.

[177] Martin Stref and Julien Lavalle. Modeling dark matter subhalos in a constrained galaxy: Global mass and boosted annihilation profiles. *Physical Review D*, 95(6):063003, March 2017.

[178] Tyler Kelley, James S. Bullock, Shea Garrison-Kimmel, et al. Phat ELVIS: The inevitable effect of the Milky Way's disc on its dark matter subhaloes. *Monthly Notices of the Royal Astronomical Society*, 487(3):4409–4423, August 2019.

[179] Raphaël Errani and Jorge Peñarrubia. Can tides disrupt cold dark matter subhaloes? *arXiv:1906.01642 [astro-ph]*, June 2019.

[180] Go Ogiya, Frank C. van den Bosch, Oliver Hahn, et al. DASH: a library of dynamical subhalo evolution. *arXiv:1901.08601 [astro-ph]*, January 2019.

[181] Vicente Rodriguez-Gomez, Shy Genel, Mark Vogelsberger, et al. The merger rate of galaxies in the Illustris simulation: a comparison with observations and semi-empirical models. *Monthly Notices of the Royal Astronomical Society*, 449(1):49–64, May 2015.

[182] Benjamin L'Huillier, Changbom Park, and Juhan Kim. The ecology of dark matter haloes –I. The rates and types of halo interactions. *Monthly Notices of the Royal Astronomical Society*, 451(1):527–538, July 2015.

[183] Andreea S. Font, Ian G. McCarthy, Amandine M. C. Le Brun, Robert A. Crain, and Lee S. Kelvin. The Diversity of Assembly Histories Leading to Disc Galaxy Formation in a $\textbackslashLambda$CDM Model. *Publications of the Astronomical Society of Australia*, 34, 2017.

[184] G. C. Myeong, N. W. Evans, V. Belokurov, N. C. Amorisco, and S. E. Koposov. Halo substructure in the SDSS–Gaia catalogue: streams and clumps. *Monthly Notices of the Royal Astronomical Society*, 475(2):1537–1548, April 2018.

[185] Amina Helmi, Carine Babusiaux, Helmer H. Koppelman, et al. The merger that led to the formation of the Milky Way's inner stellar halo and thick disk. *Nature*, 563(7729):85, November 2018.

[186] J. M. Diederik Kruijssen, Joel L. Pfeffer, Marta Reina-Campos, Robert A. Crain, and Nate Bastian. The formation and assembly history of the Milky Way revealed by its globular cluster population. *Monthly Notices of the Royal Astronomical Society*, 486(3):3180–3202, July 2019.

[187] Lina Necib, Mariangela Lisanti, and Vasily Belokurov. Dark Matter in Disequilibrium: The Local Velocity Distribution from SDSS-Gaia. *arXiv:1807.02519 [astro-ph, physics:hep-ph]*, July 2018.

[188] Ron Cowen. Andromeda on collision course with the Milky Way. *Nature News*.

[189] Sangmo Tony Sohn, Jay Anderson, and Roeland P. van der Marel. The M31 Velocity Vector. I. Hubble Space Telescope Proper-motion Measurements. *The Astrophysical Journal*, 753(1):7, July 2012.

[190] Roeland P. van der Marel, Mark A. Fardal, Sangmo Tony Sohn, et al. First Gaia Dynamics of the Andromeda System: DR2 Proper Motions, Orbits, and Rotation of M31 and M33. *The Astrophysical Journal*, 872(1):24, February 2019.

[191] Lina Necib, Mariangela Lisanti, Shea Garrison-Kimmel, et al. Under the Firelight: Stellar Tracers of the Local Dark Matter Velocity Distribution in the Milky Way. October 2018.

[192] Jonah Herzog-Arbeitman, Mariangela Lisanti, Piero Madau, and Lina Necib. Empirical Determination of Dark Matter Velocities Using Metal-Poor Stars. *Physical Review Letters*, 120(4):041102, January 2018.

[193] Jonah Herzog-Arbeitman, Mariangela Lisanti, and Lina Necib. The metal-poor stellar halo in RAVE-TGAS and its implications for the velocity distribution of dark matter. *Journal of Cosmology and Astroparticle Physics*, 2018(04):052–052, April 2018.

[194] Lina Necib, Mariangela Lisanti, and Vasily Belokurov. Inferred Evidence for Dark Matter Kinematic Substructure with SDSS–Gaia. *The Astrophysical Journal*, 874(1):3, March 2019.

[195] P. Salucci, F. Nesti, G. Gentile, and C. Frigerio Martins. The dark matter density at the Sun's location. *Astronomy & Astrophysics*, 523:A83, November 2010.

[196] Riccardo Catena and Piero Ullio. A novel determination of the local dark matter density. *Journal of Cosmology and Astroparticle Physics*, 2010(08):004–004, August 2010.

[197] M. Weber and W. de Boer. Determination of the local dark matter density in our Galaxy. *Astronomy & Astrophysics*, 509:A25, January 2010.

[198] Fabrizio Nesti and Paolo Salucci. The Dark Matter halo of the Milky Way, AD 2013. *Journal of Cosmology and Astroparticle Physics*, 2013(07):016–016, July 2013.

[199] Fabio Iocco, Miguel Pato, and Gianfranco Bertone. Evidence for dark matter in the inner Milky Way. *Nature Physics*, 11(3):245–248, March 2015.

[200] Anna-Christina Eilers, David W. Hogg, Hans-Walter Rix, and Melissa K. Ness. The Circular Velocity Curve of the Milky Way from 5 to 25 kpc. *The Astrophysical Journal*, 871(1):120, January 2019.

[201] P. F. de Salas, K. Malhan, K. Freese, K. Hattori, and M. Valluri. On the estimation of the Local Dark Matter Density using the rotation curve of the Milky Way. *arXiv e-prints*, page arXiv:1906.06133, June 2019.

[202] Jo Bovy and Hans-Walter Rix. A direct dynamical measurement of the Milky Way's disk surface density profile, disk scale length, and dark matter profile at 4 kpc $< r <$ 9 kpc. *The Astrophysical Journal*, 779(2):115, December 2013.

[203] S. Sivertsson, H. Silverwood, J. I. Read, G. Bertone, and P. Steger. The local dark matter density from SDSS-SEGUE G-dwarfs. *Monthly Notices of the Royal Astronomical Society*, 478(2):1677–1693, August 2018.

[204] Jorrit H. J. Hagen and Amina Helmi. The vertical force in the solar neighbourhood using red clump stars in TGAS and RAVE - Constraints on the local dark matter density. *Astronomy & Astrophysics*, 615:A99, July 2018.

[205] Jatan Buch, Shing Chau (John) Leung, and JiJi Fan. Using Gaia DR2 to constrain local dark matter density and thin dark disk. *Journal of Cosmology and Astroparticle Physics*, 2019(04):026, April 2019.

[206] A. Widmark. Measuring the local matter density using Gaia DR2. *Astronomy & Astrophysics*, 623:A30, March 2019.

[207] Gaia Collaboration, A. G. A. Brown, A. Vallenari, et al. Gaia Data Release 2. Summary of the contents and survey properties. *Astronomy & Astrophysics*, 616:A1, August 2018.

[208] A. Udalski, M. K. Szymański, and G. Szymański. OGLE-IV: Fourth Phase of the Optical Gravitational Lensing Experiment. *Acta Astronomica*, 65(1):1, March 2015.

[209] Gravity Collaboration, R. Abuter, A. Amorim, et al. Detection of the gravitational redshift in the orbit of the star S2 near the Galactic centre massive black hole. *Astronomy and Astrophysics*, 615:L15, July 2018.

[210] R. Schoenrich, J. Binney, and W. Dehnen. Local Kinematics and the Local Standard of Rest. *Monthly Notices of the Royal Astronomical Society*, 403(4):1829–1833, April 2010.

[211] Przemek Mróz, Andrzej Udalski, Dorota M. Skowron, et al. Rotation Curve of the Milky Way from Classical Cepheids. *The Astrophysical Journal*, 870(1):L10, January 2019.

[212] Y. Sofue, M. Honma, and T. Omodaka. Unified Rotation Curve of the Galaxy – Decomposition into de Vaucouleurs Bulge, Disk, Dark Halo, and the 9-kpc Rotation Dip –. *Publications of the Astronomical Society of Japan*, 61(2):227–236, April 2009.

[213] Y. Huang, X.-W. Liu, H.-B. Yuan, et al. The Milky Way's rotation curve out to 100 kpc and its constraint on the Galactic mass distribution. *Monthly Notices of the Royal Astronomical Society*, 463(3):2623–2639, December 2016.

[214] Walter Dehnen, Dean E. McLaughlin, and Jalpesh Sachania. The velocity dispersion and mass profile of the Milky Way. *Monthly Notices of the Royal Astronomical Society*, 369(4):1688–1692, July 2006.

[215] Miguel Pato and Fabio Iocco. `galkin`: a new compilation of the Milky Way rotation curve data. *SoftwareX*, 6:54–62, 2017.

[216] Sergey Khoperskov, Paola Di Matteo, Ortwin Gerhard, et al. The echo of the bar buckling: Phase-space spirals in Gaia Data Release 2. *Astronomy & Astrophysics*, 622:L6, February 2019.

[217] Luis Martinez-Medina, Barbara Pichardo, Antonio Peimbert, and Octavio Valenzuela. From ridges in the velocity distribution to wiggles in the rotation curve. *Monthly Notices of the Royal Astronomical Society*, 485(1):L104, May 2019.

[218] Morgan Bennett and Jo Bovy. Vertical waves in the solar neighbourhood in Gaia DR2. *Monthly Notices of the Royal Astronomical Society*, 482(1):1417, January 2019.

[219] Angus A. Williams, Vasily Belokurov, Andrew R. Casey, and N. Wyn Evans. On the run: mapping the escape speed across the Galaxy with SDSS. *Monthly Notices of the Royal Astronomical Society*, 468(2):2359–2371, June 2017.

[220] Alis J. Deason, Azadeh Fattahi, Vasily Belokurov, et al. The local high-velocity tail and the Galactic escape speed. *Monthly Notices of the Royal Astronomical Society*, 485(3):3514–3526, May 2019.

[221] G. Monari, B. Famaey, I. Carrillo, et al. The escape speed curve of the Galaxy obtained from Gaia DR2 implies a heavy Milky Way. *Astronomy & Astrophysics*, 616:L9, August 2018.

[222] T. K. Fritz, G. Battaglia, M. S. Pawlowski, et al. Gaia DR2 proper motions of dwarf galaxies within 420 kpc - Orbits, Milky Way mass, tidal influences, planar alignments, and group infall. *Astronomy & Astrophysics*, 619:A103, November 2018.

[223] Eugene Vasiliev. Proper motions and dynamics of the Milky Way globular cluster system from Gaia DR2. *Monthly Notices of the Royal Astronomical Society*, 484(2):2832–2850, April 2019.

[224] Lorenzo Posti and Amina Helmi. Mass and shape of the Milky Way's dark matter halo with globular clusters from Gaia and Hubble. *Astronomy & Astrophysics*, 621:A56, January 2019.

[225] Gwendolyn Eadie and Mario Jurić. The Cumulative Mass Profile of the Milky Way as Determined by Globular Cluster Kinematics from Gaia DR2. *The Astrophysical Journal*, 875(2):159, April 2019.

[226] Laura L. Watkins, Roeland P. van der Marel, Sangmo Tony Sohn, and N. Wyn Evans. Evidence for an Intermediate-mass Milky Way from Gaia DR2 Halo Globular Cluster Motions. *The Astrophysical Journal*, 873(2):118, March 2019.

[227] Thomas M. Callingham, Marius Cautun, Alis J. Deason, et al. The mass of the Milky Way from satellite dynamics. *Monthly Notices of the Royal Astronomical Society*, 484(4):5453–5467, April 2019.

[228] Joss Bland-Hawthorn and Ortwin Gerhard. The Galaxy in Context: Structural, Kinematic and Integrated Properties. *Annual Review of Astronomy and Astrophysics*, 54(1):529–596, September 2016.

[229] Joss Bland-Hawthorn, Sanjib Sharma, Thor Tepper-Garcia, et al. The GALAH survey and Gaia DR2: dissecting the stellar disc's phase space by age, action, chemistry and location. *Monthly Notices of the Royal Astronomical Society*, 486(1):1167–1191, June 2019.

[230] A. Burkert. The Structure of Dark Matter Halos in Dwarf Galaxies. *The Astrophysical Journal*, 447(1), July 1995.

[231] Christopher Wegg, Ortwin Gerhard, and Marie Bieth. The gravitational force field of the Galaxy measured from the kinematics of RR Lyrae in Gaia. *Monthly Notices of the Royal Astronomical Society*, 485(3):3296–3316, May 2019.

[232] Daniel Foreman-Mackey, David W. Hogg, Dustin Lang, and Jonathan Goodman. emcee : The MCMC Hammer. *Publications of the Astronomical Society of the Pacific*, 125(925):306–312, March 2013.

[233] Christopher Wegg, Ortwin Gerhard, and Matthieu Portail. MOA-II Galactic microlensing constraints: the inner Milky Way has a low dark matter fraction and a near maximal disc. *Monthly Notices of the Royal Astronomical Society*, 463(1):557–570, November 2016.

[234] E. Pouliasis, P. Di Matteo, and M. Haywood. A Milky Way with a massive, centrally concentrated thick disc: new Galactic mass models for orbit computations. *Astronomy & Astrophysics*, 598:A66, February 2017.

[235] Riccardo Catena and Piero Ullio. The local dark matter phase-space density and impact on WIMP direct detection. *Journal of Cosmology and Astroparticle Physics*, 2012(05):005–005, May 2012.

[236] Nassim Bozorgnia, Riccardo Catena, and Thomas Schwetz. Anisotropic dark matter distribution functions and impact on WIMP direct detection. *Journal of Cosmology and Astroparticle Physics*, 2013(12):050–050, December 2013.

[237] Mattia Fornasa and Anne M. Green. Self-consistent phase-space distribution function for the anisotropic dark matter halo of the Milky Way. *Physical Review D*, 89(6):063531, March 2014.

[238] J. D. Vergados, Ch. C. Moustakidis, and D. Owen. Dark matter searches employing asymmetric velocity distributions obtained via the Eddington approach. *New Astronomy*, 47:29–41, August 2016.

[239] Patrick J. Fox, Jia Liu, and Neal Weiner. Integrating out astrophysical uncertainties. *Physical Review D*, 83(10):103514, May 2011.

[240] Mads T. Frandsen, Felix Kahlhoefer, Christopher McCabe, Subir Sarkar, and Kai Schmidt-Hoberg. Resolving astrophysical uncertainties in dark matter direct detection. *Journal of Cosmology and Astroparticle Physics*, 2012(01):024–024, January 2012.

[241] Paolo Gondolo and Graciela B. Gelmini. Halo independent comparison of direct dark matter detection data. *Journal of Cosmology and Astroparticle Physics*, 2012(12):015–015, December 2012.

[242] Juan Herrero-Garcia. Halo-independent tests of dark matter direct detection signals. *PoS*, EPS-HEP2015:406, October 2015.

[243] Francesc Ferrer, Alejandro Ibarra, and Sebastian Wild. A novel approach to derive halo-independent limits on dark matter properties. *Journal of Cosmology and Astroparticle Physics*, 2015(09):052–052, September 2015.

[244] Riccardo Catena, Alejandro Ibarra, Andreas Rappelt, and Sebastian Wild. Halo-independent comparison of direct detection experiments in the effective theory of dark matter-nucleon interactions. *JCAP*, 1807(07):028, July 2018.

[245] Alejandro Ibarra, Bradley J. Kavanagh, and Andreas Rappelt. Bracketing the impact of astrophysical uncertainties on local dark matter searches. *Journal of Cosmology and Astroparticle Physics*, 2018(12):018–018, December 2018.

[246] J. D. Lewin and P. F. Smith. Review of mathematics, numerical factors, and corrections for dark matter experiments based on elastic nuclear recoil. *Astroparticle Physics*, 6(1):87–112, December 1996.

[247] A. Liam Fitzpatrick, Wick Haxton, Emanuel Katz, Nicholas Lubbers, and Yiming Xu. The effective field theory of dark matter direct detection. *Journal of Cosmology and Astroparticle Physics*, 2013(02):004–004, February 2013.

[248] Nikhil Anand, A. Liam Fitzpatrick, and W. C. Haxton. Model-independent WIMP Scattering Responses and Event Rates: A Mathematica Package for Experimental Analysis. *arXiv e-prints*, page arXiv:1308.6288, August 2013.

[249] James B. Dent, Lawrence M. Krauss, Jayden L. Newstead, and Subir Sabharwal. General analysis of direct dark matter detection: From microphysics to observational signatures. *Physical Review D*, 92(6):063515, September 2015.

[250] Fady Bishara, Joachim Brod, Benjamin Grinstein, and Jure Zupan. DirectDM: a tool for dark matter direct detection. *arXiv e-prints*, page arXiv:1708.02678, August 2017.

[251] Fady Bishara, Joachim Brod, Benjamin Grinstein, and Jure Zupan. Renormalization Group Effects in Dark Matter Interactions. *arXiv e-prints*, page arXiv:1809.03506, September 2018.

[252] Anne M. Green. Astrophysical uncertainties on the local dark matter distribution and direct detection experiments. *Journal of Physics G: Nuclear and Particle Physics*, 44(8):084001, August 2017.

[253] Youjia Wu, Katherine Freese, Chris Kelso, Patrick Stengel, and Monica Valluri. Uncertainties in Direct Dark Matter Detection in Light of Gaia. *arXiv e-prints*, page arXiv:1904.04781, April 2019.

[254] Torsten Bringmann, Jan Conrad, Jonathan M. Cornell, et al. DarkBit: a GAMBIT module for computing dark matter observables and likelihoods. *The European Physical Journal C*, 77(12):831, December 2017.

[255] Katherine Freese, Mariangela Lisanti, and Christopher Savage. Colloquium: Annual modulation of dark matter. *Reviews of Modern Physics*, 85(4):1561–1581, November 2013.

[256] Ya B. Zel'dovich, A. A. Klypin, M. Yu Khlopov, and V. M. Chechetkin. Astrophysical constrains on the mass of heavy stable neutral leptons. *Yadernaya Fizika*, 31(5):1286–1294, 1980.

[257] Joseph Silk and Hans Bloemen. A gamma-ray constraint on the nature of dark matter. *The Astrophysical Journal*, 313:L47–L51, February 1987.

[258] Kathryn M. Zurek. Multicomponent dark matter. *Physical Review D*, 79(11):115002, June 2009.

[259] Francesco D'Eramo and Jesse Thaler. Semi-annihilation of dark matter. *Journal of High Energy Physics*, 2010(6):109, June 2010.

[260] Daniel Feldman, Zuowei Liu, Pran Nath, and Gregory Peim. Multicomponent dark matter in supersymmetric hidden sector extensions. *Physical Review D*, 81(9):095017, May 2010.

[261] Ze-Peng Liu, Yue-Liang Wu, and Yu-Feng Zhou. Enhancement of dark matter relic density from late time dark matter conversions. *The European Physical Journal C*, 71(10):1749, October 2011.

[262] Mayumi Aoki, Michael Duerr, Jisuke Kubo, and Hiroshi Takano. Multicomponent dark matter systems and their observation prospects. *Physical Review D*, 86(7):076015, October 2012.

[263] Geneviève Bélanger and Jong-Chul Park. Assisted freeze-out. *Journal of Cosmology and Astroparticle Physics*, 2012(03):038–038, March 2012.

[264] Michael L. Graesser, Ian M. Shoemaker, and Luca Vecchi. Asymmetric WIMP dark matter. *Journal of High Energy Physics*, 2011(10):110, October 2011.

[265] Jason Kumar. Asymmetric dark matter. *AIP Conference Proceedings*, 1604(1):389–396, June 2014.

[266] J. McDonald. Weakly interacting massive particle densities in decaying-particle-dominated cosmology. *Physical Review D*, 43(4):1063–1068, February 1991.

[267] Marc Kamionkowski and Michael S. Turner. Thermal relics: Do we know their abundances? *Physical Review D*, 42(10):3310–3320, November 1990.

[268] Francesco D'Eramo, Nicolas Fernandez, and Stefano Profumo. When the universe expands too fast: relentless dark matter. *Journal of Cosmology and Astroparticle Physics*, 2017(05):012–012, May 2017.

[269] Lawrence J. Hall, Karsten Jedamzik, John March-Russell, and Stephen M. West. Freeze-in production of FIMP dark matter. *Journal of High Energy Physics*, 2010(3):80, March 2010.

[270] A. Sommerfeld. Über die Beugung und Bremsung der Elektronen. *Annalen der Physik*, 403:257–330, 1931.

[271] Junji Hisano, Shigeki Matsumoto, and Mihoko M. Nojiri. Explosive Dark Matter Annihilation. *Physical Review Letters*, 92(3):031303, January 2004.

[272] Junji Hisano, Shigeki Matsumoto, Mihoko M. Nojiri, and Osamu Saito. Nonperturbative effect on dark matter annihilation and gamma ray signature from the galactic center. *Physical Review D*, 71(6):063528, March 2005.

[273] R. Iengo. Sommerfeld enhancement for a Yukawa potential. *arXiv e-prints*, page arXiv:0903.0317, March 2009.

[274] S Cassel. Sommerfeld factor for arbitrary partial wave processes. *Journal of Physics G: Nuclear and Particle Physics*, 37(10):105009, October 2010.

[275] Jonathan L. Feng, Manoj Kaplinghat, and Hai-Bo Yu. Halo-Shape and Relic-Density Exclusions of Sommerfeld-Enhanced Dark Matter Explanations of Cosmic Ray Excesses. *Physical Review Letters*, 104(15):151301, April 2010.

[276] Tracy R Slatyer. The Sommerfeld enhancement for dark matter with an excited state. *Journal of Cosmology and Astroparticle Physics*, 2010(02):028–028, February 2010.

[277] Nima Arkani-Hamed, Douglas P. Finkbeiner, Tracy R. Slatyer, and Neal Weiner. A theory of dark matter. *Physical Review D*, 79(1):015014, January 2009.

[278] Konstantin Belotsky, Ruslan Budaev, Alexander Kirillov, and Maxim Laletin. Fermi-LAT kills dark matter interpretations of AMS-02 data. Or not? *Journal of Cosmology and Astroparticle Physics*, 2017(01):021–021, January 2017.

[279] James B. Dent, Sourish Dutta, and Robert J. Scherrer. Thermal relic abundances of particles with velocity-dependent interactions. *Physics Letters B*, 687(4):275–279, April 2010.

[280] Mihael Petač, Piero Ullio, and Mauro Valli. On velocity-dependent dark matter annihilations in dwarf satellites. *Journal of Cosmology and Astroparticle Physics*, 2018(12):039–039, December 2018.

[281] Steen H. Hansen and Ben Moore. A universal density slope – Velocity anisotropy relation for relaxed structures. *New Astronomy*, 11(5):333–338, March 2006.

[282] Radosław Wojtak, Ewa L. Łokas, Gary A. Mamon, et al. The distribution function of dark matter in massive haloes. *Monthly Notices of the Royal Astronomical Society*, 388(2):815–828, August 2008.

[283] Aaron D. Ludlow, Julio F. Navarro, Simon D. M. White, et al. The density and pseudo-phase-space density profiles of cold dark matter haloes: The density and PPSD profiles of CDM haloes. *Monthly Notices of the Royal Astronomical Society*, 415(4):3895–3902, August 2011.

[284] Doron Lemze, Rick Wagner, Yoel Rephaeli, et al. Profiles of dark matter velocity anisotropy in simulated clusters. *The Astrophysical Journal*, 752(2):141, June 2012.

[285] Martin Sparre and Steen H Hansen. The behaviour of shape and velocity anisotropy in dark matter haloes. *Journal of Cosmology and Astroparticle Physics*, 2012(10):049–049, October 2012.

[286] Carlos A. Vera-Ciro, Laura V. Sales, Amina Helmi, and Julio F. Navarro. The shape of dark matter subhaloes in the Aquarius simulations. *Monthly Notices of the Royal Astronomical Society*, 439(3):2863–2872, April 2014.

[287] J. An and N. W. Evans. A Cusp Slope – Central Anisotropy Theorem. *The Astrophysical Journal*, 642(2):752–758, May 2006.

[288] L. P. Osipkov. Spherical systems of gravitating bodies with an ellipsoidal velocity distribution. *Pisma v Astronomicheskii Zhurnal*, 5:77–80, February 1979.

[289] D. Merritt. Spherical stellar systems with spheroidal velocity distributions. *The Astronomical Journal*, 90:1027, June 1985.

[290] H. C. Plummer. On the Problem of Distribution in Globular Star Clusters: (Plate 8.). *Monthly Notices of the Royal Astronomical Society*, 71(5):460–470, March 1911.

[291] H. Dejonghe. A completely analytical family of anisotropic Plummer models. *Monthly Notices of the Royal Astronomical Society*, 224(1):13–39, January 1987.

[292] M. Irwin and D. Hatzidimitriou. Structural parameters for the Galactic dwarf spheroidals. *Monthly Notices of the Royal Astronomical Society*, 277:1354–1378, December 1995.

[293] Alan W. McConnachie. The observed properties of dwarf galaxies in and around the Local Group. *The Astronomical Journal*, 144(1):4, July 2012.

[294] Louis E. Strigari, Savvas M. Koushiappas, James S. Bullock, and Manoj Kaplinghat. Precise constraints on the dark matter content of Milky Way dwarf galaxies for gamma-ray experiments. *Physical Review D*, 75(8):083526, April 2007.

[295] A. Charbonnier, C. Combet, M. Daniel, et al. Dark matter profiles and annihilation in dwarf spheroidal galaxies: prospectives for present and future γ-ray observatories - I. The classical dwarf spheroidal galaxies: γ-ray from dark matter annihilation in dSphs. *Monthly Notices of the Royal Astronomical Society*, 418(3):1526–1556, December 2011.

[296] Alex Geringer-Sameth, Savvas M. Koushiappas, and Matthew Walker. Dwarf galaxy annihilation and decay emission profiles for dark matter experiments. *The Astrophysical Journal*, 801(2):74, 2015.

[297] David J. R. Campbell, Carlos S. Frenk, Adrian Jenkins, et al. Knowing the unknowns: uncertainties in simple estimators of galactic dynamical masses. *Monthly Notices of the Royal Astronomical Society*, 469(2):2335–2360, August 2017.

[298] Alejandro González-Samaniego, James S. Bullock, Michael Boylan-Kolchin, et al. Dwarf galaxy mass estimators versus cosmological simulations. *Monthly Notices of the Royal Astronomical Society*, 472(4):4786–4796, December 2017.

[299] D. Massari, M. A. Breddels, A. Helmi, et al. 3d motions in the Sculptor dwarf galaxy as a glimpse of a new era. *Nature Astronomy*, November 2017.

[300] Maarten Baes and Emmanuel Van Hese. Dynamical models with a general anisotropy profile. *Astronomy & Astrophysics*, 471(2):419–432, 2007.

[301] V. Bonnivard and others. Dark matter annihilation and decay in dwarf spheroidal galaxies: The classical and ultrafaint dSphs. *Monthly Notices of the Royal Astronomical Society*, 453(1):849–867, 2015.

[302] Matthew G. Walker, Mario Mateo, Edward W. Olszewski, et al. A universal mass profile for dwarf spheroidal galaxies? *The Astrophysical Journal*, 704(2):1274–1287, October 2009.

[303] Matthew G. Walker, Mario Mateo, and Edward W. Olszewski. Stellar velocities in the Carina, Fornax, Sculptor and Sextans dSph galaxies: Data from the Magellan/MMFS Survey. *The Astronomical Journal*, 137(2):3100–3108, February 2009.

[304] Mario Mateo, Edward W. Olszewski, and Matthew G. Walker. The velocity dispersion profile of the remote dwarf spheroidal galaxy Leo I: A tidal hit and run? *The Astrophysical Journal*, 675(1):201, 2008.

[305] Matthew G. Walker, Edward W. Olszewski, and Mario Mateo. Bayesian analysis of resolved stellar spectra: application to MMT/Hectochelle observations of the Draco dwarf spheroidal. *Monthly Notices of the Royal Astronomical Society*, 448(3):2717–2732, 2015.

[306] Meghin E. Spencer, Mario Mateo, and Matthew G. Walker. A Multi-epoch Kinematic Study of the Remote Dwarf Spheroidal Galaxy Leo II. *The Astrophysical Journal*, 836(2):202, February 2017.

[307] J. Binney and G. A. Mamon. M/L and velocity anisotropy from observations of spherical galaxies, or must M87 have a massive black hole? *Monthly Notices of the Royal Astronomical Society*, 200(2):361–375, September 1982.

[308] Giuseppina Battaglia, Amina Helmi, and Maarten Breddels. Internal kinematics and dynamical models of dwarf spheroidal galaxies around the Milky Way. *New Astronomy Reviews*, 57(3-4):52–79, September 2013.

[309] Matthew Walker. Dark Matter in the Galactic Dwarf Spheroidal Satellites. In Terry D. Oswalt and Gerard Gilmore, editors, *Planets, Stars and Stellar Systems*, pages 1039–1089. Springer Netherlands, Dordrecht, 2013.

[310] J. I. Read and P. Steger. How to break the density-anisotropy degeneracy in spherical stellar systems. *Monthly Notices of the Royal Astronomical Society*, 471(4):4541–4558, November 2017.

[311] Jonathan Goodman and Jonathan Weare. Ensemble samplers with affine invariance. *Communications in Applied Mathematics and Computational Science*, 5(1):65–80, January 2010.

[312] J. Buchner, A. Georgakakis, K. Nandra, et al. X-ray spectral modelling of the AGN obscuring region in the CDFS: Bayesian model selection and catalogue. *Astronomy & Astrophysics*, 564:A125, April 2014.

[313] F. Feroz, M. P. Hobson, E. Cameron, and A. N. Pettitt. Importance Nested Sampling and the MultiNest Algorithm. *arXiv:1306.2144 [astro-ph, physics:physics, stat]*, June 2013.

[314] M. G. Walker, C. Combet, J. A. Hinton, D. Maurin, and M. I. Wilkinson. Dark matter in the classical dwarf spheroidal galaxies: a robust constraint on the astrophysical factor for γ-ray flux calculations. *The Astrophysical Journal*, 733(2):L46, June 2011.

[315] Kimberly K. Boddy, Jason Kumar, Louis E. Strigari, and Mei-Yu Wang. Sommerfeld-enhanced J -factors for dwarf spheroidal galaxies. *Physical Review D*, 95(12), June 2017.

[316] Bo-Qiang Lu, Yue-Liang Wu, Wei-Hong Zhang, and Yu-Feng Zhou. Constraints on the Sommerfeld- enhanced dark matter annihilation from the gamma rays of subhalos and dwarf galaxies. *Journal of Cosmology and Astroparticle Physics*, 2018(04):035–035, April 2018.

[317] Sebastian Bergström, Riccardo Catena, Andrea Chiappo, et al. J-factors for self-interacting dark matter in 20 dwarf spheroidal galaxies. *arXiv:1712.03188 [astro-ph, physics:hep-ph]*, December 2017.

[318] Piero Ullio and Mauro Valli. A critical reassessment of particle Dark Matter limits from dwarf satellites. *Journal of Cosmology and Astroparticle Physics*, 2016(07):025, 2016.

[319] Paul Bode, Jeremiah P. Ostriker, and Neil Turok. Halo Formation in Warm Dark Matter Models. *The Astrophysical Journal*, 556(1):93–107, July 2001.

[320] Dan Hooper, Manoj Kaplinghat, Louis E. Strigari, and Kathryn M. Zurek. MeV dark matter and small scale structure. *Physical Review D*, 76(10):103515, November 2007.

[321] Sean Tulin and Hai-Bo Yu. Dark Matter Self-interactions and Small Scale Structure. *Physics Reports*, 730:1–57, February 2018.

[322] Tansu Daylan, Francis-Yan Cyr-Racine, Ana Diaz Rivero, Cora Dvorkin, and Douglas P. Finkbeiner. Probing the Small-scale Structure in Strongly Lensed Systems via Transdimensional Inference. *The Astrophysical Journal*, 854(2):141, February 2018.

[323] Keith Bechtol, Alex Drlica-Wagner, Kevork N. Abazajian, et al. Dark Matter Science in the Era of LSST. *arXiv:1903.04425 [astro-ph, physics:hep-ex]*, March 2019.

[324] V. Belokurov, D. B. Zucker, N. W. Evans, et al. Cats and Dogs, Hair and a Hero: A Quintet of New Milky Way Companions*. *The Astrophysical Journal*, 654(2):897, January 2007.

[325] K. Bechtol, A. Drlica-Wagner, E. Balbinot, et al. Eight new milky way companions discovered in first-year dark energy survey data. *The Astrophysical Journal*, 807(1):50, June 2015.

[326] Joshua D. Simon. The Faintest Dwarf Galaxies. *arXiv:1901.05465 [astro-ph]*, January 2019. arXiv: 1901.05465.

[327] Robert Feldmann and Douglas Spolyar. Detecting dark matter substructures around the Milky Way with Gaia. *Monthly Notices of the Royal Astronomical Society*, 446(1):1000–1012, January 2015.

[328] Malte Buschmann, Joachim Kopp, Benjamin R. Safdi, and Chih-Liang Wu. Stellar Wakes from Dark Matter Subhalos. *Physical Review Letters*, 120(21):211101, May 2018.

[329] L. Lindegren, J. Hernández, A. Bombrun, et al. Gaia Data Release 2 - The astrometric solution. *Astronomy & Astrophysics*, 616:A2, August 2018.

[330] Yong Ren and Xuemin Cheng. Review of convolutional neural network optimization and training in image processing. In *Tenth International Symposium on Precision Engineering Measurements and Instrumentation*, volume 11053, page 1105331. International Society for Optics and Photonics, March 2019.

[331] Waseem Rawat and Zenghui Wang. Deep Convolutional Neural Networks for Image Classification: A Comprehensive Review. *Neural Computation*, 29(9):2352–2449, June 2017.

[332] J. A. Fillmore and P. Goldreich. Self-similar gravitational collapse in an expanding universe. *The Astrophysical Journal*, 281:1–8, June 1984.

[333] E. Bertschinger. Self-similar secondary infall and accretion in an Einstein-de Sitter universe. *The Astrophysical Journal Supplement Series*, 58:39–65, May 1985.

[334] Anne M. Green, Stefan Hofmann, and Dominik J. Schwarz. The first WIMPy halos. *Journal of Cosmology and Astroparticle Physics*, 2005(08):003–003, August 2005.

[335] Torsten Bringmann and Stefan Hofmann. Thermal decoupling of WIMPs from first principles. *Journal of Cosmology and Astroparticle Physics*, 2007(04):016–016, April 2007.

[336] Daniel Boyanovsky. Free streaming in mixed dark matter. *Physical Review D*, 77(2):023528, January 2008.

[337] Francis-Yan Cyr-Racine, Kris Sigurdson, Jesús Zavala, et al. ETHOS—an effective theory of structure formation: From dark particle physics to the matter distribution of the Universe. *Physical Review D*, 93(12):123527, June 2016.

[338] Frank C. van den Bosch and Go Ogiya. Dark matter substructure in numerical simulations: a tale of discreteness noise, runaway instabilities, and artificial disruption. *Monthly Notices of the Royal Astronomical Society*, 475(3):4066–4087, April 2018.

[339] Till Sawala, Pauli Pihajoki, Peter H. Johansson, et al. Shaken and stirred: the Milky Way's dark substructures. *Monthly Notices of the Royal Astronomical Society*, 467(4):4383–4400, June 2017.

[340] Denis Erkal, Vasily Belokurov, Jo Bovy, and Jason L. Sanders. The number and size of subhalo-induced gaps in stellar streams. *Monthly Notices of the Royal Astronomical Society*, 463(1):102–119, November 2016.

[341] Nilanjan Banik and Jo Bovy. Effects of baryonic and dark matter substructure on the Pal 5 stream. *Monthly Notices of the Royal Astronomical Society*, 484(2):2009–2020, April 2019.

[342] Gerard Gilmore. Gaia: 3-dimensional census of the Milky Way Galaxy. *Contemporary Physics*, 59(2):155–173, April 2018.

[343] Alex Drlica-Wagner, Yao-Yuan Mao, Susmita Adhikari, et al. Probing the Fundamental Nature of Dark Matter with the Large Synoptic Survey Telescope. *arXiv:1902.01055 [astro-ph, physics:hep-ex, physics:hep-ph]*, February 2019.

[344] T. Marchetti, E. M. Rossi, and A. G. A. Brown. Gaia DR2 in 6d: Searching for the fastest stars in the Galaxy. *Monthly Notices of the Royal Astronomical Society*.

[345] Jason L. Sanders and Payel Das. Isochrone ages for ∼3 million stars with the second Gaia data release. *Monthly Notices of the Royal Astronomical Society*, 481(3):4093–4110, December 2018.

[346] Lev Davidovič Landau, Evgenij M. Lifšic, and Lev Davydovich Landau. *Mechanics*. Number by L. D. Landau and E. M. Lifshitz ; Vol. 1 in Course of theoretical physics. Elsevier, Butterworth Heinemann, Amsterdam [u.a], 3. ed., reprinted edition, 2007. OCLC: 254579166.

[347] G. Coupinot, J. Hecquet, M. Auriere, and R. Futaully. Photometric analysis of astronomical images by the wavelet transform. *Astronomy and Astrophysics*, 259:701, June 1992.

[348] Jean-Luc Starck. Multiscale Methods in Astronomy: Beyond Wavelets. *Astronomical Data Analysis Software and Systems XI*, 281:391, 2002.

[349] Teresa Antoja, Cecilia Mateu, Luis Aguilar, et al. Detection of satellite remnants in the Galactic Halo with Gaia III. Detection limits for Ultra Faint Dwarf Galaxies. *Monthly Notices of the Royal Astronomical Society*, 453(1):541–560, October 2015.

[350] Jo Bovy, David W. Hogg, and Sam T. Roweis. Extreme deconvolution: Inferring complete distribution functions from noisy, heterogeneous and incomplete observations. *The Annals of Applied Statistics*, 5(2B):1657–1677, June 2011.

[351] François Chollet et al. *Keras*. 2015.